ProQuest Number: 10183071

ProQuest 10183071

The development of catalysts for the partial oxidation of ethane

Olivier Sonntag

A thesis submitted in partial fulfilment of the requirements of The Nottingham Trent University for the degree of Doctor of Philosophy

August 2006

Abstract

In this study iron containing bulk and porous materials were developed and characterised for their application as potential heterogeneous catalysts for the partial oxidation of ethane to ethanol. The catalysts comprised bulk and supported iron phosphates as well as supported iron and bimetallic iron-gold. The chosen supports were zeolites of MFI structure and the porous silicate MCM-41, which were modified either during their synthesis or post-synthetically.

The physical properties of the catalysts were analysed by means of X-ray diffraction, atomic absorption, nitrogen adsorption at 77 K, temperature programmed reduction, ammonia adsorption and desorption, nitric oxide adsorption. The catalytic properties of the materials were evaluated by testing them for the partial oxidation of ethane in the gas phase, using either nitrous oxide or oxygen as oxidising agent. Difficulties were encountered in the synthesis of crystalline iron phosphates, but the bulk properties of the silica and silica-alumina supports were merely affected by their post-synthetic treatments; surface areas and long-range order were retained in most cases. The effect of the reducibility of transition metals present or the acidity of the materials on their catalytic properties were investigated. It is believed that some degree of Brønsted acidity is necessary for the production of the hydroxylated oxygenate. Gold only slightly enhanced the oxidative capabilities of the catalysts, and best results were obtained with Fe-ZSM-5 and Fe-MFI materials, when using nitrous oxide as oxidising agent. Following studies of the adsorption of nitrous oxide on the materials, it was decided that the active site for partial oxidative activity was an iron dimer or oligomer of Fe_4O_4 structure, similarly as to the oxidation of benzene to phenol.

Acknowledgements

Table of Contents

Chapter I: <u>Introduction</u>

I-1 Aims and scope of the thesis

This project is aimed at the development of solid catalysts for the gas phase partial oxidation of ethane to ethanol. The catalysis of the oxidation of light hydrocarbons has been long researched [1-3], however few materials developed have been found active enough for a viable industrial application [4]. The main problem lies in the activation of saturated hydrocarbons, which present a lack of functionality, often resulting in little control over the selectivity of the processes. For example alcohols, epoxides and carboxylates are easily produced from alkenes, but attempts to form them from alkanes most often results in over-oxidation [2]. Light alkanes in particular have a high activation barrier, and their functionalisation has been a concern for the petrochemical industry for decades, so as to valorise these products [5]. Recently the production of methanol and ethanol as bio-fuel alternatives for the automotive industry [6] has given research authorities a further incentive to develop good catalysts for the conversion of light alkanes to alcohols. This conversion is achieved in good yields in biological systems involving heme and non-heme [7] based monooxygenase enzymes. It is thought that an inorganic material mimicking the active centre of these enzymes may be the key to the discovery of a successful catalyst. For example iron phosphate has been considered as a mimic to the P-450 cytochrome monooxygenase, because its isolated iron active centre surrounded by phosphate groups has good electron transfer properties and shows some activity to the partial oxidation of methane and ethane to their corresponding alcohols [8]. Similarly zeolites have found uses in direct hydroxylation reactions [9]. They are particularly

interesting in heterogeneous catalysis due to their high thermal stability, ease of modification and implementation, good and tunable redox and acidic properties, and the little environmental concerns about their disposal . Iron modified silicalites of MFI (zeolite socony Mobil FIve [10]) structure are used for the direct hydroxylation of benzene, and some similarities have been found between their catalytically active site and the active centre of the methane monooxygenase enzyme [11].

This thesis proposes the study of the two stated catalysts, namely iron phosphate and iron silicalite, for the desired reaction. The strategies employed for the enhancement of their catalytic properties involve the increase of the number of potentially active sites in the bulk iron phosphate catalyst, by supporting it on silica based materials. A ZSM-5 support was chosen, due to its excellent thermal stability and isomorphism to MFI type silicalite. ZSM-5 however has a strong acidic character, which may affect the reaction, and it was also decided to support an iron phosphate phase onto the more amorphous, high surface area, MCM-41. The highly active iron silicalite is also proposed to be adapted to the partial oxidation of ethane. The structure of its active site, however, is debated [12], and effort has been put into the further characterisation of its physical properties. Indeed, many material-related parameters are believed to have an influence on the catalytic process, including pore size, surface area, structural order, framework density, metal cluster size, acidity, reducibility of the metal ions and presence of extra-framework ions. The characterisation techniques used for the study of these parameters are outlined hereafter. Some material-independent factors are also known to have an effect on catalytic conversions, including the pre-treatment of the material, the oxidising environment, concentration of reagents, presence of additives, temperature, pressure and contact time. The two last factors could not be studied during the time allocated for this project.

The following discussion presents an introduction to zeolites and catalytic systems for partial oxidation processes. This is followed by, in chapter II, the presentation of the synthetic and modification procedures used for the preparation of the potential catalysts. In chapter III, the bulk characterisation of the materials is discussed, with respect to the effect of the various preparative treatments on their surface area, crystallinity, and concentration of iron, studied respectively by physical adsorption of nitrogen, powder, x-ray diffraction, and atomic absorption spectroscopy. The reducibility of the metal species was studied by temperature programmed reduction in a hydrogen atmosphere and is presented in chapter IV. Then follows the characterisation of the acidic properties of the materials, as studied by adsorption and temperature programmed desorption of ammonia, with *in situ* infrared or mass spectrometric detection. The aggregation state and nature of the iron species present in the prepared materials was investigated by adsorption of nitric oxide with *in situ* infrared spectroscopic detection. This is discussed in chapter VI of this thesis, together with a re-assignment of the iron-nitric oxide adsorption complex vibration bands, which is disagreed upon in existing reports. Finally chapter VII presents the results of the catalytic testing of the materials in different conditions, varying the temperature of reaction, oxidising environment and pre-treatment conditions. The effect of the structural features of the catalysts on their activity is then discussed.

A general conclusion follows, presenting the findings regarding the identity of the best materials found for the partial oxidation of ethane, as well as what physical properties confer these materials with good catalytic properties in this particular application. Some mechanistic aspects of the catalytic conversion are considered.

I-2 Zeolites

I-2.1 History and common uses

The term zeolite appeared first during the 18th century when a Swedish scientist observed one behave as a boiling liquid upon rapid heating. This behaviour was caused by a quick release of water entrapped in their structure, and is more familiarly known nowadays as the appearance of a fluidised bed. This particular behaviour granted them their name, from the Greek zein, to boil, and lithos, stone, the zeolite terminology was based of this observation of a stone that boils [13].

More than 160 zeolite types have been assigned and approved by the international zeolite organisation, 48 of which are naturally occurring. The list of zeolitic frameworks is constantly sought to be expanded as new structures are imagined and synthesised [14].

Natural zeolites occur in volcanic areas, where the silicon and aluminium rich rocks and ash react with the underground alkaline water, or in shallow marine areas. Typically a naturally occurring zeolite crystal is formed over a period ranging from thousands to millions of years. A picture of naturally

Figure I-1: Photograph of faujasite and phillipsite crystals from Limberg near Sasbach, Germany. Courtesy of V. Netz,

occurring faujasite is presented in figure I-1. Natural zeolites are often found as different structures on the same site, or contaminated with minerals or various metals, and their commercial applications are therefore limited. Nevertheless, the annual production of natural zeolites is approximately 4 million tons, originating from open pit mine sites located mostly on the Eurasian continent [13]. Synthetic procedures for the production of most of the naturally occurring frameworks have been developed, and their use is varied and extensive. As most of the exploited natural zeolite market is found in the production of concrete and asphalt, the largest consumption of (synthetic) zeolites is found in the laundry detergent market [15]. Indeed, Linde type A zeolite is used in washing powders as a trap for calcium ions in hard water. More than 1,000,000 tons of zeolite were used worldwide in 1999 for this purpose. Their ion-exchanging properties are also used in other wider scale water purification processes, and in agriculture, as slow potassium and nitrogen releasing agents. Besides ion-exchange properties, zeolites possess adsorptive capabilities, possibly their most interesting feature. They are able to adsorb or desorb gases preferentially in a thermally controlled manner, without damage to their framework. Use of this property is made in the production of medical grade oxygen, where O_2 is separated from nitrogen by adsorption of the latter [16]. This property also finds extensive uses in heterogeneous catalysis chemistry, where reactions can be promoted at the surface of a zeolite. The most known of heterogeneous catalytic applications is found in the petroleum industry, where a zeolite based catalyst is used to in the fluid catalytic cracking of hydrocarbons [17]. More recent applications of zeolites focus on their use in the fuel cell technology, for safe hydrogen storage, and heating and refrigeration, making use of the exothermic character of the adsorption of water on their surface. The applications of zeolites are countless, and many more are known and used,

making benefit of their chemical and physical properties, from the most complex reaction pathway to the simple beauty of their natural crystals.

I-2.2   Structure

The properties of zeolites briefly described above come from their peculiar structures.

Most of these structures are composed of silicon, aluminium, oxygen and cations, the most common of which are protons, and sodium, potassium, calcium and magnesium ions. They possess a well-defined crystalline array of silica and alumina units in tetrahedral coordination (fig. I-2). The silicon or aluminium, commonly referred to as T-atom, is in the centre
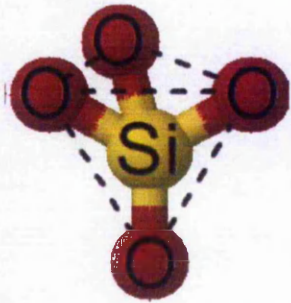
Figure I-2: SiO_4 tetrahedron.

of a tetrahedron, with oxygen atoms at its corners. These tetrahedra are linked together through their corners and arranged in various ordered ways to form the zeolite's crystalline framework [14].
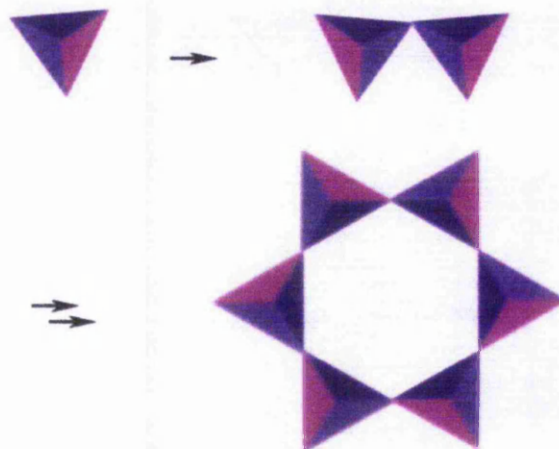
Figure I-3: Illustration of the links formed between TO_4 units resulting in larger units that can add up to form channels or cavities in zeolites.

As illustrated on figure I-3, the tetrahedra can interlink in such a way that cages or channels are formed in the long-range. These cages and/or channels are the origin of the microporous character of the aluminosilicates. The pore sizes of zeolites range approximately between 3 and 10 Å in diameter, and is determined by the number of tetrahedra forming the cavity (fig. I-4).
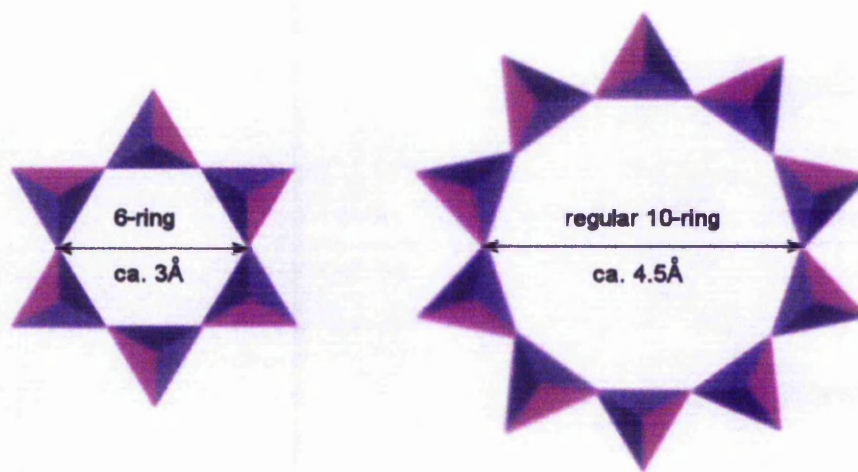
Figure I-4: Illustration of the dependence of zeolites' pore size upon the number of TO$_4$ units building the ring.

The different possible arrangements of these tetrahedra make an array of structures which can be viewed as building blocks for a larger zeolitic structure. The different building blocks possible have been studied as well as growth mechanisms of zeolites [18-20], however will not be presented here for clarity. The numerous ways in which these building blocks can be arranged give rise to the extensive zeolite structure collection known to day. Depending of these arrangements, 2- or 3-dimentional arrays of pores and cavities are created, an example of each given in figure I-5. These porous structures can have surface areas reaching hundreds of squared meters per gram.
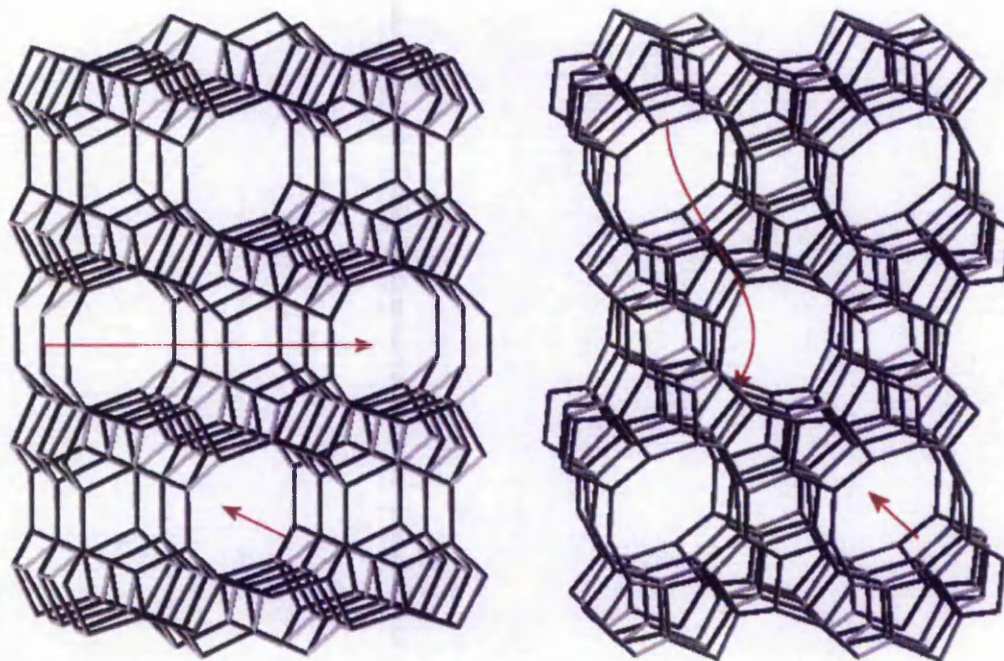
Figure I-5: Illustration of the 2- or 3-dimentional character of pores in zeolites. (left) the 2D pore network of ferrierite, and (right) the 3D network found in ZSM-5.

A variety of pore arrays is found in different zeolite structures, and their variation in shape and size is made use of in the separation of molecules, where isomers can sometimes be separated depending on their size and shape. This physical separation process is referred to as molecular sieving [21].

In other uses of zeolites, catalysis, adsorption and ion-exchange in particular, another characteristic property of zeolites is used, *i.e.* their intrinsic acidity. The presence of trivalent aluminium atoms in tetrahedral coordination creates a negative charge in the structure. Both types of acidity occur at these sites, namely Brønsted and Lewis acidity. In one molecular arrangement an oxygen atom cornering the alumina tetrahedron carries a negative charge, which can be balanced by a proton. Such protons are labile and therefore give a Brønsted acidic character to the solid. Certain heavier cations can also be coordinated to this charged oxygen atom instead of a proton, and if it carries an empty electronic orbital some Lewis acidic character is

given to the zeolite. Aluminium atoms can be found in another molecular arrangement where it can accept an electron doublet in its empty p- orbitals and therefore shows a Lewis acidic character [22]. A representation of both types of acid sites found in zeolites is given in figure I-6.
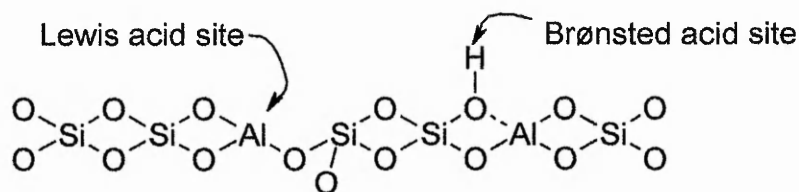
Figure I-6: Possible structure of the acid sites found in aluminosilicates.

I-2.2.1   MFI structure [23]

MFI is a crystalline structure with a 3-dimensional array of pores (fig. I-5). It is a synthetic zeolite developed by Mobil, as its aluminium containing form, ZSM-5. Other heteroatoms which can be isomorphously substituted in the framework include germanium, boron and iron. Its array of pores is formed by two channels of 10 T-atoms rings, one linear and one sinusoidal. The pore opening is on average 5.5 Å. ZSM-5 is strongly acidic and has a high thermal stability, and its most renown use is as a fluid catalytic cracking catalyst in the petroleum industry.

I-2.2.2   MCM-41 structure [24]

MCM-41 is not in itself a zeolite, but sometimes referred to as a zeotype. It is a silicate prepared from a templated synthesis in a similar manner to zeolites, however it does not have a crystalline structure and its pores are in the mesoporous range, typically ranging from 20 to 100 Å in diameter. These pores are arranged in a hexagonal array with amorphous silica walls (fig. I-7). The material, developed by Mobil, is essentially non-acidic, however its surface can be modified with

heteroatoms and acidity introduced in its structure. Due to its amorphous structure it typically contains a substantial amount of non-acidic hydroxyl groups and defects.
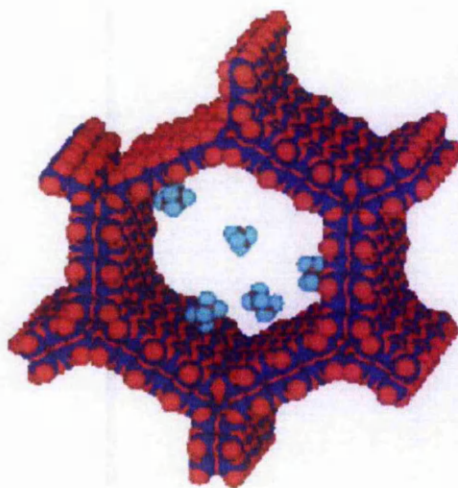
Figure I-7: Methane in a hexagonal pore of MCM-41

I-2.3   Synthesis

The existence of numerous crystal structures composed of essentially the same few elements is bound to make their synthesis a tricky procedure. Natural zeolite crystals form over hundreds of years at ambient temperature and pressure and are often impure [25]. Their industrial synthesis is typically carried out by crystallisation out of an aqueous solution containing the relevant amounts of silicon and aluminium, at high temperature and pressure in an autoclave. For commercial and research applications it is essential that a pure material is produced and therefore a good control of the crystallisation process is needed. Amongst the factors influencing the type of framework crystallising one can find the pH of the stock solution, the chemical nature of the silicon and aluminium source used, the presence of cation impurities and their concentration. Finally, most of the synthetic frameworks synthesised up to date do not occur without the presence of a structure directing agent in the reaction batch,

otherwise known as template. A brief account of the possible effect of these variables can have on the resulting crystal formed is given here.

Structure directing effects have been discovered after the observation of frequent association of alkali cations with certain types of cages. Many potential templates have been studied since, and the ones used nowadays are frequently organic ions, for example quaternary ammonium ion. Changing the length and rigidity of the carbon substituents allows the variation of the resulting crystals' pore sizes and morphology [26]. The needed high purity of the reagent sources used is obvious when the structure directing potential of some alkali cations is known. The use of technical grade materials in zeolite synthesis may result in a low reproducibility of the process, or even failure to synthesise the wanted crystal structure. The problem of silica sources are their frequent contamination with trace amounts of metals, in particular aluminium, which can prevent the synthesis of very high Si/Al ratio zeolites. An inappropriate aluminium source, on the other hand, can easily cause the formation alkali aluminium salts in solution resulting in an undesired crystal phase to grow [27]. The pH of the synthesis batch is of outmost importance in the control of the reaction. A relationship between the alkalinity of a solution, batch composition and resulting Si/Al ratio of the material was found in the study of faujasite crystallisation, for example [28].

These are only a few of the possible factors influencing the crystallisation of zeolites, and nucleation and growth mechanisms are still vastly unknown in the complex reaction mixtures used. In research oriented work the use of commercial samples of zeolites are often advantageous, however with care and good practice zeolite samples can be produced in-house with good results.

I-2.4   Modification

The properties of zeolite crystals can effectively be altered by modifying their composition post-synthetically with little to no damage to their framework. For example the introduction of d-block metals within a zeolite's pores is common practice for catalytic purposes [29-31]. Not only can this be done to alter the properties of a given zeolite, in the case when the metal is the catalyst its immobilisation on a silica surface can create a more potent and clean catalyst, by increasing its active surface area and making its recovery and reactivation, where necessary, easy. Different methods are used to introduce elements into a zeolite, for example aqueous ion-exchange, impregnation and chemical vapour deposition, which were used during this project, are presented hereafter.

The common zeolite modification methods stated above all essentially consist in the stoichiometric exchange of the solid's acidic protons with other cations. This exchange process is often a reversible equilibrium, thermodynamically driven, for which an equilibrium constant can sometimes be calculated. In most cases however complex interactions occur between the framework and the cation exchanged. Various parameters can influence the ion exchange equilibrium, including the nature of ions already present in the framework, the solvent in which the procedure is carried out and the properties and nature of the salt used as a source for the cation [32]. These parameters do not only have an influence on the equilibrium, but also on the nature of the species deposited on the surface of the zeolite. For example iron has the tendency to form hydroxyl adducts and Fe_2O_3 clusters in aqueous solution at neutral pH, the effect of which is to generally find more hematite-like clusters in aqueous solution Fe-exchanged zeolites than in the gas phase or solid state [33-35]. The properties of the resulting catalyst can greatly vary, as outlined later in this chapter.

I-2.4.1   Aqueous ion exchange

The aqueous ion-exchange of zeolites is probably the easiest ion-exchange to implement. Generally the desired zeolite is suspended in a relevant volume of solution containing the exchanging cation, left to reach equilibrium and separated again from the electrolyte by filtration. Different levels of exchange can be achieved, depending on the chemical nature of the cations exchanged and the concentration of the introduced cation in solution. When the equilibrium constant of the exchange doesn't allow sufficient levels of exchange, the latter can be driven forward by increasing the temperature of the solution and/or repeating the exchange procedure [36].

I-2.4.2   Impregnation

The post-synthetic modification of zeolites by impregnation of chemical entities can be carried out in a way similar to their aqueous ion-exchange. The zeolite is suspended in a solution of the desired cation(s), but their deposition onto the surface of the silicate is driven by precipitation. This can be achieved by forcing the precipitation of chemical species using common procedures, for example altering the pH of the solution or evaporating the solvent. Higher cation loadings can be obtained this way, as well as over-exchanged zeolites, where the quantity of cations introduced exceeds the stoichiometric number of protons available for exchange. The drawbacks of this method can be a poor dispersion of the cation on the surface of the zeolite, aggregation of the cations and little reproducibility [37].

I-2.4.3   Chemical Vapour Deposition (CVD)

Chemical vapour deposition is a process which is used in many industries for the formation of thin coatings on a substrate. A chemical reagent, in the case of transition metals often a chloride as they can be sublimed at moderate temperatures, is

transported in the gas phase, in an inert carrier gas, to a sample chamber where it either reacts with the substrate's surface or condensates on it. This technique is used in zeolite modification as it usually provides a fine dispersion of the cation on the surface. When a metal chloride is used its reaction at Brønsted acid sites of the zeolite causes the decomposition of the salt as the metal is exchanged with protons, with evolution of hydrochloric acid in the gas phase [34]. A good dispersion of the exchanged cation can be an advantage in many cases, a draw back of the method however is that strong acids, and in particular HCl, can cause the migration of aluminium atoms out of the zeolitic framework [38].

I-2.5   Activation

Following the synthesis and post-synthetic treatment of zeolites a high temperature treatment is often needed. In the first case the structure-directing agent, or template, is removed, and bonds within the material permanently fixed. Small imperfections in the framework, for example silanol nests where hydroxyl groups on the silica source have not fully reacted can be removed. In the second case, and especially when the zeolite is exchanged with metal ions, this high temperature treatment fixes the cation in place by forming permanent bonds with the framework. This step is necessary in the synthesis of zeolites and care must be given when carrying it out as before this the framework is fragile, or the exchanged cations can easily migrate on the surface of the silicate. This process is commonly referred to as calcination, or firing.

The behaviour of zeolites under heat treatment is the origin of their name, as a thermal treatment causes adsorbed water to evolve from the solid. This is commonly used and necessary prior to many experiments, as not only water is desorbed from the zeolite's surface, but any sort of contaminants adsorbed from the surrounding atmosphere,

which can greatly affect an experiment. For example in the study of the acidity of the zeolite, where a probe gas is adsorbed on acid sites, water present in the zeolite is in competition with the probe, as it is adsorbed on acid sites in the framework. This process of "cleaning" the surface of a zeolite prior to an experiment is called activation.

In some cases the activation of a zeolite does not only have the effect of cleaning its surface, but its chemical structure can be altered. When a zeolite contains a transition metal for example the thermal treatment can cause the reduction of this metal, which is needed prior to certain catalytic applications. Also the activation of a zeolite in a certain atmosphere can be needed in order to form reactive species on its surface. Both latter treatments have been shown to have an influence on the direct hydroxylation of benzene over Fe-MFI catalysts, where pre-reduction of the metal or its activation in the presence of steam favour the formation of active sites for the decomposition of the oxidising agent [39].

Besides all the benefits of the thermal treatment of zeolites, certain unwanted effects can occur at high temperature. The first of these effects is the collapse of the porous framework, generally to produce an amorphous silica-alumina. This occurs particularly easily in zeolites with a high alumina content, as these show a high acidity, in the form of labile protons, which weaken Al-O bonds during thermal treatments [40]. The aluminium atoms in a zeolitic framework can also be driven out of it, or leach out, by interaction with water at high temperature in a process called steam dealumination [41, 42]. In certain zeolites the framework's crystalline structure can be altered by heat, for example the MFI framework which exists in an orthorhombic and monoclinic configurations [43]. Some of these adverse effects can be avoided by applying careful conditions when activating a zeolite, and generally a

slow heating gradient has to be used when heating up the material. The exclusion of water is of particular importance to avoid dealumination of the framework.

I-3 Oxidation of light hydrocarbons

Oxygenated hydrocarbons are particularly important in the petrochemical and fine chemical industry due to their use as intermediates in numerous chemical reactions [1]. Some oxygenated chemicals can be obtained from the corresponding saturated hydrocarbon, however in some cases the development of a viable industrial process for the conversion of alkanes is highly challenging. This is most true in methane and ethane partial oxidation, the reasons for which are explained in this chapter. The discussed reactions are however thermodynamically feasible, and research in this area is focused on the development of catalysts able to ease the reaction conditions enough to be implemented in a profit-based company. One of the main problems of partial oxidation chemistry is the lack of selectivity of the reactions involved, partly arising from the radical character of the oxidising agents used in the gas phase, partly from the lack of reactivity of the alkane reagents. Gas phase processes are preferred in reactions involving light hydrocarbons, due to their ease of implementation. The use of solid catalysts to promote the oxidation reaction is particularly indicated as the technology involved is now well established and they are easy to handle. Some problems associated with the development of heterogeneous catalysts for partial oxidation purposes, as well as the current state of knowledge, are presented in this section.

I-3.1   Catalysis

A catalyst is a substance that allows the alteration of the speed of a chemical reaction, while itself remaining chemically unchanged [44]. Its mechanism of action is by effectively reducing the activation energies needed for particular chemical conversions. The catalyst can be in the same phase as the reagents, and the process called homogeneous catalysis, or it can be in a different phase – generally solid in a liquid or gaseous phase reacting mixture – and the process is named heterogeneous catalysis. Heterogeneous catalysts have the ability to adsorb chemical species which can be decomposed on the solid surface, or simply more effectively brought into contact for a chemical reaction to occur (fig. I-8).
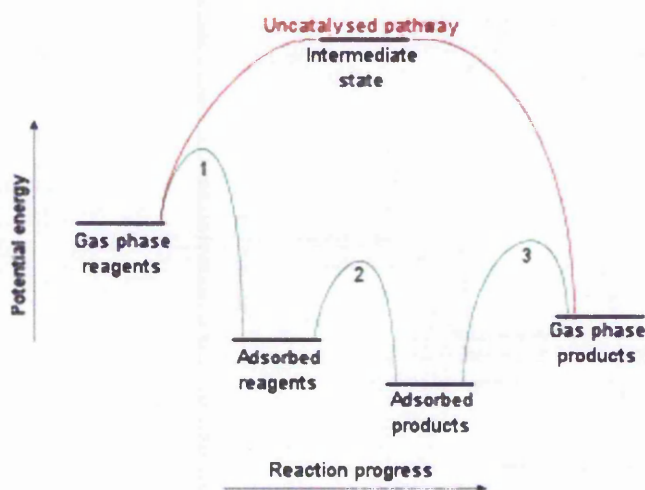
Figure I-8: Schematic diagram of the activation energies needed for an uncatalysed and a catalysed reaction pathway. The catalysed mechanism involves three major steps: (1) diffusion of the reagents and adsorption, (2) migration on the solid surface and reaction, (3) desorption and diffusion away from the active site.

I-3.1.1   Physical aspects of catalysis

There are five important steps in the physical process of catalysis:

- diffusion of the reagent through the pores of the catalyst to active sites

- adsorption of the reagents

- reaction

- desorption of the products

- diffusion of the products away from the active sites

For the purpose of calculation of orders of reaction, step 2, 3 and 4 are usually considered together. Indeed the order of reaction depends on either diffusion when the latter is slow, or on the kinetics of the chemical transformation itself. The rate of diffusion depends on the material's pore size and shape, as reagents have to travel through the pore to reach chemically active sites.

I-3.1.2   Chemical aspects of catalysis

When the physical factors influencing a heterogeneous catalytic process can be ignored or eliminated, i.e. when the reaction itself is the rate-limiting step, a few problems remain to be solved. These arise from the molecular character of the catalytic process, occurring at discreet active sites on the solid catalyst's surface. The following problems are usually included [2]:

- The characterisation of the reactive solid surface

- The identification of the surface species involved in the reaction

- The steps involved in the reaction path

- The structures and energies of the reaction intermediates

Many methods are available for the completion of these steps, which commonly involve various spectroscopic methods, for example infrared spectroscopy can be used

in or *ex situ* for the identification of reaction intermediates. Surface oxygen species, particularly important in oxidation catalysis, can be observed using techniques such as electron spin resonance or x-ray photon spectroscopy, their involvement in a reaction pathway can also be determined using isotopic labelling. The isotopic exchange of other elements in reagents has also been extensively used for the identification of reaction steps and intermediates [1]. Other surface characterisation techniques are common in the study of catalytic pathways, which have been used in this project and are presented in detail in subsequent chapters of this thesis.

I-3.2   History and evolution of systems

It is common knowledge that there is a large incentive by authorities to develop green ways to produce ethanol, mainly due to its potential application as an alternative fuel for the automotive industry. Most industrial processes for the manufacture of ethanol therefore involve the fermentation of organic materials such as grains, fruit and wood. Fossil fuels however are still commercially viable raw materials for this industry, and especially natural gas, *i.e.* light hydrocarbons.

Most past studies have concentrated on the conversion of olefins to oxygenates as their functionalisation is easier than their corresponding saturated hydrocarbon. Indeed the conversion of ethene to an oxygenate involves the formation of a C-H and a C-O bond, which is bound to be thermodynamically more favourable than the C-H breaking followed by C-O formation necessary in the conversion of the saturated hydrocarbon, as the enthalpy of dissociation of a C-H bond is approximately 413 kJ mol^{-1} [45].

For example ethanol is traditionally produced by steaming of ethene over a silica-supported phosphoric acid catalyst at 573 K, in a cyclic reactor that allows overall

95% conversion. A recent study reported the ability to increase the efficiency of the process by combining the phosphoric acid catalyst with a metal, and that a $Sn(HPO_4)_2$ catalyst improved the activity by 20 times approximately [46]. Using a zeolite catalyst, ZSM-5, was also shown to improve the yield of ethanol from this reaction [47]. A disadvantage of the process however is the use of water as oxidant, which has to be separated from ethanol by subsequent distillation, and the azeotropic mixture cannot be separated to 100% ethanol by distillation. The polymerisation of ethene at high pressure also limits the potential of this catalytic process.

The use of ethane as feedstock for the production of ethanol could overcome this problem, however the process is less commercially viable and little research has been reported yet. Avoiding the production of water during the process could be achieved by using nitrous oxide as an oxidant, as the letter can react stoichiometrically with ethane to produce only ethanol and nitrogen. Ultimately oxygen may be used as an oxidising agent, when a selective catalyst is known. Most of the reports known to date involve the use of iron phosphate catalysts for the partial oxidation of ethane to ethanol [48, 49]. It was found that the main problem in ethane partial oxidation was its over-oxidation, where ethylene and carbon dioxide are produced easily. For example nickel, magnesium, chromium and platinum are amongst the transition metals favouring dehydrogenation to hydration [50-53]. The problems specific to the partial oxidation for alcohol production are further discussed hereafter.

I-3.3   Challenges in partial oxidation catalysis

Heterogeneous gas phase partial oxidation is extremely interesting for industry due to the relative ease of setting up the procedures; an easy to handle solid catalyst bed is used, gaseous feedstock is fed onto it in a heated tubular reactor, and products are left

with no further purification needed in the case of highly selective processes. Such reactors are already set up for a number of processes and the cost of adapting them for a new application is minimal.

There are however a few hurdles to overcome for such a process to be viable [5], the first of which is using dioxygen as oxidising agent. Free radical chain oxidation often predominates when using oxygen as it is a triplet biradical. These reactions, even though having generally a higher rate of conversion than redox reactions, suffer from a lack of selectivity due to their intrinsic mechanism. As a result a "melting pot" of several oxidation products and by-products is obtained.

A second important challenge is to avoid over oxidation, as generally the first oxygenate obtained is more susceptible to oxidation than the feedstock itself, especially in the reacting conditions used for gas phase oxidations. This fact is directly related to the third main challenge to overcome, which is the lack of reactivity of the feedstock; due to its lack of functionality it is susceptible to different oxidative transformations.

Moreover, lower alkanes have high C-H bond dissociation energies, much higher than the corresponding partially oxidised products, as a result harsh conditions are needed for activation, where several processes are in competition and therefore a fine balance is essential for the development of a successful process.

The temperature of reaction, structure of the catalyst, type of oxidising agent, and the presence of additives are considered in this study, among other factors, and a good knowledge of the structure and reactivity of the reagents was needed for the tuning of reaction conditions. Following the structure and reactivity of oxygen and nitrous

oxide are presented, and a brief discussion of the catalytic activation of hydrocarbons given.

I-3.4 The oxidising system

I-3.4.1 Dioxygen structure and reactivity

Dioxygen is the preferred oxidising agent for most oxidation reactions, readily available and highly reactive. Some studies use it following a biomimetic approach of the oxygen-ferredoxin complex, as outlined hereafter. The reactivity of oxygen comes from its triplet biradical structure (fig. I-9). It has two equal spin electrons in degenerate π anti-bonding orbitals [5].
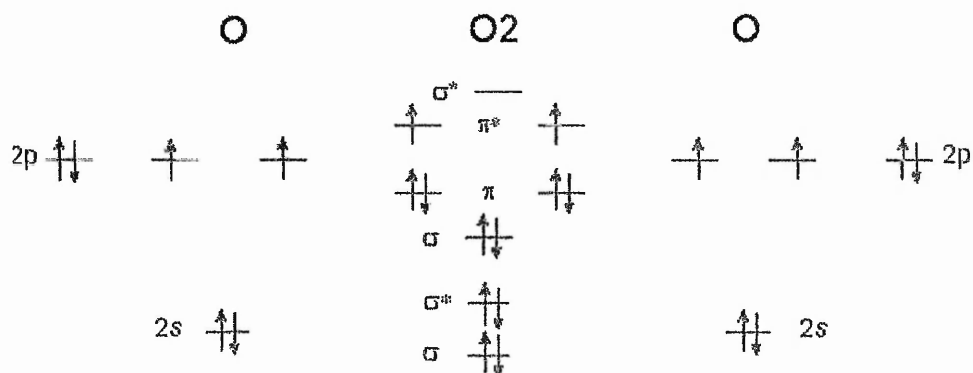
Figure I-9: Schematic diagram of the molecular electronic configuration of dioxygen

This confers the molecule its advantage and disadvantage for oxidative purposes at the same time. Its radical character is the origin of its high reactivity, however radical mechanisms usually have a poor selectivity to a particular product [54]. The activation of oxygen over an active site conferring a more ionic character may be of interest in partial oxidation reactions. Such an activation can be achieved through energy input, converting oxygen to its excited state, or oxidation, yield an anion-radical and eventually a dianion (fig. I-10) [55].

$$\bullet O - O \bullet \quad \xrightarrow{\Delta} \quad O - O :$$

$$\bullet O - O \bullet \quad \xrightarrow{- \ e^-} \quad \bullet O - O^- \quad \xrightarrow{- \ e^-} \quad {}^- O - O^-$$
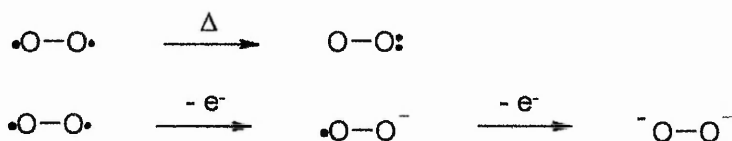
Figure I-10: Representation of dioxygen as a diradical, and its activation pathways.

I-3.4.2   Nitrous oxide structure and reactivity

Nitrous oxide, also known as laughing gas, has long been considered a rather harmless gas. In the chemical industry, its main source is as an unwanted product during the synthesis of nitric acid [56]. Recently its abatement has raised a lot of interest as the molecule is involved in the depletion of stratospheric ozone. Its reaction with ozone, even though detrimental for the environment, highlights its potential as a monoxidation agent. It easily dissociates to dinitrogen and an active oxygen molecule (fig. I-11), which is involved in the formation of molecular oxygen from ozone [57].

$$N \equiv \overset{+}{N} - O^- \quad \longleftrightarrow \quad \overset{-}{N} = \overset{+}{N} = O$$

$$2 \, N_2O \quad \longrightarrow \quad 2 \, N_2 \quad + \quad 2 \, O \bullet \quad \longrightarrow \quad 2 \, N_2 \quad + \quad O_2$$
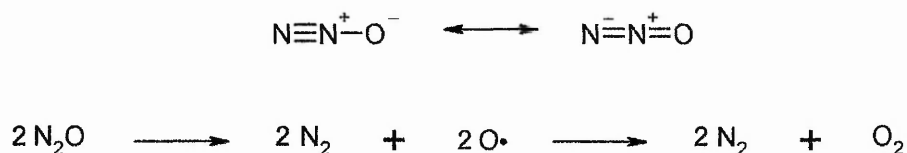
Figure I-11: The chemical structure of nitrous oxide and its decomposition to nitrogen and oxygen.

This dissociation was found to be catalysed by iron species, especially in isomorphously substituted Fe-ZSM-5 materials [39, 58-61]. The structure of the iron species involved in this decomposition has been studied extensively recently, and an account of the mechanisms proposed is given later in this chapter. The oxygen species formed from the decomposition of nitrous oxide over iron catalysts is often referred to as "alpha" oxygen.

I-3.4.3   Poisons and radical scavengers

A short note is given here on poisons for catalysts, and radical scavengers, as it has been seen that both the oxidising agents proposed in this work can be source of

oxygen radicals. This discussion is specific to the gas-phase oxidation of hydrocarbons, where two major poisoning phenomena occur. The first major poison encountered in catalytic reactions involving hydrocarbons is sulphur. This is found as an impurity in fossil fuels, and irreversibly binds to catalytically active sites [62]. This problem did not apply during our study as pure hydrocarbon feedstocks were used. The second major poisoning, or deactivation, phenomenon in hydrocarbon oxidation is coking [63, 64]. Coke results from the incomplete oxidation of hydrocarbons, and its accepted formula is generally $(CH)_n$. Coke deposits on the surface of catalysts, over time forming a coating which prevents the feedstock from accessing the active sites, resulting in deactivation of the catalyst.

When radicals are formed and undesired during a chemical reaction, the co-feeding a radical scavenger to the reagents can be of great help to improve the selectivity of the process. These radical scavengers are chemical species that react quickly and easily with radicals, forming stable products and avoiding the cascade of reactions possible [65]. Numerous scavengers are known, and the easiest to add to a gas-phase reaction where oxygen radicals are involved is molecular hydrogen. The products of the reaction of these are water and hydrogen peroxide, which itself is decomposed by hydrogen to water.

I-3.5   Activation of alkanes

I-3.5.1   C-H bond activation by transition metals

The activation of the C-H bonds of saturated hydrocarbons was one of the most important challenges in catalysis at the end of the 1960s [2]. The activation of these bonds in uncatalysed chemistry involves particularly reactive species, such as strong oxidisers. Their relative inertness was thought at first to prevent the bond activation

under mild conditions, however at the time activation processes for hydrogen existed, which led researchers to believe the feasibility of the process, as the H-H bond is stronger than a C-H one. Similarly catalytic processes were used in reactions involving aromatic hydrocarbons, and therefore the strength of the C-H bond does not prevent its reaction. Moreover reactions of alkanes at the surface of metal oxides were known since the 1930s, and functionalisation was known to occur, catalysed by metal enzymes [66]. The research led to the development of catalysts which can be divided into two categories, on one side metal complexes, and on the other, inorganic materials with a structure modelled on known enzymes, which are discussed in the following section. The transition metal complexes that were found to possess a particular activity towards alkane functionalisation contained platinum, used in chlorination, hydroxylation and hydrogenation [67]. Iridium and rhodium complexes were also found active for the oxidative addition of alkanes to form alkyl hydrides. An example of C-H bond activation over a transition metal complex is given in figure I-12, for a HD exchange reaction [66].
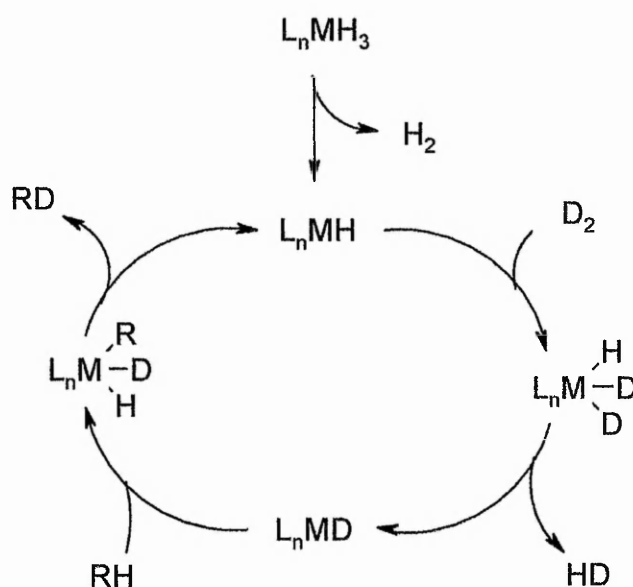
Figure I-12: A proposed catalytic cycle for the HD exchange of alkanes over transition metal complexes.

I-3.5.2   Biomimetic approach using O_2 activation

The oxidation catalysts developed based on an enzymatic reaction model are based on the P450 cytochrome monooxygenase enzyme. The active centre in these enzymes is an iron centre coordinated to a porphyrin group (fig. I-13).
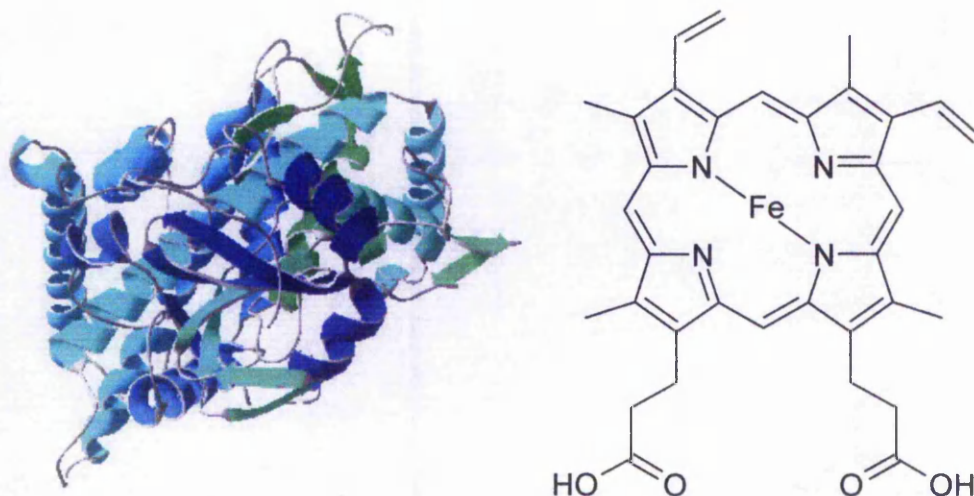
Figure I-13: (left) The ribbon representation of the P-450 cytochrome monooxygenase and (right) the structure of its active site.

This cytochrome is involved in the monooxygenation of alkane methyl groups in various organisms. A C-H bond is hydroxylated with simultaneous oxidation of NADH or NADPH [68, 69]. The catalytic cycle can be summarised as presented on figure I-14, and involves a redox activity of the iron centre.
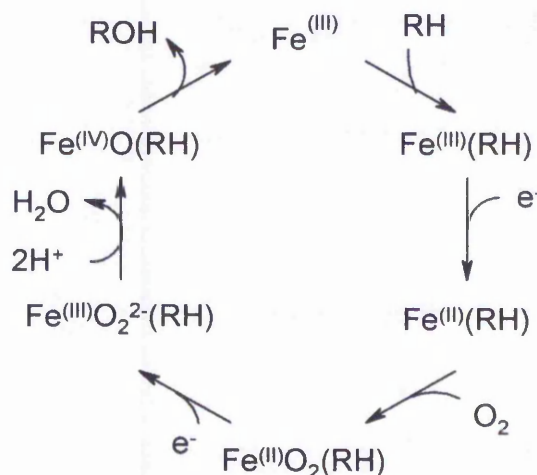
Figure I-14: A proposed mechanism for the hydroxylation of hydrocarbons over the P-450 cytochrome monooxgenase.

A second biomimetic system also involves the redox activity of iron, however not surrounded by a porphyrin group in this case. Methane monooxygenase contains a μ-oxo bridged iron dimer as active centre (fig. I-15), similar to the one found in hemerythrin, an oxygen carrier [70]. It involves a complex mechanism of reaction which is not presented here, however the process involves a homolytic O-O bond cleavage, and the hydroxylation reaction can be summarised as follows [71, 72]:
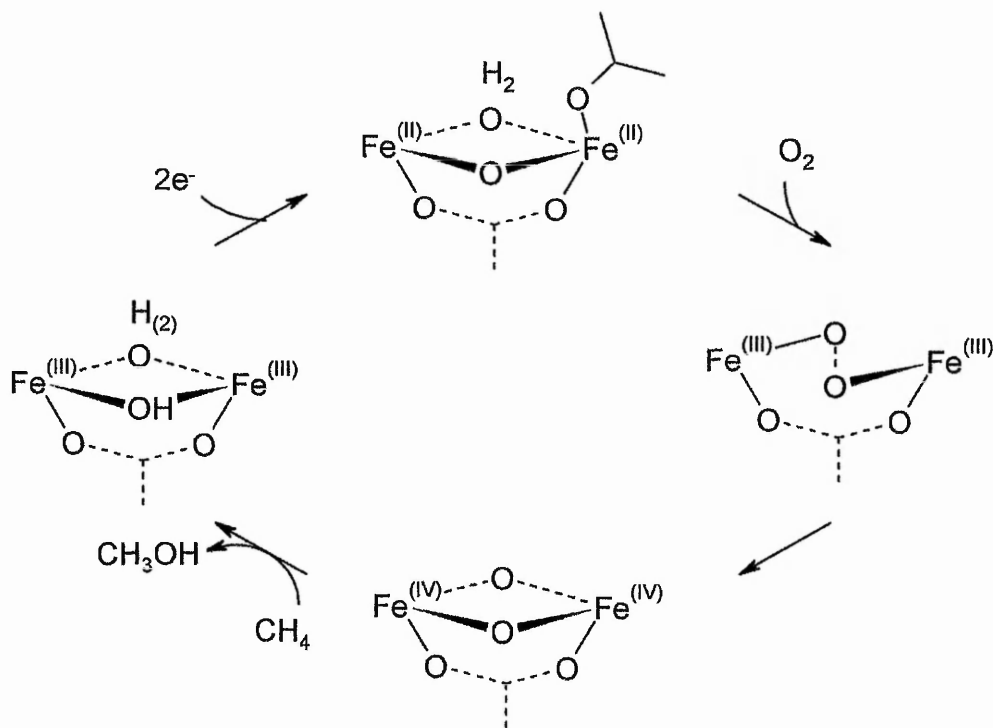
Figure I-15: A proposed mechanism for the activation of oxygen resulting in hydroxylation of hydrocarbons by the methane monooxygenase enzyme.

Both biological catalytic systems involve the activation of molecular oxygen at a reducible iron site. It is known that such sites also catalyse the homolytic decomposition of hydrogen peroxide, which can be an advantage for the hydroxylation of alkanes.

In the following section the analogies between the active site found in methane monooxygenase and other iron-containing materials are pointed out and related to the current project.

I-4 Catalysis by iron

It has been outlined that the catalysts which were found most active or selective for partial oxidation purposes were transition metal complexes or enzyme systems. Of both types of catalysts more focus is put towards the latter as they appear more promising for the development of a clean, low temperature catalytic process. Two main biological systems catalyse the hydroxylation of hydrocarbons, and in particular alkanes, which both contain iron as the active centre.

Firstly, an iron-porphyrin complex, characteristic of heme enzymes, catalyses the hydroxylation of alkanes through the activation of oxygen. The catalytic cycle involves redox reactions of an isolated iron centre, and the presence of a reducing agent, NADH or NADPH in biological systems, is necessary in order to complete the cycle [73]. Besides the studies using iron-porphyrin complexes as a biomimetic species with oxidative properties [73-75], a report was published, proposing that an iron phosphate catalyst had similar oxygen-activating properties as cytochrome P-450 [8, 48, 49]. It was observed that in the biological system both electron and proton donation was necessary to the catalytic cycle, and that an appropriate inorganic catalyst could fulfil both roles by activation of hydrogen:

$$H_2 \longrightarrow 2 H^+ + 2 e^-$$

The iron phosphate catalyst was reported active for the partial oxidation of methane and ethane to methanol with a mixture of oxygen and hydrogen at 673 K. Following kinetic studies of the proposed system, a reaction mechanism was proposed:
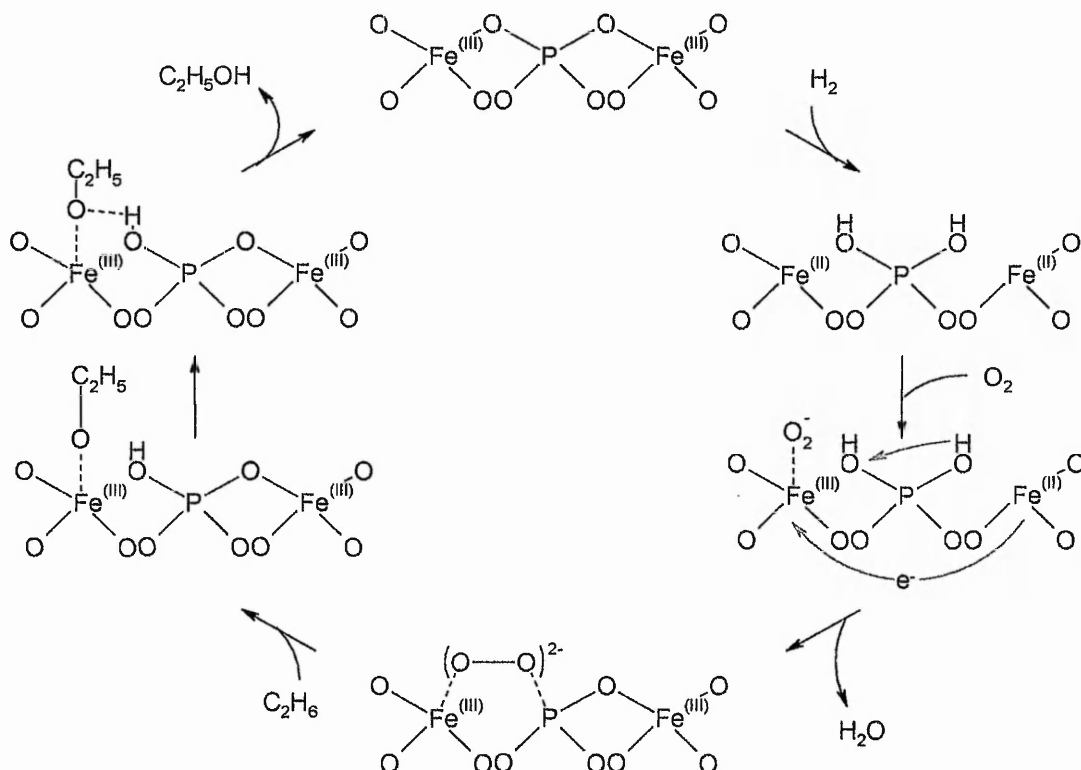
Figure I-16: A proposed mechanism for the activation of oxygen resulting in hydroxylation of hydrocarbons by iron phosphate catalysts.

This mechanism is similar to the one presented for the P-450 oxygenase in the fact that the hydroxylation of the hydrocarbon occurs at a single iron site and involves proton and electron donation from neighbouring atoms. The reported conversion of ethane is low, at approximately 10^{-4} mol g^{-1} h^{-1}, however an interesting 20% selectivity to ethanol was stated. The problem of a low conversion rate is thought to be due to a poor availability of the active iron site in the bulk iron phosphate used, which can be overcome by strategies presented in the following chapters.

The second biological system showing a significant activity for the hydroxylation of hydrocarbons is the methane monooxygenase enzyme, where a μ-oxo bridged iron

dimer is thought to be the active centre [76]. The mechanism of reaction of this enzyme is less known than the heme-system, and the activation of the hydrocarbon seems to follow a more complicated pathway [7, 77, 78]. Iron dimers with a structure similar to the ones found in the methane monooxygenase enzyme have been reported to occur in zeolites, in particular ZSM-5 [11] and MCM-41 [79, 80]. The iron sites found in ZSM-5s, both ion-exchanged and isomorphously substituted, have been studied extensively [34, 39, 58-60, 81-92], however some disagreement is found in this literature. This mainly arises from the inability to control the formation of iron species in the zeolite's framework, where it is present in various aggregation states [12]. Nevertheless, a specific structure was found to be highly active in the direct hydroxylation of benzene, which is believed to be a μ-oxo bridged dimeric iron species [58, 93, 94]. These species are commonly referred to as "alpha" sites, and are particularly potent for the activation of nitrous oxide, following the mechanism proposed in figure I-17. It is thought that these sites are also active for the activation of oxygen, however the iron centres could not be reduced after the reaction, effectively poisoning the active site.
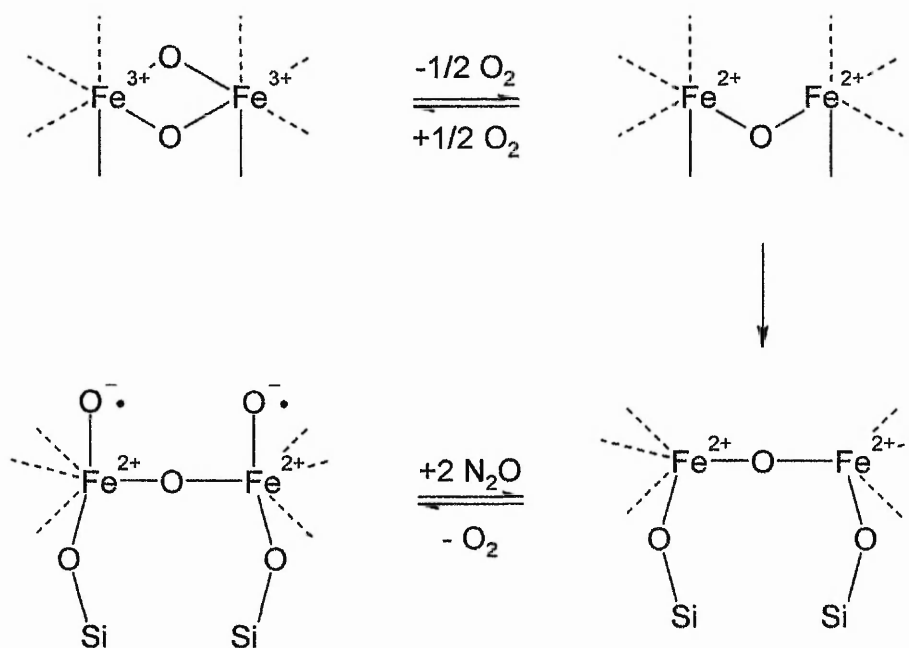
Figure I-17: The proposed mechanism of formation of "alpha" sites in Fe-MFI zeolites and their mechanism of activation of nitrous oxide.

These "alpha" sites have been proposed to be formed upon high temperature treatment of iron-containing zeolites, where the reduction of iron occurs with evolution of oxygen. The authors proposed that the iron dimers then had to undergo a transformation in order to avoid re-oxidation when the system was cooled down. This transformation is possibly a migration of the iron atoms out of the framework, however strong evidence of this was not obtained, but assumed following steaming experiments, which has the tendency to drive heteroatoms out of the silica framework [95]. The "alpha" sites formed after this transformation have the ability to decompose nitrous oxide to nitrogen and oxygen in a redox process. The molecular oxygen, intermediate of this decomposition, is thought to be the active species in the direct hydroxylation of benzene, and it is thought here that the system can be applied successfully to lower linear chain alkanes.

I-5 Catalysis by gold

Gold has long been considered an inert metal with little catalytic prospect. However in the past decades its activity towards the oxidation of carbon monoxide to carbon dioxide below ambient temperature [96, 97] has focused the attention on the metal's catalytic properties. The latter were discovered by achieving ultra-fine dispersion of metal particles. Large gold clusters cannot adsorb molecules to a significant extent, however small particles tend to lose some of their metallic character and are able to activate molecules such as CO, oxygen or hydrogen [98]. Since the discovery of the ability of gold to catalyse the oxidation of CO, several applications for the metal have been reported, including the selective oxidation of some hydrocarbons, including methane, some alkanes and methanol [29, 99, 100]. The conversions and selectivities recorded in the reported applications were however insufficient to be compared to catalytic systems used in the relevant industrial applications.

It is also thought that, similarly to platinum, nickel and palladium, gold particles are able to catalyse reactions with hydrogen through its dissociative adsorption. Some activity for the activation and dissociation of oxygen have been measured as well, during the study of the mechanisms of oxidation of carbon monoxide [31].

It follows, in this study, that gold is a potential catalyst for the partial oxidation of ethane to ethanol. Even though the activation of saturated hydrocarbons other than methane has not been reported, it is believed that a combination of the properties of gold and iron may favour the hydroxylation reaction. Indeed, finely dispersed supported gold catalysts have been shown to promote the formation of hydrogen peroxide from a hydrogen and oxygen feedstock [101, 102]. The expected reaction of iron with alkanes and hydrogen peroxide was outlined previously in this chapter.

I-6 References

1. Hucknall, D.J., *Selective Oxidation of Hydrocarbons*. 1974, London: Academic Press Inc. Ltd.
2. Voge, H.H., *Problems in heterogeneous catalytic oxidation*. Advances in Chemistry Series, 1968. **No. 76**: p. 242-53.
3. Halpern, J., *Homogeneous catalysis of hydrogenation, oxidation, and related reactions*. Discussions of the Faraday Society, 1968. **No. 46**: p. 7-19.
4. Lin, M.R. and A. Sen, *A Highly Catalytic-System for the Direct Oxidation of Lower Alkanes by Dioxygen in Aqueous-Medium - a Formal Heterogeneous Analog of Alkane Monooxygenases*. Journal of the American Chemical Society, 1992. **114**(18): p. 7307-7308.
5. Buijs, W., *Challenges in oxidation catalysis*. Topics in Catalysis, 2003. **24**(1-4): p. 73-78.
6. Florida, U.o. *Biomass-to-Ethanol Technology Could Help Replace Half of U.S. Auto Fuel*. 2005 [cited; Available from: http://www.monsanto.co.uk/news/ukshowlib.phtml?uid=8911.
7. Zhang, J., et al., *Basis for specificity in methane monooxygenase and related non-heme iron-containing biological oxidation catalysts*. Journal of Molecular Catalysis a-Chemical, 2006. **251**(1-2): p. 54-65.
8. Wang, Y. and K. Otsuka, *Catalytic-Oxidation of Methane to Methanol with H-2-O-2 Gas- Mixture at Atmospheric-Pressure*. Journal of Catalysis, 1995. **155**(2): p. 256-267.
9. Rodkin, M.A., et al., *Room-temperature oxidation of hydrocarbons over FeZSM-5 zeolite*. Studies in Surface Science and Catalysis, 2000. **130A**(International Congress on Catalysis, 2000, Pt. A): p. 875-880.
10. Baur, W. and R. Fischer, *Landolt-Börnstein - Group IV Physical Chemistry*. Landolt-Börnstein - Group IV Physical Chemistry : Zeolite-Type Crystal Structures and their Chemistry. Framework Type Codes LTA to RHO. Vol. Volume 14D. 2006: Springer Berlin Heidelberg. 1-31.
11. Panov, G.I., et al., *Biomimetic oxidation on Fe complexes in zeolites*. Studies in Surface Science and Catalysis, 1996. **101**(Pt. A, 11th International Congress on Catalysis--40th Anniversary, 1996, Pt. A): p. 493-502.
12. Mul, G., et al., *NO adsorption on ex-framework Fe,X MFI catalysts: novel IR bands and evaluation of assignments*. Catalysis Letters, 2002. **80**(3-4): p. 129-138.
13. contributors, W. *Zeolites*. [cited 2005; Available from: http://en.wikipedia.org/w/index.php?title=Zeolite&oldid=94764043.
14. *British Zeolite Association Website*. [cited 31/01/2005]; Available from: www.bza.org.
15. Glennie, E.B., et al., *Phosphates and alternative detergent builders*. 2002, WRc Swindon.
16. Jee, J.-G., J.-S. Lee, and C.-H. Lee, *Air Separation by a Small-Scale Two-Bed Medical O2 Pressure Swing Adsorption*. Industrial & Engineering Chemistry Research, 2001. **40**(16): p. 3647-3658.
17. Harding, R.H., A.W. Peters, and J.R.D. Nee, *New developments in FCC catalyst technology*. Applied Catalysis, A: General, 2001. **221**(1-2): p. 389-396.

18. Davis, T.M., et al., *Mechanistic principles of nanoparticle evolution to zeolite crystals.* Nature Materials, 2006. **5**(5): p. 400-408.

19. Agger, J.R., C.B. Chong, and M.W. Anderson, *3D computer simulation of zeolite a crystal growth,* in *Recent Advances in the Science and Technology of Zeolites and Related Materials, Pts a - C.* 2004, ELSEVIER SCIENCE BV: AMSTERDAM. p. 1282-1288.

20. Anderson, M.W., et al., *Crystal growth in framework materials.* Solid State Sciences, 2001. **3**(7): p. 809-819.

21. Porath, J. and E.B. Lindner, *Separation methods based on molecular sieving and ion exclusion.* Nature FIELD Full Journal Title:Nature, 1961. **191**: p. 69-70.

22. Joyner, R.W., et al., *The local structure of aluminium sites in zeolites.* Physical Chemistry Chemical Physics, 2004. **6**(23): p. 5435-5439.

23. Baerlocher, C., W.M. Meier, and D.H. Olson, *Atlas Of Zeolite Framework Types.* 5th ed. 2001: Elsevier.

24. Zhao, X.S., et al., *Comprehensive study of surface chemistry of MCM-41 using Si-29 CP/MAS NMR, FTIR, pyridine-TPD, and TGA.* Journal of Physical Chemistry B, 1997. **101**(33): p. 6525-6531.

25. Kuliev, A.M., R.A. Bagirov, and E.M. Ali-Zade, *Study of the physicochemical and technological properties of natural zeolites.* Klinoptilolit, Tr. Simp. Vopr. Issled. Primen. Klinoptilolita, 1977: p. 52-9.

26. Wilson, S.T., *Templating in molecular sieve synthesis,* in *Verified Syntheses of Zeolitic Materials,* H. Robson, Editor. 2001, Elsevier Science. p. 27-31.

27. Kuhl, G., *Source materials for zeolite synthesis.* Microporous and Mesoporous Materials, 1998. **22**(4-6): p. 515-516.

28. Lechert, H., *The pH value and its importance for the crystallization of zeolites.* Microporous and Mesoporous Materials, 1998. **22**(4-6): p. 519-523.

29. Hodges, C.N. and L.C. Roselaar, *Gold and Platinum Catalyzed Oxidation of Methanol.* Journal of Applied Chemistry and Biotechnology, 1975. **25**(8): p. 609-614.

30. Weiss, M., G. Ertl, and F. Nitschke, *Adsorption and decomposition of ammonia on iron(110).* Applications of Surface Science (1977-1985), 1979. **2**(4): p. 614-35.

31. Lee, T.H. and K.M. Ervin, *Reactions of Copper Group Cluster Anions with Oxygen and Carbon-Monoxide.* Journal of Physical Chemistry, 1994. **98**(40): p. 10023-10031.

32. Dyer, A., *An Introduction to Zeolite Molecular Sieves.* 1988: John Wiley and Sons Ltd.

33. Batista, M.S., et al., *Iron species present in Fe/ZSM-5 catalysts prepared by ion exchange in aqueous medium or in the solid state.* Studies in Surface Science and Catalysis, 2001. **135**(Zeolites and Mesoporous Materials at the Dawn of the 21st Century): p. 2347-2354.

34. Marturano, P., et al., *The mechanism of formation of the Fe species in Fe/ZSM-5 prepared by CVD.* Physical Chemistry Chemical Physics, 2001. **3**(24): p. 5585-5595.

35. Milojevic, M., et al., *Characterization of an Fe-ZSM-5 catalyst prepared by ion exchange in solutions of Fe citrate and Fe oxalate.* Tehnika (Belgrade, Serbia and Montenegro), 2006. **61**(1): p. NM7-NM13.

36. Wolf, F., K. Pilchowski, and K.H. Bergk, *The synthesis and use of zeolitic molecular sieves. Part II. Ion exchange on zeolites from aqueous solutions.* Sprechsaal, 1980. **113**(6): p. 463-8.

37. Romanowski, W. and J.M. Jablonski, *Nickel, cobalt, and iron in the lattice of synthetic zeolites.* Catal. Zeolites, 1988: p. 277-312.

38. Zhang, W., R. Li, and W. Dong, *Effects of dealumination of HZSM-5 on product distribution in cracking of diesel oil.* Sekiyu Gakkaishi, 1989. **32**(1): p. 11-14.

39. Zhu, Q., et al., *N2O decomposition over Fe/ZSM-5: effect of high-temperature calcination and steaming.* Catalysis Letters, 2002. **81**(3-4): p. 205-212.

40. Li, C.Y. and L.V.C. Rees, *Ion-Exchange, Thermal-Stability and Water Desorption Studies of Faujasites with Different Si Al Ratios.* 1988. **7**(2-3): p. 89-99.

41. Berreghis, A., et al., *Dealumination of zeolites .6. Influence of the hydrothermal treatment of EMT zeolites on their framework composition and on their porosity.* Journal De Chimie Physique Et De Physico-Chimie Biologique, 1996. **93**(9): p. 1525-1542.

42. Kornatowski, J., et al., *Dealumination of Large Crystals of Zeolite Zsm-5 by Various Methods.* Journal of the Chemical Society-Faraday Transactions, 1992. **88**(9): p. 1339-1343.

43. Hay, D.G. and H. Jaeger, *Orthorhombic Monoclinic Phase-Changes in Zsm-5 Zeolite Silicalite.* Journal of the Chemical Society-Chemical Communications, 1984(21): p. 1433-1433.

44. Bowker, M., *The Basis and Applications of Heterogeneous Catalysis.* 1998. 96 pp.

45. Lide, D.R., *Handbook of Chemistry and Physics.* 81st ed. 2000: CRC.

46. Isobe, A., et al., *Gas-phase hydration of ethene over Me(HPO$_4$)(2)center dot nH(2)O (Me=Ge, Zr, Ti, and Sn).* Applied Catalysis a-General, 2000. **194**: p. 395-401.

47. Ishihara, T., et al., *Porous H-ZSM-5 zeolite tube as a novel application of catalyst for the synthesis of ethanol by hydration of ethylene.* Industrial & Engineering Chemistry Research, 1997. **36**(10): p. 4427-4429.

48. Wang, Y. and K. Otsuka, *Direct Conversion of Methane and Ethane to the Corresponding Alcohols Using Nitrous-Oxide over Iron Phosphate Catalysts.* Journal of the Chemical Society-Faraday Transactions, 1995. **91**(21): p. 3953-3961.

49. Wang, Y. and K. Otsuka, *Partial oxidation of ethane by reductively activated oxygen over iron phosphate catalyst.* Journal of Catalysis, 1997. **171**(1): p. 106-114.

50. Zheng, X.M., et al., *Oxidative Dehydrogenation of Ethane over Modified Magnesium Oxides,* in *Acid-Base Catalysis Ii.* 1994, ELSEVIER SCIENCE PUBL B V: Amsterdam. p. 451-456.

51. Heracleous, E., et al., *Investigation of Ni-based alumina-supported catalysts for the oxidative dehydrogenation of ethane to ethylene: structural characterization and reactivity studies.* Journal of Catalysis, 2005. **231**(1): p. 159-171.

52. Lillehaug, S., et al., *Catalytic dehydrogenation of ethane over mononuclear Cr(III) surface sites an silica. Part I. C-H activation by sigma-bond metathesis.* Journal of Physical Organic Chemistry, 2004. **17**(11): p. 990-1006.

53. Silberova, B., J. Holm, and A. Holmen, *Oxidative dehydrogenation of ethane over Pt-Sn catalysts*, in *Natural Gas Conversion Vii*. 2004, ELSEVIER SCIENCE BV: AMSTERDAM. p. 685-690.

54. Arnaud, P., *Chimie Organique*. 15th ed. 1996, Paris: Dunod.

55. Bernard, M., *Cours de Chimie Minerale*. 2nd ed. 1994, Paris: Dunod.

56. Kolesnikov, V.P., A.L. Mikhaylichenko, and L.V. Peshkova, *Formation and distribution of nitrous oxide in nitric acid production*. Khimicheskaya Tekhnologiya (Moscow, Russian Federation), 2005(5): p. 5-8.

57. Michael, J.V., J.E. Allen, Jr., and W.D. Brobst, *Temperature dependence of the nitrous oxide + ozone reaction rate from 195 to 369 K*. Journal of Physical Chemistry, 1981. **85**(26): p. 4109-17.

58. Perez-Ramirez, J., *Active iron sites associated with the reaction mechanism of N2O conversions over steam-activated FeMFI zeolites*. Journal of Catalysis, 2004. **227**(2): p. 512-522.

59. Starokon, E.V., et al., *Mechanisms of iron activation on Fe-containing zeolites and the charge of alpha-oxygen*. Topics in Catalysis, 2003. **23**(1-4): p. 137-143.

60. Dubkov, K.A., et al., *Evolution of iron states and formation of alpha-sites upon activation of FeZSM-5 zeolites*. Journal of Catalysis, 2002. **207**(2): p. 341-352.

61. Bordiga, S., et al., *Structure and reactivity of framework and extraframework iron in Fe-silicalite as investigated by spectroscopic and physicochemical methods*. Journal of Catalysis, 1996. **158**(2): p. 486-501.

62. Hall, W.K. and X. Feng, *Overexchanged FeZSM-5: An active durable catalyst for SCR of NO into N2*. Book of Abstracts, 212th ACS National Meeting, Orlando, FL, August 25-29, 1996: p. COLL-184.

63. Karge, H.G., W. Niessen, and H. Bludau, *In-situ FTIR measurements of diffusion in coking zeolite catalysts*. Applied Catalysis a-General, 1996. **146**(2): p. 339-349.

64. Cavallaro, S., *Ethanol steam reforming on Rh/Al₂O₃ catalysts*. Energy & Fuels, 2000. **14**(6): p. 1195-1199.

65. Daintith, J., *A Dictionary of Chemistry*. 4th ed, ed. J. Daintith. 2000, Oxford: Oxford University Press.

66. Shilov, A.E., *Historical Evolution of Homogeneous Alkane Activation Systems*, in *Activation and Functionalization of Alkanes*, C.L. Hill, Editor. 1989, John Wiley and Sons: Atlanta, Georgia.

67. Bruns, B. and K. Ablezova, *Mechanism of the hydrogenation of ethylene on a platinum catalyst*. Acta Physicochimica URSS, 1934. **1**: p. 90-6.

68. Sligar, S.G., *Proton wires and nanobilayers: Oxygen activation in the P450 monoxygenases*. Book of Abstracts, 216th ACS National Meeting, Boston, August 23-27, 1998: p. INOR-357.

69. Otsuka, K. and Y. Wang, *Direct conversion of methane into oxygenates*. Applied Catalysis a-General, 2001. **222**(1-2): p. 145-161.

70. Kryatov, S.V., E.V. Rybak-Akimova, and S. Schindler, *Kinetics and Mechanisms of Formation and Reactivity of Non-heme Iron Oxygen Intermediates*. Chemical Reviews (Washington, DC, United States), 2005. **105**(6): p. 2175-2226.

71. Valentine, A.M., *Bioinorganic hydrocarbon oxidation: mechanistic and kinetic studies of the soluble methane monoxygenase from Methylococcus capsulatus (Bath)*. 1998. p. No pp given.

72. Kryatov, S.V., et al., *A Mechanistic Study of the Reaction between a Diiron(II) Complex [FeII₂(m-OH)₂(6-Me₃-TPA)₂]²⁺ and O₂ to Form a Diiron(III) Peroxo Complex.* Inorganic Chemistry, 2001. **40**(10): p. 2220-2228.

73. Sorokin, A.B., et al., *Model of cytochrome P-450 active center. Iron(III) porphyrin-catalyzed alkane oxidation in microheterogeneous media.* Doklady Akademii Nauk SSSR, 1984. **279**(4): p. 939-41 [Phys Chem].

74. Ellis, S. and I.V. Kozhevnikov, *Homogeneous oxidation of methyl isobutyrate with oxygen catalysed by metal complexes: polyoxometalates versus metalloporphyrins and metallophthalocyanines.* Journal of Molecular Catalysis a-Chemical, 2002. **187**(2): p. 227-235.

75. Lyons, J.E., P.E. Ellis, Jr., and V.A. Durante, *Active iron oxo centers for the selective catalytic oxidation of alkanes.* Studies in Surface Science and Catalysis, 1991. **67**(Struct.-Act. Sel. Relat. Heterog. Catal.): p. 99-116.

76. Costas, M., K. Chen, and L. Que, *Biomimetic nonheme iron catalysts for alkane hydroxylation.* Coordination Chemistry Reviews, 2000. **200-202**: p. 517-544.

77. Bassan, A., et al., *A density functional study on a biomimetic non-heme iron catalyst: insights into alkane hydroxylation by a formally HO-FeV=O oxidant.* Chemistry--A European Journal, 2005. **11**(2): p. 692-705.

78. Bassan, A., et al., *A Density Functional Study of O-O Bond Cleavage for a Biomimetic Non-Heme Iron Complex Demonstrating an FeV-Intermediate.* Journal of the American Chemical Society, 2002. **124**(37): p. 11056-11063.

79. Wang, Y., et al., *Characterizations of iron-containing MCM-41 and its catalytic properties in epoxidation of styrene with hydrogen peroxide.* Journal of Catalysis, 2002. **209**(1): p. 186-196.

80. Stockenhuber, M., M.J. Hudson, and R.W. Joyner, *Preparation, characterization, and unusual reactivity of Fe- MCM-41.* Journal of Physical Chemistry B, 2000. **104**(14): p. 3370-3374.

81. Jia, J.F., et al., *Identification of highly active iron sites in N₂O-activated Fe/MFI.* Catalysis Letters, 2002. **82**(1-2): p. 7-11.

82. Brabec, L., et al., *Fe in MFI metallosilicates, characterization and catalytic activity.* Applied Catalysis a-General, 1998. **170**(1): p. 105-116.

83. Knops-Gerrits, P.P. and W.A. Goddard, *Methane partial oxidation in iron zeolites: theory versus experiment.* Journal of Molecular Catalysis a-Chemical, 2001. **166**(1): p. 135-145.

84. Zhu, Q., et al., *Effect of high-temperature treatment on Fe/ZSM-5 prepared by chemical vapor deposition of FeCl3II. Nitrous oxide decomposition, selective oxidation of benzene to phenol, and selective reduction of nitric oxide by isobutane.* Journal of Catalysis, 2004. **221**(2): p. 575-583.

85. Theunissen, E., et al., *Preferential siting of iron atoms in an MFI-type ferrisilicate zeolite framework: An attempt to explain experimental data with TPA-silicate solution chemistry.* European Journal of Inorganic Chemistry, 2003(7): p. 1296-1298.

86. Selli, E., A. Isernia, and L. Forni, *FTIR characterisation of Fe-silicalite catalysts for benzene oxidation to phenol by N₂O.* Physical Chemistry Chemical Physics, 2000. **2**(14): p. 3301-3305.

87. Handreck, G.P. and T.D. Smith, *A physicochemical study of iron(III)-containing MFI zeolitic materials: the iron(III) isomorph of zeolite ZSM-5.* Journal of the Chemical Society, Faraday Transactions 1: Physical Chemistry in Condensed Phases, 1989. **85**(10): p. 3195-214.

88.   Milanesio, M., et al., *Iron Location in Fe-Silicalites by Synchrotron Radiation Single Crystal X-ray Diffraction.* Journal of Physical Chemistry B, 2000. **104**(43): p. 9951-9953.

89.   Grubert, G., et al., *The room temperature, stoichiometric conversion of N_2O to adsorbed NO by Fe-MCM-41 and Fe-ZSM-5.* Journal of Catalysis, 2000. **196**(1): p. 126-133.

90.   Stockenhuber, M., et al., *Transition metal containing mesoporous silicas - redox properties, structure and catalytic activity.* Microporous and Mesoporous Materials, 2001. **44**: p. 367-375.

91.   Joyner, R. and M. Stockenhuber, *Preparation, Characterization, and Performance of Fe-ZSM-5 Catalysts.* Journal of Physical Chemistry B, 1999. **103**(29): p. 5963-5976.

92.   Lobree, L.J., et al., *Investigations of the State of Fe in H-ZSM-5.* Journal of Catalysis, 1999. **186**(2): p. 242-253.

93.   Kubanek, P., B. Wichterlova, and Z. Sobalik, *Nature of active sites in the oxidation of benzene to phenol with N_2O over H-ZSM-5 with low Fe concentrations.* Journal of Catalysis, 2002. **211**(1): p. 109-118.

94.   Ivanov, A.A., et al., *Kinetics of benzene to phenol oxidation over Fe-ZSM-5 catalyst.* Applied Catalysis a-General, 2003. **249**(2): p. 327-343.

95.   Pillai, K.S., J.F. Jia, and W.M.H. Sachtler, *Effect of steaming on one-step oxidation of benzene to phenol with nitrous oxide over Fe/MFI catalysts.* Applied Catalysis a-General, 2004. **264**(2): p. 133-139.

96.   Haruta, M., et al., *Gold Catalysts Prepared by Coprecipitation for Low-Temperature Oxidation of Hydrogen and of Carbon-Monoxide.* Journal of Catalysis, 1989. **115**(2): p. 301-309.

97.   Haruta, M., et al., *Ultrafine gold particles immobilized with oxides of iron, cobalt, or nickel for the catalytic oxidation of carbon monoxide at -70 Deg.* Proc. - Int. Congr. Catal., 9th, 1988. **3**: p. 1206-13.

98.   Bond, G.C. and D.T. Thompson, *Catalysis by gold.* Catalysis Reviews-Science and Engineering, 1999. **41**(3-4): p. 319-388.

99.   Cant, N.W. and W.K. Hall, *Catalytic Oxidation .4. Ethylene and Propylene Oxidation over Gold.* Journal of Physical Chemistry, 1971. **75**(19): p. 2914-&.

100.   Blick, K., et al., *Methane oxidation using Au/MgO catalysts.* Catalysis Letters, 1998. **50**(3-4): p. 211-218.

101.   Okumura, M., et al., *Direct production of hydrogen peroxide from H_2 and O_2 over highly dispersed Au catalysts.* Chemistry Letters, 2003. **32**(9): p. 822-823.

102.   Landon, P., et al., *Direct synthesis of hydrogen peroxide from H_2 and O_2 using Pd and Au catalysts.* Physical Chemistry Chemical Physics, 2003. **5**(9): p. 1917-1923.

Chapter II: Materials Preparation

II-1 Unsupported iron phosphates FePO$_4$

II-1.1   FePO$_4$

Unsupported iron phosphate was synthesised following the method reported by Y.Wang and K. Otsuka [1].

The catalyst with iron to phosphorus molar ratio of 1 was prepared from mixed aqueous solutions of iron phosphate nonahydrate (Fe(NO$_3$)$_3$.9H$_2$O, Fischer, >99%) and ammonium dihydrogen phosphate (NH$_4$H$_2$PO$_4$, Aldrich, 99.99+%). The solution was evaporated to dryness a 363 K with stirring and the residue dried at 363 K in a furnace, followed by calcination at 823 K for 5 h in static air, using a 5 K min^{-1} heating gradient.

II-1.2   FePO$_4$ pH6

Another FePO$_4$ catalyst, with iron to phosphorus molar ratio of 1, was prepared using a co-precipitation method at neutral pH.

Each Fe(NO$_3$)$_3$ and NH$_4$H$_2$PO$_4$ were each dissolved in 100 mL distilled water. The solutions were mixed and stirred at 500 rpm using an overhead stirrer. The pale yellow solution, pH 1.3, was heated to 363 K and neutralised to pH 6 using a 1 M aqueous ammonia solution, causing precipitation of a beige product. The suspension was stirred for a further 2 h at 363 K, left to cool down overnight with stirring, and the solid residue separated by centrifugation. The residue was then washed three times with 100 mL distilled water, briefly dried at 363 K, and calcined at 823 K for 5 h in static air, using a 5 K min^{-1} heating gradient.

II-2 Iron silicalite (Fe-MFI)

Iron containing silicalite was prepared using the procedure reported by A. Brückner *et.al.* [2]

5.62 g of iron (III) sulphate nonahydrate (Aldrich, 99%) were dissolved in 100 mL of distilled water and 22 g of sulphuric acid (Fischer, 98%).

The silica source used was 85.26 g of sodium metasilicate (Aldrich, 99%) dissolved in 160 mL of distilled water.

The silicate solution was added slowly to the iron solution with vigorous stirring (500 – 1000 rpm) using an overhead stirrer. The resultant gel was stirred for 2 h prior to addition of the template, 13.31 g tetrapropylammonium bromide (Aldrich,), and the mixture stirred vigorously for a further 30 min to ensure homogeneity.

The templated gel was transferred to a PTFE lined stainless steel autoclave for crystallisation. The autoclave was heated to 170 C for 72 h, then left to cool down and the residue was then filtered and washed several times with distilled water. The washed powder was kept in a dry atmosphere for 24 h (cobalt chloride) prior to removal of the template by calcination at 773 K for 4 h, using a 1 C min^{-1} heating gradient.

Iron silicalites with different Fe/Si ratios were prepared using this general procedure, adapting the amount of iron sulphate used to obtain the relevant Fe/Si ratio. The white to beige powders obtained were labelled Fe-MFI SYNx, where x is the materials' iron to silicon ratio.

II-3 ZSM-5s

An ammonium ZSM-5 (NH$_4$-ZSM-5) with a silica to alumina ratio of 30 (Zeolyst, CBV3024E) was used as support for the following procedures.

The zeolite was systematically converted to its proton form (H-ZSM-5) prior to introduction of active phases in the matrix. This was achieved by calcining the NH$_4$-ZSM-5 at 823 K in static air for a minimum of 5 h, using a 10 K min^{-1} heating gradient.

II-3.1   Ion-exchanged Fe-ZSM-5

The Fe-ZSM-5 was prepared using a three fold ion exchange procedure. 1 g H-ZSM-5 was stirred in 50 mL of a 10^{-2} M aqueous solution of Fe(NO$_3$)$_3$ for 12 h at room temperature. The suspension was then filtered over a slow filter paper with vacuum. The residue was dried briefly at 363 K in an oven and finely ground prior to the following exchange. After this procedure was repeated three times the beige to orange residue was washed with 50 mL distilled water, filtered, dried briefly at 363 K, finely ground and calcined at 773 K in static air for 5 h, using a 10 K min^{-1} heating gradient. The beige-brown residue obtained from this procedure is labelled Fe-ZSM-5 EX hereafter.

II-3.2   Chemical vapour deposited Fe-ZSM-5

The procedure described by H.-Y. Chen and W.M.H. Sachtler [3] was used for this preparation.

5.0 g of the calcined H-ZSM-5 was loaded into one side of a U-shaped reactor, and 1.0 g iron (III) chloride (FeCl$_3$, Fischer, > 97%) into the other side of the same reactor, under nitrogen atmosphere. A porous frit kept the zeolite separated from the

$FeCl_3$. Sublimation of iron was carried out in a 100 mL min^{-1} N_2 flow (BOC), the reactor heated to 590 K with a 10 K min^{-1} gradient. A homogeneous yellow/green sample was obtained after 2 h of reaction when the parent material was initially carefully dried and finely ground. A bright yellow material was obtained after washing the zeolite with 250 mL distilled water, which turns to off-white/beige upon calcinations at 773 K for 4 h in a flow of oxygen, using a 1 K min^{-1} heating gradient. The sample obtained is labelled Fe-ZSM-5 CVD hereafter.

II-3.3   ZSM-5 supported iron phosphate

A co-precipitation/impregnation and an ion exchange/impregnation procedure were used for the preparation of ZSM-5 supported iron phosphate.

II-3.3.1   Co-precipitation / impregnation

The co-precipitation preparation was adapted after the procedure reported by G.O. Alptekin et.al. [4]. The solution of $Fe(NO_3)_3$ and $NH_4H_2PO_4$ described for the preparation of bulk $FePO_4$ was used to impregnate the activated H-ZSM-5 to 2% in weight. The aqueous suspension was evaporated with stirring at 363 K, and resultant pale beige material calcined at 823 K for 5 h in static air, using a 5 K min^{-1} heating gradient. The catalyst obtained is labelled $FePO_4$-ZSM-5 hereafter.

II-3.3.2   Ion-exchange / impregnation

The ion exchanged iron phosphate-ZSM-5 preparation consisted in impregnation of phosphate groups from $NH_4H_2PO_4$ onto Fe-ZSM-5 EX. The amount of $NH_4H_2PO_4$ used was calculated to achieve a Fe:P molar ratio of 1. Ammonium phosphate was dissolved in distilled water, and the zeolite suspended in this solution. The solvent was then evaporated at 363 K to dryness, with stirring. The beige residue was calcined

at 823 K in static air for 5 h, using a 5 K min^{-1} heating gradient, and is labelled PO$_4$-Fe-ZSM-5 hereafter.

II-3.4   Gold containing ZSM-5

II-3.4.1   Ion-exchange

Gold was introduced into the relevant zeolites following an ion-exchange procedure adapted after the preparation of gold and iron containing faujasite reported by J.-N. Lin *et.al.* [5]. The amount of gold used was calculated to reach a theoretical iron to gold ratio of 20.

1 g of the calcined zeolite was suspended in 50 mL distilled water, and the pH of the suspension adjusted to 6 using a 1 M aqueous ammonia solution. After the equilibrium was reached the suspension was filtered over a slow filter paper under vacuum, the residue briefly dried at 363 K and finely ground. This neutralised zeolite was then suspended in an aqueous solution of gold chloride hydrochloride. The concentration of the gold solution was calculated to achieve the desired gold loading on the zeolite, assuming 100% exchange. The suspension was stirred at 363 K for 12 h, left to cool down and filtered over a slow filter paper under vacuum. The residue was washed with an equivalent volume of distilled water (50 mL per g of zeolite), filtered, dried briefly at 363 K, finely ground and calcined at 773 K for 5 h in static air, using a 10 K min^{-1} heating gradient.

II-3.4.2   Impregnation

A gold sample was prepared by an impregnation method, derived from the ion exchange method above. The overall procedure is similar, the zeolite was suspended and neutralised with 1 M aqueous ammonia solution, then stirred at 363 K in a gold

chloride aqueous solution. After 12 h stirring at 363 K the solvent was evaporated at 363 K under vacuum, with stirring. The dry residue was washed and calcined as for the ion-exchanged sample.

II-4 MCM-41s

II-4.1   Siliceous MCM-41

The siliceous MCM-41 support was prepared following a procedure reported by M. Grün *et.al.* [6].

38.8 g cetyltrimethylammonium bromide (CTAB, Sigma, 99%) were suspended in 2 L distilled water at room temperature and stirred until most of it was dissolved. 128 mL aqueous ammonia (Fischer, 35%) were then added to the solution, which was stirred for a further 1 h before adding 160 mL tetraethylorthosilicate (TEOS, Aldrich, 98%). Stirring speed was reduced on TEOS addition until no surface vortex was visible. The mixture was stirred slowly for 3 h and allowed to age overnight without stirring. The MCM-41 precipitate was then filtered over a no.2 glass sinter under vacuum. The residue was heated to 773 K under a flow of nitrogen, using a 1 K min^{-1} heating gradient, and calcined at this temperature in a flow of air until no template could be seen in the sample. The chalk-white catalyst obtained is labelled Si-MCM-41 hereafter.

II-4.2   Aluminium containing MCM-41

Aluminium was grafted into the Si-MCM-41 framework using a procedure reported by R. Mokaya and W. Jones [7].

Si-MCM-41 was suspended in a small volume of dry hexane (Aldrich, >95% HPLC). The amount of aluminium isopropoxide (Al(OPr^i)$_3$, Aldrich, 99.99+%) calculated to achieve a Si/Al ratio of 10 was dissolved in dry hexane, and added to the Si-MCM-41 suspension. The reaction volume was 100 mL hexane per gram of Si-MCM-41. The mixture was stirred vigorously for 10 min and left to age without stirring for 24 h at room temperature. The suspension was then filtered over a slow filter paper with vacuum, dried on the filter and calcined at 823 K in static air for 5 h, with a 5 K min^{-1} heating gradient. The calcined white solid was labelled Al-MCM-41.

II-4.3   Iron-modified MCM-41

Iron was introduced into Si-MCM-41 and Al-MCM-41 following an "ion-exchange" procedure.

A 10^{-2} M ethanolic solution of Fe(NO$_3$)$_3$.9H$_2$O was prepared and dried over calcium sulphate (CaSO$_4$, FSA, technical grade). 1 g of MCM-41 was suspended in 50 mL of this dried solution and stirred gently for 12 h at room temperature. The mixture was then filtered and the residue washed with an equivalent volume of dried ethanol, prior to calcination at 773 K for 5 h in static air, using a 5 K min^{-1} heating gradient. The beige product obtained was labelled Fe-MCM-41.

II-4.4   MCM-41 supported iron phosphate

The same type of procedure as for the preparation of ZSM-5 supported iron phosphate was used, i.e. a co-precipitation/impregnation and an "ion-exchange"-impregnation method.

Co-precipitation of iron phosphate onto Si-MCM-41 was carried out in aqueous solution. The amount of iron and phosphorus were calculated to achieve a 5% loading

in weight, with Fe:P molar ratio of 1. $Fe(NO_3)_3.9H_2O$ and $NH_4H_2PO_4$ were dissolved in a minimal volume of distilled water. Si-MCM-41 was suspended in the solution, stirred briefly and the solvent evaporated under vacuum at 363 K with stirring. The beige residue was calcined at 823 K in static air for 4 h, using a 5 K min^{-1} heating gradient, and labelled $FePO_4$-MCM-41 hereafter.

Alternatively phosphate groups were impregnated onto Fe-MCM-41. For this purpose the amount of $NH_4H_2PO_4$, calculated to achieve a Fe:P molar ratio of 1, was dissolved in a minimum amount of distilled water. Fe-MCM-41 was suspended in this solution and stirred, briefly and gently. The solvent was then evaporated at 363 K under vacuum, with stirring, and the dry residue calcined 5 h at 773 K in static air, using a 5 K min^{-1} heating gradient. This very light beige material was labelled PO_4-Fe-MCM-41.

II-5 References

1. Wang, Y. and K. Otsuka, *Direct Conversion of Methane and Ethane to the Corresponding Alcohols Using Nitrous-Oxide over Iron Phosphate Catalysts.* Journal of the Chemical Society-Faraday Transactions, 1995. **91**(21): p. 3953-3961.

2. Bruckner, A., et al., *Epr Study on the Incorporation of Fe(Iii) Ions in Zsm-5 Zeolites in Dependence on the Preparation Conditions.* Zeolites, 1992. **12**(4): p. 380-385.

3. Chen, H.Y. and W.M.H. Sachtler, *Activity and durability of Fe/ZSM-5 catalysts for lean burn NOx reduction in the presence of water vapor.* Catalysis Today, 1998. **42**(1-2): p. 73-83.

4. Alptekin, G.O., et al., *Methane partial oxidation by unsupported and silica supported iron phosphate catalysts - Influence of reaction conditions and co-feeding of water on activity and selectivity.* Journal of Catalysis, 1999. **181**(1): p. 104-112.

5. Lin, J.N., et al., *Gold supported on surface acidity modified Y-type and iron/Y-type zeolite for CO oxidation.* Applied Catalysis B-Environmental, 2002. **36**(1): p. 19-29.

6.   Grun, M., et al., *Novel pathways for the preparation of mesoporous MCM-41 materials: control of porosity and morphology.* Microporous and Mesoporous Materials, 1999. **27**(2-3): p. 207-216.

7.   Mokaya, R. and W. Jones, *Grafting of Al onto purely siliceous mesoporous molecular sieves.* Physical Chemistry Chemical Physics, 1999. **1**(1): p. 207-213.

Chapter III: Surface Area, Transition Metal Concentration and Crystallinity

III-1 Introduction

The physical characterisation of synthetic materials is of particular importance for quality assurance and understanding of their mechanisms of reaction, in the case of catalysts. The techniques used vary depending on the type of material synthesised. In the case of solids for heterogeneous catalysis purposes it is worthwhile to systematically measure the crystallinity and specific surface area of synthesised materials.

As modification of solid supports is concerned, zeotypic supports can have variable stability under different conditions, and their framework can collapse under the effect of temperature or pressure for example. Due to the variety of framework types and their extensive chemistry, it is difficult to predict their stability towards certain treatments, even though guidelines for well studied systems can be found. A routine analysis of the support's structure is therefore also necessary.

The necessity to measure the amount of transition metal on a solid support, or in a solid material, is obvious, as it is a potential active catalytic site.
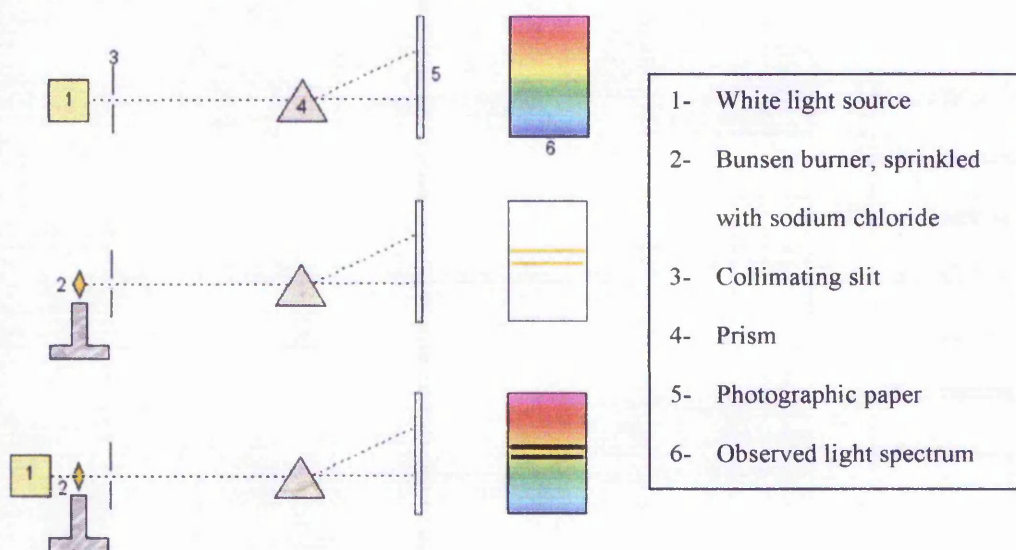
In this chapter the techniques used for the bulk characterisation of these three properties of the studied materials are presented, followed by a brief discussion of the results obtained.

III-2 Background and Methods

III-2.1 Atomic absorption spectroscopy (AAS)

III-2.1.1 Background

Flame AAS in an analytical method used to determine low concentrations of elements in solution. It is based on the absorption of UV/Visible radiation by free atoms, which was first demonstrated in Kirchhoff's experiment [1].

1-	White light source
2-	Bunsen burner, sprinkled with sodium chloride
3-	Collimating slit
4-	Prism
5-	Photographic paper
6-	Observed light spectrum

Figure III-1: Kirchhoff's experiment of light absorption/emission by sodium atoms

Absorption or emission of radiation is a result of the transition of electrons between energy levels in an atom. The wavelength of the radiation absorbed or emitted depends on the energy gap between these levels, and is therefore specific to each element. Transitions can occur between two or more electronic levels, resulting in absorption or emission of light at one or more wavelengths, usually referred to as spectral lines. The intensity of these lines depends on the population of atoms in their ground or excited state.

In Flame AAS, the sample molecules are dissociated in a hot flame to atomic elements, which absorbance at the relevant wavelength is measured over the optical path of the instrument, and compared to standard solutions. Proportionality is observed between the absorbance of the sample and its concentration in solution, with linearity of the spectrometer usually observed only at low concentrations, typically below 3 ppm. A typical setup for an atomic absorption spectrometer is presented in figure III-2. Light with an energy corresponding to the spectral line of the studied element is emitted from a hollow cathode lamp, and passes through the flame. The lamp consists in an anode and metallic cathode enclosed in a leak tight chamber containing low pressures of ultra pure argon or neon. As a potential is applied to the anode, the gas in the chamber is ionised and accelerated towards the cathode by the electrical gradient. Ions hitting the cathode then provoke excitation of the metal atoms, and emission of their characteristic light. The flame is assumed as containing free elements in the ground state, hence able to absorb energy from the light source. The unabsorbed radiation is subsequently monochromated before hitting a photodetector, which measures the difference in transmitted signal in presence and absence of analyte [2].
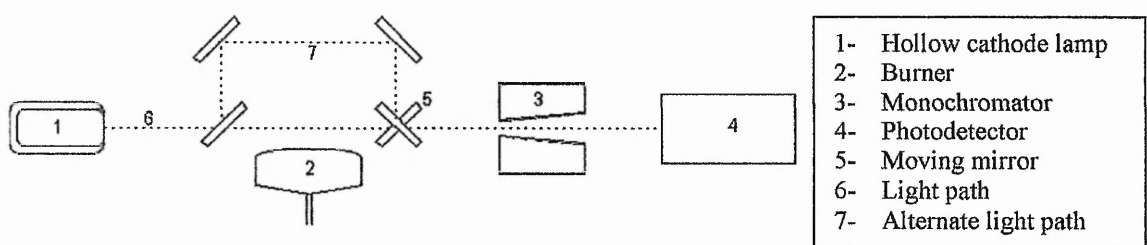
Figure III-2: Schematic diagram of a typical atomic absorption spectrometer

III-2.1.2   Experimental method:

- *Zeolite dissolution method:*

30 mg of sample were placed in a PTFE beaker, where 5 mL of nitric acid HNO_3 (Aldrich, 70%), 1 mL of hydrochloric acid HCl (Aldrich, 37%), and 1 mL of hydrofluoric acid HF (Aldrich, 48%) were added. The solution was heated to 353 K until dry. Then 1 mL HNO_3 was added to the dry sample, along with a small amount of distilled water, until the solid was completely dissolved.

The solution was then finally diluted to a total volume of 25 mL and analysed by atomic absorption spectrometry, together with the relevant standards.

- *Analysis of samples*

The spectrometer used was a Perkin-Elmer 3110 UV spectrometer using a hollow cathode lamp as light source. Iron was titrated by nebulising the dissolved samples into an air/acetylene flame and measuring the absorbance at 248.3 nm. The radiation was detected by means of a photoelectric detector, converting the radiant energy to an electrical signal, recorded on an arbitrary scale. Under standard conditions, iron produces 1% absorption at 0.12 mg L^{-1} and a linear response up to about 5 mg/L.

III-2.2   Surface area measurement

III-2.2.1   Background

The surface area and properties of materials can vary significantly depending on properties such as their particle size or porosity. Particle size definition and classification will not be discussed here, focus will be kept on porosity, pore size, and

surface area measurement. Porous materials are usually classified in three categories, presented in the following table:

Table III-1: IUPAC classification of pore sizes

Label / Category	Pore size
Microporous	< 2 nm
Mesoporous	2 nm to 50 nm
Macroporous	> 50 nm

Specific methods have been developed to measure pore size and surface area of solid materials, the physical adsorption of nitrogen at 77 K being the most widely used. Physisorption is regarded as a non-material specific phenomenon, as nitrogen forms an adsorbed monolayer depending only on the size of the N_2 molecule at low temperatures. Molecules are packed as closely as allowed on the solid surface. This non-specificity is however also source of the complexity of the adsorption process, as multilayers of adsorbate usually form whilst the monolayer is being filled.

Depending on the pore or particle size of the studied material, the adsorption isotherms show different profiles, studied and classified by Brunauer, Deming, Deming and Teller [3]:
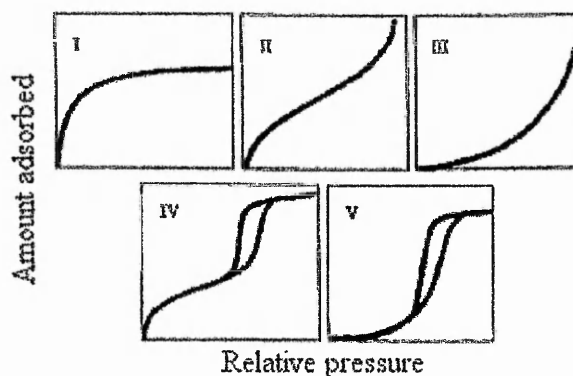
Figure III-3: The Brunauer, Deming, Deming and Teller (BDDT) classification of adsorption isotherms, as recommended by the IUPAC [4]

A model has been developed by Brunauer, Emmet, and Teller [5], to take account of this fact and obtain an accurate representation of the adsorption process. The linearised form of the model proposed, relating volume adsorbed to partial pressure of nitrogen, is presented here:

Equation III-1: The linearised form of the B.E.T. model of physical adsorption of gases

$$\frac{P}{V(P_0 - P)} = \frac{1}{V_m \cdot C} + \frac{C-1}{V_m \cdot C} \cdot \frac{P}{P_0}$$

where P is the equilibrium pressure for a particular surface coverage, P_0 the atmospheric pressure, V the volumetric uptake of nitrogen, V_m the volume required to cover the surface to one monolayer thickness and C a constant.

This model is valid at partial pressures of nitrogen P/P_0 in the range 0.03 to 0.35 [6], where a linear relationship is observed between $\frac{P}{V(P_0 - P)}$ and $\frac{P}{P_0}$ in mesoporous materials. In microporous materials the adsorption potentials of the surface of pores partly overlap, resulting in complete filling of the pores at lower pressures. They show a type I isotherm in the B.D.D.T. classification, and a consequence is that linearity may not be observed in the B.E.T. equation [7]. Surface areas can nevertheless be calculated from modified adsorption models based on the B.E.T. theory. An accepted model is the t-plot method, where amount of nitrogen adsorbed is plotted versus the statistical thickness of adsorbed multilayers. The slope of this plot is equal to the non-microporous area of the sample. As micropore filling occurs at low pressure their volume does not contribute to the formation of multilayers, restricted to the outer surface of the material. The De Boer statistical model of multilayers was used, which theory will not be discussed here. In some cases the Barrett, Joyner and Halunda (BJH) model of adsorption as used to calculate the pore size distribution within
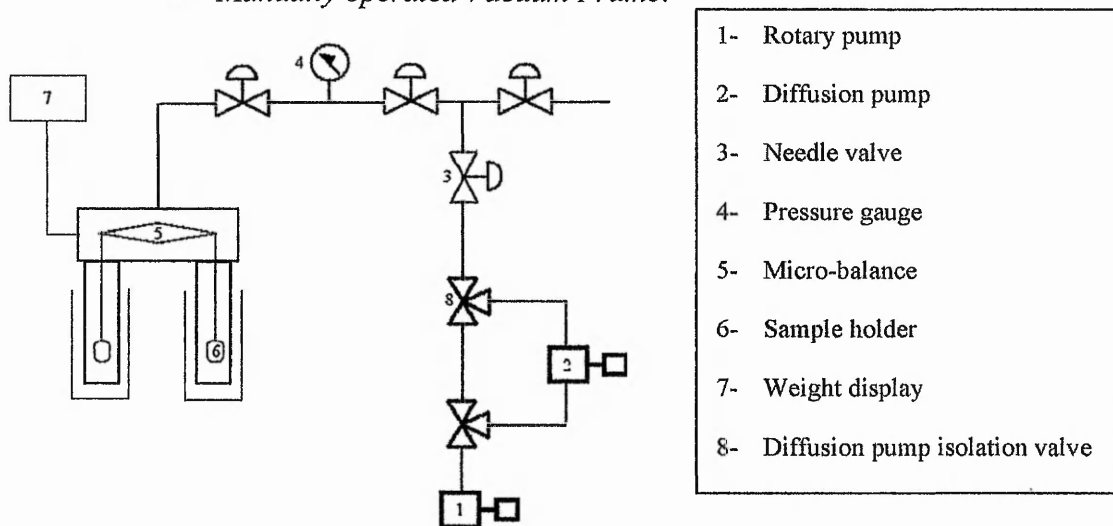
materials. In this model the Kelvin equation and t-plot models are combined to calculate the correlate the amount of nitrogen desorbed by capillary evaporation to pore size. The capillary evaporation and film thickness are taken into account at various nitrogen partial pressures and related to pore radius, in the form of a plot of amount of nitrogen desorbed as a function of the pore size. An accurate picture of the pore size distribution of the materials can be obtained using this model [8].

III-2.2.2   Experimental setup

Three different setups were available for BET surface area and porosity measurement:

-   a manually operated vacuum frame

-   a custom built, automated nitrogen adsorption apparatus

-   a Quantachrome Nova 3200 automated gas adsorption instrument

•   *Manually operated Vacuum Frame:*

1-	Rotary pump
2-	Diffusion pump
3-	Needle valve
4-	Pressure gauge
5-	Micro-balance
6-	Sample holder
7-	Weight display
8-	Diffusion pump isolation valve

Figure III-4: Schematic diagram of the manually operated nitrogen adsorption frame available.

30 – 70 mg of sample were loaded in a small glass crucible attached to a microbalance, and vacuum applied through diffusion and rotary pumps. The sample was typically degassed overnight at 423 K, followed by stepwise adsorption of

nitrogen at 77K. The system was left to equilibrate for 15-30 min at each pressure, and amount of nitrogen adsorbed was determined by recording the sample's weight increase. Desorption isotherms could be measured in a similar manner.
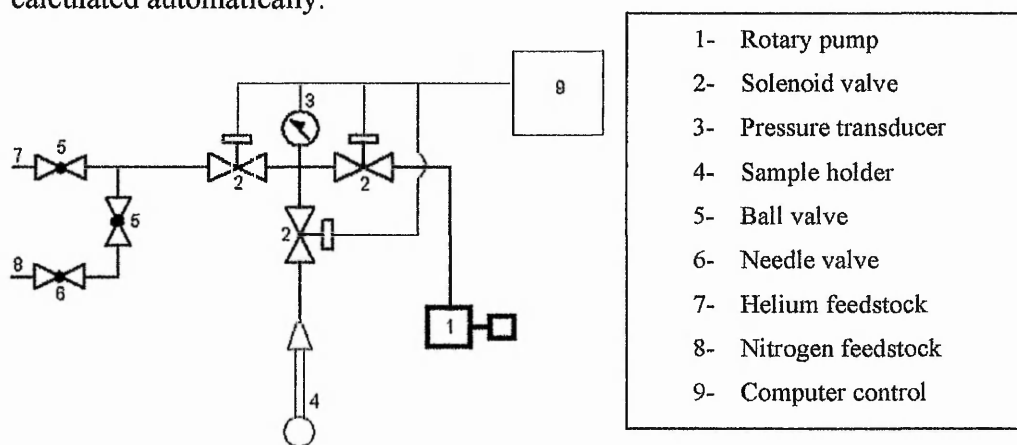
- *Automated N$_2$ adsorption:*

50 mg up to 1g of sample could be loaded in a small glass round-bottomed flask. A low vacuum could be achieved using a rotary pump, and the sample was typically degassed at 423 K overnight in vacuum.

The sample chamber was then purged with helium, and nitrogen dosed in at partial pressures in the BET range using computer controlled relays.

The program output was in the form of BET plots, with $\dfrac{P_E}{V_{N_2}(P_0 - P_E)}$ plotted versus P/P_0. The intercept, Monolayer coverage, C constant and BET surface area were calculated automatically.

1-	Rotary pump
2-	Solenoid valve
3-	Pressure transducer
4-	Sample holder
5-	Ball valve
6-	Needle valve
7-	Helium feedstock
8-	Nitrogen feedstock
9-	Computer control

Figure III-5: Schematic diagram of the custom-built automated nitrogen adsorption apparatus.

- *Quantachrome Nova 3200:*

The Quantachrome Nova is a fully automated adsorption setup. Typically 30 mg of sample were placed in glass tubes, attached to the analyser, and degassed at 393 K for

1 h in vacuum. The samples were then cooled to 77 K and the adsorption isotherms were recorded automatically at relative pressures P/P_0 ranging from 0.01 to 1, the amount of nitrogen adsorbed measured as a volume per gram of sample.

III-2.3   Powder x-ray diffraction (XRD)

III-2.3.1   Background [9]

Powder x-ray diffraction is a powerful tool used to identify the crystalline phases present in a material, by comparison of measured diffraction patterns with those of known standards collected in databases. It is a non-destructive analysis technique which can be used to measure a range of structural properties of a given ordered material. These include strain state, grain size, phase composition, preferred orientation and defect structure. Its main disadvantage comes from the fact that the intensity of diffracted x-rays is proportional to the size, hence atomic number of the element studied. It is therefore inconvenient for the analysis of light elements.

The fundamental principle of XRD relies on the diffraction of incident x-rays by atomic planes in a given crystal. Any crystal can be classified according to the number of symmetry points that can be found in the atomic network. There are seven possible simple arrangements of atoms, in which one or more of five special cases can be found, altogether defining 14 possible lattices, the Bravais lattices (table III-2).

The possible ways of packing these lattices together in a crystal, through symmetry, translation, rotation, define 32 groups called point groups, and the combination of these point groups with the Bravais lattices define together 230 possible space groups. Planes can be found within the crystal packing, by which X-rays are scattered, and under certain conditions, given by Bragg's law, constructive interference gives rise to a diffraction peak.

Equation III-2: Bragg's law for light diffraction

$$\lambda = 2d_{hkl}\sin\theta_{hkl}$$
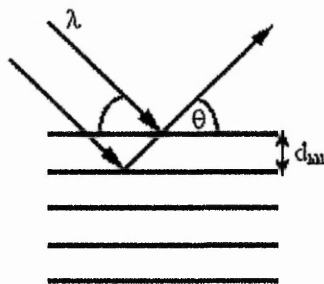
Figure III-6: Illustration of the diffraction of light according to Bragg's law conditions

with λ being the wavelength of the incident x-rays, d_{hkl} the d-spacing between parallel planes, dependent on the size of the unit cell, and θ_{hkl} half of the diffraction angle.

The intensity of the diffracted peaks depends on the order within the crystal, the thickness of the studied sample and the relative position and size of atoms in the matrix.
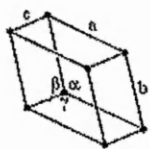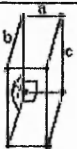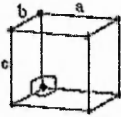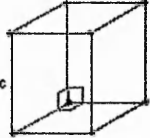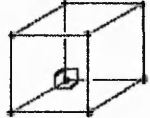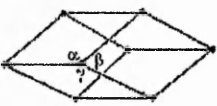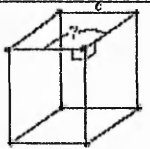
In powder diffraction patterns, the width of a given peak depends on the average size of crystallites R, reflected in the Scherrer equation.

Equation III-3: Scherrer equation relating the width of diffraction peaks to crystallite size.

$$FWHM = K\frac{2\pi}{R}$$

where FWHM is the full width at half maximum height of a given peak, and K is the Scherrer constant, which varies with the dispersion of crystallite sizes in the powder [10].

Table III-2: The seven types of Bravais lattices and possible atom arrangements within the lattice type.

Name	Conditions	Illustration	Possible variations
Triclinic	$a \neq b \neq c$ $\alpha \neq \beta \neq \gamma \neq 90°$		
Monoclinic	$a \neq b \neq c$ $\alpha = \beta = 90° \neq \gamma$		End-centred
Orthorhombic	$a \neq b \neq c$ $\alpha = \beta = \gamma = 90°$		Body-centred, Face-centred, End-centred
Tetragonal	$a = b \neq c$ $\alpha = \beta = \gamma = 90°$		Body-centred
Cubic	$a = b = c$ $\alpha = \beta = \gamma = 90°$		Body-centred, Face-centred
Rhombohedral	$a = b = c$ $\alpha = \beta =$ $\gamma < 120° \neq 90°$		
Hexagonal	$a = b \neq c$ $= \beta = 90°$ $\gamma = 120°$		

III-2.3.2   Experimental setup

Powder X-ray Diffraction (XRD) patterns were recorded on a Philips X'Pert diffractometer equipped with a copper K_α X-ray source. The incident X-ray beam was

generated using a 40 kV and 35 mA power supply, and monochromated on a crystal monchromator, effectively suppressing $K_{\alpha2}$ and K_β radiation from the source.

The powdered sample was packed in the sample holder, which was spun at a 1 revolution per second in order to minimise effects from preferential orientation and generally reduce the background noise.

An Anton Paar 1200 oven sample stage could also be fitted on the diffractometer, allowing the collection of diffractograms in a controlled heated atmosphere. Copper windows allowed the collection of diffracted beam between 0.5 and 140 degrees 2θ. Samples could be heated up to 1473 K with heating gradients varying from 1 to 60 K min^{-1}.

The diffracted beam was detected on an X'Celerator, a multi strip detector allowing faster data collection without loss of signal intensity, compared to standard single point detectors.
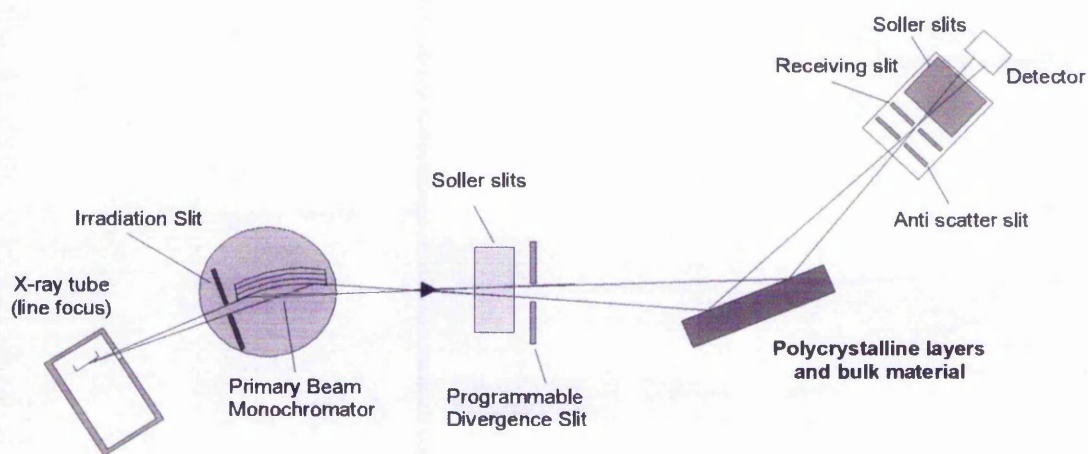
Figure III-7: Schematic diagram of the PANalytical X'Pert powder diffractometer used. (Courtesy of PANalytical UK)

Diffraction patterns were recorded typically using a 0.01 degrees 2θ step and dwell time of 20 s per step.

III-3 Results and discussion

III-3.1 Unsupported FePO$_4$

The experimental determination of iron content of all iron phosphate samples was not achieved, due to a lack of solubility of the materials using the stated method. The theoretical iron content was used instead, assuming a Fe:P molar ratio of one.

Iron phosphate prepared by co-precipitation has been reported to have a low surface area, approximately 9 m^2 g^{-1} [11]. Nitrogen adsorption on our automated B.E.T. setup resulted in a linear B.E.T. plot, with a calculated specific surface area in the range 8.5 to 12.5 m^2 g^{-1}, which was accepted as relevant.

The powder diffraction pattern of FePO$_4$ showed four peaks in the range 1 to 45 degrees 2θ (figure III-8). Crystalline iron phosphates with a quartz-like tetrahedral structure have been reported to show diffraction peaks at 20, 26 and 30 degrees 2θ [11], which was not observed in our case. Peaks centred at 20 and 26 degrees 2θ are observed, together with two broad peaks at 21 and 23 degrees 2θ. Routine curve fitting of these peaks revealed that the FWHM varied by a factor of approximately two between those two sets of peaks, possibly indicating particle size heterogeneity within the crystal phase or asymmetry of the crystals present. The presence of mixed crystalline phases in the material is also possible. The intensity of the peaks is generally weak, which was interpreted as due to the presence of a mostly amorphous phase with some crystalline centres. A reference pattern matching all the peaks observed for FePO$_4$ could not be found in the Inorganic Crystal Structure Database (ICSD). The peaks centred at 20 and 26 degrees 2θ could correspond to the reported quartz-like iron phosphate phase. The peaks centred at 21 and 23 degrees 2θ did not

match any referenced iron phosphate or iron oxide phase. A final feature of this diffraction pattern to be noted is the high background threshold, explained by X-ray fluorescence of the iron in the sample [12].
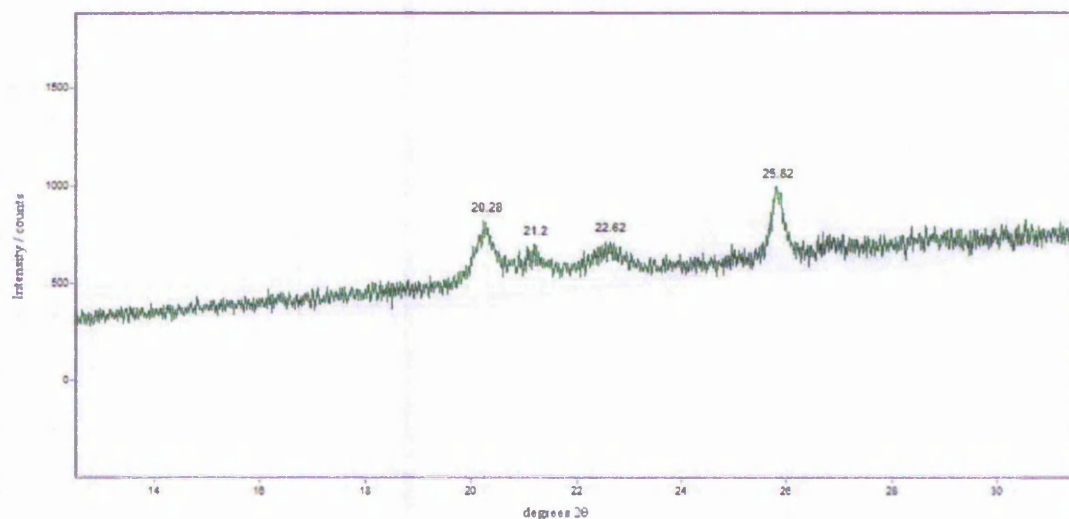
Figure III-8: Powder XRD pattern for co-precipitated FePO$_4$

The co-precipitation of iron phosphate at neutral pH, FePO$_4$ pH6, resulted in an amorphous material, as only iron fluorescence appears on its diffraction pattern (figure III-9).
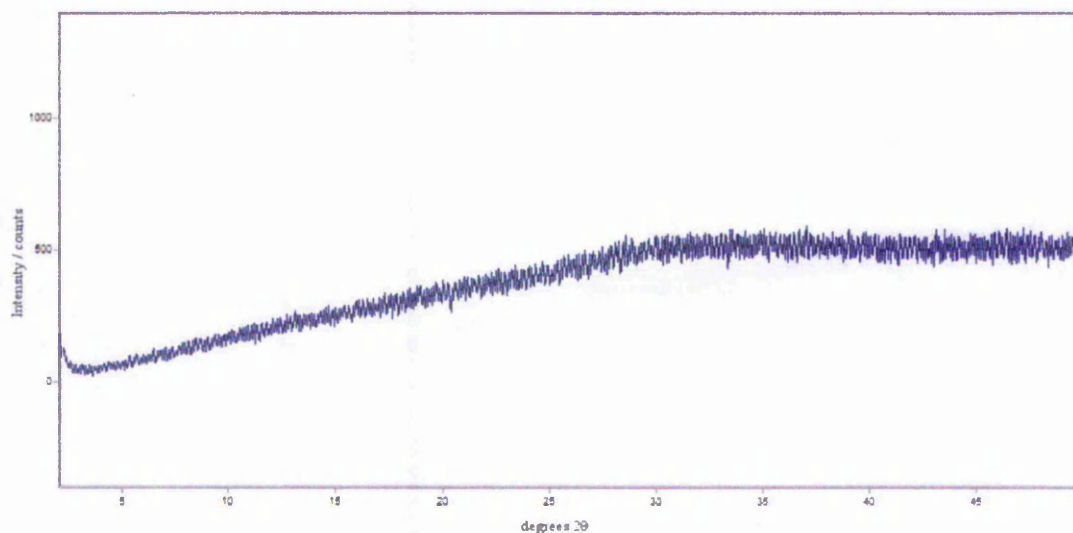
Figure III-9: Powder XRD pattern for FePO$_4$, pH6

The calcination of this material has been studied in situ by XRD. The sample was heated with a 5 K min^{-1} gradient to 823 K in air, and diffractograms recorded every

50 K. An isothermal plateau was programmed during data acquisition. The sample was left to cool to room temperature after a 1 h dwell time at 823 K, and a final diffractogram recorded. The results of this study are presented in figure III-10:
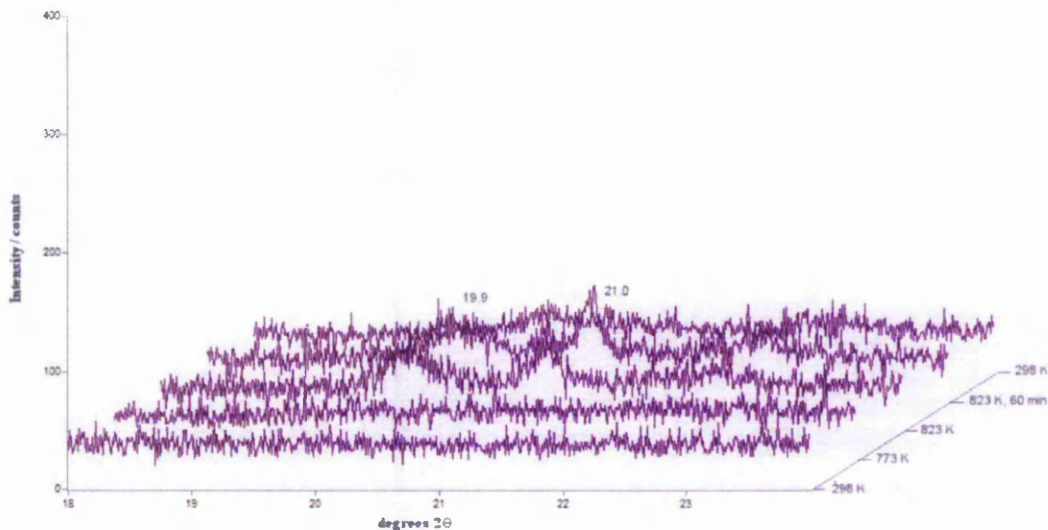
Figure III-10: The effect of temperature on the crystal structure of FePO$_4$ pH6.
The study revealed that three diffraction peaks appear at 823 K, around 19, 20 and 22.5 degrees 2θ. This high temperature structure however seemed to revert to an amorphous phase after cooling of the sample to room temperature. Again it has proven difficult to clearly identify a classified iron phosphate phase from this data. High temperatures can significantly alter peak positions and relative intensities due to the modification of cell parameters trough thermal excitation of atoms. Furthermore, due to the extensive phosphate chemistry and numerous reported FePO$_4$ crystal phases, speculation on the formation of a specific phase was not attempted.

The nitrogen adsorption isotherm of FePO$_4$ pH6 was recorded on the Quantachrome instrument, and shows little adsorption in the low pressure region. Determination of the material's surface area and micropore volume using the t-plot method resulted in a total surface area of ca. 100 m^2 g^{-1}, with absence of micropores. A hysteresis loop is observed around a relative pressure of 0.8, which was calculated to correspond to a

pore diameter of ca. 150 Å and pore opening of 100 Å, using the BJH model. This mesoporosity was interpreted as irregular channels between small iron phosphate particles. As powder diffractograms suggest, a long-range order is not assumed to be present in the material.
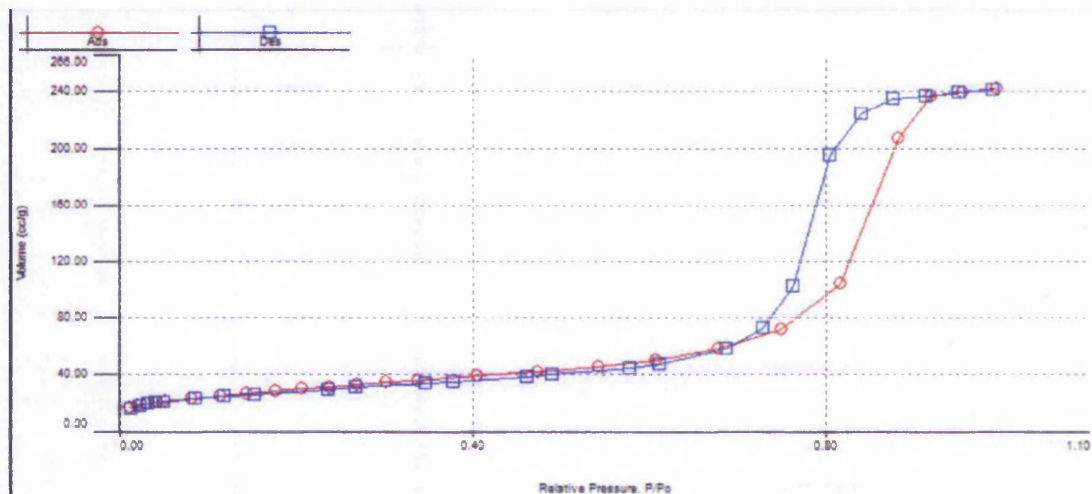
Figure III-11: Adsorption and desorption isotherms of nitrogen at 77 K on FePO$_4$ pH6

A fine dispersion of gold particles in iron phosphate was not achieved using the stated preparation method, as suggested by the diffraction pattern of the resulting material (figure III-12).
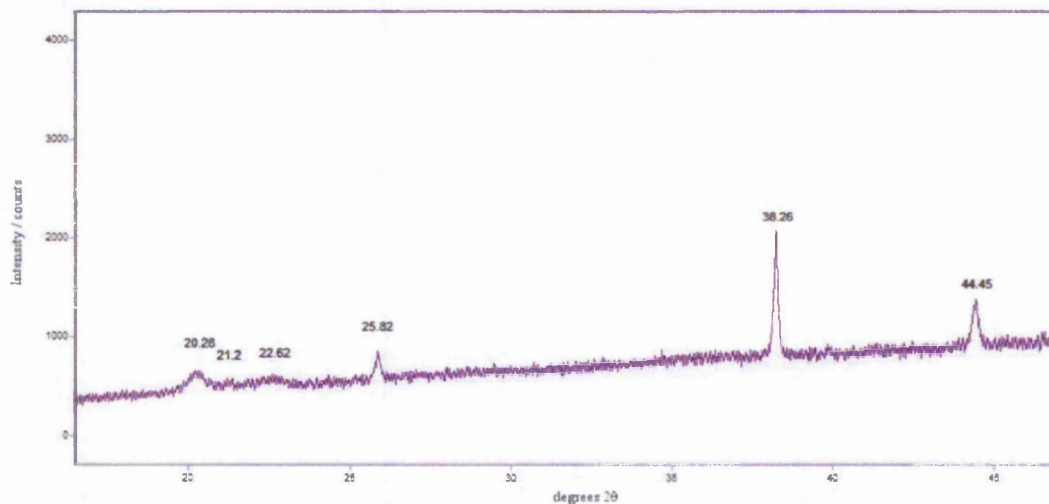
Figure III-12: Powder XRD pattern for Au/FePO$_4$

In addition to the four peaks observed for iron phosphate, between 20 and 26 degrees 2θ, two more intense peaks are observed at 38 and 44 degrees 2θ. These additional

peaks arise from the presence of large gold clusters in the material, as matched in the ICSD [13].

The gold crystallite size calculated by applying the Sherrer equation to the gold (100) peak was found to be 44 nm. The diffraction peaks arising from the iron phosphate phase are at the same positions as for $FePO_4$ prepared using the method reported by Alpetkin *et.al.* ([11], also chapter II-1.1, pp. 39) In addition the material was found to have a low surface area, around 10 m^2 g^{-1}, in agreement with the results reported for this preparation method.

III-3.2   MCM-41

As described earlier MCM-41 has an amorphous structure (see chapter I-2.2.2, pp. 9). The material nevertheless has an array of pores organised in the long-range, in the form of cylindrical pores arranged in hexagonal arrays, which causes the diffraction of X-rays at low angles. The (100) plane of diffraction cuts through the pore system perpendicularly to its direction, resulting in a diffraction peak around 2 degrees 2θ. Diffraction peaks due to the (110) and (200) planes are also observed, and in the case of very regular materials a peak corresponding to the (210) plane.

The diffraction pattern recorded for the Si-MCM-41 synthesised after Grün et.al. [14] is presented in figure III-13:
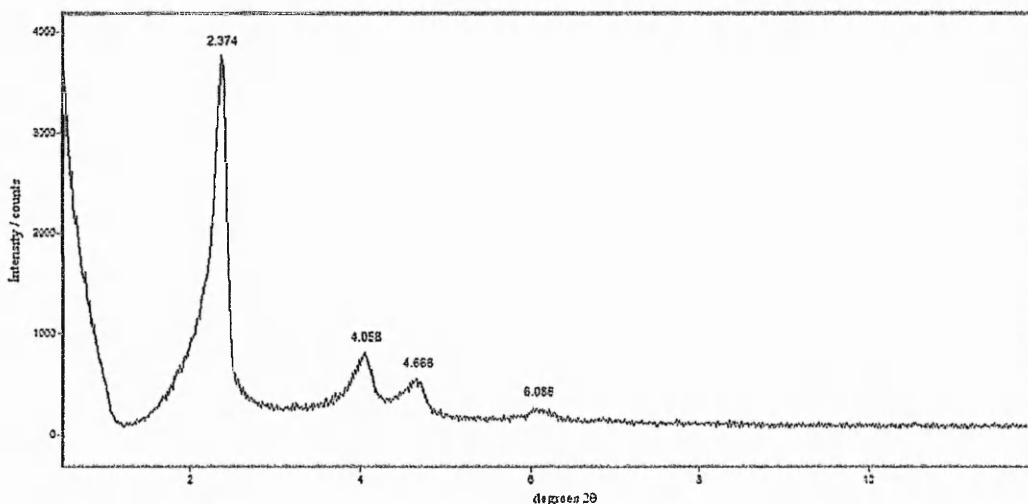
Figure III-13: Powder XRD pattern of a calcined siliceous MCM-41.

The four expected diffraction peaks are visible on the diffractogram, around 2.4, 4.0, 4.7 and 6.1 degrees 2θ. FWHM was measured to be 0.20 degrees 2θ for this material's (100) diffraction, corresponding to a particle size of 31 nm.

From the position of the (100) peak it is possible to calculate the d-spacing of the unit cell, and subsequently the average distance between the centre of two successive pores. Application of the Bragg equation to this diffraction peak allowed the calculation of a d-spacing of 37.8 Å, and pore distance of 43.6 Å. Combination of this data with the pore size calculated from nitrogen adsorption, thereafter, allows to determine the average wall thickness in the material. When the Si-MCM-41 is subsequently modified the measurement of wall thickness can be used to assess the integrity of the framework.

A typical nitrogen adsorption isotherm at 77 K on Si-MCM-41 is presented in figure III-14. This isotherm was recorded using the manual dosing frame and microbalance available. This isotherm shows little hysteresis, indicating the presence of pores with a constant diameter. This diameter was evaluated using the B.J.H. model of adsorption, plotting the derivative of the volume adsorbed versus pore radius (figure III-15)

showed an average pore radius of 15.8 Å. The wall thickness in the prepared material

is therefore slightly below 12 Å on average.
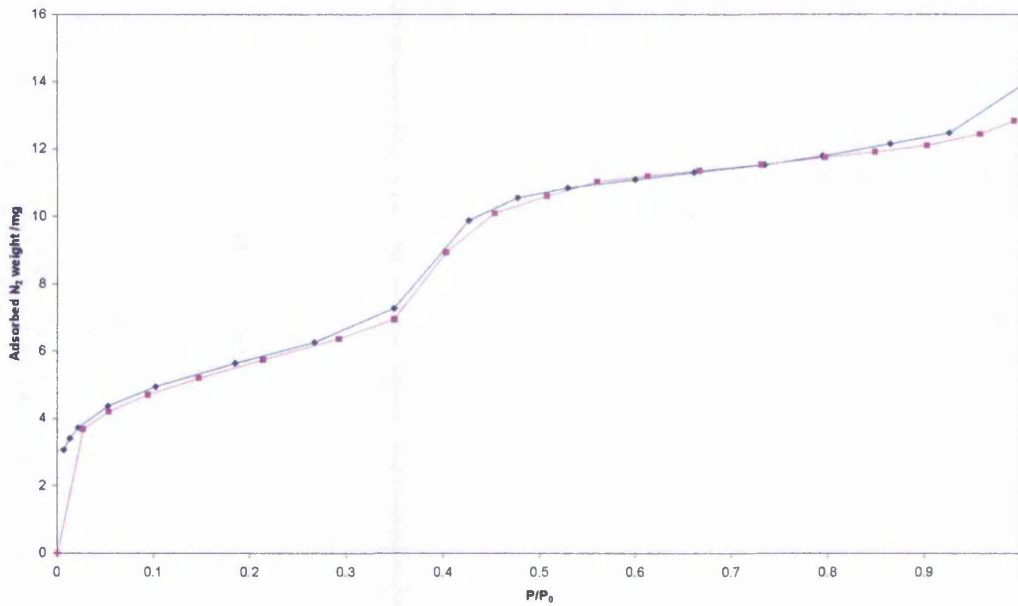
Figure III-14: Typical nitrogen adsorption-desorption isotherm at 77 K for a siliceous MCM-41.
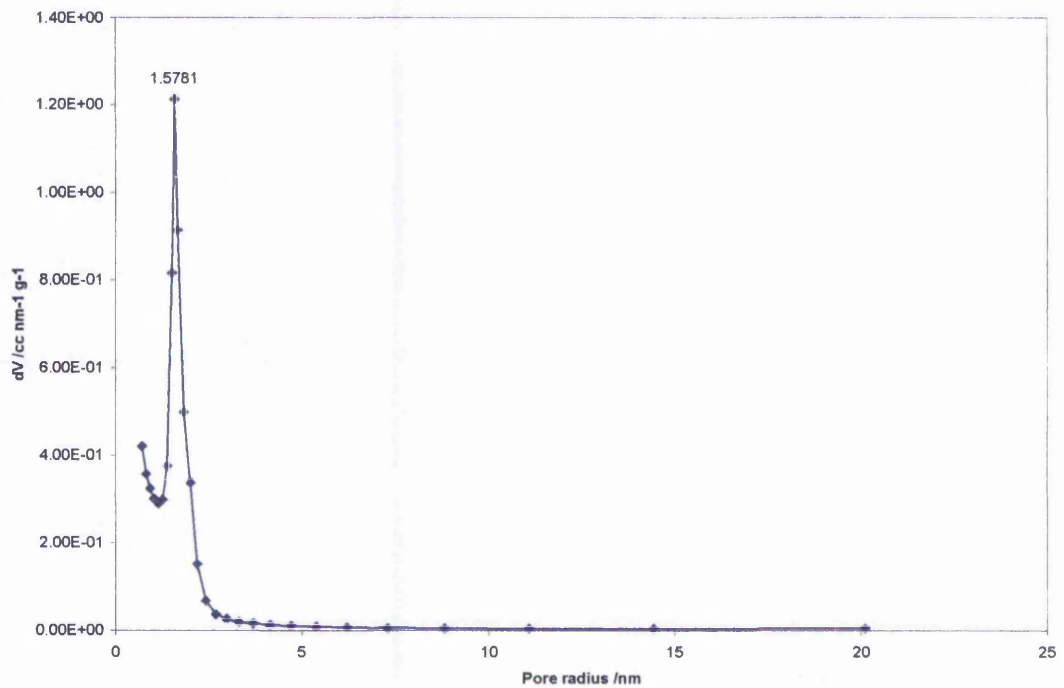
Figure III-15: Pore size distribution for Si-MCM-41, calculated using the BJH method [11].

The B.E.T. plot for the adsorption of nitrogen at 77 K on Si-MCM-41 (figure III-16) allowed the calculation of a specific surface area of approximately 1200 m^2 g^{-1}.

The post-treatment of this parent Si-MCM-41, such as its impregnation with iron, had notable effects on its surface area and structure (figures III-17 and 18). The long-range order in the material is significantly decreased, reflected in a general loss of signal intensity in XRD patterns (figure III-18). Diffraction peaks are also shifted to slightly higher angles, indicating changes in the cell parameters of the produced materials. The calculated distance between pore centres was 42.9 Å for Fe-MCM-41.
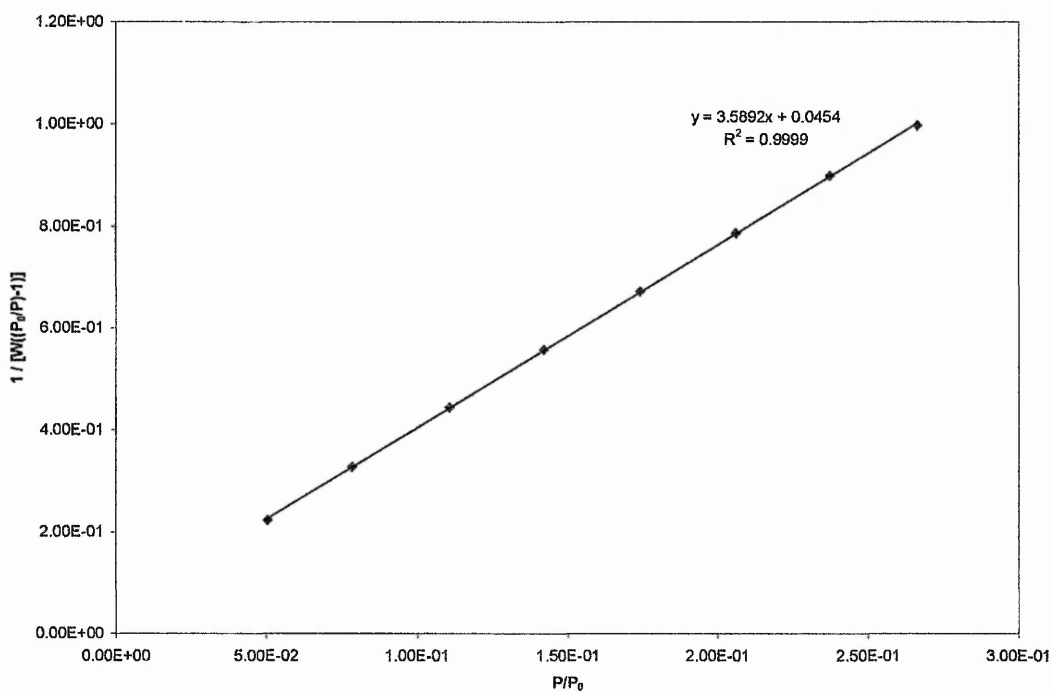
Figure III-16: B.E.T. plot for the adsorption of nitrogen on Si-MCM-41 at 77 K.
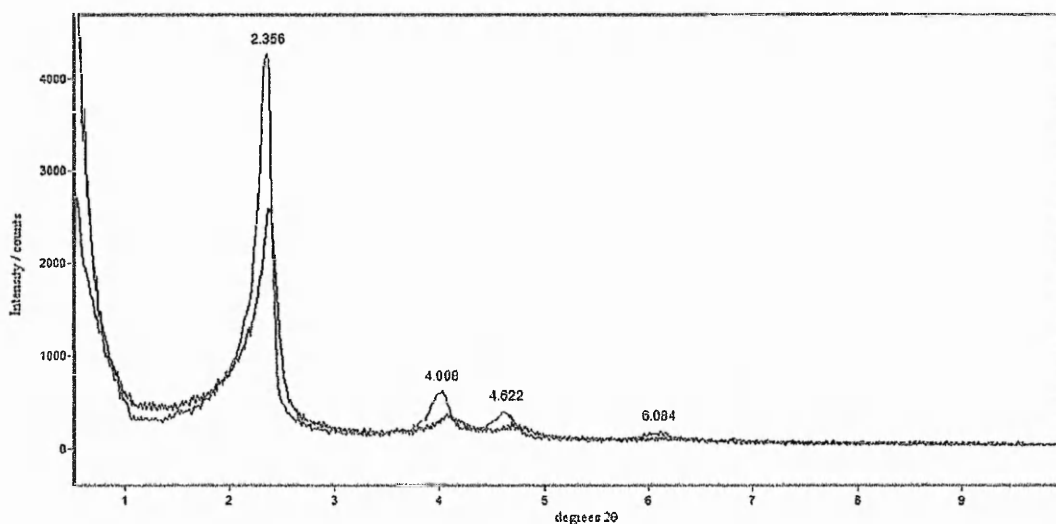
Figure III-17: Effect of the impregnation of iron on the powder XRD pattern of MCM-41s. (green) siliceous MCM-41, (blue) Fe-MCM-41

The nitrogen adsorption isotherms on the same material revealed that its specific surface area was also significantly decreased, around 940 m^2 g^{-1}. This decrease was interpreted as being mainly due to the partial collapse of the MCM-41 framework, as reflected in the intensity loss in XRD patterns, rather than sintering or the unlikely blockage of the pore system. Indeed, the calculated average pore radius after impregnation increased to 16.7 Å, and hence average wall thickness decreased to around 9.5 Å. This latter decrease can confirm a certain degradation of pore walls in MCM-41 through ion exchange, ultimately resulting in the collapse of the said system.
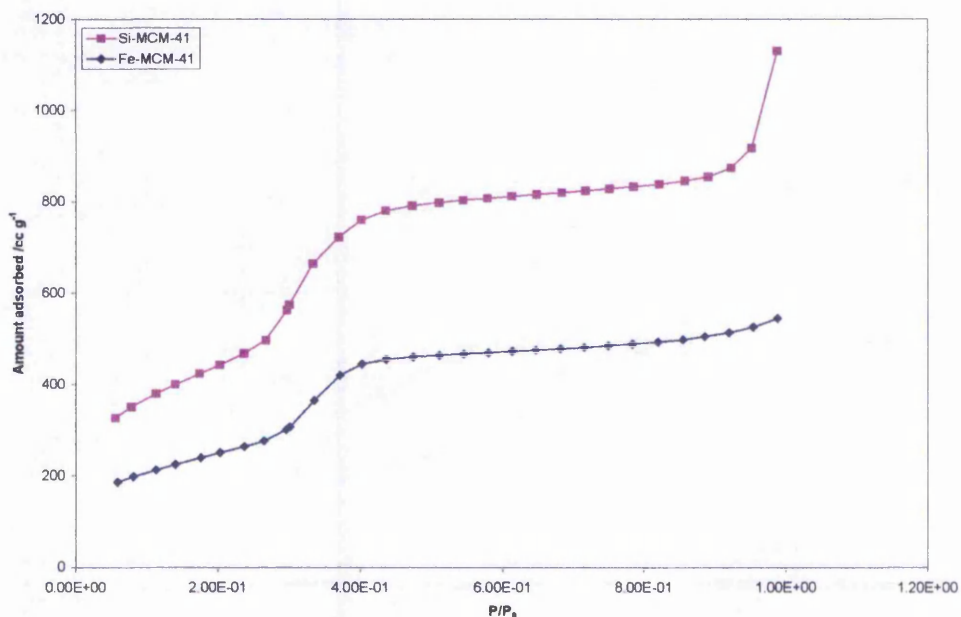
Figure III-18: Effect of the impregnation of iron on MCM-41 on their nitrogen adsorption isotherms at 77 K. (purple) siliceous MCM-41, (blue) Fe-MCM-41
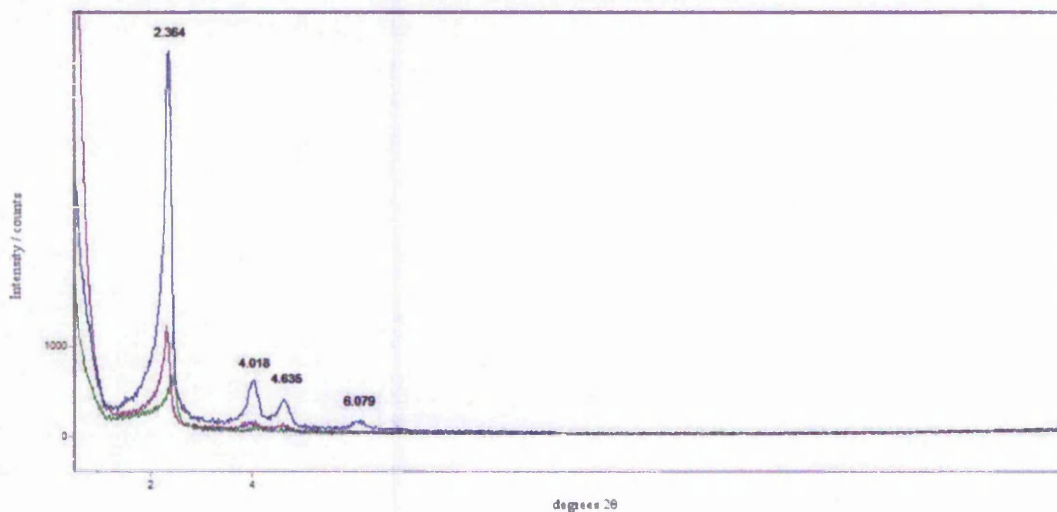
Figure III-19: Effect of the post-synthetic introduction of aluminium in MCM-41 framework and subsequent ion exchange of iron, observed by powder XRD. (blue) siliceous MCM-41, (purple) Al-MCM-41, (green) Fe-Al-MCM-41

The MCM-41 framework collapse was even more drastic when aluminium was introduced into the sample, as observed by XRD (figure III-19).

Attempts to introduce phosphorus, as phosphate groups, in the MCM-41 framework consistently resulted in complete collapse of the framework, as shown in figure III-20. All characteristic diffraction peaks are absent from the recorded diffractogram, instead

a broad feature centred around 24 degrees 2θ, typical of amorphous materials, arise.

Several methods of introducing phosphorus were attempted, which are not presented

or discussed here as in all cases the observed result was the same.
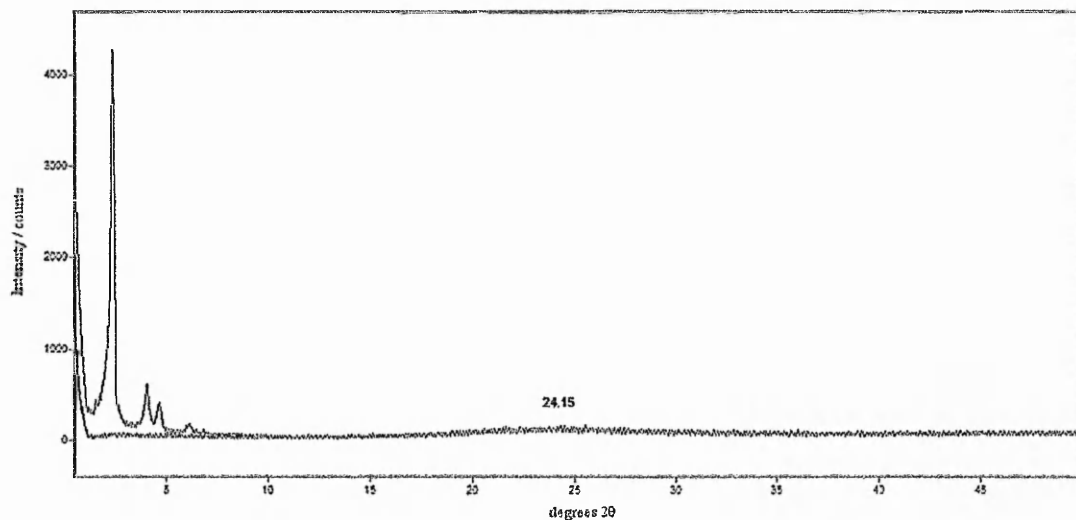
Figure III-20: Effect of the treatment of MCM-41 with phosphorous on its framework, as observed by powder XRD. (purple) siliceous MCM-41, (blue) Fe-PO₄-MCM-41

Three of the phosphorus-containing MCM-41s, even though being amorphous, are

discussed in subsequent chapters, as exhibiting other chemical features of interest.

III-3.3 MFI

One reason for the extensive industrial importance of ZSM-5 zeolite is its particular

stability. Indeed, the preparative treatments inflicted to our materials merely affected

their crystalline structure. As an example a comparison between the powder

diffraction patterns of H-ZSM-5 and the corresponding Fe-ZSM-5 EX is presented in

figure III-21. Degradation of the framework, or change from its orthorhombic to

monoclinic crystal structure are not observed. The latter is usually indicated by the

loss of the doublet at 24.4 degrees 2θ [15]. The diffraction pattern of all samples

prepared by post-synthetic modification of H-ZSM-5 showed an intact orthorhombic

MFI structure.
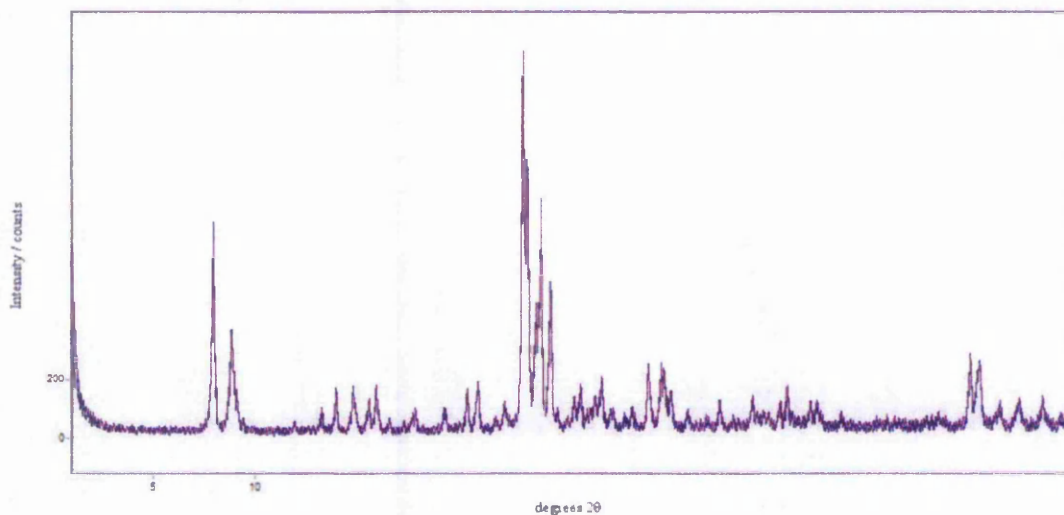
Figure III-21: Comparison of the powder XRD patterns of (purple) an aqueous ion-exchanged Fe-ZSM-5 and (blue) its parent H-ZSM-5.

The sample presented here however has an iron loading of 0.66 wt.%, as determined

by atomic absorption, and local changes around iron centres in the zeolite would not

appear on the recorded diffraction patterns, nor would the iron structure be

observable. Indeed, the intensity of the diffracted beam depending on the size of the

scattering atom [16], it is usually accepted that iron phases in the matrix would be

detectable by XRD at around 2 to 3 wt.% concentrations, when present as bulk

phases, rather than randomly dispersed in the zeolite matrix [17].

The XRD patterns of the samples prepared by CVD do illustrate this fact (fig. III-22).

In these samples, careful, slow calcination is needed to prevent the metal to diffuse

and aggregate to a hematite phase [18]. The diffraction pattern of a Fe-ZSM-5 CVD

calcined carelessly clearly shows an additional peak at 33.1 degrees 2θ, corresponding

to the most intense diffraction peak of hematite. This sample contained 4.36 wt.%

iron, as determined by AAS. In a Fe-ZSM-5 CVD, calcined carefully and containing

2.53 wt.%, the hematite peak could not be observed.
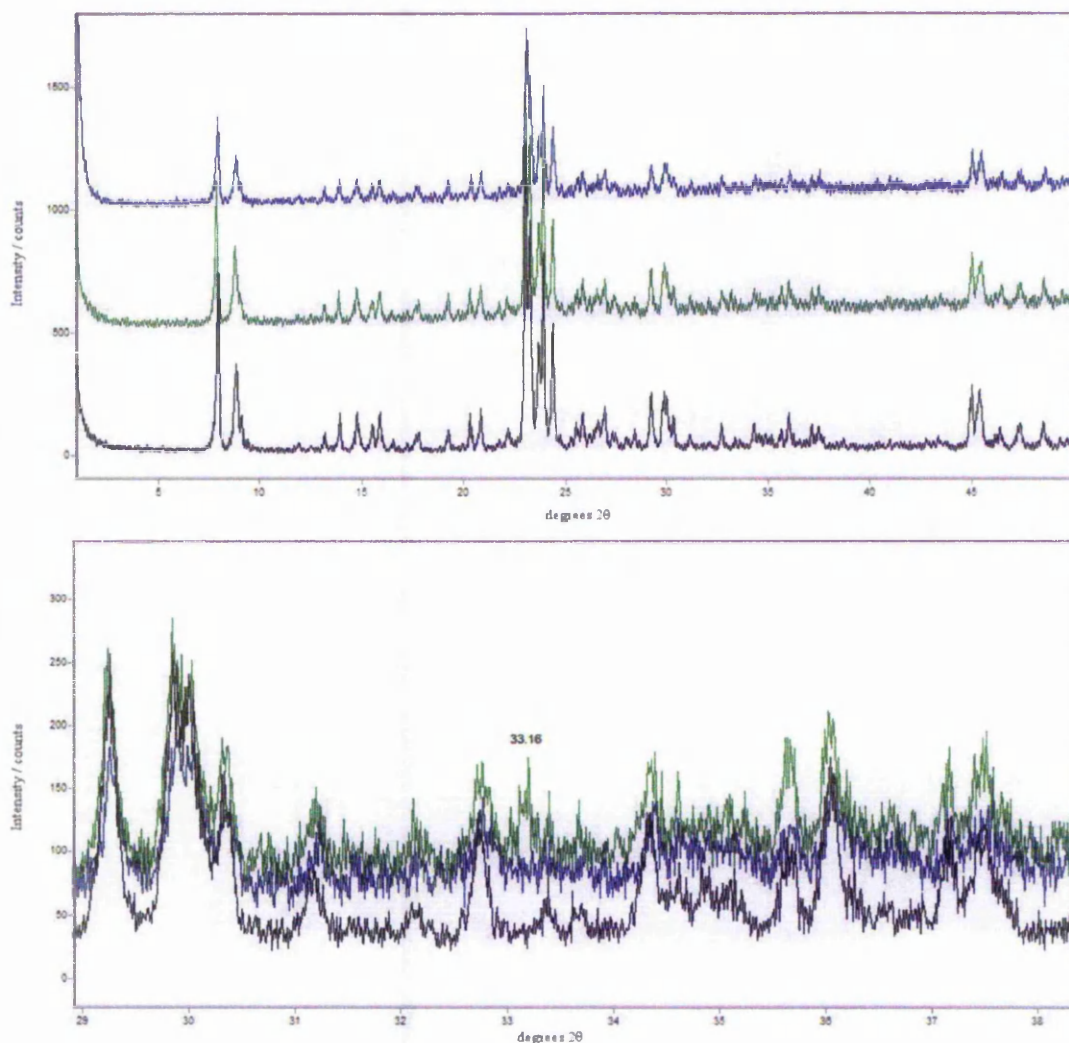
Figure III-22: Comparison of the powder XRD patterns of Fe-ZSM-5s prepared by chemical vapour deposition and their parent H-ZSM-5. (black) H-ZSM-5, (green) Fe-ZSM-5 CVD hematite, (blue) Fe-ZSM-5 CVD.

The iron concentration in the modified zeolites, measured by atomic absorption, is summarised in table III-3 (see pp. 74).

In most ZSM-5s prepared by post-synthetic modification, the micropore volume or surface area of the support was only slightly affected. A typical adsorption and desorption isotherm is presented in figure III-23. This isotherm has been recorded using the Quantachrome NOVA instrument, where very low pressures were not measured. This adsorption and desorption of nitrogen at 77K on Fe-ZSM-5 EX shows a type I isotherm in the BDDT classification, typical of microporous samples. Some

hysteresis at high relative pressure was attributed to inter-particle condensation. Application of the t-plot method of micropore analysis resulted in a micropore volume of 0.265 cm^3 g^{-1} and micropore area of ca. 540 m^2 g^{-1} for this sample.
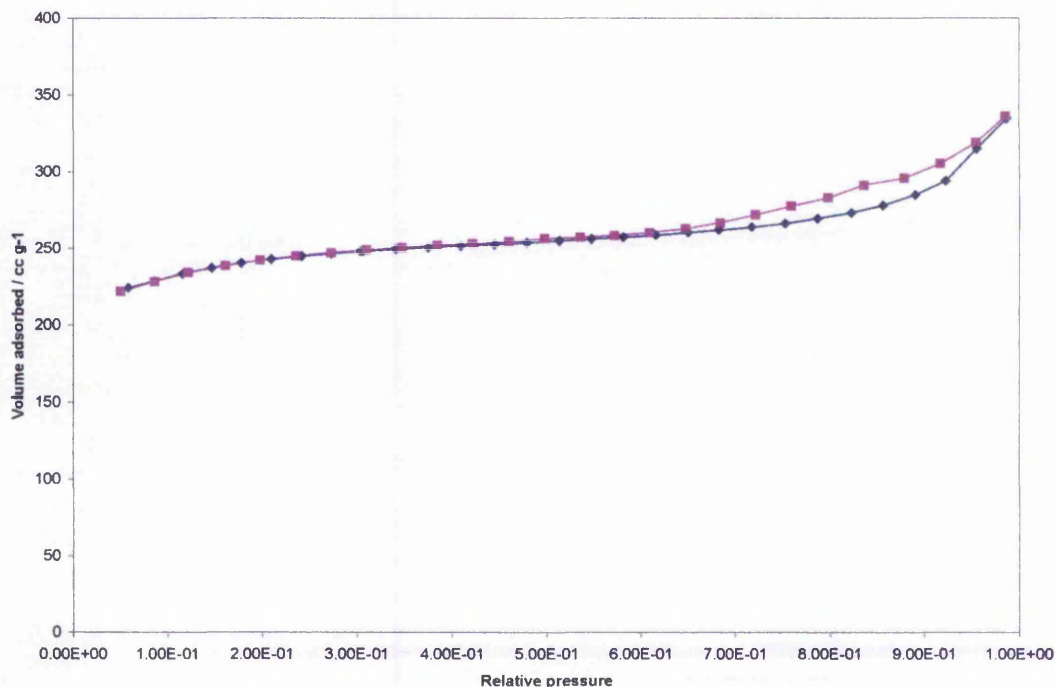
Figure III-23: Nitrogen adsorption and desorption isotherms recorded at 77 K for Fe-ZSM-5 EX.

The method of exchange of iron into the parent zeolite did not affect its micropore volume or area, with calculated values similar to the one found for Fe-ZSM-5 EX, i.e. pore volumes around 0.26 cm^3 g^{-1} and micropore areas of ca. 550 m^2 g^{-1}.

A slight reduction of the micropore volume and area was observed upon subsequent incorporation of phosphorus or gold into the materials, with average reduction by 0.03 to 0.05 and 50 to 100 units respectively. This decrease in micropore volume was directly attributed to the deposition of large entities within the pore system, rather than any degradation of the matrix, as XRD patterns showed consistently intact crystal structures.

Table III-3: Measured iron concentration in post-synthetically modified ZSM-5s.

Material	Iron concentration / wt.%
Fe-ZSM-5 EX	0.68
Fe-ZSM-5 CVD	2.53
FePO$_4$-ZSM-5	1.62
PO$_4$-Fe-ZSM-5	0.36
Au/Fe-ZSM-5 EX	0.55
Au/Fe-ZSM-5 IMP	0.72*

The higher measured iron concentration in Au/Fe-ZSM-5 IMP compared to Fe-ZSM-5 EX, its parent material, was attributed to experimental error in sample preparation for AA.

Crystallisation of iron containing zeolites of MFI structures, following the procedure reported by Brückner et.al. [19], was successful in all cases, as reflected by their powder diffractograms presented in figure III-24. The orthorhombic form of the MFI crystal was produced after removal of the template, as indicated by the presence of a doublet at 24.4 degrees 2θ. A good agreement between the diffraction patterns of our MFIs and the commercial NH$_4$-ZSM-5 used for post-synthetically modified catalysts (figure III-24-a) was observed. Minor differences were observed as the silicon to iron ratio was increased. Peaks between 7 and 10, 22.5 and 25, and around 30 degrees 2θ do not have the same relative intensities, which is assumed to be due to the presence of the two MFI crystal phases, orthorhombic and monoclinic, in different ratios. It was not attempted to quantify the amount of each phase in the materials as this is not expected to affect their catalytic properties.
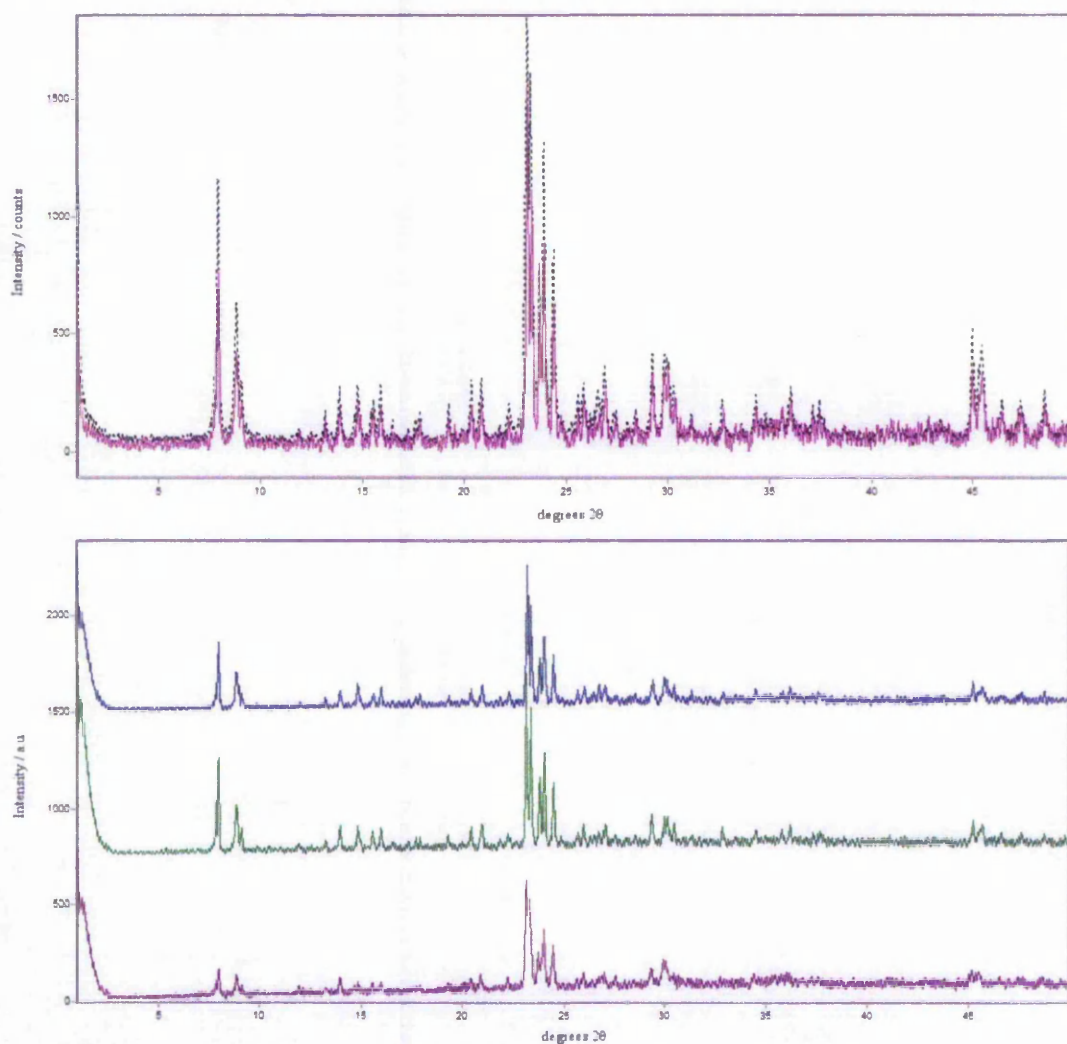
Figure III-24: powder XRD patterns for (top) Fe-MFI SYN24 (purple), compared with a commercial NH$_4$-ZSM-5 (dotted black) with Si/Al = 15. (bottom) (blue) Fe-MFI SYN24, (green) Fe-MFI SYN48 and (purple) Fe-MFI SYN96.

The materials showed type I isotherms in the BDDT classification upon adsorption of nitrogen at 77 K. Their calculated micropore volumes and areas were in the range 0.086 – 0.094 cm^3 g^{-1}, and 198 – 210 m^2 g^{-1}. There wasn't any relationship between the surface area of the samples and their iron concentrations, which were measured to be 5.70, 8.69 and 11.03 wt.%. These concentrations were significantly higher than the theoretical iron content. It is unlikely that the values are due to experimental error, however reproducibility could not be verified for technical reasons. The crystallisation mechanisms of zeolites are still largely unknown, and insights have only been

obtained recently with the use of atomic force microscopy [20]. The reasons for iron and/or silicon to leach in and out of solution are numerous during the synthesis, a definite hypothesis for these high concentrations cannot be laid. It will be assumed in subsequent discussions that these concentrations are accurate. The measured low micropore volumes, compared to commercial samples, could indicate that a significant part of the material is in an amorphous state, however the characteristic broad peak in XRD was not observed, and the peaks arising from the crystal phase had a high intensity. These Fe-MFIs will therefore be regarded as being successfully synthesised.

III-4 Summary

The structural properties and iron concentration of all prepared materials were characterised by means of powder x-ray diffraction, physical adsorption of nitrogen at 77K, and atomic absorption. The two first methods are non-destructive and gave information about the crystallinity and porosity of samples respectively. The integrity of supports was checked, following various treatments, as well as the structure of synthesised supports and bulk materials. For the determination of iron concentrations in samples using atomic absorption, materials had to be digested using a specific method.

Bulk iron phosphates have heterogeneous structures depending on the synthetic method used, and a low surface area, as expected. The crystal phase formed, if any, could not be matched with any known reference from the Inorganic Crystal Structure Database, and in general diffraction peaks were of weak intensity, indicating mostly amorphous materials.

The MCM-41 support synthesised showed a respectable long-range order and good surface area, ca. 1200 m^2 g^{-1}. Subsequent modifications of the support, introduction of iron, aluminium and phosphorus irremediably reduced diffraction peak intensities and measured surface areas, attributed to a collapse of the framework. In the case of iron and aluminium impregnation the effect was limited, however phosphorus as phosphate groups caused the complete collapse of the silica matrix.

Samples of MFI structure were by far the most stable to any treatment, with little to no alteration of their framework upon exchanges. The formation of extensive hematite phases on the zeolite's surface could be avoided in general. The introduction of iron into an MFI framework during its synthesis was successful, producing materials with micropore volumes lower than commercial catalysts but with good crystallinity.

III-5 References

1. Rouessac, F. and A. Rouessac, *Chemical Analysis - Modern Instrumentation Methods and Techniques*. 5th ed, ed. J.W. Sons. 2000.
2. Willard, H.H., *Instrumental methods of analysis*. 7th . ed. 1988, Belmont, CA: Wadsworth.
3. Brunauer, S., et al., *Multimolecular adsorption of gases on silica gels*. Journal of the American Chemical Society, 1940. **62**: p. 1723.
4. Sing, K.S.W., et al., *Reporting physisorption data for gas/solid systems with special reference to the determination of surface area and porosity (Recommendations 1984)*. Pure and Applied Chemistry, 1985. **57**(4): p. 603-19.
5. Brunauer, S., P.H. Emmet, and E. Teller, *Adsorption of Gases in Multimolecular Layers*. Journal of the American Chemical Society, 1938. **43**(11): p. 2285-2286.
6. Brunauer, S., P.H. Emmett, and E. Teller, *Adsorption of gases in multimolecular layers*. Journal of the American Chemical Society, 1938. **60**: p. 309-19.
7. Bhambhani, M.R., et al., *Analysis of nitrogen adsorption isotherms on porous and nonporous silicas by the BET [Brunauer-Emmett-Teller] and as methods*. Journal of Colloid and Interface Science, 1972. **38**(1): p. 109-17.
8. Barrett, E.P., L.G. Joyner, and P.P. Halenda, *The determination of pore volume and area distributions in porous substances. I. Computations from nitrogen isotherms*. Journal of the American Chemical Society, 1951. **73**: p. 373-80.

9.   Brundle, C.R., J. C.A. Evans, and S. Wilson, *Encyclopedia of Materials Characterization. Surfaces, Interfaces, Thin Films*, ed. C.R. Brundle and J. Charles A. Evans. 1992: Butterworth-Heinemann.

10.   Pielaszek, R., *Diffraction studies of microstructure of nanocrystals exposed to high pressure*, in *Department of Physics*. 2003, Warsaw University.

11.   Alptekin, G.O., et al., *Methane partial oxidation by unsupported and silica supported iron phosphate catalysts - Influence of reaction conditions and co-feeding of water on activity and selectivity.* Journal of Catalysis, 1999. **181**(1): p. 104-112.

12.   Bridou, F., J.P. Chauvineau, and A. Mirone, *Fluorescence study in a periodic Fe/C multilayer by high luminosity grazing incidence primary monochromatic x-ray.* Journal de Physique IV: Proceedings, 1998. **8**(PR5, Rayons X et Matiere): p. Pr5/309-Pr5/316.

13.   Swanson, H.E. and E. Tatge, *Standard x-ray diffraction powder patterns.* National Bureau of Standards Circular (U. S.), 1953. **539**(Vol. I): p. 95 pp.

14.   Grun, M., et al., *Novel pathways for the preparation of mesoporous MCM-41 materials: control of porosity and morphology.* Microporous and Mesoporous Materials, 1999. **27**(2-3): p. 207-216.

15.   Kokotailo, G.T., et al., *Structure of Synthetic Zeolite ZSM-5.* Nature, 1978. **272**(5652): p. 437-438.

16.   Hammond, C., *The basics of crystallography and diffraction / Christopher Hammond.* International Union of Crystallography texts on crystallography ; 3. 1997: International Union of Crystallography [and] Oxford University Press.

17.   Angus, J.G., J.B. Raynor, and M. Robson, *Reliability of experimental partition coefficients in carbonate systems: evidence for inhomogeneous distribution of impurity cations.* Chemical Geology, 1979. **27**(3): p. 181-205.

18.   Marturano, P., et al., *The mechanism of formation of the Fe species in Fe/ZSM-5 prepared by CVD.* Physical Chemistry Chemical Physics, 2001. **3**(24): p. 5585-5595.

19.   Bruckner, A., et al., *Epr Study on the Incorporation of Fe(III) Ions in Zsm-5 Zeolites in Dependence on the Preparation Conditions.* Zeolites, 1992. **12**(4): p. 380-385.

20.   Anderson, M.W., et al., *Growth models in microporous materials.* Microporous and Mesoporous Materials, 2001. **48**(1-3): p. 1-9.

Chapter IV: <u>Reducibility of the transition metal</u>

IV-1 Introduction

Temperature-programmed reduction is a technique used to study the kinetic reduction profile of materials, producing patterns that can be used as fingerprints. As the reduction is normally kinetically driven rather than thermodynamically [1], there can be substantial differences between the reduction profiles of materials with the same local structure, but different chemical environment, as outlined below.

All the synthesised materials containing reducible centres have been studied by TPR as the partial oxidation of alkanes' catalytic cycle is expected to involve oxidation and reduction of the active site [2, 3].

The recorded profiles will be discussed to the best of knowledge and gained experience, however in some cases several hypotheses may be applicable and will not be discriminated. Some information about the ease of reducibility and total amount of reducible species could be obtained for all materials, and will be related to their catalytic activity in chapter VII: Oxidation studies (see pp. 183).

IV-2 Background and method

IV-2.1 Temperature-programmed reduction (TPR)

IV-2.1.1 Background [1]

Temperature-programmed reduction is a technique used for the characterisation of solids. Its essence is the dynamic reduction of a solid sample in a flow of gas, typically hydrogen. Information about the chemical state of the solid is obtained by

measuring the composition of the outlet gas as a function of temperature, and can be used as a "fingerprint" of the material. The technique makes the identification of complex reduction mechanisms possible in some cases due to its high sensitivity. TPR has proven itself essential in the study of redox catalysis. It is a helpful tool in the study of the effects of particle size, interaction between solids, and influence of thermal treatment on such catalysts.

Its limitations come from the kinetic character of reduction processes and hence dependency of reduction profiles on the experimental setup. Some guidelines have been reported on the set-up acquisition of a series of successful and meaningful reduction profiles [4]. Monti and Baiker report variables such as heating rate, reducing gas concentration, total flow rate and amount of reducible species in the sample to have a significant effect on TPR pattern. The first two variables influence the temperature of maximum reduction rate, while the total flow rate influences the time lag and dispersion of the original signal between the reactor and detector. A characteristic number, K, relating to these variables, is defined to ease the choice of settings.

Equation IV-1: Monti and Baiker equation for the optimisation of parameters in TPR studies.

$$K = \frac{S_0}{V \cdot c_0}$$

where K should be equal to 100 ± 30 s^{-1}, S_0 is the amount of reducible species is μmol, V is the total flow rate in cm^3 s^{-1} and c_0 the concentration of reducing gas in μmol cm^{-3}.

IV-2.1.2   Experimental setup

The TPR setup consisted in a ¼ in. tubular quartz reactor placed in a horizontal furnace, connected to a thermal conductivity detector (TCD). A cold trap at dry ice temperature was placed between the reactor outlet and the detector to prevent non-permanent gases from entering the latter and biasing the measurement of hydrogen gas concentration. The total flow rate was checked with a bubble meter at the system outlet (fig. IV-1). The catalyst, in an amount calculated according to the Monti and Baiker equation (eq. IV-1), was kept in place in the tube using quartz wool plugs, and placed in a central position in the furnace. The side openings of the furnace were plugged with insulating tape to prevent diffusion of heat to the outside and ensure better temperature control.

Feedstock gas — Furnace — TCD — Exhaust / Flow measurement

Cold Trap
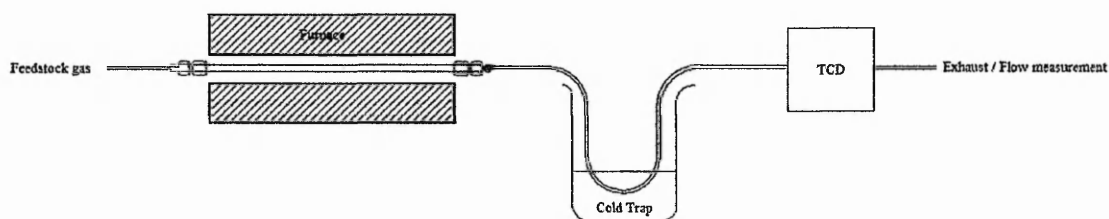
Figure IV-1: Schematic diagram of the setup used for temperature-programmed reduction experiments

The samples were pre-oxidized in a 75 mL min^{-1} flow of air (B.O.C.), at 773 K for 1 h typically. The heating gradient varied, depending on the material, either 5 or 10 K min^{-1}, accordingly with calcination conditions.

The reduction was carried out in a 10 mL min^{-1} flow of 5% hydrogen in argon (B.O.C.), heating up to 1273 K with a 10 K min^{-1} gradient. The TCD signal was recorded as a function of temperature. As the signal from the TCD was directly related to the amount of hydrogen in the outlet gas feed, a hydrogen uptake from the reduction of the metal appears as a peak on the recorded trace, area of which is representative of the amount of molecules of hydrogen used for the reduction of the

metal. This could then be used to calculate the amount of metal reduced, provided some information was known about the state of the metal at the start of the experiment. The TCD signal was calibrated using a metal oxide known for its ease of reducibility, nickel oxide.

IV-3 Results and discussion

IV-3.1 Iron Phosphates and derivatives

The reduction of a pure iron phosphate by hydrogen is expected to follow the pathway presented in equation IV-2. Two hydrogen uptake peaks would result from this stepwise reduction, with areas with a relative ratio of 1:2. Iron phosphates precipitated using different methods show different reductive behaviours (figure IV-2).

Equation IV-2: Schematic pathway of reduction of FePO$_4$ by H$_2$

$$Fe^{3+}PO_4^{3-} \xrightarrow{1/2\ H_2} Fe^{2+}HPO_4^{2-} \xrightarrow{H_2} Fe + H_3PO_4$$

FePO$_4$, co-precipitated by evaporation of the solvent, has a relatively smooth reduction peak centred around 910 K. Two sharp shoulders appear at lower temperatures, which might be attributed to a stepwise reduction of the iron (III) centre to metallic iron. This hypothesis can be easily dismissed as a ratio of hydrogen uptake to moles of iron present of 0.30 was found, which corresponds to less than a one-electron transfer step. Furthermore it can be noticed that another reduction step occurs at higher temperatures, indicated by the increase of hydrogen uptake at 1273 K. The latter more than likely corresponds to a reduction of ferric species to metallic iron.

Such shoulders can also be attributed to particle size heterogeneity. Indeed in temperature-programmed reduction the peak widths and maxima increase with increasing particle dimension [1]. It was accepted, after XRD study of the sample

before reduction, that particle size heterogeneity may be present in the sample (see pp. 60), which corroborates this hypothesis.

Due to the nature of the preparation method for the material, i.e. equimolar amounts of iron and phosphorus present in an acidic medium and forced, quick, precipitation by removal of the solvent, the hypothesis of particle size heterogeneity is considered to be reasonable.
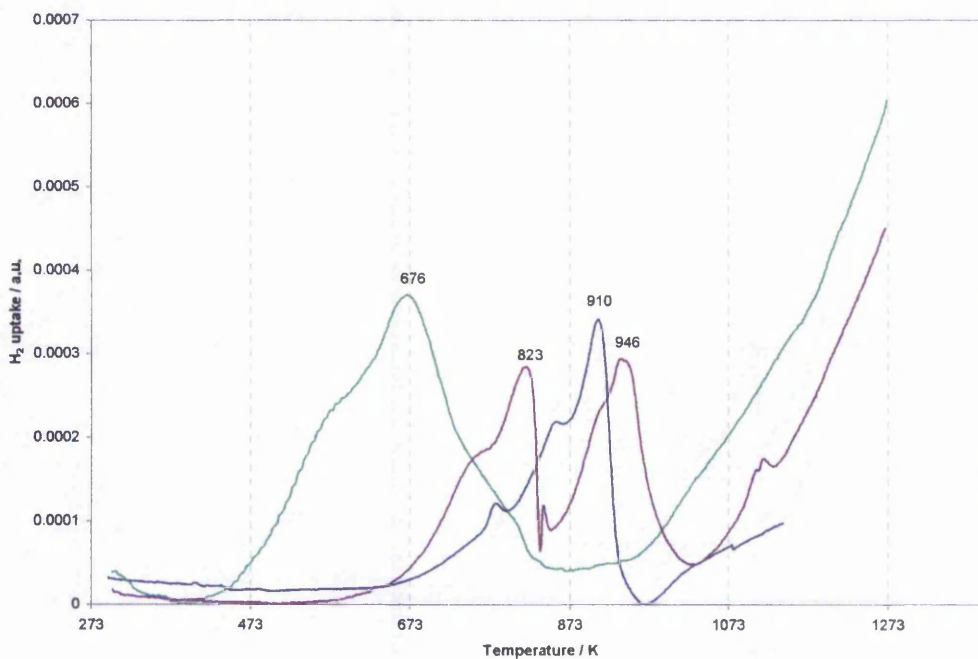
Figure IV-2: TPR profiles for unsupported iron phosphates. (blue) FePO$_4$, (purple) FePO$_4$, pH6, (green) Au/FePO$_4$. The profiles were recorded with a 5 K min^{-1} heating gradient, 10 mL min^{-1} flow of 5% H$_2$/Ar.

It is likely, in the case of FePO$_4$, pH6, that an iron oxide or hydroxide phase has precipitated in this case; this is known to occur readily at neutral to basic pH [5]. The reduction has two maxima, at 823 and 946 K, both showing defined H$_2$ uptake peaks, and shoulders attributed to particle size heterogeneity. There is no evidence in XRD patterns for phase differentiation, as only an amorphous pattern was observed at room temperature. When the sample was heated in air however, some crystalline character was observed in the material, through the appearance of three diffraction peaks,

around 873 K (see pp. 62), which corresponds to the temperature at which hydrogen uptake suddenly drops in our TPR experiment. The attribution of a quenching of the reduction process directly to the structural rearrangement of the material is highly speculative, due to the differences in experimental conditions, i.e. atmosphere and flow conditions, but is thought to be possible.

The lower reduction temperature of the gold-containing sample has to be noted. Maximum intensity for hydrogen uptake on this sample was found around 676 K, 200 K lower than the gold free samples. The hydrogen uptake to moles of iron ratio has also increased for this sample, 0.57, compared to 0.37 for gold free samples. This increase could be attributed to the additional reduction of gold (III) to its metallic state at low temperature. If gold reduction occurs at temperatures similar to iron reduction, the increase in hydrogen uptake for this sample does correspond to the total reduction of 5 wt.% Au (III) in this sample.
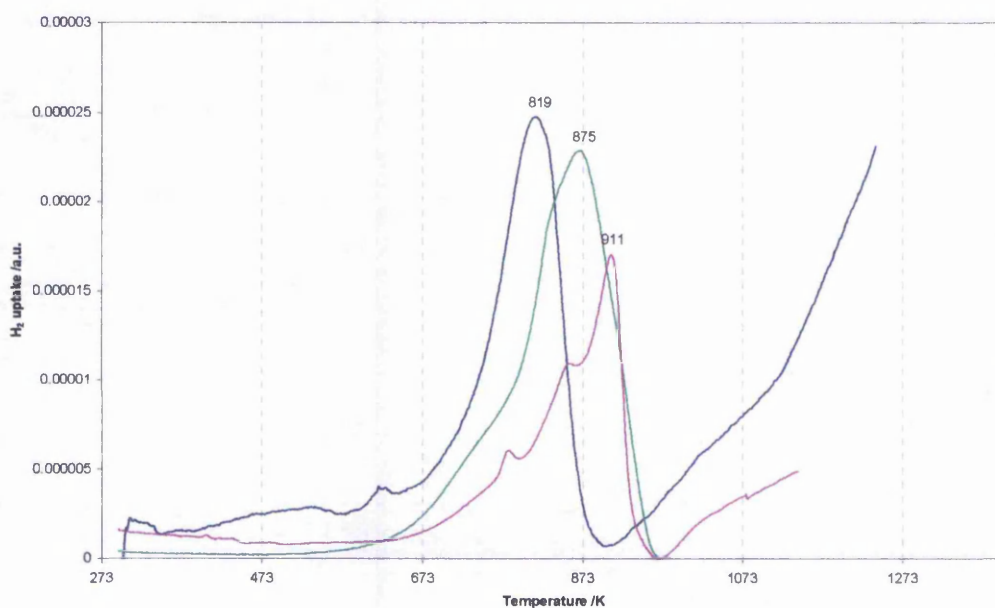
Figure IV-3: TPR profiles for supported iron phosphates. (purple) reference FePO$_4$, (blue) FePO$_4$-ZSM-5, (green) FePO$_4$-MCM-41. The profiles were recorded with a 5 K min^{-1} heating gradient, 10 mL min^{-1} flow of 5% H$_2$/Ar.

Iron phosphate supported on ZSM-5 or MCM-41 show hydrogen uptake maxima at lower temperature than an unsupported $FePO_4$, respectively 800 and 875 K. A homogenous, single step reduction was recorded for $FePO_4$-ZSM-5, with a hydrogen uptake to moles of iron ratio of 0.47. This indicates the full reduction of Fe centres from a +III to +II oxidation state. The observed reduction maximum occurs at a higher temperature than in Fe-ZSM-5 (see. IV-3: MFIs, pp. 90) and can be attributed to the presence of phosphorus in the vicinity of iron in the material, i.e. an iron phosphate phase has indeed been formed on the support. The possibility, however, that this effect is solely due to a concentration effect, cannot be ruled out, and will be taken into account in further discussions.

In MCM-41 the reduction shows a maximum hydrogen uptake at 875 K, with two shoulders at lower temperatures, and a hydrogen uptake to moles of iron ratio of 1.00. Different iron/phosphate structures are therefore likely to be deposited on the MCM-41 support. A mixed phosphate phase is favoured compared to the presence of pure iron clusters, due to the high reduction temperature observed and the low occurrence of the latter on MCM-41. In this mixed phosphate phase, the total reduction of some iron centres is promoted, as indicated by the hydrogen uptake to moles of iron ratio. This explanation is preferred to the stabilisation of a +I oxidation state of iron in the material. Indeed, such an oxidation state for iron has not been reported previously, is not naturally occurring, and there isn't any evidence of it occurring in any of the other materials prepared.

The stepwise introduction of iron and phosphorus in MCM-41 led to different reductive behaviours. Where iron was introduced last (Fe-PO_4-MCM-41), a sharp reduction feature centred around 706 K is found, with a hydrogen uptake to moles of iron ratio of 0.15. This reduction profile is typical of isolated iron species, as observed

in Fe-MCM-41. The peak maximum is located at a higher temperature than for the latter, and it is therefore assumed that iron has been exchanged where phosphorus was present in the MCM-41 matrix. The concentration of reducible iron in the material is however very low, which will be taken into account in further discussions. A similar hydrogen uptake to moles of iron ratio was calculated in PO_4-Fe-MCM-41, in this case however peak maximum is at 783 K, with a small additional reduction around 900 K and a further reduction above 1073 K. Again, heterogeneity of the iron phosphate phase could explain such behaviour, with one or several phosphate groups surrounding a single iron site and having a stabilising effect on the metal.
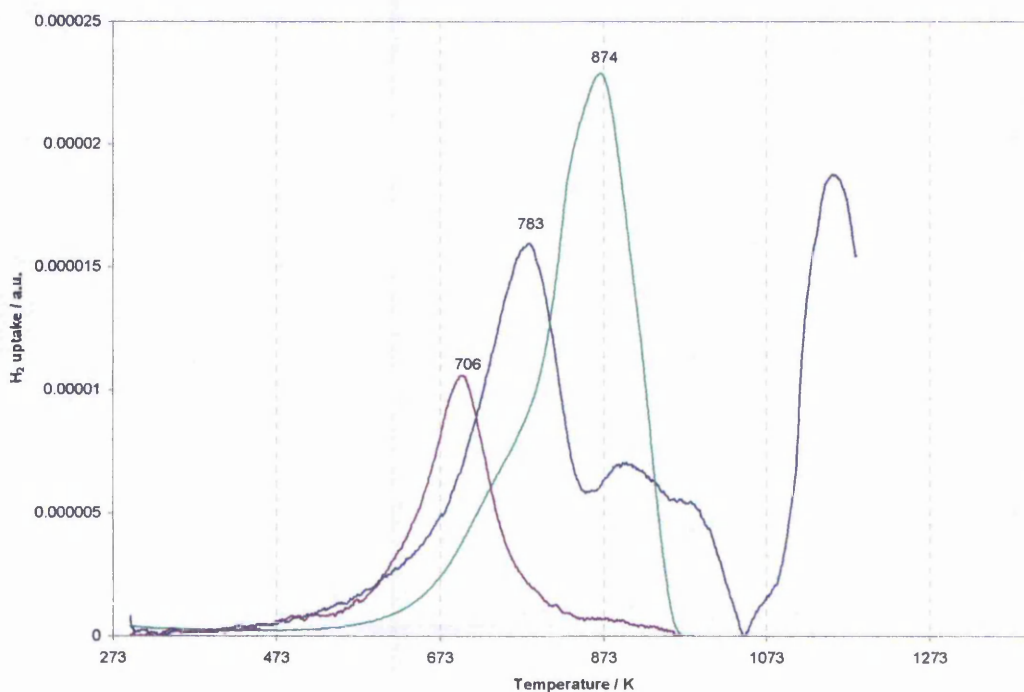
Figure IV-4: Influence of the preparation method on the TPR profiles of MCM-41-supported iron phosphates. (green) FePO$_4$-MCM-41, (purple) Fe-PO$_4$-MCM-41, (blue) PO$_4$-Fe-MCM-41. The profiles were recorded with a 5 K min^{-1} heating gradient, 10 mL min^{-1} flow of 5% H$_2$/Ar.

In both latter cases the hydrogen uptake to moles of iron ratio was low, indicating low iron exchange levels or stabilisation of Fe(III) species in the material. The first hypothesis is preferred as such stabilisation was not observed in the case of $FePO_4$ co-

precipitated on MCM-41, however it was not possible to confirm the iron concentration by atomic absorption.

A summary of hydrogen uptakes to moles of iron present is presented in the following table:

Table IV-1: Hydrogen uptake and hydrogen-to-iron molar ratio for iron phosphate and related materials

Material	nH_2 /mol g^{-1}	nH_2/nFe
$FePO_4$	2.00 e-3	0.30
$FePO_4$, pH6	2.51 e-3	0.37
$Au/FePO_4$	3.61 e-3	0.57
$FePO_4$-ZSM-5	1.36 e-4	0.47
$FePO_4$-MCM-41	8.98 e-4	1.00
$Fe-PO_4$-MCM-41	5.38 e-5	0.15
PO_4-Fe-MCM-41	6.22 e-5	0.17

IV-3.2 MCM-41s

Depending on their preparation method, MCM-41s have a poor to medium thermal stability. The collapse of their framework can occur at temperatures as low as 823 to 873 K [6, 7]. In TPR traces, this is reflected by a "negative" feature caused by hydrogen evolution when the collapse occurs. Indeed, hydrogen released from the defects in the MCM-41 framework, i.e. hydroxyl- groups, as the structure collapses to amorphous silica, SiO_4, would cause an interference with the signal. From the recorded TPR traces, it appears that the synthesised Si-MCM-41 has a good thermal stability in reductive conditions, as this negative feature was not observed up to 1073 K. Metal exchanged MCM-41 however do exhibit this feature, at temperatures decreasing as the number of treatments the material has undergone increases. For

examples the feature is present around 923 K for Fe-MCM-41 (not shown on graph), and 873 K for Fe-Al-MCM-41. This is in agreement with the thinning of the pore walls deduced from surface area and XRD measurements (see pp. 68), the stability of the material depending on the thickness of the amorphous pore walls [8].

Iron (III) in MCM-41 shows a relative ease of reducibility to its +II oxidation state, with a single sharp reduction peak centred at 622 K. The metal's +II oxidation state has been reported to be stabilised by the silicate framework, with reduction from its +III to +II state occurring easily and fully [9]. The calculated hydrogen uptake to iron ratio of 0.28 would therefore indicate that the amount of iron present in the material is lower than expected, and a concentration of 1 wt.% is accepted hereafter for Fe-MCM-41.
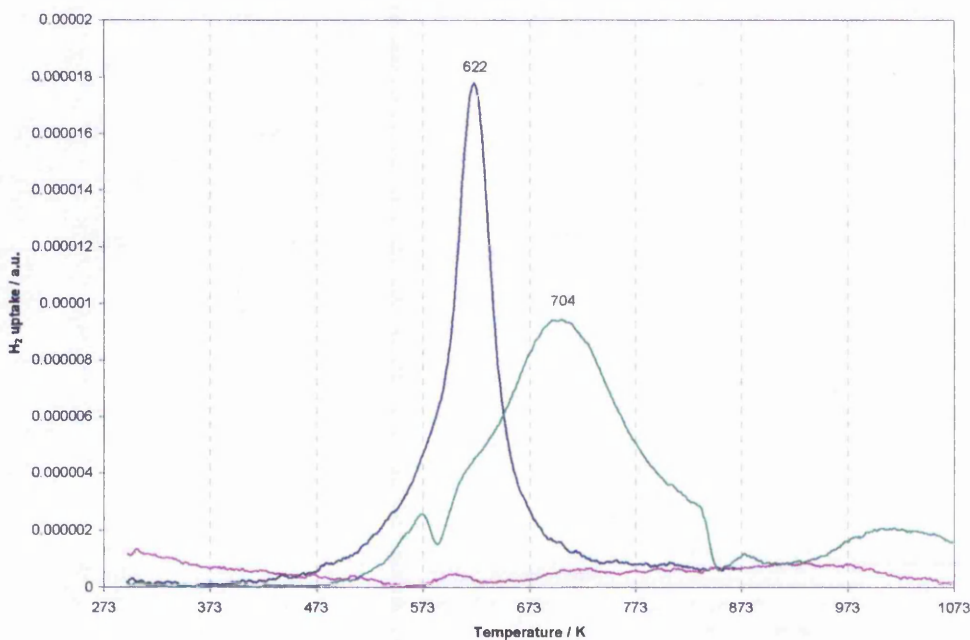
Figure IV-5: TPR profiles for (purple) Si-MCM-41, (blue) Fe-MCM-41, (green) Fe-Al-MCM-41. The profiles were recorded with a 5 K min^{-1} heating gradient, 10 mL min^{-1} flow of 5% H$_2$/Ar.

Iron supported on aluminium modified MCM-41 is reduced at higher temperatures than the corresponding aluminium-free Fe-MCM-41 (fig. IV-5). A broad reduction

feature shows a maximum at 704 K. The aluminium was introduced at a theoretical 1 wt.% loading, and assuming that all aluminium is present in tetrahedral conformation and iron was subsequently exchanged at all sites, a hydrogen uptake to iron ratio of 0.76 was calculated. Heterogeneity of the distribution over the reduction peak, appearing as a non-perfect Gaussian distribution with shoulders and valleys, suggests complex mechanisms of reduction or structural heterogeneity of the iron centres, or both. The shoulder located around 620 K could be due to Fe-MCM-41 like isolated iron sites deposited away from the aluminium atoms. If this shoulder and the negative feature around 873 K are subtracted from the rest of the curve, a reduction pattern similar to hematite appears. Indeed, hematite, Fe_2O_3, is primarily reduced to magnetite, Fe_3O_4, and subsequently to metallic iron, with a 1:9 ratio between peak integrals. The formation of hematite clusters on the surface of MCM-41, due to the presence of aluminium, could explain the heterogeneous reduction pattern, as well as the irrelevant hydrogen uptake to iron ratio. The quantification of the separate reduction steps through peak fitting was not possible, due to the complexity of the overall pattern and asymmetry of the peaks. Further information concerning the structure of iron in these materials was obtained from FTIR adsorption data and is discussed in chapter VI: On the nature of iron species (see pp. 148).

A summary of observed hydrogen uptake to iron content ratios is presented in table IV-2:

Table IV-2: Hydrogen uptake and hydrogen-to-iron molar ratio for phosphorus free MCM-41s

Material	nH_2 /mol g^{-1}	nH_2/nFe
Si-MCM-41	0	0
Fe-MCM-41	1.00e-4	0.28
Fe-Al-MCM-41	1.35e-4	0.76
Au/Fe-MCM-41	1.50e-4	0.42

IV-3.3   MFIs

The reduction profiles of Fe-ZSM-5s and Fe-MFIs show multiple peaks in most cases, making the interpretation of their chemical meaning uncertain. As a reference, to help clarify the patterns, the reduction profile of an intimate mixture of H-ZSM-5 and hematite in 99:1 weight ratio was recorded (figure IV-6).
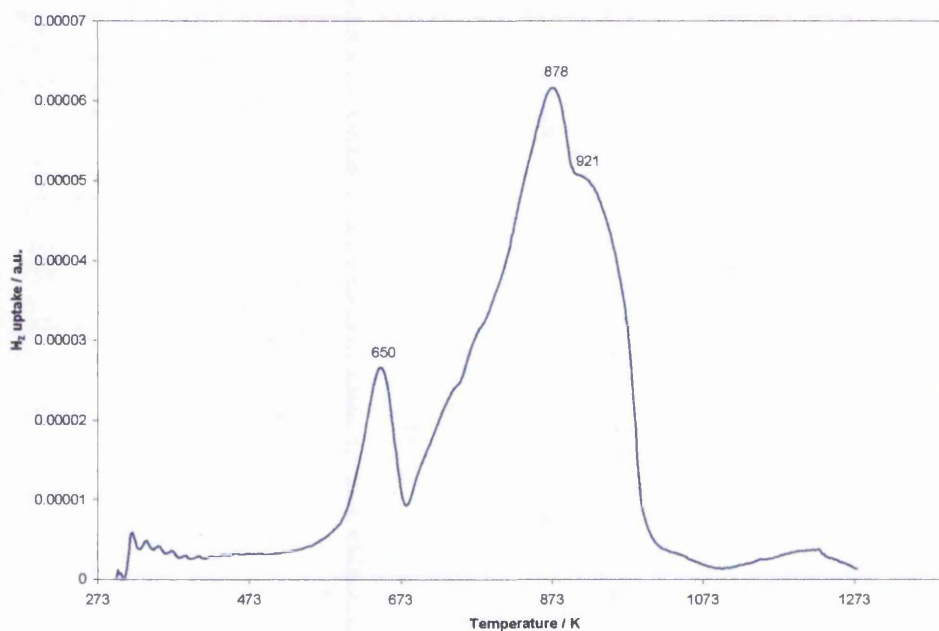
Figure IV-6: TPR profile for a physical mixture of H-ZSM-5 with Si/Al=15 and hematite Fe$_2$O$_3$. The profile was recorded with a 10 K min^{-1} heating gradient, 10 mL min^{-1} flow of 5% H$_2$/Ar.

Three main peaks could be marked on the trace, at 650, 878, and 921 K. The trace is a characteristic illustration of the influence of a foreign species on the reduction pattern of metals. Pure hematite, shows two reduction peaks with a 1:9 ratio at around 600 and 850K. In the following discussion, the relative intensities and general shape of the pattern will be considered as fingerprint for iron oxide on ZSM-5, rather than their absolute position, as it is known that the metal's concentration can significantly alter the latter [1].

The reduction patterns of Fe-ZSM-5 prepared by various synthetic methods were recorded and compared (figure IV-7). As for Fe-MCM-41 (figure IV-5, pp. 88), iron present as isolated sites was expected to be reduced in a single step, appearing as a sharp hydrogen uptake peak. Such a pattern was observed only for Fe-ZSM-5 CVD, calcined in pure oxygen. This reduction peak is centred at 723 K, with a hydrogen uptake to iron ratio of 1.01. This ratio can be explained by the partial exchange of iron with protons in the zeolite in a solid state exchange manner, where the +II oxidation state of the metal is then stabilised by the aluminosilicate. The reduction temperature is higher than for Fe-MCM-41, which can be explained either by the higher iron concentration in Fe-ZSM-5 CVD, 2.50 wt.%, cf. ca. 1 wt.% for Fe-MCM-41, or by location of iron at ion-exchange sites, the presence of aluminium in its vicinity having an effect on its reduction kinetics. Aluminium had already been noticed to have a similar effect on the reducibility of iron in Fe-Al-MCM-41, as presented on figure IV-5, pp. 88.

When Fe-ZSM-5 prepared by CVD was calcined in air – Fe-ZSM-5 CVD (hem) – a hematite phase appeared on XRD patterns (see chapter III, pp. 72). Its TPR trace shows three to four main peaks. Two broad peaks around 881 and 968 K are attributed to hematite reduction, as similar to the fingerprint of our reference Fe_2O_3/H-ZSM-5.

Another peak showing a maximum at 743 K has a high asymmetry, possibly due to the first reduction step of hematite, together with isolated or dimeric iron at ion-exchange sites.
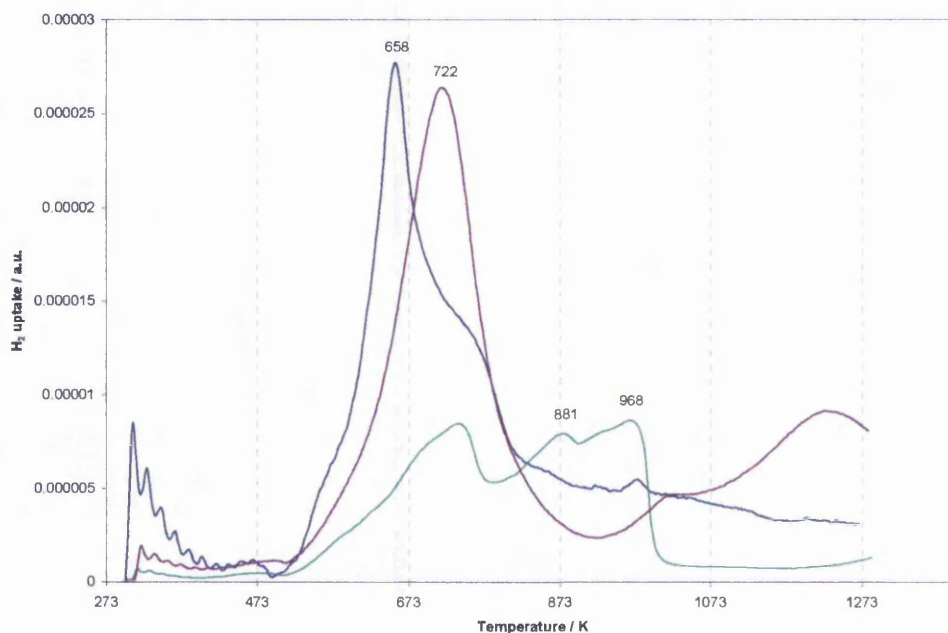
Figure IV-7: TPR profiles for Fe-ZSM-5 prepared using different methods. (blue) Fe-ZSM-5 EX, (purple) Fe-ZSM-5 CVD, (green) Fe-ZSM-5 CVD (hem).

The reduction pattern of Fe-ZSM-5 EX shows the same main peak, attributed to mono- or dimeric iron species, finding its maximum at 668 K. It was admitted that the lower peak maximum, in this case, was due to the consequently lower iron concentration in the zeolite matrix (0.68 wt.%), compared to the other Fe-ZSM-5s. Two shoulders appear on this reduction peak, one on either side of the main reduction, at 576 and 757 K respectively. These shoulders were not attributed to an iron oxide phase on the zeolite, as the peaks appear to be broad and smooth, to the contrary of the high temperature Fe_2O_3/H-ZSM-5 reduction step. A further argument against the presence of hematite clusters in Fe-ZSM-5 EX is the hydrogen uptake to iron ratio of 0.50, reflecting a single electron reduction. In all materials containing iron oxide

clusters this ratio varied considerably from 0.5, due to the uptake of hydrogen caused by the total reduction of iron.

Apart from mono-, dimeric iron and iron oxide clusters, a fourth structure has been reported, following an EXAFS study, to exist in Fe-ZSM-5s, namely oligomers of formula Fe_4O_4 [10]. Such oligomers, of cubane structure, have been reported to be stabilised in some coordination compounds, over five oxidation states [11]. Although a model for these sites has not been developed, it is thought by the authors that some sites in the zeolite pores may favour, or stabilise, the formation of such cubane-like structures. Only little information about the reduction pattern of these oligomers has been reported, and it could be argued that the two shoulders observed in the TPR for Fe-ZSM-5 are due to such sites. The peak ratio of 1:3 would indicate a two-step reduction of the iron atoms, and it could be imagined that the $Fe(II)Fe(III)_3O_4$ structure is stabilised through interactions with the aluminosilicate. It is however highly challenging to find proof for the existence of such oligomers in zeolite ZSM-5. Main causes for this are the difficulty to exchange them as a sole structure in the zeolite and the difficulty to implement their characterisation. It has been attempted to speciate these oligomers by means of adsorption experiments, as discussed further on (see chapter VI, pp. 146).

The ion-exchange or impregnation of gold with/on Fe-ZSM-5 however contradicts the attribution of the shoulders besides iron's main reduction peak (figure IV-8). Indeed, as Fe-ZSM-5 EX was neutralised, suspended in an acidic gold chloride solution, and filtered or dried, its reduction pattern radically changed, with a decrease in intensity of the central peak at 665 K accompanied by an increase of the peaks at 618 and 821 K. The most probable explanation for these changes is the back-exchange of iron at isolated sites in the zeolite with ammonia, used to neutralise the intrinsic acidity of the

material, followed by migration of iron ions and clustering. The hypothesis of formation of Fe_4O_4 nanoclusters during the process could be argued, but the sole presence of gold in the material could lead to such a difference in reductive behaviour [1]. The hydrogen uptake to iron ratios in these materials, respectively 0.63 and 1.03 for Au/Fe-ZSM-5 EX and Au/Fe-ZSM-5 IMP, calculated from the integration of the three peaks attributed to iron, suggest the reduction of some iron sites to their metallic state. As in previous cases, the higher hydrogen uptake can also be attributed to the total reduction of iron in hematite clusters on the zeolite's surface. From this it can't however be excluded that iron oligomers exist in Fe-ZSM-5 EX, as well as in gold modified ZSM-5, and that their reduction profile is as discussed. Due to the complexity of the reduction profiles and the number of parameters affecting them, conclusions cannot be drawn from single patterns. The structure of iron in these materials will be discussed further in chapter VI of this thesis.
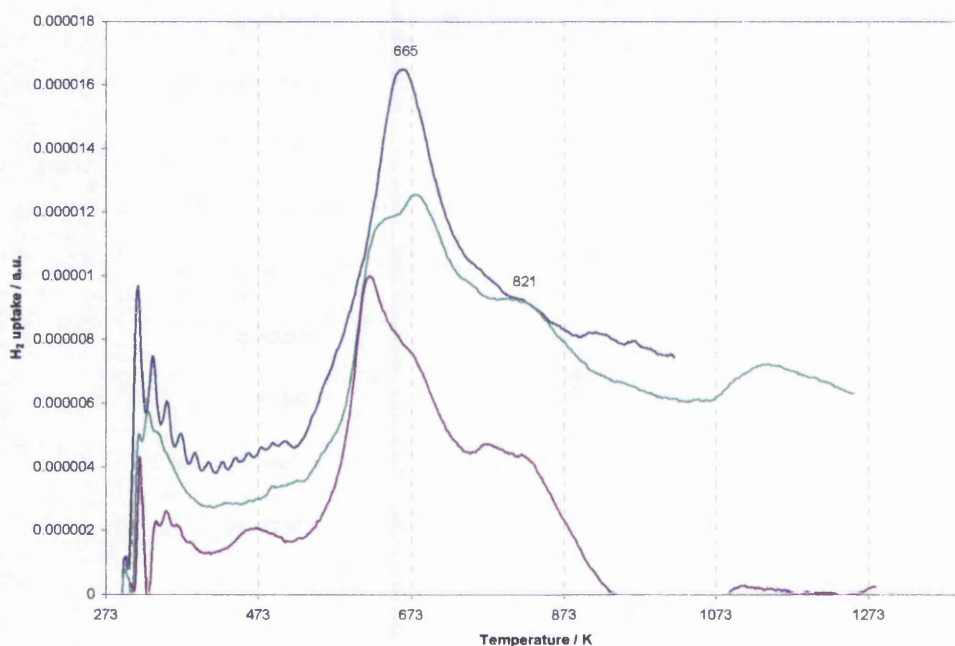
Figure IV-8: TPR profiles for (blue) Fe-ZSM-5 EX, (purple) Au/Fe-ZSM-5 EX, (green) Au/Fe-ZSM-5 IMP. The profiles were recorded with a 10 K min⁻¹ heating gradient, 10 mL min⁻¹ flow of 5% H₂/Ar.

A reduction peak for gold could be identified in Au/Fe-ZSM-5 IMP, centred around 473 K, not observed in Au/Fe-ZSM-5 EX. The hydrogen uptake to gold ratio was calculated to be 0.5, based on this peak's integral only. This corresponds to a single electron reduction of gold atoms in the zeolite. A sensible explanation is that gold is present in its +I oxidation state in the zeolite, being reduced to its metallic form at low temperature, as it has been reported that gold is easily reduced at temperatures below 573 K [12]. This reduction is not visible in the ion-exchanged sample's profile, and the most probable reason for it is its insufficient gold loading. A slow exchange rate, an equilibrium for the Au/H exchange in favour for gold in solution, the gold being only weakly bound to the aluminosilicate framework and therefore easily back-exchanged when the sample is washed with water are possible reasons for a gold loading lower than expected.

A final point to be noted on the reduction patterns of ZSM-5s (figures IV-6-8) is that the sinusoid-like feature near ambient temperature is material independent, most likely due to an imbalance in the analytical system as the reactor is switched on and data acquisition started.

Iron in SYN samples is reduced at much higher temperatures than when exchanged in aluminium-containing ZSM-5s. Three main reduction peaks are observed for these samples, centred at 765, 982 and 1151 K (figure IV-9). The highest temperature reduction feature shows two maxima at close temperatures with heights and shape resembling the Fe_2O_3/H-ZSM-5 reference's reduction pattern. As this could indicate the presence of hematite clusters in the silica matrix, the hydrogen uptake to iron ratios are calculated as respectively 0.46, 0.47 and 0.37 for Fe-MFI SYN24, SYN48 and SYN96. Apart from the latter sample, these uptakes correspond to a complete reduction of Fe(III) to Fe(II), assuming that all iron present in the sample is in its +III

oxidation state, and at the solid/gas interface. Such an event is unlikely as the iron was introduced in the material prior to its crystallisation, it is inevitable that some iron atoms are located in the bulk of the structure. As for aluminium there is a lack of knowledge on the exact siting of atoms substituted in MFI type zeolites [13], and despite the report of preferential siting of Fe in the ring structure [14], it is assumed in this study that part of the iron is located at inaccessible sites. For this reason, the probability of the presence of small iron clusters in Fe-MFI SYNs will be described here as likely. As, to a first approach, this is in contradiction with XRD studies on these materials, it is possible that such small clusters do not present a long enough order to cause significant diffraction intensity. Confirmation of the presence of iron clusters was obtained by FTIR in-situ adsorption studies (see chapter VI).
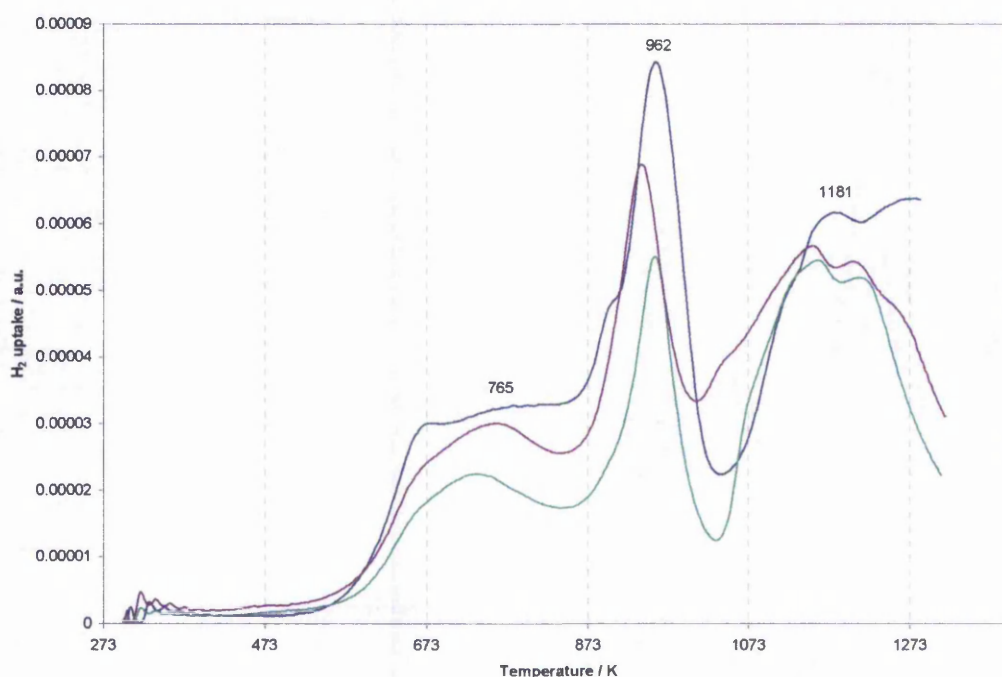
Figure IV-9: TPR profiles for (purple) Fe-MFI SYN, (blue) Fe-MFI SYN, (green) Fe-MFI SYN. The profiles were recorded with a 10 K min^{-1} heating gradient, 10 mL min^{-1} flow of 5% H$_2$/Ar.

The increased reduction temperature of iron at isolated sites, assigned here to the peak centred at 962 K, was attributed to the absence of aluminium in the samples and probable different coordination of iron atoms in the matrix.

A summary of hydrogen uptake to moles of iron ratios for Fe-MFI reduction is presented in the following table:

Table IV-3: Hydrogen uptake and hydrogen-to-iron molar ratio for phosphorus free ZSM-5s and MFIs

Material	nH_2 /mol g^{-1}	nH_2/nFe
Fe-ZSM-5 EX	6.06e-5	0.50
Fe-ZSM-5 CVD	4.53e-4	1.01
Au/Fe-ZSM-5 EX	8.19e-5	0.64
Au/Fe-ZSM-5 IMP	1.02e-4	1.03
Fe-MFI SYN24	9.07e-4	0.46
Fe-MFI SYN48	7.29e-4	0.47
Fe-MFI SYN96	3.85e-4	0.38

IV-4 Summary

The reducibility of the transition metals in our materials has been studied by means of temperature programmed reduction, using hydrogen as reducing agent and thermal conductivity detection.

This study revealed the general particle size heterogeneity of unsupported iron phosphate materials. It is also believed that $FePO_4$ based materials, supported and unsupported, possess some structural heterogeneity, indicated by the complex shape of the reduction profiles recorded. Iron phosphates prepared by different methods showed different reduction patterns. Mostly the temperature at maximum hydrogen uptake was affected when the iron phosphate was supported on ZSM-5 or MCM-41,

compared to the unsupported materials. This could indicate the successful introduction of the iron phosphate on the support, with the drop in reduction temperature associated with interactions with the support, particle size, or concentration. Single peak reduction features were recorded for Fe-MCM-41 and Fe-Al-MCM-41, however broadening occurred in the latter. The reduction of isolated iron (III) species to iron (II) is assumed to occur in Fe-MCM-41. Fe-Al-MCM-41, however, is believed to contain a wider range of iron species at different positions on the support, reduced at higher temperature than in Fe-MCM-41. The analysis of the data recorded for the reduction of iron in materials of MFI structure was more uncertain due to the variety of iron species believed to be present on the support. These include isolated sites, dimers, oligomers and larger clusters. The presence of hydrogen uptake peaks above 900 K was associated to the reduction of iron in clusters to its metallic state. It was not possible to differentiate smaller iron species using TPR, but their presence in different relative concentrations in Fe-ZSM-5 and Fe-MFI prepared by different procedures was suggested. In gold containing samples, a reduction for gold (I) to metallic gold could be observed at around 473 K for the impregnated sample, which was absent in the ion-exchanged sample, attributed to a slow exchange rate or equilibrium in favour of gold in solution. The reduction pattern of iron in these materials was significantly altered compared to their parent Fe-ZSM-5 EX, possibly indicating changes in the structure of iron species on the zeolite's surface. Further studies of the structure of iron species in the prepared materials are needed for further interpretation of the data, which is presented in a subsequent chapter.

IV-5 References

1.   Jones, A. and B.D. McNicol, *Temperature-programmed reduction for solid material characterization*, ed. A. Jones and B. McNicol. 1986, New York-Basel: Marcel Dekker Inc.

2.   Wang, Y. and K. Otsuka, *Direct Conversion of Methane and Ethane to the Corresponding Alcohols Using Nitrous-Oxide over Iron Phosphate Catalysts.* Journal of the Chemical Society-Faraday Transactions, 1995. **91**(21): p. 3953-3961.

3.   Wang, Y. and K. Otsuka, *Partial oxidation of ethane by reductively activated oxygen over iron phosphate catalyst.* Journal of Catalysis, 1997. **171**(1): p. 106-114.

4.   Monti, D.A.M. and A. Baiker, *Temperature-Programmed Reduction - Parametric Sensitivity and Estimation of Kinetic-Parameters.* Journal of Catalysis, 1983. **83**(2): p. 323-335.

5.   Greenwood, N. and A. Earnshaw, *Chemistry of the Elements.* 1st ed. ed. 1984: Oxford.

6.   Luechinger, M., et al., *A mechanistic explanation of the formation of high quality MCM- 41 with high hydrothermal stability.* Microporous and Mesoporous Materials, 2003. **64**(1-3): p. 203-211.

7.   Mori, T., et al., *Preparation of a water-resistant siliceous MCM-41 sample, through improvement of crystallinity, and its prominent adsorption features.* Langmuir, 2002. **18**(5): p. 1595-1603.

8.   Bengoa, J.F., et al., *Iron oxide nanoparticles inside the MCM-41 channels. Study of the structural stability of the support.* Microporous and Mesoporous Materials, 2005. **84**(1-3): p. 153-160.

9.   Dixon, J.M., *Structure, Bonding and Catalytic Activity of Modified Mesoporous Silicates.* 2004, Nottingham Trent University: Nottingham.

10.   Joyner, R. and M. Stockenhuber, *Preparation, Characterization, and Performance of Fe-ZSM-5 Catalysts.* Journal of Physical Chemistry B, 1999. **103**(29): p. 5963-5976.

11.   Raptis, R.G., I.P. Georgakaki, and D.C.R. Hockless, *A FeIII/oxo cubane contained in an octanuclear complex of T symmetry that is stable over five oxidation states.* Angewandte Chemie, International Edition, 1999. **38**(11): p. 1632-1634.

12.   Bond, G.C. and D.T. Thompson, *Catalysis by gold.* Catalysis Reviews-Science and Engineering, 1999. **41**(3-4): p. 319-388.

13.   Gabova, V., J. Dedecek, and J. Cejka, *Control of Al distribution in ZSM-5 by conditions of zeolite synthesis.* Chemical Communications, 2003(10): p. 1196-1197.

14.   Theunissen, E., et al., *Preferential siting of iron atoms in an MFI-type ferrisilicate zeolite framework: An attempt to explain experimental data with TPA-silicate solution chemistry.* European Journal of Inorganic Chemistry, 2003(7): p. 1296-1298.

Chapter V: <u>Acidity of the prepared materials</u>

V-1 Introduction

A major role is attributed to acidity in many catalytic oxidation systems. A common method to study the acidity of solids is the adsorption and/or desorption of probe basic molecules which can interact with acidic sites in ways described hereafter. In zeolite chemistry two common basic probes are ammonia and pyridine. In this study ammonia was chosen, for its ease of use, gaseous at room temperature, and smaller size, allowing it to diffuse through small pores more easily. Adsorption interactions with the prepared materials were characterised by infrared spectroscopy, and a quantification of the amount of probe adsorbed on the catalyst surface was achieved by mass spectrometry detection of thermally desorbed compounds. The principles and applications of both techniques are described in a first part of this chapter, followed by a discussion of the characteristics of different materials, and the influence of preparative treatments on their intrinsic acidity. A brief summary of results is included at the end of the chapter, comparing the acidic properties of the three types of catalysts discussed, bulk iron phosphates, and MCM-41 or MFI supported.

V-2 Background and Methods

V-2.1   Background

V-2.1.1   Adsorption and desorption

Adsorption and desorption are key steps in any heterogeneous catalytic reaction. Distinction is made between physical and chemical adsorption. In the first one,

adsorbed molecules do not undergo any significant modification of their electronic properties, opposed to the second type, where electronic distribution, or the structure of the adsorbed molecule, is changed. Physical and chemical adsorption are extensively used in the characterisation of porous catalysts, physical adsorption of nitrogen for example is used to characterise the surface area and porosity of materials (see chapter III). The chemisorption of probe molecules is more specific to the characterisation of metals and/or acidic solids.

In this study the chemisorption of ammonia was used to characterise the acidity of solid samples. Ammonia gas, being basic, has the ability to adsorb both onto Lewis and Brønsted acid sites in a solid acid (fig. V-1), making the qualitative and quantitative speciation of both types of acidity possible in materials, using the combination of two techniques, namely Mass Spectrometry – Temperature Programmed Desorption (MS-TPD), and Fourier Transform InfraRed spectroscopy (FTIR) *in-situ* adsorption. Both techniques are described in more detail hereafter.
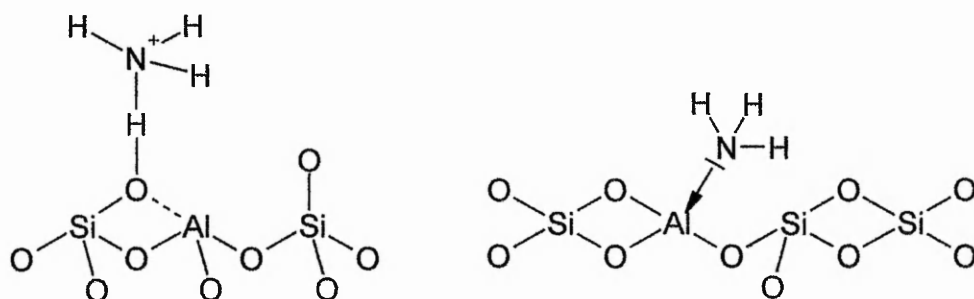
Figure V-1: Ammonia adsorbed onto Brønsted (left) and Lewis (right) acid sites of a zeolite

Due to the nature of infrared spectroscopy, it was also possible to use the adsorption of other probe molecules to characterise the aggregation state of target metals exchanged in the aluminosilicate (see chapter VI).

V-2.1.2 *Mass spectrometry (MS)*

Mass spectrometry allows the determination and identification of species in samples by means of separation according to their atomic or molecular masses. A small quantity of sample is ionised and the charged species accelerated and separated using an electric and/or magnetic field before being directed towards an ion counting detector. Several combinations of ionisation, separation and detection methods are available in different instruments [1].

The mass spectrometer available during this project was an electron ionisation, quadrupole mass spectrometer equipped with a Channeltron® electron multiplier detector. The principles of this instrument's components only will be presented here.

Electron ionisation (EI) is the most widely used ionisation method in mass spectrometry. Electrons are emitted from a filament by a thermoionic process. A potential is applied between the filament and the chamber, effectively accelerating the electrons produced. Collision of electrons with the sample gas in the ionisation chamber results in the production of ions. The efficiency of EI is generally in the order of one ion produced for 10,000 molecules present [2]. As EI is considered as a "hard ionisation" method, fragmentation of the target molecules is likely to occur, the extent of which depends on the molecule being ionised and the kinetic energy of electrons in the chamber, and therefore the potential difference between filament and electrode. The ionisation potential can be tuned and if kept constant the fragmentation pattern of target molecules is reproducible, allowing their identification from the detected fragments. The EI process is summarised in figure V-2:
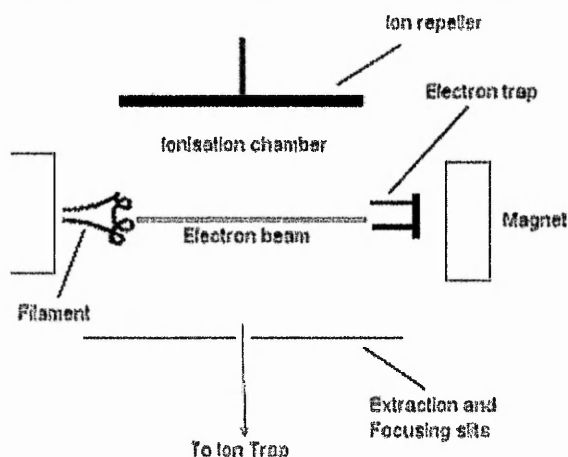
Figure V-2: Schematic of a typical electron ioniser for mass spectrometry

Quadrupole mass analysers have a somewhat lower performance than other types of ion filters, but allow the build of smaller and less expensive systems finding use in many industrial processes [2].

A quadrupole electrical field is generated using four parallel electrodes coupled in pairs. A potential U is applied between the electrode pairs. The velocity and position of a charged molecule entering the filter will determine its trajectory through it, with the positive and negative electrodes having respectively a focusing and defocusing effect on the trajectory. If an AC voltage is superimposed on the DC voltage it becomes possible to separate ions according to their mass using their response to the electrical field in the quadrupole.

The response of lighter and heavier atoms to the components of this electrical field is used to filter them through, the two positive electrodes constituting a high-pass filter, and the two negative ones a low-pass filter, thus making it possible to selectively let particles of a certain mass-to-charge ratio pass through the filter, the rest being deflected and colliding with the electrodes. The desired mass range can be scanned in two ways, either by keeping voltages constant and scanning the radiofrequency, or by

maintaining the radiofrequency constant and scanning the voltages through together, keeping their ratio fixed.
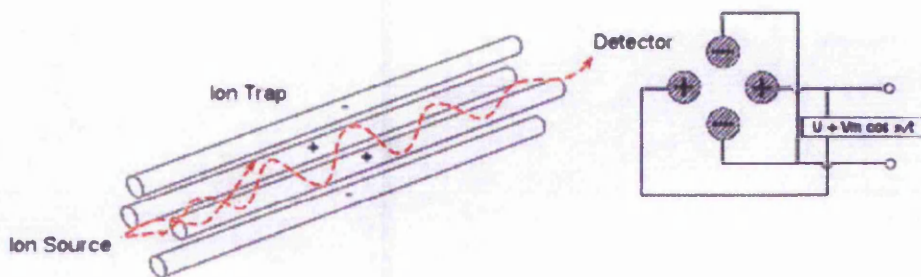
Figure V-3: Schematic diagram of a quadrupole ion filter

Detectors in mass spectrometry are based on the measurement of the total electrical charge carried by the ions. Electron multipliers, as is the Channeltron® are particularly reliable devices, with nanosecond response times [3]. A Channeltron®, or continuous dynode detector, is a spiral tube, with a widened opening, made of heavily lead-doped glass. A potential is applied along the length of the device, and when ions strike the glass electrons are ejected and move along the surface. More electrons are ejected with every impact on the surface (fig. V-4), effectively amplifying the signal which can then be recorded through a pulse counter.
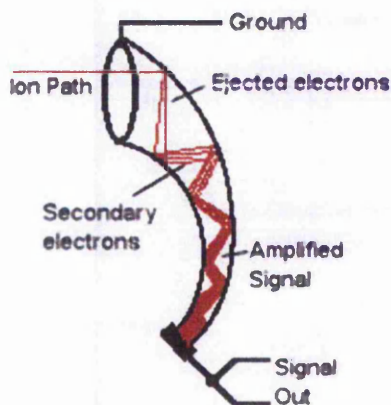
Figure V-4: Schematic diagram of a continuous dynode detector (Channeltron®)

The output from a Channeltron is approximately one million electrons for each ion arriving at the glass surface [2].

V-2.1.3   Fourier-transform infrared spectroscopy (FTIR)

Infrared spectroscopy relies on the ability of molecules to absorb or reflect electromagnetic radiation in the infrared region, i.e. at wavelengths between 1 and 1000 µm. Within this range the mid-infrared region has been proven most useful in chemical applications, comprising wavelengths between 2.5 and 25 µm. The absorption bands present in this frequency range form molecular "fingerprints", allowing the deduction of many structural features.

In modern instruments the sample is placed in the infrared beam path and the ratio of transmitted light intensity with and without sample measured at each wavelength. This ratio is termed transmittance (T), or absorbance ($A = \log(1/T)$), and is plotted as a function of the wavelength, commonly expressed in terms of wavenumbers $\nu = \frac{1}{\lambda}$, where λ is the wavelength in cm. The mid-infrared region for example comprises wavenumbers between 400 and 4000 cm^{-1}.

The absorption of radiation in the infrared range originates from the interaction of the electrical vector of the electromagnetic wave with the electrical dipole of a chemical bond. Molecules or bonds possessing a permanent dipole moment can therefore absorb energy from the light wave when its frequency is equal to the frequency of their vibrations [4]. Molecules possessing a centre of symmetry, like N_2, do not have a permanent dipole moment and are therefore 'invisible' in infrared spectroscopy.

Molecules in the gas phase possess many vibrational modes, each giving rise to an absorption band in adequate conditions. The number of possible modes for a given

molecule is described by its number of degrees of freedom, 3n-6, where n is the number of atoms in the molecule [5]. As molecules become more complex this number increases, however inter- or intra-molecular interactions can alter the degrees of freedom of a molecule and as a consequence the observed vibration modes are altered. This can be a useful tool in the study of structural changes within molecules or intermolecular interaction. Indeed, as the absorption wavelength is directly related to the bond strength, changes in absorption frequency can be expected upon chemical reaction of a given species.

In zeolites this fact can be exploited to study the adsorption of chemical species onto the aluminosilicate's surface. A common feature of interest is their intrinsic acidity, thought to play a role in numerous catalytic reactions [6-8], and which can be studied by adsorption of basic probe molecules such as ammonia or pyridine. The Lewis and Brønsted acid character of zeolites can be probed using these molecules in infrared *in-situ* adsorption experiments. A clean zeolite surface exposed to a partial pressure of probe basic gas will adsorb it onto both Lewis and Brønsted acid sites, for example giving rise to vibrations at respectively 1450 and 3130 cm^{-1} for NH_3 coordinated at a Lewis site, and 1250, 1630, and 3330 cm^{-1} for its protonated form NH_4^+ [9]. Further structural information about the zeolites can be obtained from infrared spectrometry, such as the presence of bridged, external, and very high frequency hydroxyl- groups, giving rise to absorption bands at respectively 3572-3641 cm^{-1}, 3643-3679 cm^{-1}, and 3769-3794 cm^{-1} [10].

A step forward for infrared spectroscopy occurred in the 1970s when the Fourier transform was used in scanning methods. Fourier Transform Infrared spectrometers (FTIR) are single-beam instruments having a Michelson interferometer (fig. V-5) placed between the source and the sample, replacing the monochromator of the earlier

dispersive instruments. The irradiating wave is split through a semi-transparent mirror, half of the beam is directly reflected on a fixed mirror and the other half on a moving mirror, which distance from the beam splitter varies. Both parts of the beam are then recombined and exit the interferometer to follow their path to the sample chamber. The key part of a Michelson interferometer is the moving mirror, which, through its scanning motion, induces a phase loss between the two parts of the beam, resulting in constructive or destructive interactions between phases. The differences in light composition of the beam allows the detection of the whole range of desired wavelengths in one scan, producing an interferogram which is converted to a single beam spectrum through the application of a fast Fourier transform technique developed by Cooley [11]. The position of the mirror is determined accurately using a neon laser beam travelling alongside the IR beam.
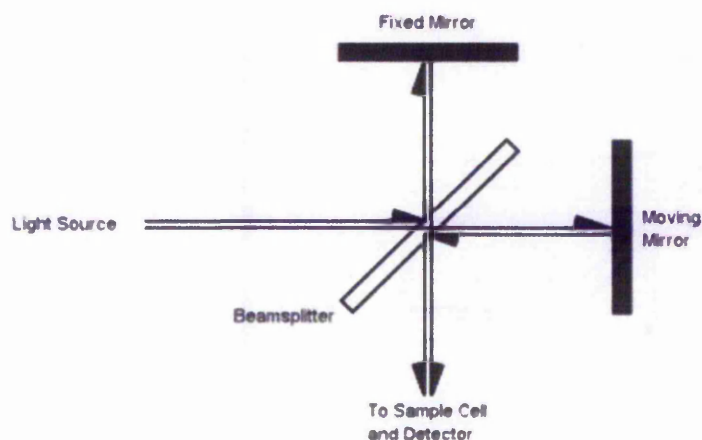
Figure V-5: Schematic diagram of a Michelson interferometer

Detectors used in FTIR spectrometry include thermocouples, making use of the thermal effect of infrared radiation, pyroelectric detectors, whose polarisation varies with the radiation received, and photovoltaic detectors, which are made of a photoconducting film and usually operated at liquid nitrogen temperature.

General advantages of FTIR spectroscopy compared to traditional IR, apart from the decreased scanning time, are a brighter signal, the detector receiving more energy due to the presence of less optical components in the instrument, a higher signal-to-noise ratio, increased by accumulation of several scans for a single spectrum, a higher precision of the calculated wavelengths and constant resolution throughout the domain studied [12].

V-2.2   Experimental setup

V-2.2.1   *Mass spectrometry, temperature programmed desorption (MS-TPD)*

The temperature-programmed desorption setup is schematised on figure V-6.
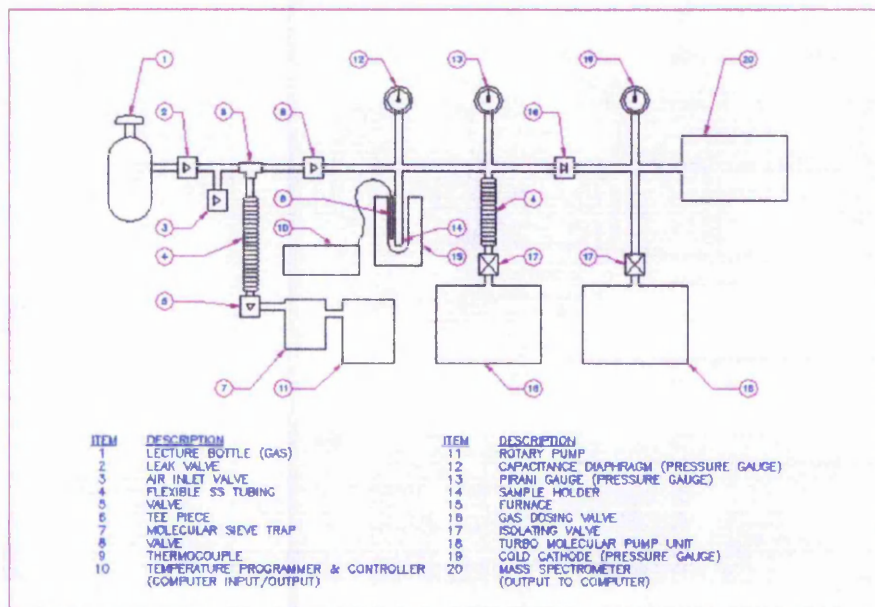
Figure V-6: Schematic of the setup used for temperature-programmed desorption experiments [13]

Typically 100 mg of sample were loaded into a purpose-made glass tube, held in place using a small plug of quartz wool and fitted onto the vacuum system. The sample was

then degassed and activated at high temperature, typically 823 K, in vacuum. A slow heating gradient, 5 or 10 K min^{-1}, was used, depending on the sample studied.

Ammonia was then adsorbed onto the sample at 423 K, a temperature chosen to minimise the amount of physisorption [14]. Ten millibars of ammonia gas were admitted in the sample chamber through a copper seal regulator valve and left to adsorb to equilibrium for typically 30-60 minutes. The system was then evacuated in to ca. 10^{-8} mbar, for 30 minutes prior to desorption.

Desorption was carried out using a 10 K min^{-1} linear heating gradient up to 873 K, the desorbed products being leaked through a precision sapphire poppet valve to a Balzers Quadstar 422 quadrupole mass spectrometer with a 60 eV ion source energy and Channeltron$^{®}$ detector with 1200 eV emission voltage. The pressure within the mass spectrometer during the whole desorption experiment was in the range 10^{-8} mbar.

Ion counts were recorded through an analogue DC converter and amplifier and plotted as m/z intensity versus temperature. The signal from $m/z = 16$ (NH_2^-) was used for quantification of desorbed ammonia, rather than $m/z = 17$ (NH_3^+), to avoid any contribution from hydroxyl ions from residual water. The amount of ammonia desorbed from unknown samples was referenced to the amount desorbed from a sample with known number of acidic sites.

V-2.2.2   FTIR in situ adsorption and desorption (FTIR)

FTIR *in situ* adsorption and desorption experiments were carried out in a purpose built stainless steel cell equipped with CaF$_2$ windows (fig. V-7). The cell was connected to a vacuum system allowing pumping to a base pressure of around 10^{-7} mbar (fig. V-8).
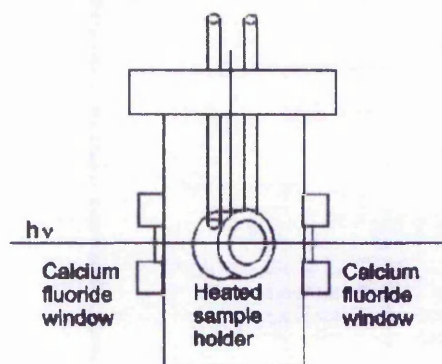
Figure V-7: Schematic of the vacuum cell used in infrared *in-situ* adsorption experiments
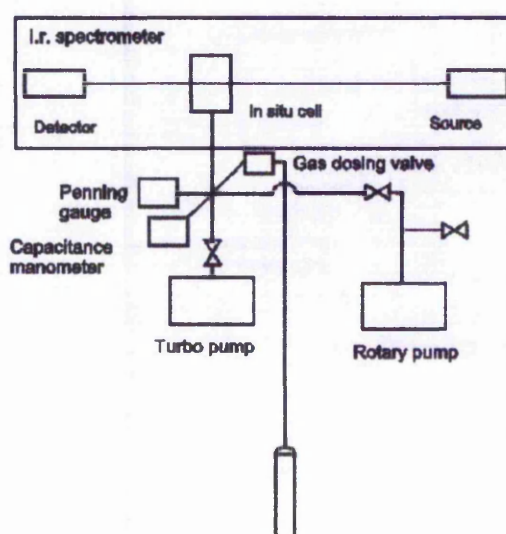
Figure V-8: Schematic of the vacuum system connected to the IR cell.

Approximately 15-20 mg of sample were pressed into a 10 mm diameter self-supported wafer at ca. 2 tonnes cm^{-2}. The wafer was held on a copper sample holder placed in a heating coil allowing heating to temperatures of ca. 923 K.

Samples were activated in vacuum typically at 823 K for 1h, using a 5 or 10 K min^{-1} heating gradient depending on sample stability. The probe gas was admitted in the sample cell through a precision sapphire poppet leak valve for adsorption. Probe gases were adsorbed in the range 10^{-4} to 10 mbar in order of magnitude steps, leaving the system to equilibrate for 30 minutes at each pressure. The system was evacuated back

to base pressure for 30 minutes prior to desorption. The desorption was carried out with a linear heating gradient of 10 K min^{-1} up to 873 K.

It has to be pointed out that the whole vacuum system was heated to 423 K during the activation of all catalysts and adsorption or desorption of ammonia, to prevent any foreign gas from adsorbing on the inside wall of the stainless steel framework, eventually interfering with probe gases used.

Infrared spectra were recorded on a Mattson Research Series 1 FTIR spectrometer equipped with a Mercury Cadmium Telluride (MCT) cryodetector. Spectra were recorded in transmission mode with a 4 cm^{-1} resolution, every 10 K during heating phases and every 2 minutes during the adsorption of gases.

The obtained spectra were recorded on a computer for subsequent treatment. Baseline correction was calculated first by subtracting the spectrum of an empty cell from the sample spectra. These were then normalised to wafer thickness for comparison, by dividing the intensity on the whole frequency range by the value of the integral of the three Si-O-Si deformation vibration peaks, present in the range 1600-2000 cm^{-1}. To the adsorption and desorption series, baseline corrected, spectra was subtracted the spectrum of the clean activated, baseline corrected, sample studied, in order to highlight differences brought upon adsorption of small quantities of probe molecule. The latter are referred to as *delta* spectra in the following discussion.

V-3 Results and discussion

V-3.1   Unsupported Iron Phosphates

Unsupported iron phosphates FePO$_4$ showed little acidity, present as a mixture of Brønsted and Lewis acidic sites, as observed on the FTIR spectrum of ammonia

strongly adsorbed on $FePO_4$ after exposure to 10 mbar NH_3 at 423 K and evacuation to a base pressure of 10^{-5} mbar (fig V-9). The bands for ammonia adsorbed on Brønsted and Lewis acid sites are centred at respectively 1425 and 1604 cm^{-1} in the case of co-precipitated iron phosphate.
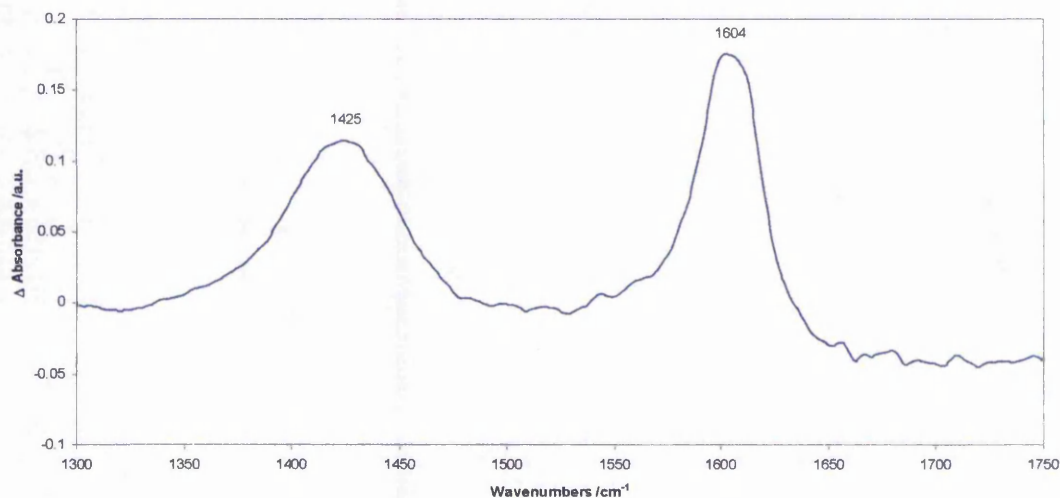
Figure V-9: *Delta* **FTIR spectrum for ammonia strongly adsorbed on co-precipitated FePO$_4$ at 10^{-5} mbar and 423 K.**

The Lewis acidic character of the material can arise from iron as well as phosphorus atoms, however it is attributed to iron as the coordination sphere of phosphorus is saturated in $FePO_4$, and hindered from external species by the four surrounding oxygen atoms. The Brønsted acidic character of the material was attributed to terminal hydroxyl groups, P-OH, in the form O=P-OH or O=P(OH)$_2$. These acids have very broad hydroxyl stretching vibration bands, with maxima located in the regions 3725-3525 and 3350-3080 cm^{-1} [15]. The strength of both types of acid sites was similar, as observed in the desorption patterns. A single desorption peak was recorded in TPD (fig V-10), centred at around 515 K, which was calculated to correspond to ca. 5×10^{-5} moles of acidic sites per gram of material (mol$_{ac}$ g^{-1}). The baseline-corrected spectrum of $FePO_4$ activated at 773 K in vacuum, not presented here, showed some

bands at high wavenumbers, however flattened. Other bands were observed at 2017, 1652, and 1448 cm^{-1}, corresponding to P=O vibrations [16].

FePO$_4$, pH6 did not present any significant acidic character, some ammonia was desorbed from the material in TPD experiments, with ca. 7 x 10^{-6} mol$_{ac}$ g^{-1} and a maximum at around 530 K. The strength of the acidic sites was therefore considered as unaffected by the preparation method, as the desorption temperatures at maximum intensity are considered to be the same, within experimental error. Adsorbed ammonia could not be observed in infrared spectra, due to the low concentration of acidic sites and high noise generated by the lattice. The spectra of activated FePO$_4$, pH6 showed less absorption of light than co-precipitated FePO$_4$ in the 2500-1500 cm^{-1} range, and a broad feature between 3500 and 2500 cm^{-1}. This could be due to an effect called phonon adsorption, occurring readily in highly ordered ionic species [17]. Little specific documentation on phonon absorption was found and it is difficult to suspect a direct relationship between these phenomena. This effect would confirm the structural differences between both materials, even though the exact reasons for such an interaction with infrared light is unclear. FePO$_4$, pH6 has a mixed structure, containing iron oxide and hydroxide phases as well as the iron phosphate. A further indication of the heterogeneity of the material is the presence of several weak bands between 1600 and 2100 cm^{-1}, 2900 and 3400 cm^{-1}, and 3600 and 3800 cm^{-1}. These were attributed to, respectively, vibration of P=O groups, O=P-OH and O=P(OH)$_2$, and various hydroxyl groups in different chemical environments [18].

As summary of the acidity study of iron phosphates a plot of the evolution of the m/z = 16 ion as a function of temperature is presented in figure V-10.
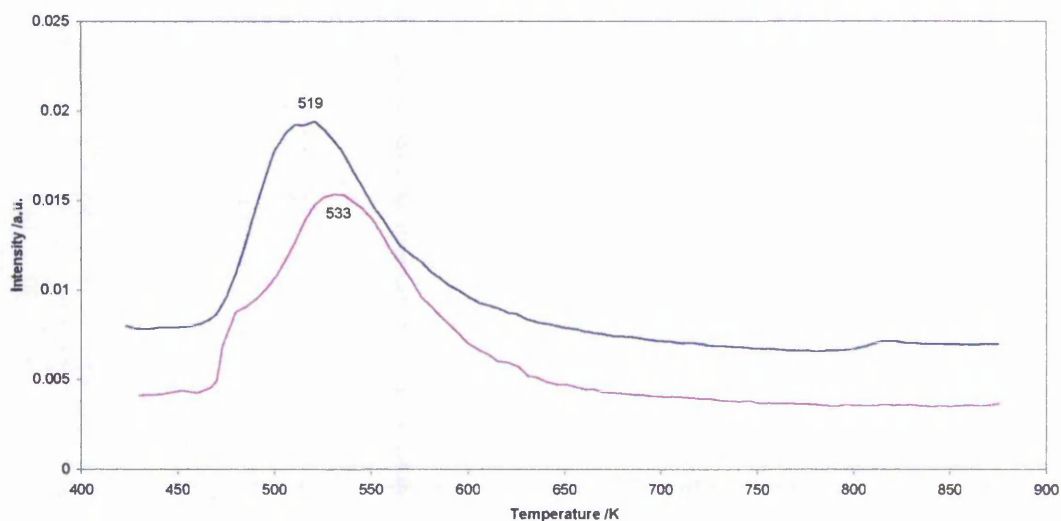
Figure V-10: Recorded traces for the evolution of the $m/z = 16$ ion in TPD of ammonia from unsupported iron phosphate materials. Traces normalised to the amount of acidic sites in the sample. (blue) FePO$_4$; (purple) FePO$_4$.

Of both bulk iron phosphates prepared the co-precipitated material showed the greatest number of acid sites, a factor of 10 larger than FePO$_4$, pH6. Both Lewis and Brønsted acidity could be observed upon adsorption of ammonia onto FePO$_4$, with similar desorption temperatures, hence binding strength. The acidic character of FePO$_4$, pH6 could not be observed by infrared, however ammonia MS-TPD traces suggest the presence of both types of acidity, with a main peak centred at 533 K and a shoulder around 475 K. As the Lewis acidic character of these materials is most likely located at iron sites, Brønsted acidity is thought to be associated with the presence of phospho-hydroxyl groups at defects.

V-3.2   MCM-41s

As outlined earlier siliceous MCM-41 presents only little to no acidity. Some acidic character arises from defects in the amorphous silica, in the form of Brønsted acid sites [19, 20]. Siliceous MCM-41 also typically contains non-acidic silanol groups, appearing in infrared as a sharp band centred around 3740 cm^{-1} (fig V-11). The

shoulder appearing around 3640 cm^{-1} has been attributed to silanol nests in the bulk of the material, and the group of three bands between 1600 and 2000 cm^{-1} to Si-O-Si deformation vibrations [19].
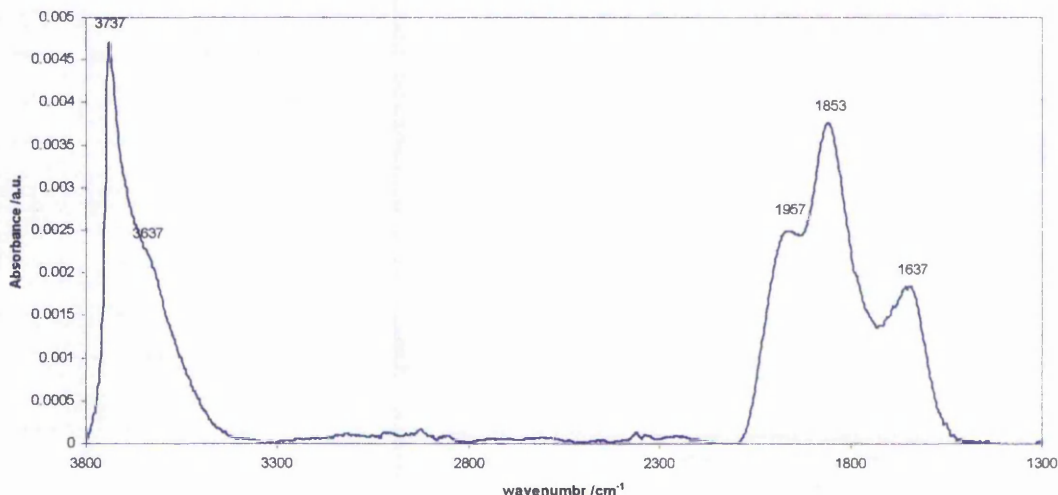
Figure V-11: Typical Fourier-transform Infrared Spectrum of a vacuum-activated Si-MCM-41.

Upon adsorption of ammonia a slight reduction of intensity can be observed at around 3700 cm^{-1}, together with appearance of a peak around 1600 cm^{-1}, corresponding to ammonium ions on the surface, formed upon adsorption of ammonia on Brønsted acid sites [21]. The intensity of these bands is however very weak, due to the low concentration of such sites. The low signal-to-noise ratio is poor and so spectra will not be presented here.

It was possible to quantify the amount of acidic sites present in the material through TPD-MS of ammonia, which resulted in a concentration of 2.44 x 10^{-6} mol$_{ac}$ g^{-1}, where a desorption maximum was found at 603 K. As compared to the prepared iron phosphates (see pp. 112), a similar number of acidic sites was present in Si-MCM-41, with slightly stronger binding forces, desorption maximum being found ca. 100 K higher. The possibility that this temperature difference is due to diffusion effects in

the MCM-41 pores is doubtful, considering the low van der Waals radius of ammonia, ca. 1.65 Å [22], compared to the calculated pore radius of 15.7 Å for MCM-41 and the random distribution of acidic hydroxyl groups on the surface of the material.

Upon introduction of iron in Si-MCM-41 the number of acid sites in the material increased significantly, by one order of magnitude, to 5.11×10^{-5} mol_{ac} g^{-1}. The strength of these acid sites was only slightly reduced, with an intensity maximum found at 586 K in TPD-MS experiments (table V-1). The reduction of acid strength was not considered significant, due to the possible experimental error noted earlier (see pp. 113). Exclusively Lewis acidity was generated from the post-treatment of Si-MCM-41 with iron, in agreement with literature [23].

It is also possible to enhance the acidity of MCM-41 by introducing aluminium in its framework or phosphate groups on its surface [24-26]. It has been noted previously, however, that the post-treatment of the silica had a detrimental effect on its long-rang order (see chapter III, pp. 69). In particular reported methods for the introduction of phosphorus were not found to be reproducible, causing full collapse of the porous structure in the worst cases.

In successful cases the long-range order of materials and their surface area were significantly altered, but the array of pores was assumed to maintain its hexagonal, one-dimensional, character. The number of acidic sites in these materials was increased, as observed in TPD-MS experiments, and summarised in table V-1.

The introduction of aluminium in MCM-41 had the effect of increasing the number of acidic sites by two orders of magnitude, however slightly decreasing the acid strength of the material, with a peak maximum around 512 K, cf. 603 K for the siliceous MCM-41.

Table V-1: Calculated number of acid sites present in synthesised and modified MCM-41 materials.

Material	Desorption temperature /K	No. of acidic sites /mol g^{-1}
Si-MCM-41	603	2.5×10^{-6}
Fe-MCM-41	586	5.11×10^{-5}
Al-MCM-41	512	1.58×10^{-4}
Fe-Al-MCM-41	519	1.18×10^{-4}
Fe-PO$_4$-MCM-41	363	3.7×10^{-5}
PO$_4$-Fe-MCM-41	529	5.6×10^{-5}

The study of the adsorption of ammonia on Al-MCM-41 at 423 K revealed that acidity has been introduced in the material in the form of Lewis and Brønsted sites (fig. V-12), even though this synthetic method had been reported to favour the generation of Brønsted acid sites [21].

The subsequent exchange of iron into Al-MCM-41 slightly reduced its number of acidic sites, with a similar recorded desorption temperature of ammonia. Upon adsorption of ammonia in the infrared setup however it appeared that Fe-Al-MCM-41 had more acid sites than Al-MCM-41 – a similar number of Lewis sites with an increased Brønsted character (fig. V-12).

A possible explanation for this inconsistency is that a problem arose upon baseline-correction of the single beam spectra. Indeed, thin or broken wafers can lead to low absorption of radiation, and thereafter artefacts due to signal to noise ratio and overlap of overtones bands with adsorbed ammonia vibration bands. A possible rationalisation can be obtained when comparing the hydroxyl- region of the spectra of the activated samples (fig V-13).
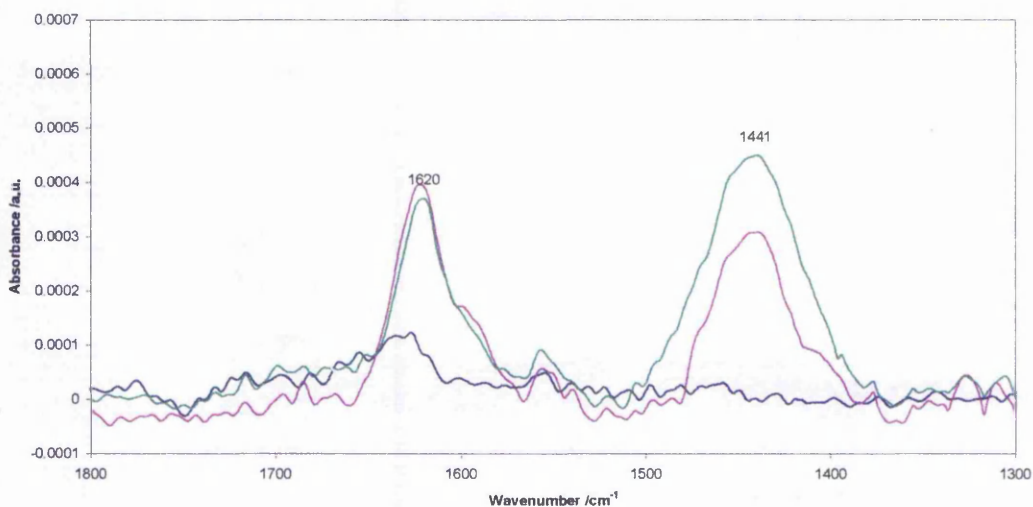
Figure V-12: Adsorbed ammonia vibration region of the *delta* infrared spectra of (blue) Si-MCM-41, (purple) Al-MCM-41, (green) Fe-Al-MCM-41.
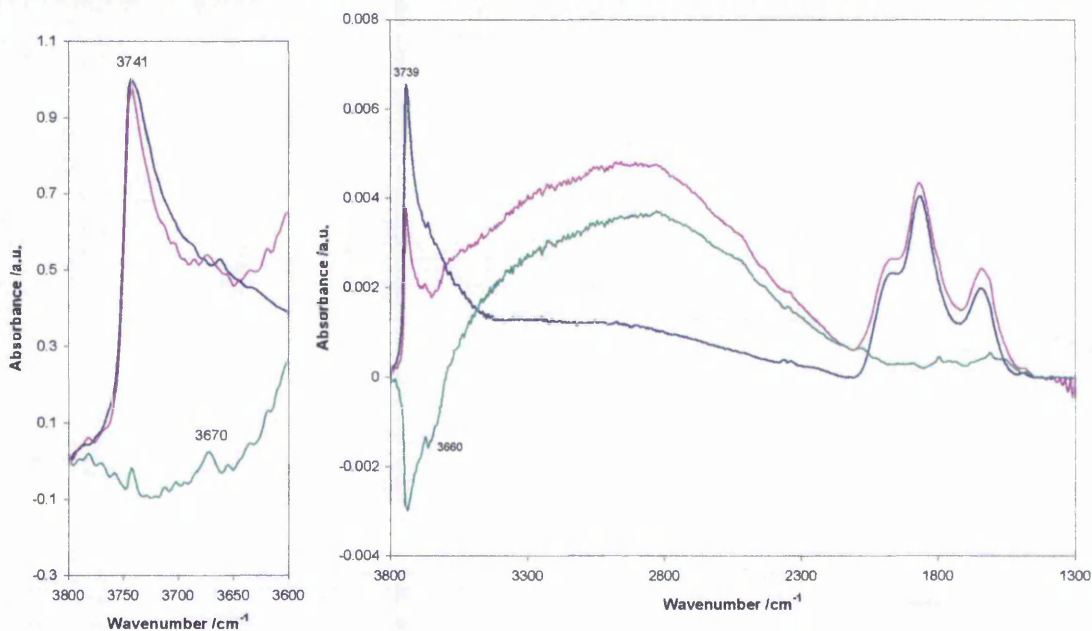
Figure V-13: Baseline corrected FTIR spectra of (blue) Al-MCM-41 and (purple) Fe-Al-MCM-41. The green trace corresponds to the subtraction of the infrared spectrum of Al-MCM-41 from Fe-Al-MCM-41

When normalised to the intensity of the overtones, subtraction of the spectrum of Al-MCM-41 from Fe-Al-MCM-41 revealed differences between them. The broad feature centred at 2500 cm^{-1} could originate from phonon absorption by iron atoms, as

assumed for all samples containing a significant amount of this metal (see pp. 113). A more significant difference between the materials is the loss of intensity of end silanol groups, as well as an apparent loss of intensity of a band located between 3660 and 3670 cm^{-1}, likely to correspond to Brønsted acidic hydroxyl group vibration [19]. The difference was more obvious when the same subtraction was performed on the spectra normalised to the intensity of the end silanol vibration band. Again, when TPD-MS traces for both materials are normalised to maximum signal intensity it becomes obvious that an ammonia desorption peak is present in Fe-Al-MCM-41 around 680 K (fig. V-14).
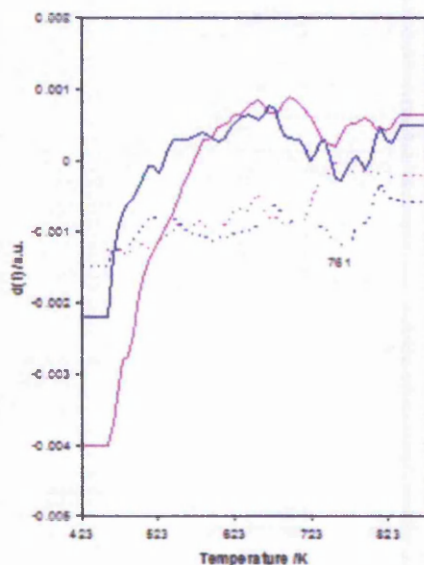
Figure V-14: Derivative of the TPD-IR traces of (blue) Al-MCM-41 and (purple) Fe-Al-MCM-41. The plain and dotted lines correspond to the differentiated area of the ν-NH$_4^+$ peak (Brønsted acid sites) and ν-NH$_3$ peak (Lewis acid sites) respectively.

Confirmation of the presence of this desorption peak was obtained upon analysis of TPD-IR data. Both ammonia and ammonium vibration bands were integrated separately and plotted as a function of time, then differentiated to identify possible inflexion point positions (fig. V-15).
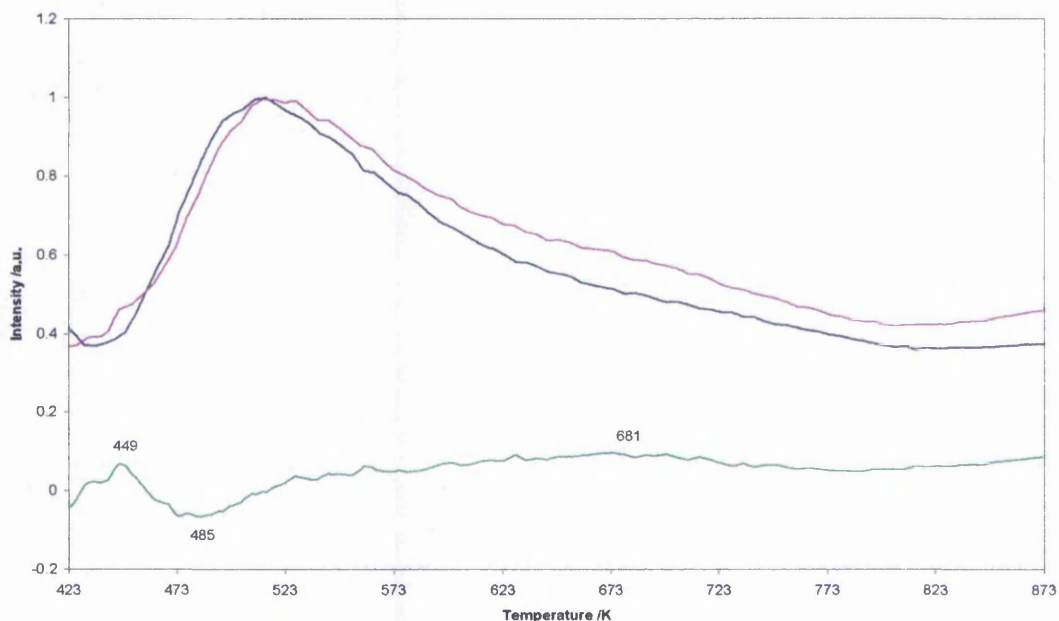
Figure V-15: Ammonia TPD-MS traces (m/z = 16) for (blue) Al-MCM-41 and (purple) Fe-Al-MCM-41. The green trace corresponds to the subtraction of the trace for Al-MCM-41 from Fe-Al-MCM-41, showing that the latter contains more strong acid sites.

The main desorption from all sites occurs at low temperature. The intensity of the ammonium vibration band, associated with Brønsted acid sites, shows a second inflexion point around 750 K, which is not present to a significant extent on the other desorption traces.

All the stated evidence confirms the increased Brønsted acidic character of the prepared Fe-Al-MCM-41, as observed in the ammonia adsorption experiment. The total amount of acidity in the sample however is likely to be decreased as compared to Al-MCM-41, accordingly with TPD-MS experiments. Fe-Al-MCM-41 seems to contain a proportion of stronger Brønsted acid sites, possibly resulting from the introduction of iron nearby aluminium sites and generation of bridging hydroxyl groups.
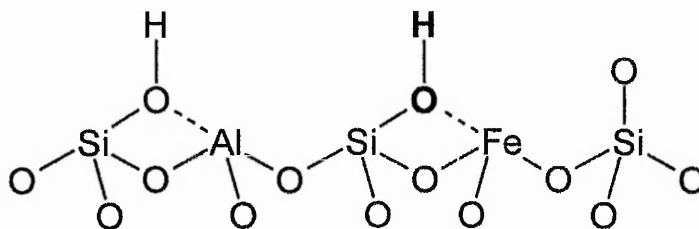
Figure 16: Possible structure of the stronger Bronsted acid sites observed in Fe-Al-MCM-41, due to the introduction of iron into the MCM-41 "framework" nearby aluminium atoms.

The exchange of iron at aluminium Lewis sites, generating coordinated species of structure Al-Fe(OH)$_2$ could explain a reduction in Lewis character accompanied by an increase in weak Brønsted acidic character. Ammonia adsorbed at such sites might be desorbed at temperatures below 423 K, and therefore result in a decreased apparent number of acidic sites in the discussed experiments.

Addition of phosphorus into MCM-41 was less effective than aluminium in increasing the acidity of the material, however the number of acidic sites was increased by an order of magnitude on average. The highest increase in acidity, compared to Si-MCM-41, was observed when phosphate ions were impregnated onto Fe-MCM-41 (table V-1, pp. 117). However, and as outlined in the following paragraphs, most of the acidic character in the material arises from the introduction of iron into Si-MCM-41, rather than phosphorus. Indeed the amount of acid sites and ammonia desorption temperature in Fe-MCM-41 and PO$_4$-Fe-MCM-41 are very similar, the small differences observed cannot be considered significant.

Where phosphorus was introduced first (see chapter II, pp. 45) the total number of acid sites generated is slightly lower than for PO$_4$-Fe-MCM-41, however it appears that this reduction can be directly attributed to the exchange of iron at phosphate sites. Indeed, the spectrum of an activated PO$_4$-MCM-41 (fig. V-17) reveals the presence of a band near 3665 cm^{-1} and a broad band centred around 3000 cm^{-1}, attributed to P-OH

groups. These bands disappear when iron is exchanged into the material, together with a reduction of the silanol band intensity and increase of the bridged –hydroxyl broad band centred at 3560 cm^{-1}.
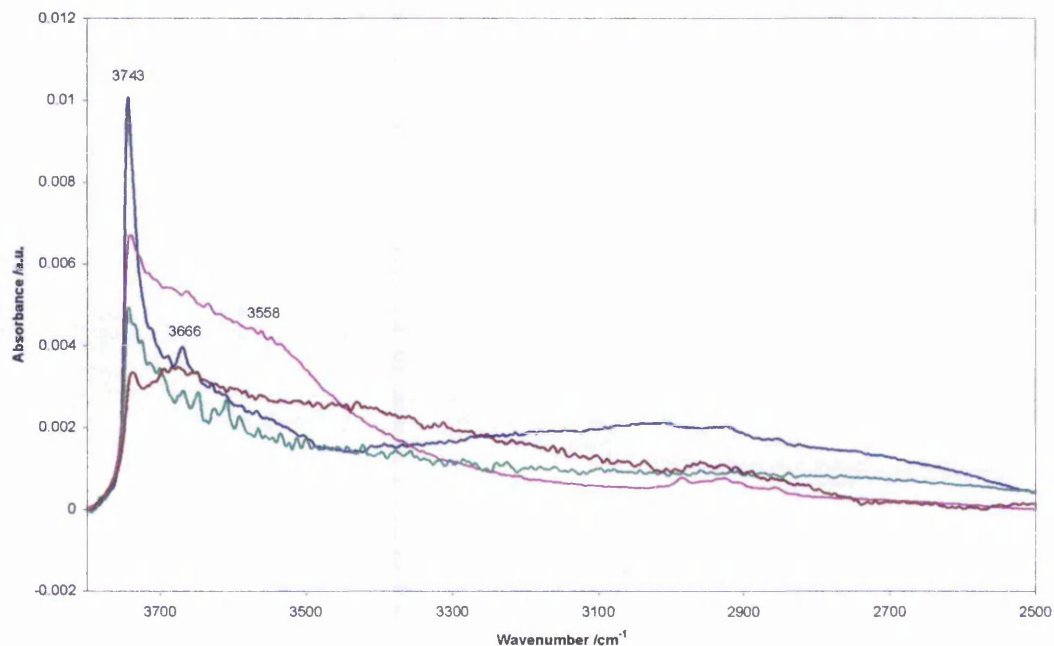
Figure V-17: Baseline-corrected infrared spectra of activated (blue) PO$_4$-MCM-41, (purple) Fe-PO$_4$-MCM-41, (green) PO$_4$-Fe-MCM-41, (brown) FePO$_4$-MCM-41

It is reasonable to state that acidic hydroxyl groups are present in PO$_4$-MCM-41, which protons can be exchanged with iron. This is confirmed when ammonia is adsorbed on both materials, PO$_4$-MCM-41 presenting exclusively Brønsted acidity, where Fe-PO$_4$-MCM-41 mostly has a Lewis acidic character (fig. V-18). The binding strength of these sites is very low, as in TPD-MS experiments ammonia was completely removed at 363 K. Quantification of the number of these sites could therefore only be achieved by adsorbing ammonia onto the material at 323 K, as opposed to 423 K in all other cases.
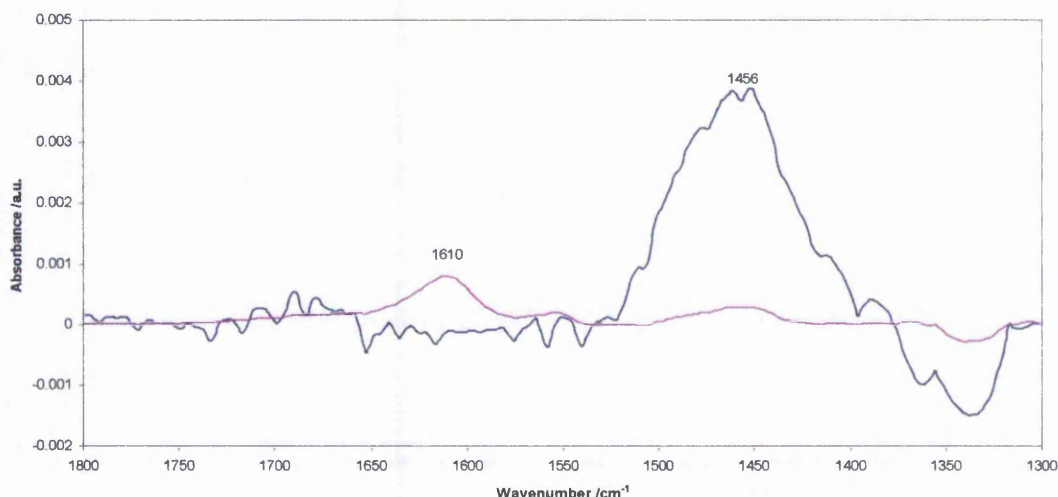
Figure V-18: Ammonia vibration region of the *delta* FTIR spectra of (blue) NH$_4$-PO$_4$-MCM-41 and (purple) Fe-PO$_4$-MCM-41

The phosphorus-containing MCM-41 showing the least acidic sites was prepared by co-precipitation / impregnation of FePO$_4$ onto Si-MCM-41, with 1.26×10^{-5} mol$_{ac}$ g^{-1}. The strength of these sites was slightly less than of PO$_4$-Fe-MCM-41 and Fe-MCM-41, with a maximum intensity of the m/z = 16 peak recorded at 488 K in TPD-MS (see table V-1, pp. 117).

A general trend relating acid strength and number of acid sites in these materials could not be found (fig. V-19). As the acid strength of zeotypic materials is dependent on their structure, rather than their concentration of acid sites [27], it is likely that all phosphorus-containing MCM-41 prepared contain definite iron phosphate phases, rather than isolated iron and phosphate centres.

In all cases the introduction of phosphorus in the form of phosphate groups in MCM-41 resulted in acid sites with lower binding strength to ammonia compared to Fe-MCM-41. Little similarity was observed between different preparation methods, and more information about the chemical environment of iron in these materials

should be acquired to formulate a more definite hypothesis for the origin of the acidity of these materials.
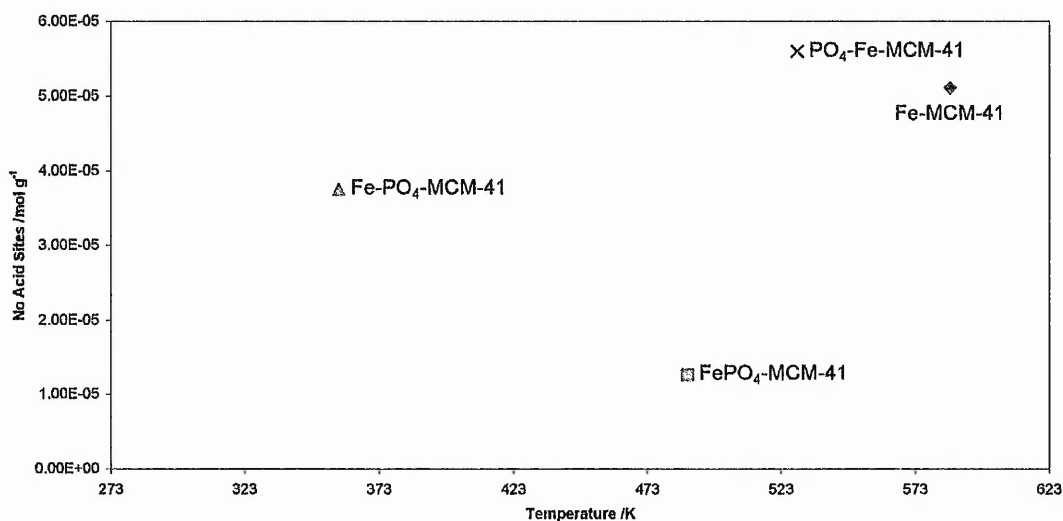
Figure V-19: Number of acid sites as function of desorption temperature of iron/phosphorus containing MCM-41s, as determined by TPD-MS experiments.

V-3.3   ZSM-5s

ZSM-5 and MFI zeolites were the most acidic upon materials studied in this project, both in terms of the number and strength of the acid sites. Their infrared spectra show several bands characteristic of zeolites, which can be divided into two groups. Framework Si-O-Si deformation vibrations, or overtone bands, are found around 1990, 1880, and 1635 cm^{-1}[28]. Hydroxyl stretching vibrations are also found in these materials, with a band centred at 3670 cm^{-1} assigned to extraframework species, one at 3600-3610 cm^{-1} assigned to bridging, acidic OH groups, and one at 3740 cm^{-1} assigned to terminal silanol groups.

The parent ZSM-5 used for exchange of iron had a silica to alumina ratio of 15, and showed a concentration of acid sites near 1 x 10^{-3} mol_{ac} g^{-1}. A maximum in intensity of the m/z = 16 peak in TPD-MS was found around 615 K, and acid sites in the zeolite were mostly of Brønsted type. Some Lewis character was found, as trace,

perhaps due to metal impurities in the material. The concentration of Lewis acid sites in the parent material was however accepted as negligible. Their contribution was attributed to the shoulder noticeable on TPD-MS traces around 500 K, but were not easily observed in FTIR studies of ammonia adsorption (fig. V-20).

The extent of exchange of protonic sites with iron, when wet methods were used, was only limited, as indicated by the little decrease in intensity of the hydroxyl bands in the spectra of activated zeolites (fig V-21).
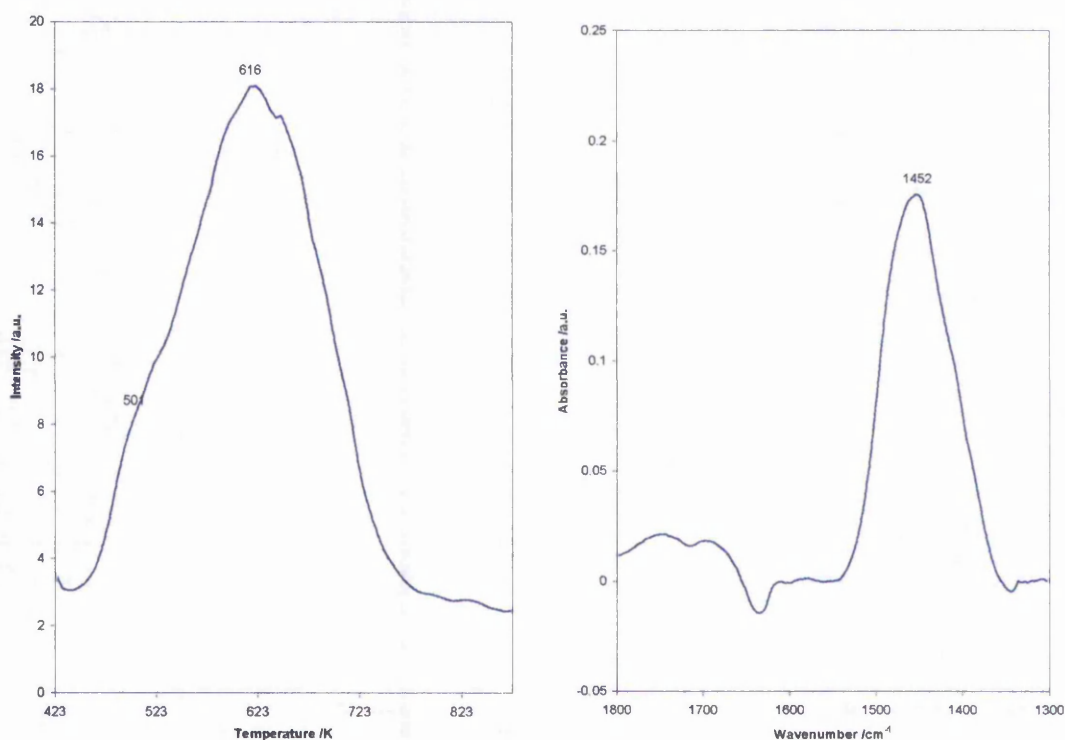
Figure V-20: Ammonia m/z = 16 TPD-MS trace (left) and FTIR spectrum of H-ZSM-5 activated in vacuum, evacuated after exposure to 10 mbar ammonia.

The decrease in intensity of the hydroxyl bands can be taken as an indication of the amount of iron exchanged with protonic sites. It can however not be used for the quantification of iron at exchange sites, as other parameters can influence the intensity of these bands. For example dealumination of the sample can occur under certain

conditions [29, 30], or the signal can be "flattened" in the detector due to high absorption of radiation.
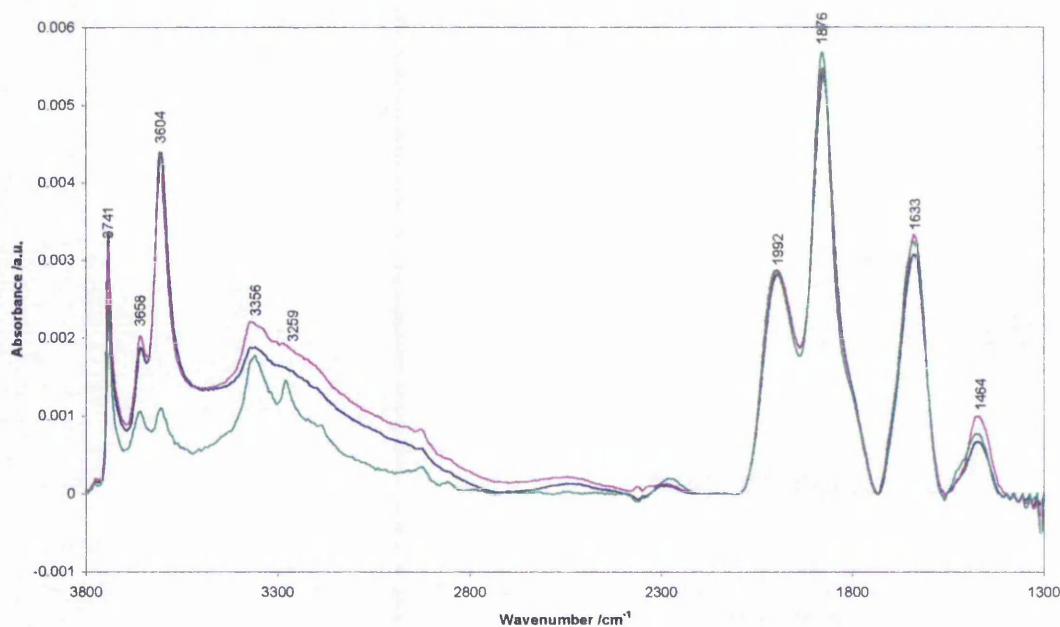
Figure V-21: Baseline-corrected FTIR spectra of vacuum-activated iron-containing ZSM-5 prepared by various exchange methods and their parent H-ZSM-5. (blue) H-ZSM-5, (purple) Fe-ZSM-5 EX, (green) Fe-ZSM-5 CVD.

The low level of exchange of iron in wet conditions can therefore be confidently assumed from recorded spectra, whereas near-total exchange of protons when iron was introduced in the zeolite by CVD couldn't. As the decrease of Brønsted acidic character of the latter (fig V-22) excluded the hypothesis of a spectral artefact causing the decrease in hydroxyl band intensity, the possibility of dealumination could not be excluded. The intensity of the $M-NH_4^+$ vibration, located at 1452 cm^{-1}, showed a good agreement with the intensity of bridging hydroxyl bands in the different materials (fig. V-23), as expected, as both other types of hydroxyl groups in ZSM-5 show only limited acidity and iron was not expected to be exchanged to a significant extent at these positions.
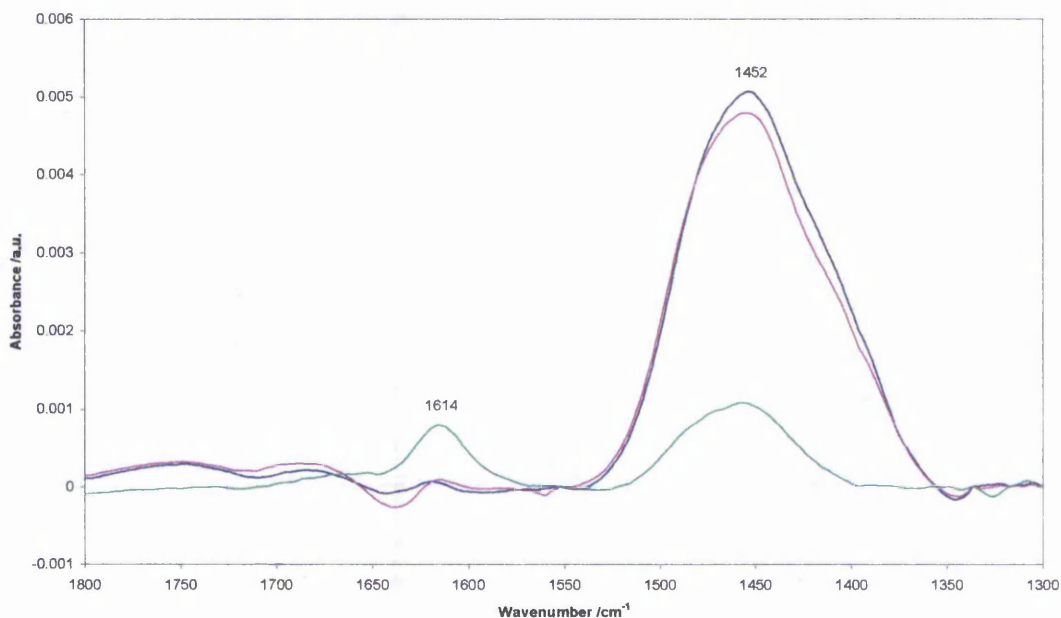
Figure V-22: Adsorbed ammonia vibration region of the *delta* FTIR spectra of iron containing ZSM-5s and their parent H-ZSM-5. (blue) H-ZSM-5, (purple) Fe-ZSM-5 EX, (green) Fe-ZSM-5 CVD.
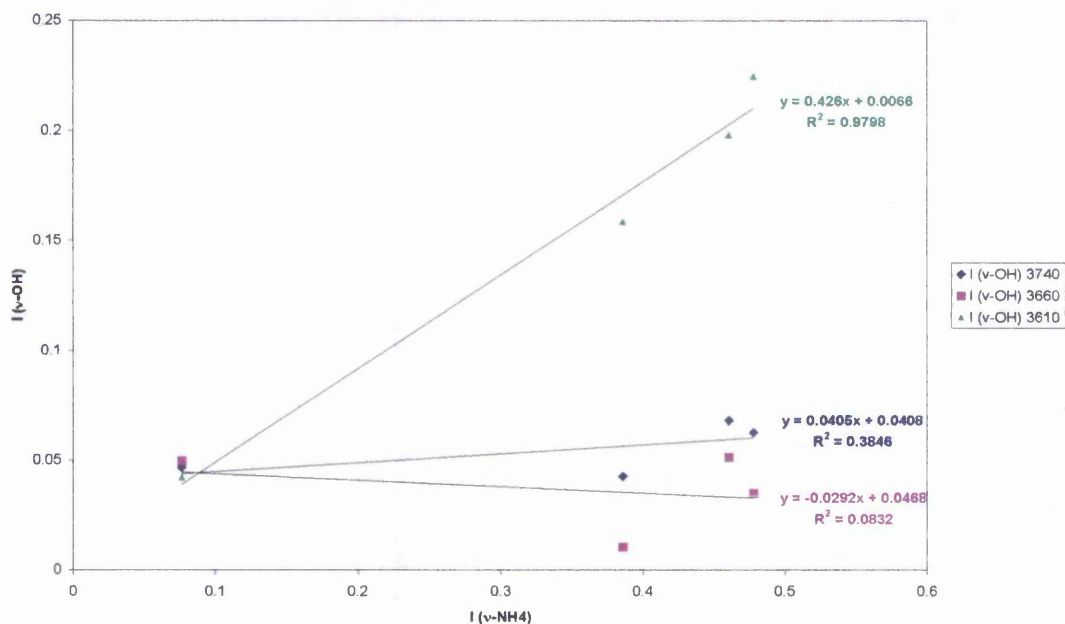
Figure V-23: Intensity of the hydroxyl vibration bands present in Fe-ZSM-5 EX as a function of the intensity of the v-NH$_4$ vibration band, as determined from *delta* FTIR spectra of ammonia adsorbed onto the material at increasing NH$_3$ partial pressure.

On the other hand a stronger Lewis acid band, at 1614 cm^{-1}, confirms a higher loading of metal in the zeolite. Materials prepared by wet exchange have a lower iron loading as determined by atomic absorption (see chapter III, pp. 74), and do not show any significant Lewis acidic character upon adsorption of ammonia. The increase in intensity of the M-NH$_3$ vibration is only limited and could not definitely be isolated from the background signal.

The extent of iron exchange was calculated with regard to the number of acidic protons exchanged. The latter was calculated from the intensity of the M-NH$_4^+$ vibration band and the quantification of the number of acid sites in TPD-MS experiments. It was assumed that the contribution of Lewis acidity to the total amount of ammonia desorbed from the parent ZSM-5 was negligible. The material could therefore be used as a reference with 0% of acid protons exchanged. Results of this calculation are presented in table V-2.

Table V-2: Iron content to protons exchanged ratios for the prepared Fe-ZSM-5s.

Material	Iron content		Acidic protons		Fe/H$^+_{exchanged}$
	/ wt. %	/ mol g^{-1}	Present /mol g^{-1}	Exchanged /%	
H-ZSM-5	0	0	9.75 x 10^{-4}	0	n/a
Fe-ZSM-5 EX	0.68	1.22 x 10^{-4}	8.91 x 10^{-4}	14.4	0.87
Fe-ZSM-5 CVD	2.50	4.48 x 10^{-4}	5.53 x 10^{-6}	99.4	0.46

Only in the sample prepared by vapour deposition did the amount of iron introduced exceed the theoretical value for 100% exchange, calculated as Fe/Al = 0.33. The amount of protons exchanged as well deviated from the expected values for a straight-forward exchange of iron (III) into the zeolite. Fe/H$^+_{exchanged}$ is lower than expected in

the case of Fe-ZSM-5 EX and Fe-ZSM-5 CVD. The low proton exchange in Fe-ZSM-5 EX is most likely due to the formation of iron oxy hydroxide clusters in aqueous solution at pH near neutral, subsequently exchanged into the zeolite [31]. The value obtained for the sample prepared by chemical vapour deposition, however, could reflect the exchange of iron (II) as isolated species. It was reported that iron (III) chloride was exchanged in the form of $FeCl_2^+$ species, most of which subsequently migrated to form binuclear Fe (III) complexes upon aqueous washing [32]. In all cases the presence of heterogeneous iron phases in the zeolite is suggested, and confirmed after adsorption of nitric oxide with *in situ* IR, discussed in the following chapter (see pp. 154).

The distribution of hydroxyl bands in infrared was significantly different when iron was introduced into the zeolite framework during its crystallisation, in the absence of aluminium (fig. V-24). The intensity of the bands was generally much lower than in our commercial ZSM-5. Two bands could be isolated, at 3739 and 3620 cm^{-1}, attributed respectively to end silanol group and acidic bridging hydroxyl group stretching vibrations. The intensity of the end hydroxyl groups appears to increase with increasing iron loading, whereas the intensity of the acidic hydroxyl band was not found to be affected to a significant extent. A very broad and intense feature is present in all cases between 2300 and 3300 cm^{-1}. It is possible that this band corresponded to O-H stretching vibrations from water present in the zeolite, either residual on the surface or trapped in defects of the structure [33]. However water adsorbed onto the zeolite's surface would lead to an increased intensity of the band located at 1633 cm^{-1}, as its deformation vibrations overlay with the framework overtones. This broad band was therefore attributed, as for $FePO_4$, to phonon absorption phenomena due to the high concentration of iron ions in the framework.
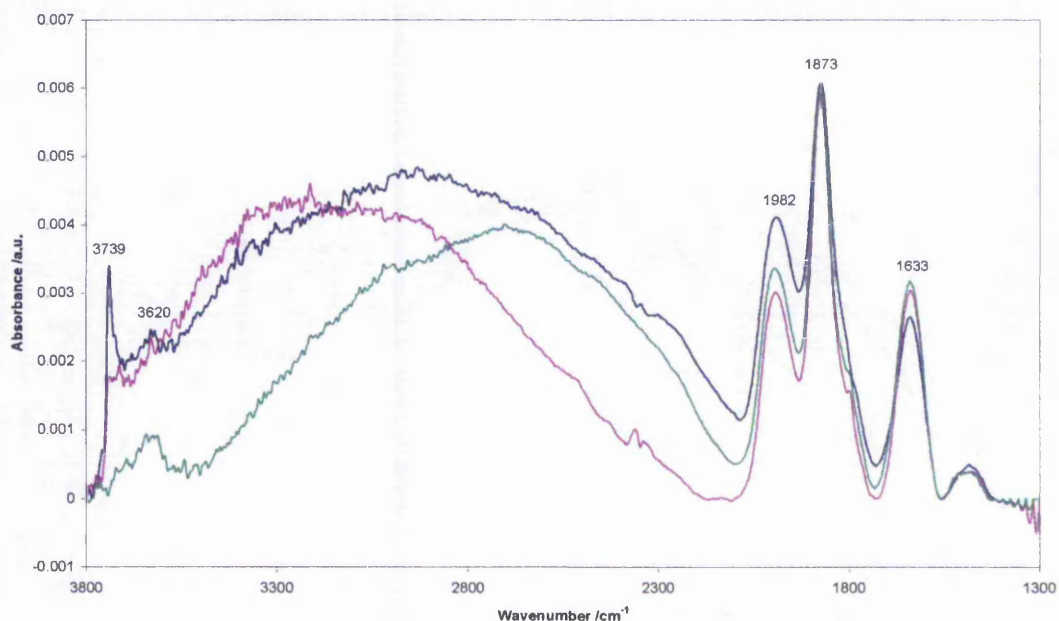
Figure V-24: Baseline-corrected FTIR spectra of vacuum-activated synthesised Fe-MFI samples. (blue) Fe-MFI SYN24, (purple) Fe-MFI SYN48, (green) Fe-MFI SYN96.

The amount of acid sites in the materials, determined by TPD-MS of ammonia, was calculated to be 4.48×10^{-4}, 2.73×10^{-4} and 2.05×10^{-4} mol_{ac} g^{-1} for respectively Fe-MFI SYN24, -SYN48 and -SYN96. A fairly linear relationship was found between iron concentration and number of acid sites generated, however the average mol_{Fe}/mol_{ac} ratio was 5.20, suggesting that less than one in five atoms of iron produced one acid site. This ratio, together with the prominent Lewis acidic character of the materials (fig. V-25), could be interpreted as due to the presence of iron clusters and inaccessible iron sites in the framework. Iron oxide clusters were indeed already suggested from temperature-programmed reduction profiles (see chapter IV, pp. 96). On the other hand the MFI framework structure and porosity leave little room for inaccessible sites (see chapter I, pp. 9). The materials were shown to have a good crystallinity and porosity and iron oxide was not observed in their diffraction patterns (see chapter III, pp. 75). It is, however, known that small size clusters are invisible in

powder X-Ray diffractometry, therefore the hypothesis of the presence of iron oxide nanoclusters in the framework is considered here as most likely explanation for these materials' behaviour. Further evidence for this hypothesis will be discussed in the subsequent structural study (see chapter VI, pp. 166-170).
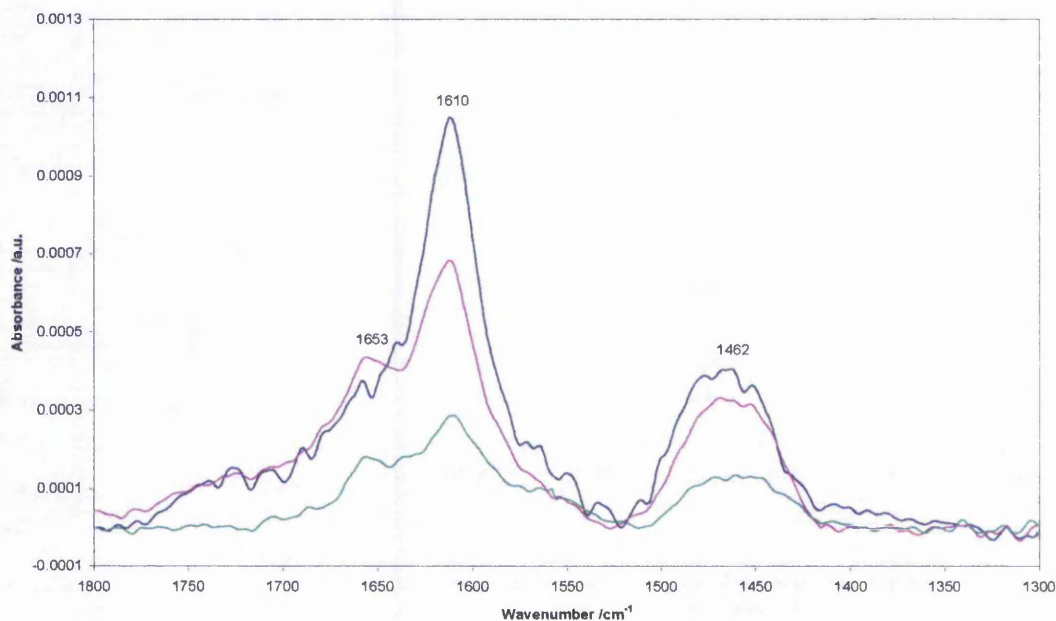
Figure V-25: Adsorbed ammonia vibration region of the *delta* FTIR spectra of Fe-MFIs. (blue) –SYN24, (purple) –SYN48, (green) –SYN96.

The detection of strong Brønsted acidity upon ammonia adsorption indirectly supports the presence of framework tetrahedral iron, through the presence of the stated acidic bridging hydroxyl groups. The Lewis character of the material could also originate from framework iron, however not exclusively. The Lewis acidity could indeed originate from the suspected iron nanoclusters Fe_4O_4 [28], which could be located partially in the zeolite's framework, or at extraframework positions.

The shoulder present at 1650 cm^{-1} was found particularly in the prepared MFI materials and attributed to some Lewis acidic character, however the exact reason for such a shift in NH_3 vibration is unclear. The band appears significantly upon

evacuation of the system following exposure of the samples to 10 mbar of ammonia (fig. V-26).
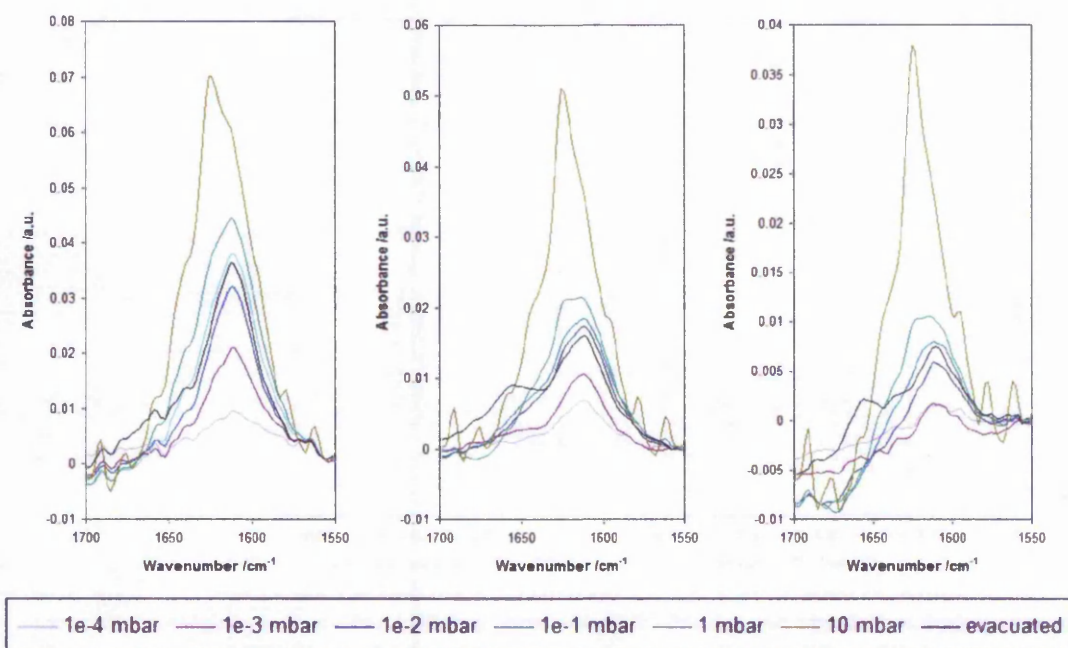
Figure V-26: δ-NH$_3$ region of the adsorption spectra of Fe-MFIs. *Delta* **FTIR spectra of ammonia adsorbed onto Fe-MFIs at increasing NH$_3$ partial pressure. (Left) Fe-MFI SYN24; (Middle) –SYN48; (Right) –SYN96.**

The δ-NH$_3$ infrared band position has been shown to be independent of surface coverage, due to the independence of the dipole moment of the adsorbate [34, 35]. This vibration has been reported to be affected by the nature of the chemical species coordinated through ammonia's lone electron pair. The effect is attributed to the weakening of the N-H bond, however δ-NH$_3$ vibration is the mode least sensitive to this effect, hence shifting of the peak is minimal [16].

Two hypotheses are suggested for the presence of the shoulder at 1650 cm^{-1}, the first of which is a spin state change of the adsorbing iron site, occurring upon desorption of weakly bound ammonia. This has been reported to occur upon adsorption of small target molecules such as NO, evidenced by electron paramagnetic resonance (EPR) [36]. A second possibility is a reduction of the degree of freedom of the adsorbed

ammonia molecule through, for example, hydrogen bonding with neighbouring acid sites. The 1650 cm^{-1} shoulder can be noticed on spectra taken at low ammonia surface coverage, i.e. low pressure. Its intensity would be limited at higher surface coverage by the presence of ammonia molecules adsorbed on the acid site responsible for hydrogen bonding. Upon evacuation of the system, "space" is made on the surface through partial desorption of ammonia, allowing the discussed hydrogen bond to form. Such an effect could not be proven using the techniques available during this project, however a similar phenomenon has been reported in the past, upon adsorption of acetylacetone on an Fe-MFI sample [37]. The material was reported to have a less even distribution of acid sites than ZSM-5, explaining why the effect was not observed in the latter.
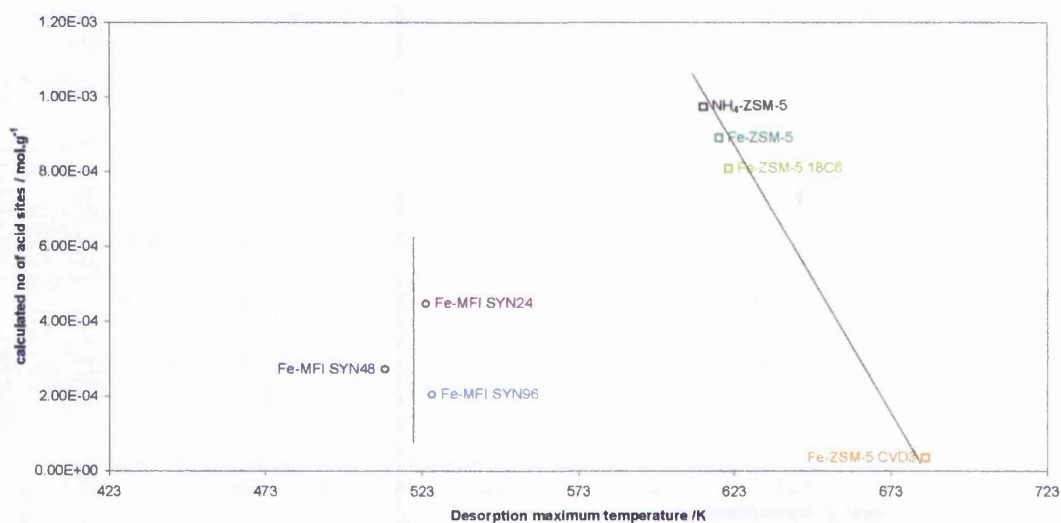
Figure V-27: Number of acid sites as a function of ammonia desorption temperature for some of the prepared silicates of MFI structure, as determined by TPD-MS experiments.

A comparison of the number of acidic sites as a function of the position of the main ammonia desorption peak is presented in figure V-27. The acid strength of ZSM-5s, prepared by ion exchange of iron into the framework, is higher than the one of aluminium-free samples. This acidity is present mainly as strong Brønsted sites in the

former, which binding strength to ammonia increases slightly as more proton sites are exchanged with iron. On the other hand the acid strength of Fe-MFIs is merely affected by the concentration of iron in the sample. The number of acid sites, however, is in direct relationship with the amount of iron in the framework, and is present as a mixture of Brønsted and Lewis acid sites.

As final word concerning the acidity of the prepared materials, it can be noted that the introduction of gold into Fe-ZSM-5 did not affect its acidity to a significant extent, both exchanged and impregnated materials showed a similar number of acid sites, present as almost exclusively Brønsted acidity.
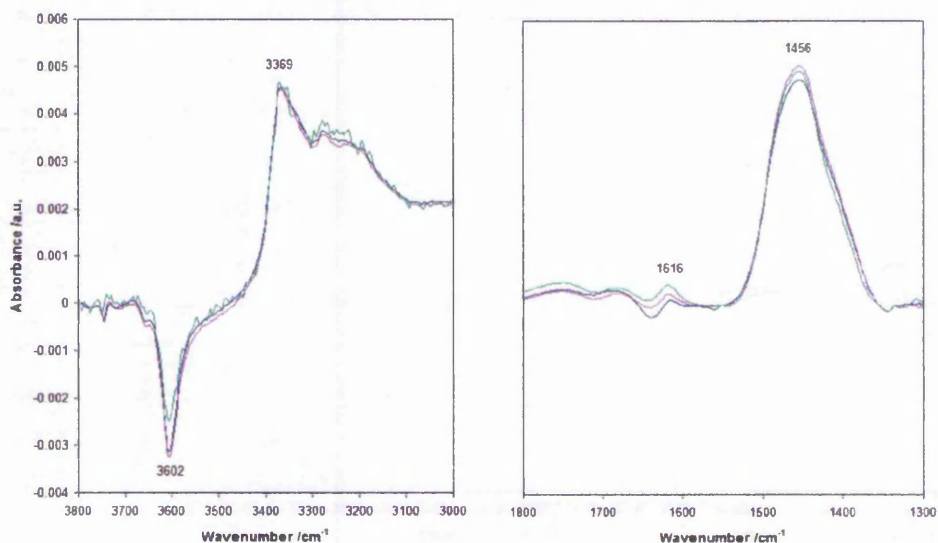
Figure V-28: Hydroxyl- and adsorbed ammonia vibration regions of the *delta* FTIR spectra of gold-containing Fe-ZSM-5. Spectra recorded after exposure to 10 mbar ammonia and evacuation to base pressure. (blue) Fe-ZSM-5 EX, (purple) Au/Fe-ZSM-5 IMP, (green) Au/Fe-ZSM-5 EX.

A slight increase of the number of acid sites in Au/Fe-ZSM-5s compared to Fe-ZSM-5 supports the hypothesis of displacement of iron from ion-exchange sites during the suspension of the material in the gold solution used for ion-exchange. There wasn't any evidence of ammonia adsorbed onto gold particles, likely to be due

to the low concentration of gold in the framework and/or its presence as clusters having weak binding interactions with ammonia.

V-4 Summary

The acidity of the prepared solid catalysts is thought to be an important factor influencing their activity in partial oxidation reactions. The type of acid sites, their strength and concentration were studied by means of ammonia adsorption with *in-situ* infrared detection, and temperature-programmed desorption coupled with either *in-situ* infrared or mass spectrometric detection.

Following the study the materials can be broadly separated in two groups, according to the amount of sites strongly coordinating ammonia. Iron phosphates and aluminium free MCM-41s form a group showing little acidic character, typically in the range 1×10^{-6} to 1×10^{-5} moles of acid sites per gram of material. Most materials in this group possess a mixture of both Lewis and Brønsted acid sites, with the exception of Fe-MCM-41 which contains mostly Lewis acidity. Unsupported iron phosphates and siliceous MCM-41 are considered non-acidic, adsorbing only minor amounts of ammonia at 423 K.

The second group refers to materials containing a calculated concentration of acid sites above 1×10^{-4} mol_{ac} g^{-1}. Aluminium containing MCM-41s and all silicates of MFI structure are included here. Within this group different acidic characters were observed. Low exchange level ZSM-5s, i.e. all Fe-ZSM-5s except Fe-ZSM-5 CVD showed mostly Brønsted acid sites, present as bridging hydroxyl groups in the zeolite. Fe-ZSM-5 CVD, Al-MCM-41 and Fe-Al-MCM-41 contained a mixture of both types of acidity with an apparent Brønsted/Lewis ratio close to 1. Fe-MFIs as well showed both types of acid sites, however present as mostly Lewis type. It is thought that the

latter materials contain a significant part of non-acidic iron sites as well, which structure is unclear yet. Most materials showed similar acid strength, desorbing ammonia around 500 K. Brønsted sites in ZSM-5s showed a stronger acidic character, ammonia desorption occurring around 673 K, and phosphorus containing MCM-41s showed a variable acid strength depending upon their preparation method.

V-5 References

1.   Hoffmann, E.d. and V. Stroobant, *Mass spectrometry : principles and applications*. 2nd ed ed. 2001, Chichester: John Wiley. xii, 407 p.
2.   Barker, J., *Mass Spectrometry*. 2nd ed, ed. D.J. Ando. 1999, Greenwich: John Wiley & Sons.
3.   Burle, *Channeltron electron multiplier handbook for mass spectrometry applications*, Burle, Editor. 2004.
4.   John T. Yates, J. and T.E. Madey, *Vibrational Spectroscopy of Molecules on Surfaces*. Methods of surface characterisation, ed. C.J. Powell, et al. Vol. 1. 1987, New York: Plenum Press.
5.   Banwell, C.N., *Fundamentals of Molecular Spectroscopy*. 1977. 320 pp.
6.   Cairon, O., et al., *Acid-catalysed benzene hydroconversion using various zeolites Bronsted acidity, hydrogenation and side-reactions*. Applied Catalysis a-General, 2003. **238**(2): p. 167-183.
7.   Casades, I., et al., *Evidence for an acid-catalysed reaction subordinated to the occurrence of a previous electron transfer in the incorporation of an electron-rich alkene within NaY zeolite (pg 982, 2001)*. Chemical Communications, 2002(7): p. 794-794.
8.   Vos, A.M., et al., *Calculation of reaction rate constants for hydrogen-deuterium exchange reactions of methane catalysed by acid zeolites*. Chemical Communications, 2001(12): p. 1108-1109.
9.   Tsyganenko, A.A., D.V. Pozdnyakov, and V.N. Filimonov, *Infrared Study of Surface Species Arising from Ammonia Adsorption on Oxide Surfaces*. Journal of Molecular Structure, 1975. **29**(2): p. 299-318.
10.   Busca, G., et al., *FT-IR studies of internal, external and extraframework sites of FER, MFI, BEA and MOR type protonic zeolite materials*. Studies in Surface Science and Catalysis, 2002. **142A**(Impact of Zeolites and Other Porous Materials on the New Technologies at the Beginning of the New Millennium): p. 975-982.
11.   Cooley, J.W., P.A.W. Lewis, and P.D. Welch, *Application of Fast Fourier Transform Algorithm to Estimation of Spectra and Cross-Spectra*. Journal of Sound and Vibration, 1970. **12**(3): p. 339-&.
12.   Griffiths, P.R. and J.A.P.R.G.a.J.A.d.H. De Haseth, *Fourier transform infrared spectrometry*. Chemical analysis ; v. 83. 1986, New York ; Chichester: Wiley. p. cm.
13.   Dixon, J.M., *Structure, Bonding and Catalytic Activity of Modified Mesoporous Silicates*. 2004, Nottingham Trent University: Nottingham.

14. Long, R.Q. and R.T. Yang, *Temperature-programmed desorption/surface reaction (TPD/TPSR) study of Fe-exchanged ZSM-5 for selective catalytic reduction of nitric oxide by ammonia.* Journal of Catalysis, 2001. **198**(1): p. 20-28.

15. Lin-Vien, D., et al., *The Handbook of Infrared and Raman Characteristics Frequencies of Organic Molecules.* 1991. 503 pp.

16. Nakamoto, K., *Infrared and Raman Spectra of Inorganic and Coordination Compounds.* 4th ed. 1986: Wiley-Interscience.

17. Hawkins, G.J., *Spectral Characterisation of Infrared Optical Materials and Filters*, in *Department of Cybernetics.* 1998, The University of Reading: Reading.

18. Lin-Vien, D., et al., *The Handbook of Infrared and Raman Characteristic Frequencies of Organic Molecules*, ed. A. press. 1991.

19. Jentys, A., N.H. Pham, and H. Vinek, *Nature of hydroxy groups in MCM-41.* Journal of the Chemical Society-Faraday Transactions, 1996. **92**(17): p. 3287-3291.

20. Zhao, X.S., et al., *Comprehensive study of surface chemistry of MCM-41 using Si-29 CP/MAS NMR, FTIR, pyridine-TPD, and TGA.* Journal of Physical Chemistry B, 1997. **101**(33): p. 6525-6531.

21. Burgess, G., R.W. Joyner, and M. Stockenhuber, *A comparative study of literature methods of introducing acidity into MCM-41*, in *Recent Advances in the Science and Technology of Zeolites and Related Materials, Pts a - C.* 2004, ELSEVIER SCIENCE BV: Amsterdam. p. 446-452.

22. Schulz, G.E. and R.H. Schirmer, *Principles of Protein Structure.* 1979. 314 pp.

23. Lazar, K., et al., *Coordination and oxidation states of iron incorporated in mesoporous MCM41.* Hyperfine Interactions, 2002. **139**(1-4): p. 19-31.

24. Kawi, S., S.C. Shen, and P.L. Chew, *Generation of Bronsted acid sites on Si-MCM-41 by grafting of phosphorus species.* Journal of Materials Chemistry, 2002. **12**(5): p. 1582-1586.

25. Huang, L.M. and Q.Z. Li, *Improvement on thermal stability and acidity of mesoporous materials with post-treatment of phosphoric acid.* Studies in Surface Science and Catalysis, 2000. **129**(anoporous Materials II, Proceedings of the Conference on Access in Nanoporous Materials, 2000): p. 93-98.

26. Mokaya, R. and W. Jones, *Grafting of Al onto purely siliceous mesoporous molecular sieves.* Physical Chemistry Chemical Physics, 1999. **1**(1): p. 207-213.

27. Katada, N., et al., *Determination of the acidic properties of zeolite by theoretical analysis of temperature-programmed desorption of ammonia based on adsorption equilibrium.* Journal of Physical Chemistry B, 1997. **101**(31): p. 5969-5977.

28. Joyner, R. and M. Stockenhuber, *Preparation, Characterization, and Performance of Fe-ZSM-5 Catalysts.* Journal of Physical Chemistry B, 1999. **103**(29): p. 5963-5976.

29. Berreghis, A., et al., *Dealumination of zeolites .6. Influence of the hydrothermal treatment of EMT zeolites on their framework composition and on their porosity.* Journal De Chimie Physique Et De Physico-Chimie Biologique, 1996. **93**(9): p. 1525-1542.

30. Kornatowski, J., et al., *Dealumination of Large Crystals of Zeolite ZSM-5 by Various Methods.* Journal of the Chemical Society-Faraday Transactions, 1992. **88**(9): p. 1339-1343.

31. Greenwood, N. and A. Earnshaw, *Chemistry of the Elements.* 1st ed. ed. 1984: Oxford.

32. Marturano, P., et al., *The mechanism of formation of the Fe species in Fe/ZSM-5 prepared by CVD.* Physical Chemistry Chemical Physics, 2001. **3**(24): p. 5585-5595.

33. Pelmenschikov, A.G. and R.A. van Santen, *Water adsorption on zeolites: ab-initio interpretation of IR data.* Journal of Physical Chemistry, 1993. **97**(41): p. 10678-80.

34. Khvoshchev, S.S., S.P. Zhdanov, and T.N. Sakharova, *Adsorption of ammonia by zeolites as influenced by variations in cation density.* Doklady Akademii Nauk SSSR, 1968. **181**(5): p. 1189-92.

35. Weiss, M., G. Ertl, and F. Nitschke, *Adsorption and decomposition of ammonia on iron(110).* Applications of Surface Science (1977-1985), 1979. **2**(4): p. 614-35.

36. Volodin, A.M., et al., *Spin design of iron complexes on Fe-ZSM-5 zeolites.* Catalysis Today, 2005. **110**(3-4): p. 247-254.

37. Handreck, G.P. and T.D. Smith, *A physicochemical study of iron(III)-containing MFI zeolitic materials: the iron(III) isomorph of zeolite ZSM-5.* Journal of the Chemical Society, Faraday Transactions 1: Physical Chemistry in Condensed Phases, 1989. **85**(10): p. 3195-214.

Chapter VI: <u>On the nature of iron species</u>

VI-1 Introduction

It is accepted that the species responsible for the oxidative activity of iron containing MFI zeolites in the direct hydroxylation of benzene have a specific structure, which is still being debated [1-7]. The involvement of these sites in the partial oxidation of light hydrocarbons has not been proven and is out of the scope of this chapter, however the extent of the work reported about the benzene to phenol system illustrates the difficulty of identifying the active site in a zeolite catalysed reaction. It is believed that a further knowledge of the active species in a catalytic process is essential for the efficient development of a highly selective and active catalyst. This chapter therefore focuses on the identification of the iron phase(s) present in the materials prepared. Some hypotheses regarding this structure have been formulated in previous chapters, which confirmation will be attempted here. Several analytical techniques are available for the determination of the local environment of elements, which can be difficult to implement when studying zeolites. The most widely used spectroscopic methods for this purpose are extended x-ray absorption spectroscopy (EXAFS) and x-ray photoelectron spectroscopy (XPS), both of which were inappropriate in our case, respectively due to the averaging effect of the first, making the study of mixtures of structures difficult, and the low penetrative power of electrons of the second, preventing the observation of atoms in the pores of the zeolites. Two techniques are known to be able to overcome these deficiencies, namely Mossbauer and infrared spectroscopies. The first was unfortunately unavailable during the course of this project and therefore the following discussion is solely based

on the analysis of infrared spectra of an adsorbed probe. The vibration frequencies of a few adsorbed probe molecules are known to be highly dependent on the local chemistry of the substrate, two of which are carbon monoxide CO (ref) and nitric oxide NO [8]. The second was used here. The principles of the technique will be discussed first, followed by a literature review of the current state of assignment of vibration bands to specific NO complexes. As some disagreement has arisen between authors it will be attempted to formulate a critical assignment of vibration bands present. This assignment will be used to compare and analyse the different preparation methods used and their influence on the structure of iron in our materials. A summary of findings is included at the end of this chapter, together with a preliminary discussion concerning the oxidative potency of the materials.

VI-2 Background and Method

VI-2.1 FTIR *in-situ* adsorption of nitric oxide

The principles of Fourier transform infrared spectroscopy are discussed in chapter V: acidity of the prepared materials. In *in situ* adsorption of nitric oxide experiments the same instrument as for the adsorption of ammonia was used, schematics of which can be found on page 110 of this thesis.

The local chemical environment around adsorbed nitric oxide (NO) molecules can easily alter its internal vibration frequency. The energy needed for the oscillation of a chemical bond is essentially related to its strength [9]. Changes in electron distribution within the molecule can easily alter this energy, in the case of adsorbed probes through the (de)population of bonding or anti-bonding orbitals, by forward or back donation of electrons to the adsorbate or substrate. Bonding in NO is similar to carbon

monoxide CO, and both act as σ-donors and π-acceptors and figure VI-1 shows the different bonding interactions in CO coordinated to a transition metal [10].
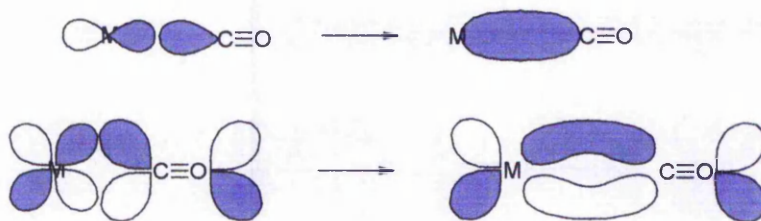
Figure VI-1: Schematic representation of the (top) sigma and (bottom) π bonds in a metal-carbonyl complex. (blue) filled orbitals, (white) empty orbitals.
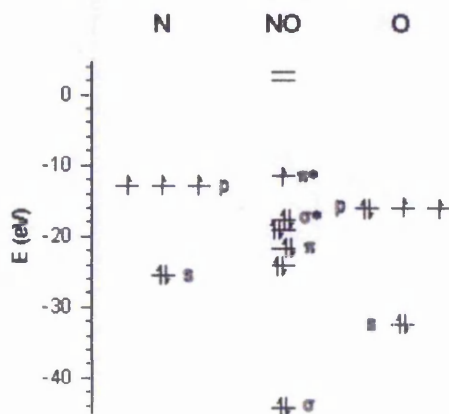
Figure VI-2: Molecular orbital diagram for nitric oxide NO.

In M-CO complexes the σ bond is formed by donation of the carbonyl sigma electrons to the empty orbital of the metal. The π bond is formed by back-donation of the metal's d electrons to the empty π anti-bonding orbital of CO. NO however has one more electron than CO, located in a π anti-bonding orbital. As a result the M-NO bond is usually weaker than the corresponding M-CO bond, which is reflected by a blue shift of the corresponding infrared vibration. Similarly the back-donation of electrons from the metal causes a blue shift of the M-NO vibration band. The sigma forward donation from the ligand on the other hand causes a red shift of the vibration band, as its σ orbital has a slightly anti-bonding character [9-11]. The loss of one electron from nitric oxide is easy and confers the molecule a good stability, as this is

lost from the $2p\pi^*$ orbital (fig. VI-2). The resulting nitrosonium ion NO^+ therefore shows $\nu(NO)$ vibration at around 2200 cm^{-1}, whereas in the nitrosyl form NO this band is located around 1900 cm^{-1} [11].

In a review publication G. Mul compiled reported vibration frequencies of NO adsorbed onto iron in different zeolites [12]. This data and his assignments are presented in table VI-1.

The band at around 2133 cm^{-1} was assigned to NO^+ species adsorbed at cationic sites in the zeolite, i.e. Brønsted acid sites. Its kinetics of adsorption was reported to be slow, the following process having been suggested [13]:
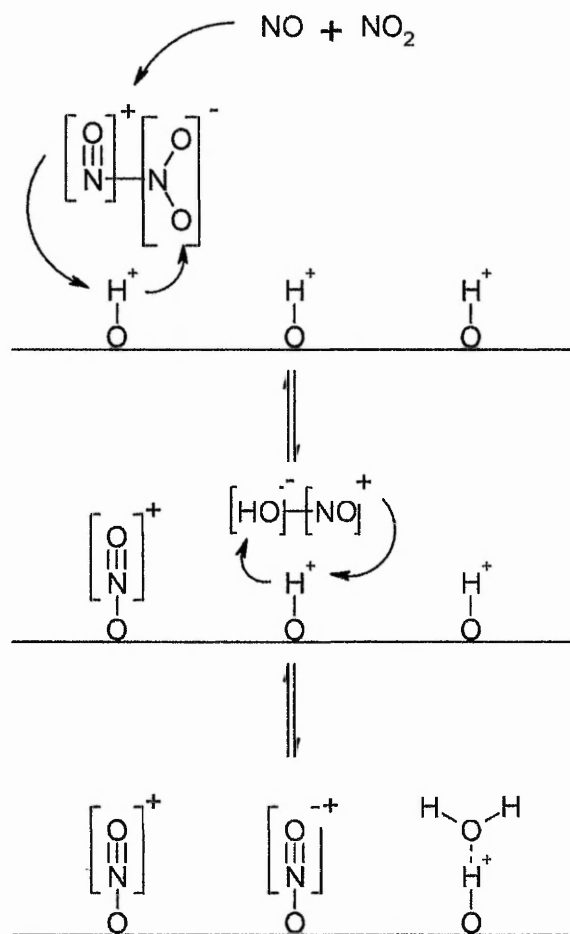
Figure VI-3: Mechanism proposed by Hadjiivanov et.al. [13] for the adsorption of NO^+ species at cationic sites in zeolites.

The bands at around 1910 and 1800 cm^{-1} have been assigned by several authors to vibrations of a di-nitrosylic species adsorbed onto isolated iron sites in ZSM-5 and Y zeolites. The former was also assigned to poly-nitrosyl species adsorbed onto iron silicalites, and associated with the band at 1765 cm^{-1}. In one publication the band at around 1800 cm^{-1} was assigned to a second molecule of nitric oxide adsorbed onto Fe_4O_4 type nanoclusters (see table VI-1 for references).

The mononitrosylic equivalent of the latter species was reported by the same authors to show a vibration band at around 1880 cm^{-1}. This band has also been associated with isolated iron sites in ZSM-5 and Y zeolites, in undenominated or at γ positions (5-membered ring of the MFI structure). It has been pointed out that this vibration is very close to the gas phase value for NO, namely 1875 cm^{-1} [12].

The band at around 1850 cm^{-1} provoked greatest disagreement. It was assigned to nitrosyl species adsorbed onto iron in the 6-membered rings of MFI and Y zeolites, or onto iron clusters in MFI zeolites. The reported positions of the vibration varied considerably, between 1839 and 1852 cm^{-1}, and it is not excluded that two different iron sites could contribute to this band.

The vibration band at around 1765 cm^{-1} has been assigned both to di-nitrosylic species adsorbed onto isolated iron sites in Fe-silicalite and to a low-spin iron (I) mono-nitrosylic complex.

The band at around 1635 cm^{-1} has unanimously been attributed to NO_2 species adsorbed onto the zeolites. The location of these species will not be discussed in this study, nor will it be attempted to refine iron structure-location relationships for these species.

Table VI-1: Reported vibration frequencies of NO on iron containing zeolites and their assignment.

Frequency /cm^{-1}	Assignment	Catalyst	Reference
2133	Cat*-(NO)$^+$	Fe-ZSM-5	[13]
1910	Fe^{II}(NO)$_2$(α)	Fe-Y	[14]
	Fe^{II}(NO)$_2$	Fe-ZSM-5	[13, 15, 16]
	Fe^{II}(NO)$_{n>2}$(α)	Fe-silicalite	[17]
1880	Fe^{II}(NO), Fe^{II}(NO)(γ)	Fe-Y	[14]
	Fe^{II}(NO)(γ)	Fe-ZSM-5	[15]
	Fe^{II}(NO)	Fe-ZSM-5	[13, 16]
	Fe$_4$O$_4$-(NO)	Fe-ZSM-5	[18]
1850	Fe^{II}(NO)iso(β)	Fe-Y	[14]
	Fe^{II}(NO)(β)	Fe-ZSM-5	[15, 18]
	Fe^{II}O$_x$-NO (α)	Fe-ZSM-5	[16]
	(Fe^{II}O)$_n$-NO(α), Fe^{II}(NO)$_{n>2}$(α)	Fe-silicalite	[17]
1800	Fe^{II}(NO)$_2$(α)	Fe-Y	[14]
	Fe^{II}(NO)$_2$	Fe-ZSM-5	[13]
	Fe^{II}(NO)$_2$(α)	Fe-ZSM-5	[15, 16]
	Fe$_4$O$_4$-(NO)$_2$	Fe-ZSM-5	[18]
	Fe^{II}(NO)$_{n>2}$(α)	Fe-silicalite	[17]
1765	Fe^{II}(NO)$_2$(α)	Fe-silicalite	[17]
	Fe^{II}(NO)(α)	Fe-ZSM-5 / Fe-Y	[14, 15]
	Fe^{II}-(NO)	Fe-ZSM-5	[13, 16, 18]
1635	Adsorbed NO$_2$	Fe-ZSM-5	[17]

In addition to the bands presented in the previous table, it was also reported that nitrosyl species adsorbed onto large extra-framework $FeAlO_x$ clusters absorb infrared light at around 1870 cm^{-1}.

A broad summary of iron species present and their location in the MFI framework is presented on figure VI-4.
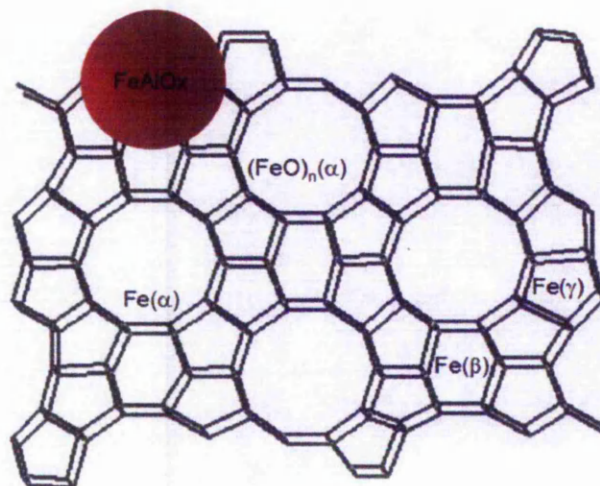
Figure VI-4: Schematic representation of the reported possible iron structures and their location in the MFI framework.

The review published by G. Mul rightly points out the disagreement and possible errors found in the interpretation of adsorbed nitrosyl infrared bands from various studies. It will be attempted in this study to formulate a critical assignment of the bands observed in the prepared materials. The established work will be used as starting point for the assignment of infrared peaks. The data discussed in previous chapters and resulting hypotheses formulated will be considered throughout this study, with the aim of formulating a logical assignment of peaks and determine the structure of iron within the prepared materials.

VI-3 Results and discussion

VI-3.1 FePO$_4$

Iron phosphate prepared by co-precipitation did not show any significant adsorption of nitric oxide NO, indicated by the absence of bands in the range 1750-2150 cm^{-1}. A minor amount of adsorbed nitrogen dioxide was observed when 1 mbar NO was admitted to the sample chamber, indicated by the presence of a peak centred at around 1650 cm^{-1}. The intensity of this peak however was below 0.01 arbitrary units, which is negligible when compared to spectra recorded for other materials (see below). It can be assumed from this data that FePO$_4$ has some oxidative activity, however the absence of peaks for adsorbed NO prevents any discussion regarding the nature of the active sites. A definite structure match was not found for FePO$_4$ by XRD or TPR and the material is virtually non-acidic.

When nitric oxide was adsorbed on FePO$_4$, pH6, a single M-NO vibration peak was observed at around 1850 cm^{-1} (fig. VI-5). Its maximum intensity was quickly reached at low pressure.

This peak was attributed to nitrosyl species adsorbed on iron sites in a FePO$_4$ matrix. As nitric oxide adsorbed onto iron oxide was reported to have a M-NO vibration frequency of 1810 cm^{-1} [19], the absence of large iron oxide clusters in this material, as suggested from XRD traces, is confirmed. As the position of this peak indirectly suggests a certain order in the material, its symmetry and presence as a lone peak strongly indicate adsorption at iron sites with very similar chemical and electronic environments. Iron in its +2 oxidation state only is involved in the coordination of nitrosyl species, however, in a "pure" FePO$_4$ structure electrical neutrality laws force the iron ion to its +3 oxidation state to counter-balance the charge from the phosphate

group. A simple explanation could be the presence of hydroxyl defects in the material, with protons partly balancing the charge. These protonic sites were observed in co-precipitated $FePO_4$ upon ammonia adsorption, but were not seen on $FePO_4$, pH6. Infrared spectra of the activated $FePO_4$, pH6 have less absorbance in the hydroxyl region (see chapter V, pp. 111). Moreover co-precipitated $FePO_4$ did not adsorb any nitrosyl species. It is suggested that iron in such a chemical environment does not possess the ability to strongly coordinate nitrosyl ions, and a different structure is responsible for nitrous oxide adsorption.
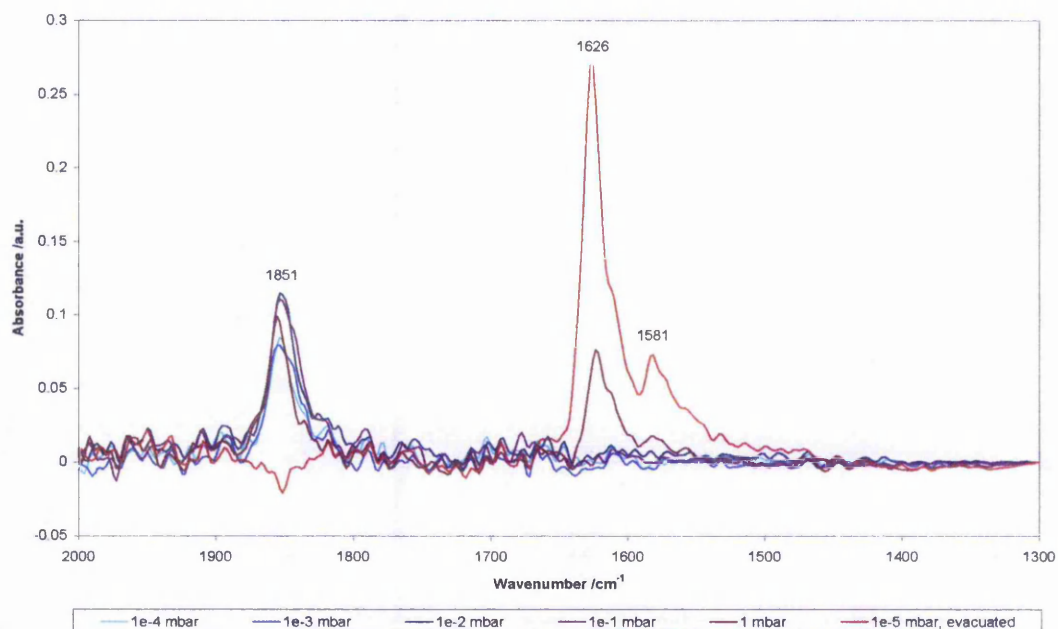
Figure VI-5: FTIR spectra of nitric oxide adsorbed onto FePO4, pH6

As discussed earlier $FePO_4$, pH6 has an amorphous structure with some crystalline character appearing upon heating at high temperature (see chapter III, pp. 62). The material also causes a strong and broad infrared light absorption feature centred around 2000 cm^{-1}, which was attributed to phonon absorption phenomena, caused by an organised iron distribution in the material (see chapter V, pp. 113). An arrangement of alternating charged iron nanoclusters with phosphate ions can be

assumed, iron being present in mixed oxidation states. Confirmation or structure elucidation was not attempted further as beyond the scope of this thesis, and the material will be considered as having a different and specific structure in further discussions. It has to be noted that this material seems to exhibit a higher activity than its co-precipitated pair for the conversion of nitric oxide to adsorbed nitrogen dioxide.

VI-3.2   MCM-41

It was reported that iron introduced post-synthetically into MCM-41 was present on the surface of the silicate as mostly isolated species [20]. Following TPR studies it was proposed that Fe-MCM-41 prepared post-synthetically from Si-MCM-41 and iron nitrate contained a single iron phase, possibly as isolated ions or dimers of Fe-O-Fe structure (see chapter IV, pp. 87).

The adsorption of nitric oxide onto this material gives rise to an apparent single vibration band centred at 1815 cm^{-1}, with shoulders at 1900 and 1750 cm^{-1}. These shoulders were attributed to the symmetric and anti-symmetric vibrations of di-nitrosyl species adsorbed on a single iron site. These shoulders have been observed previously upon adsorption of NO onto Fe-silicalite, with vibration frequencies of 1910 and 1765 cm^{-1} [17]. The 10 cm^{-1} shift of these bands to lower frequencies observed in Fe-MCM-41 could be attributed to the non-crystalline character of MCM-41 leading to a weaker interaction between the iron and coordinated NO molecules. The band centred at 1815 cm^{-1} presents a slight asymmetry at lower surface coverage. A second component to this band was isolated using a Gaussian-Lorentzian curve fitting function with 70% Gaussian character. The band was found to be centred at 1840 cm^{-1}, which corresponds to the position of the vibration band remaining after evacuation of the system. In Fe-silicalite, this band was reported to

correspond to either poly-nitrosyl species on isolated iron sites or mono-nitrosyl species on iron sites of $(FeO)_n$ structure (see table VI-1). The hypothesis of poly-nitrosyl species adsorbed onto the material's surface can be excluded, as it is believed that such species would be weakly adsorbed on the material and readily desorbed upon evacuation of the system to base pressure.

The 1840 cm^{-1} band can therefore be attributed to mono-nitrosyl species on iron dimers, as larger iron species have been found not to occur in MCM-41. These dimers would have an apparent slightly stronger binding interaction with NO than the isolated species. This is surprising considering the general weaker binding interaction of larger iron structures [21, 22]. It is possible that the adsorbed nitrosyl species is stabilised by interaction of the oxygen's lone electron pairs with a neighbouring iron atom. It has to be noticed, finally, that neither of these iron species in Fe-MCM-41 exhibit any activity towards the oxidation of adsorbed NO to NO_2, as indicated by the absence of bands around 1650 cm^{-1}.

Al-MCM-41 shows two nitric oxide adsorption bands in the infrared region, centred at around 2181 and 1973 cm^{-1} (fig. VI-6). These were attributed respectively to NO^+ species coordinated to protonic sites (Brønsted acid sites) and mono-nitrosyl species adsorbed onto isolated aluminium sites in octahedral coordination. The position and intensity of these two bands will be considered in the discussion of the adsorption of NO onto Fe-Al-MCM-41 hereafter, with regards to the location of iron in the latter. Al-MCM-41 exhibits a strong oxidising character, indicated by the presence of intense NO_2 vibration bands between 1550 and 1700 cm^{-1}, which could be formed by reaction of NO with lattice oxygen, or dissociation at an iron site, followed by reaction with another NO molecule.
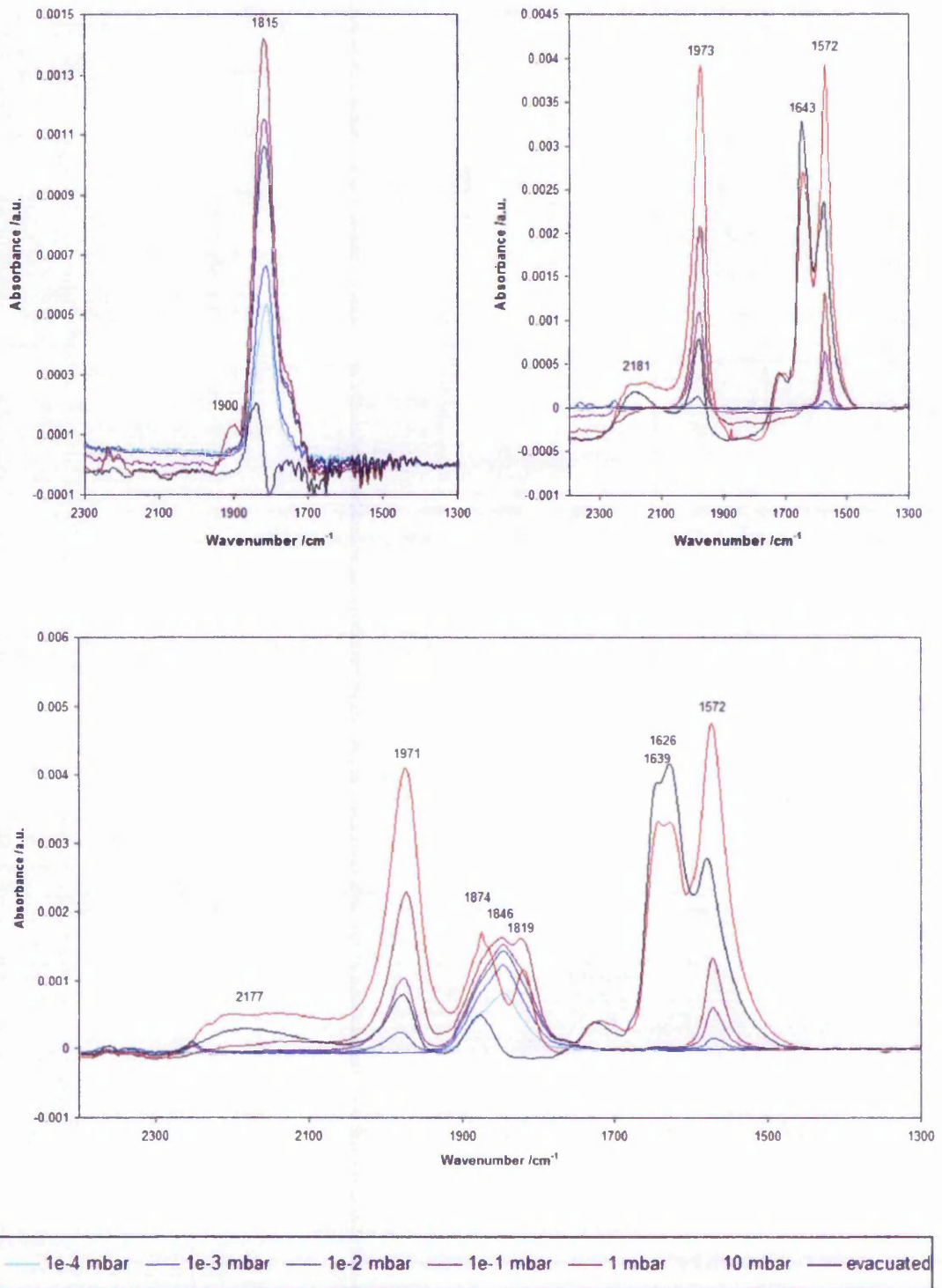
Figure VI-6: Recorded delta FTIR spectra of nitric oxide adsorbed onto (top left) Fe-MCM-41, (top right) Al-MCM-41, (bottom) Fe-Al-MCM-41.

When NO was adsorbed onto Fe-Al-MCM-41 a complex pattern was observed in infrared. Bands at 2177, 1971, and 1819 cm^{-1} were found in Al-MCM-41 and Fe-MCM-41, and attributed respectively to vibrations of nitrosyl species coordinated to protonic sites, isolated aluminium sites, and isolated iron sites respectively. These bands, together with the adsorbed NO$_2$ vibrations between 1500 and 1700 cm^{-1}, are the most intense vibrations observed on spectra recorded at high nitric oxide partial pressure. At lower pressures, however – at or below 10^{-1} mbar NO – the main vibration bands are centred at 1819, 1846 and 1874 cm^{-1}. The three peaks were fitted with a 70% Gaussian – 30% Lorentzian function at different NO partial pressure in order to determine their effective area. A plot of the calculated areas as a function of pressure is presented in figure VI-7.
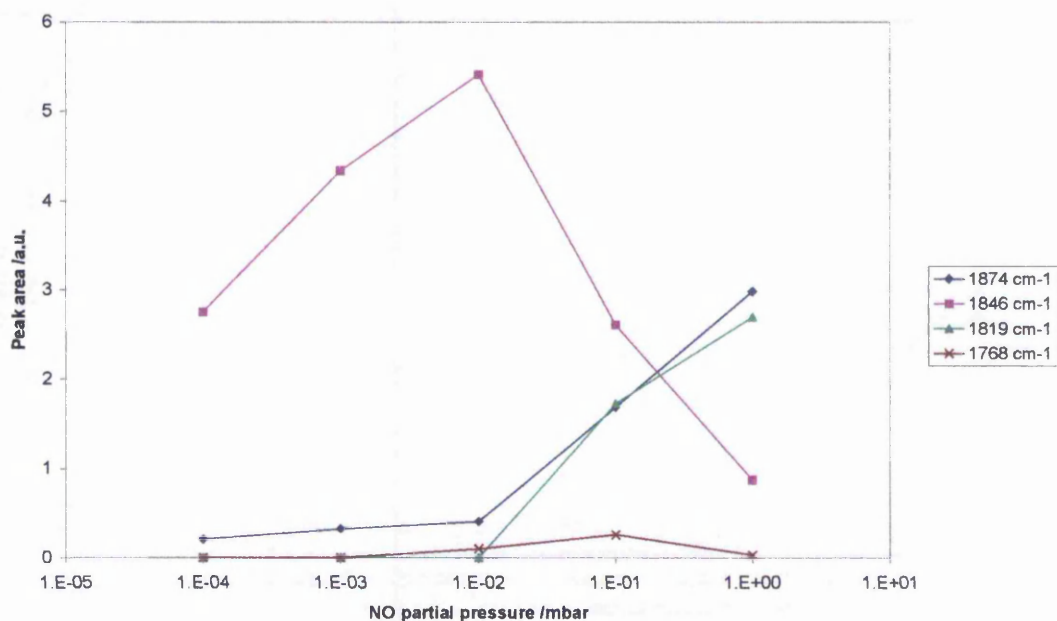
Figure VI-7: Evolution of the area of selected nitrosyl peaks observed upon adsorption of NO onto Fe-Al-MCM-41 as a function of the partial pressure of NO.

At lower NO partial pressure the peak centred at 1846 cm^{-1} is predominant with only a minor contribution from the bands at 1819 and 1874 cm^{-1}. This tendency is reversed

as pressure increases, a direct relationship between the intensities of the 1819 and 1874 cm^{-1} bands is revealed, and both are inversely proportional to the intensity of the 1846 cm^{-1} band.

From this it seems probable that the three peaks originate from the vibration of species adsorbed onto the same site in the material. It is reasonable to assume that the band located at 1846 cm^{-1} corresponds to a mono-nitrosyl species and those at 1815 and 1874 cm^{-1} to the symmetric and anti-symmetric vibrations of di-nitrosyl species on a single iron site. The three discussed vibration bands were not present in either spectra of Fe-MCM-41 or Al-MCM-41 and are therefore attributed to nitrosyl species adsorbed onto isolated iron sites at ion-exchange positions. A 35 cm^{-1} red shift is observed between the Fe(NO) and AlFe(NO) bands (fig. VI-8), indicating a slightly increased ionic character of the Fe-NO bond, possibly originating from the withdrawal of electron density from iron ions by the neighbouring aluminium. It is possible to calculate the angle between NO molecules adsorbed in dinitrosyl species, as their intensity ratio of their symmetric and anti-symmetric vibrations are related to the bond angle by:

Equation VI-1:

$$\frac{I_{sym}}{I_{asym}} = \text{cotan}^2\,\theta\,[23]$$

In the bond angle calculations presented in this chapter it is assumed that the symmetric NO vibration occurred at higher frequency than the anti-symmetric one [9]. In the equation above, I_{sym} denotes the intensity of the symmetric - and I_{asym} the intensity of the anti-symmetric vibration band of dinitrosyl species. The ON-M-NO bond angle is measured as 2θ. The bond angle calculated for dinitrosyl species adsorbed onto (FeAl) sites of Fe-Al-MCM-41 was ca. 87 degrees, which is reasonably

consistent with the symmetry expected from iron in an octahedral environment. When the method was applied to dinitrosyl species adsorbed onto isolated iron sites in Fe-MCM-41 a bond angle of 154 degrees was obtained. This corresponds to a highly distorted octahedral geometry, which is difficult to account for. There was however no disagreement in the past in the assignment of these vibration bands, and a high error is assumed on the determination of the concerned peaks intensities. Indeed they are present as shoulders around the main mono-nitrosyl band, which made the application of the peak-fitting routine difficult.
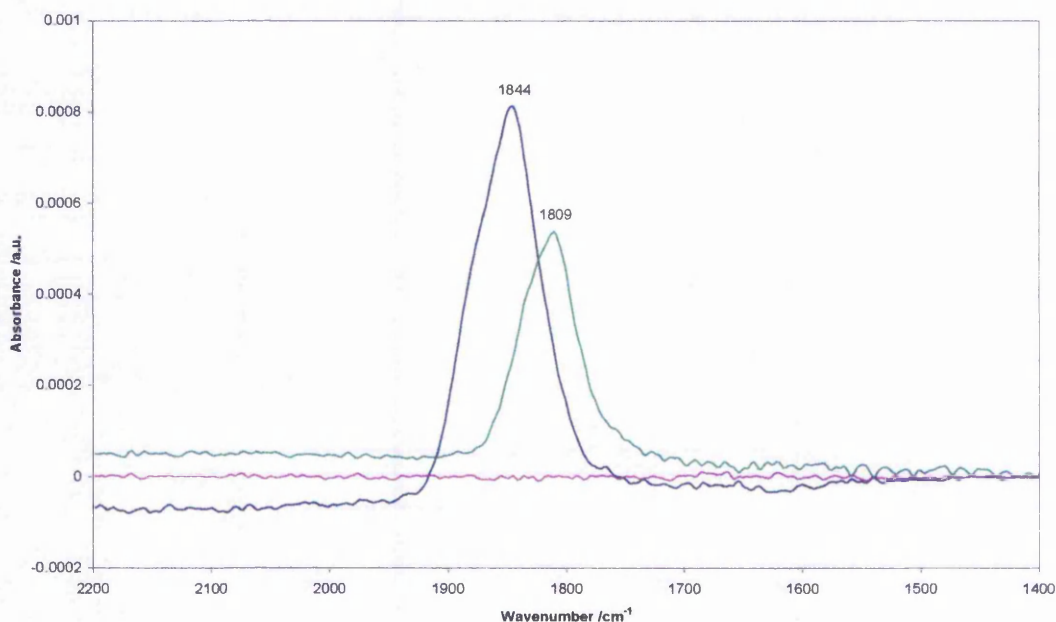
Figure VI-8: Comparison of delta FTIR spectra recorded for the adsorption of NO at 10^{-4} mbar onto (blue) Fe-Al-MCM-41, (purple) Al-MCM-41, and (green) Fe-MCM-41

The increased intensity of the peaks located at 1815-1820 cm^{-1} at higher NO partial pressure, and the presence of a vibration band at around 1970 cm^{-1} indicate a heterogeneous dispersion of iron and aluminium atoms in the MCM-41 structure, with the presence of (Al), (Fe), and (FeAl) sites. The exchange of iron at aluminium sites is therefore not complete, as was already suggested by the residual Brønsted acidic

character of Fe-Al-MCM-41 observed in the ammonia adsorption experiments (see chapter V, pp. 118).

VI-3.3   MFI

The adsorption of nitric oxide onto iron containing zeolites of MFI structure has been studied by various authors, however their interpretation of spectra vary and often disagree [12]. In the following discussion it will be attempted to rationalise and confirm the attribution of the various Fe-NO infrared vibration bands. Hypotheses discussed previously in this thesis will be considered together with the adsorption data in order to elucidate the structure of the various MFIs prepared.

It has to be noted first that, similarly to NO adsorbed onto iron phosphate and Fe-(Al)-MCM-41, a band corresponding to the vibration of nitrosyl species at isolated iron sites is expected at around 1845 cm^{-1}, which should progressively disappear at high NO partial pressures to be replaced by two bands, a symmetric and an anti-symmetric vibration of dinitrosyl species adsorbed on the same site. These two bands were found at around 1880 and 1815 cm^{-1} in Fe-Al-MCM-41 and are expected to have a similar vibration frequency in Fe-ZSM-5s. A slight variation in these vibration frequencies is not excluded due to the higher strain within the pores of MFIs and their crystalline character, affecting the bond strength. Indeed they were reported at 1910 and 1800 cm^{-1} in previous studies [13, 15, 16]. Spectra recorded for the adsorption of NO onto Fe-ZSM-5 EX reveal, besides an intense cat-NO^{+} band at 2131 cm^{-1} and some adsorbed NO_2 between 1500 and 1700 cm^{-1}, the presence of at least two bands in the 1800-1900 cm^{-1} region (fig. VI-9).
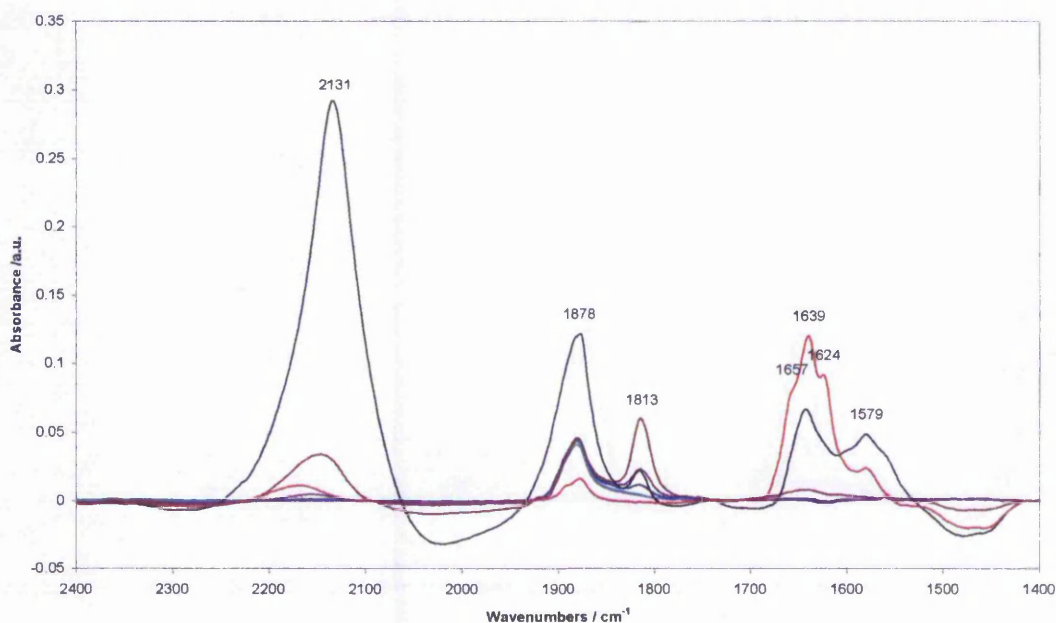
Figure VI-9: Recorded delta infrared spectra of NO adsorbed onto Fe-ZSM-5 EX at different NO partial pressures.

The two bands found were centred at around 1878 and 1813 cm^{-1} and presented a certain asymmetry, which was interpreted as due to the overlap of several peaks in the same range. It was attempted to deconvolute the peaks using a 70% Gaussian – 30% Lorentzian distribution function. Converged solutions were obtained in most cases where peaks were placed at around 1910, 1890, 1880, 1865, 1845, 1815 and 1760 cm^{-1}, and peaks outside the 2000 – 1700 cm^{-1} range were ignored. A typical fitting result is presented in figure VI-10, for the difference FTIR spectrum of NO adsorbed onto Fe-ZSM-5 EX at 10^{-2} mbar and left to equilibrate for 30 minutes.
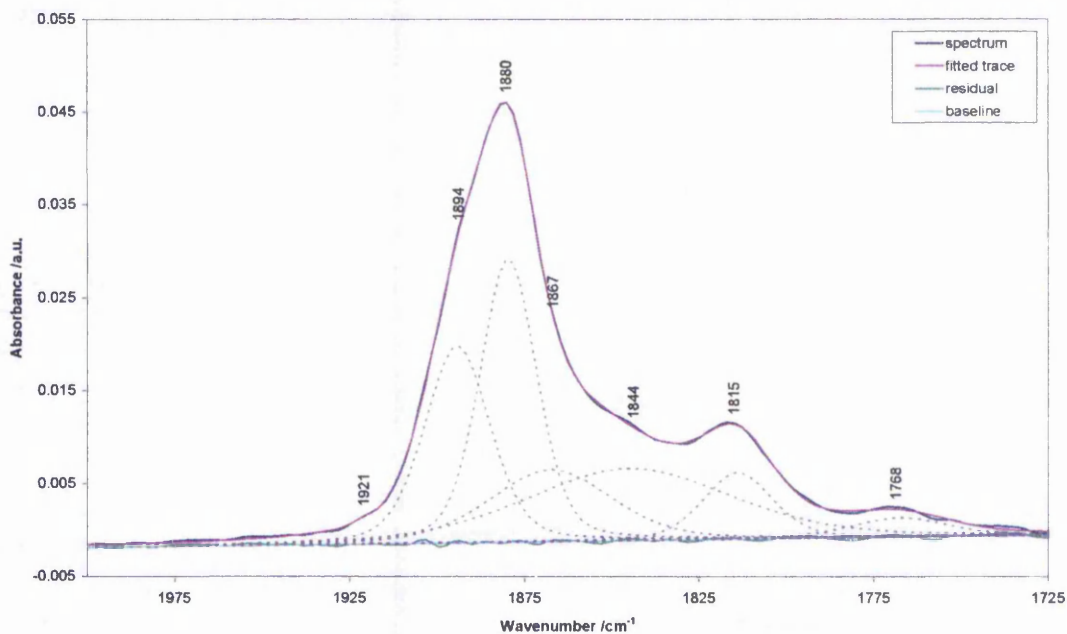
Figure VI-10: Typical peak-fitting result presented for the delta FTIR spectrum of NO adsorbed onto Fe-ZSM-5 at 10^{-2} mbar.

The evolution of the listed peaks areas as a function of the nitric oxide partial pressure, when NO was adsorbed onto Fe-ZSM-5 EX, is presented in figure VI-11.
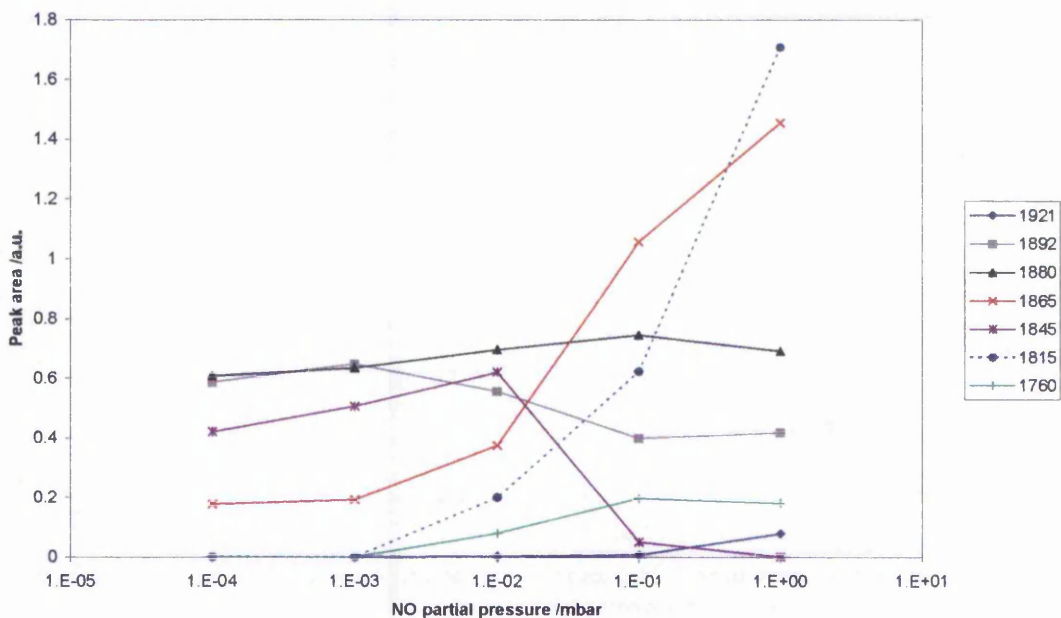
Figure VI-11: Intensity of the peaks fitted for the adsorption of NO onto Fe-ZSM-5 EX as a function of NO partial pressure.

The peaks centred at 1845 cm^{-1}, and 1921 and 1815 cm^{-1}, are easily attributed to respectively mono- and di-nitrosyl species adsorbed onto isolated iron sites. Both literature reports and the decrease of the peak at 1845 cm^{-1} accompanied by an increase of both peaks at 1921 and 1815 cm^{-1} confirm this analysis. The angle calculated between NO molecules in dinitrosyl species was 155 degrees. A highly distorted octahedral geometry is assumed, yet again the intensity of the 1921 cm^{-1} band may have been under-estimated due to its low intensity and a high background and correction level, therefore over-estimating the bond angle.

The band at around 1865 cm^{-1} was attributed to nitrosyl species adsorbed on larger iron oxide clusters, probably of hematite structure. Such clusters were detected on the powder x-ray diffractogram of Fe-ZSM-5 CVD (hem) (see chapter III, pp. 72). A plot of the area of the latter IR peak, normalised to wafer thickness and iron content, as a function of the partial pressure of NO is presented in figure VI-12.
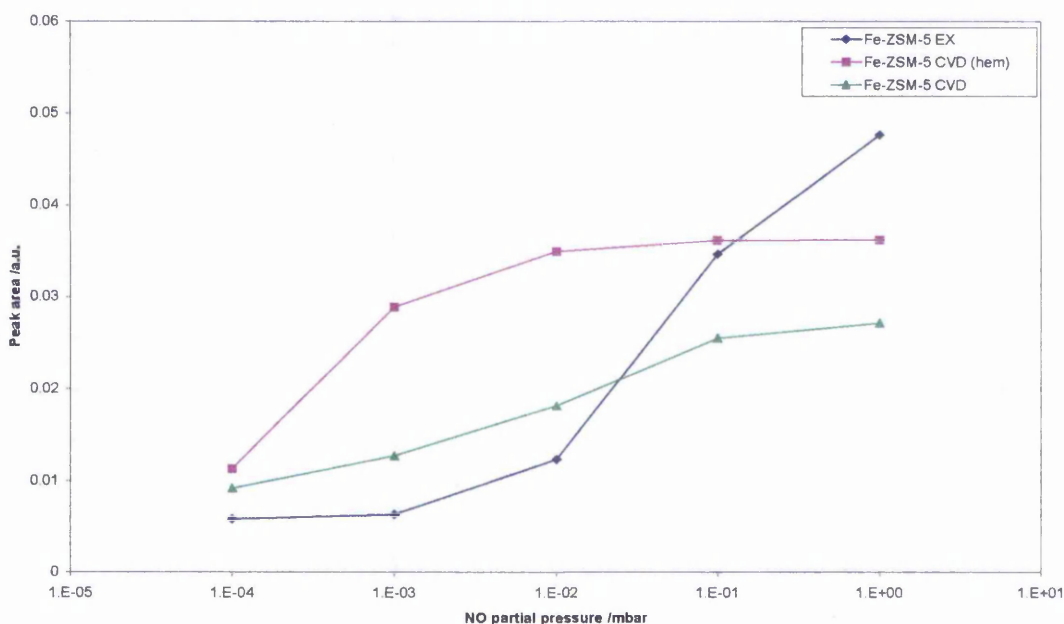
Figure VI-12: Comparison of the intensity of the band centred at 1865 cm^{-1} as a function of pressure for selected ion-exchanged Fe-ZSM-5s.

This reveals that Fe-ZSM-5 EX contains more large iron clusters than the samples prepared by CVD, relatively to other iron structures present in the samples. These were not detected in powder XRD due to the significantly lower iron concentration of the sample prepared by wet exchange. It can be noticed, however, that nitric oxide adsorbs onto iron clusters at lower pressure in Fe-ZSM-5 CVD (hem) than in other Fe-ZSM-5s.

This difference in rate of adsorption of NO was directly attributed to the higher concentration of iron in the sample. It was determined following atomic absorption experiments that the sample contained 4.06 wt.% of iron, calculated to correspond to 200% of the amount needed for full exchange of the protons in the framework (see chapter III, pp. 74). A significant amount of iron therefore has to be present at extra-framework positions, in the form of easily-accessible hematite-like clusters, believed to be formed in the material after migration of isolated iron atoms on the aluminosilicate surface upon calcination in the presence of water [24]. It is believed that in both other ion exchanged ZSM-5 samples nitric oxide is preferentially adsorbed onto less clustered iron sites, possibly located within the pore structure, therefore showing a different adsorption isotherm. Indeed the higher iron concentration in Fe-ZSM-5 CVD (hem) favours the formation of large clusters at random positions in and out of the zeolite's pore structure.
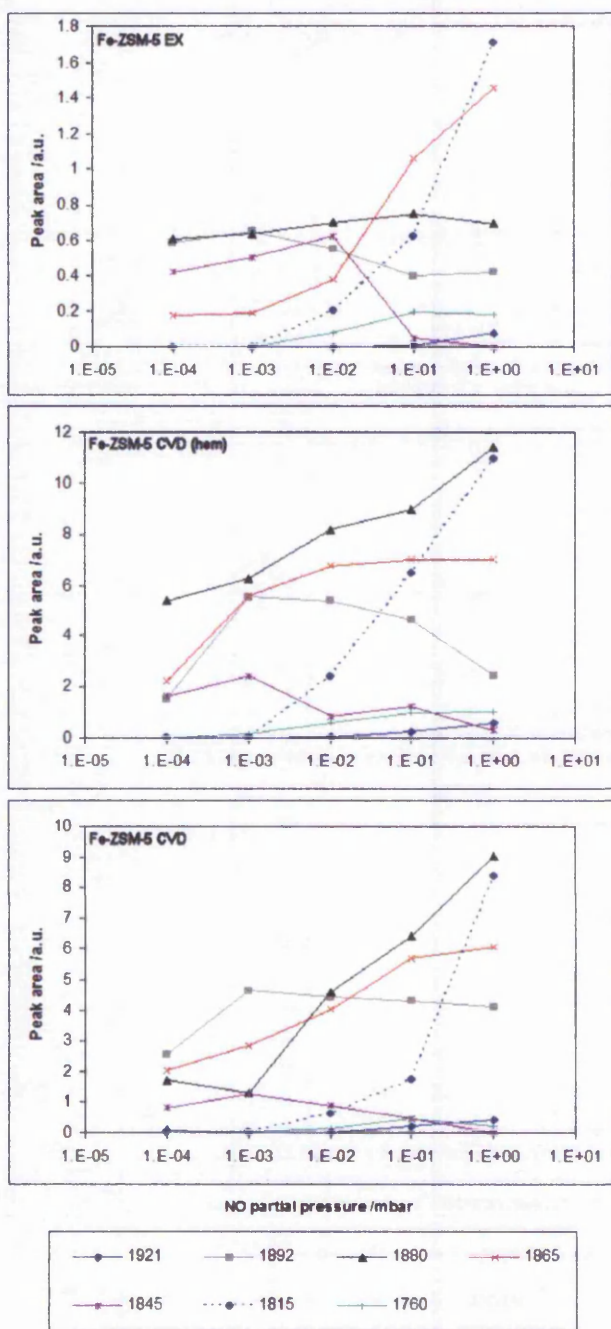
Figure VI-13: Intensity of the peaks fitted for the adsorption of NO onto selected ion-exchanged Fe-ZSM-5s as a function of NO partial pressure

Figure VI-13 illustrates the variation of all fitted infrared vibration bands in our three ion-exchanged ZSM-5s as a function of the partial pressure of nitric oxide. Out of all peaks three have not yet been attributed to specific iron-nitrosyl species, namely 1892, 1880 and 1760 cm^{-1}, the first of which had not been reported in the literature previously. A definite relationship between the intensity of this band centred at 1892 cm^{-1} and the one at 1760 cm^{-1} can however definitely be noticed, in the case of Fe-ZSM-5 EX. A good linear relationship could not be devised in the case of Fe-ZSM-5s prepared by CVD, even though a similar trend is observed. A correlation between the decrease in intensity of the 1892 cm^{-1} band and another band of the spectra could not be found, which excludes the hypothesis of a second nitric oxide molecule adsorbing onto the same site, in a similar way to the effect observed with isolated iron atoms. A consequent change in the electronic distribution of the Fe-NO bond giving rise to both

bands found at higher frequencies were attributed to NO adsorbed onto protonic sites and the ones found at lower frequencies to adsorbed NO_2.

An average shift of 10 cm^{-1} to lower frequencies was observed compared to exchanged ZSM-5 samples, which was directly attributed to the absence of aluminium in the vicinity of iron centres.
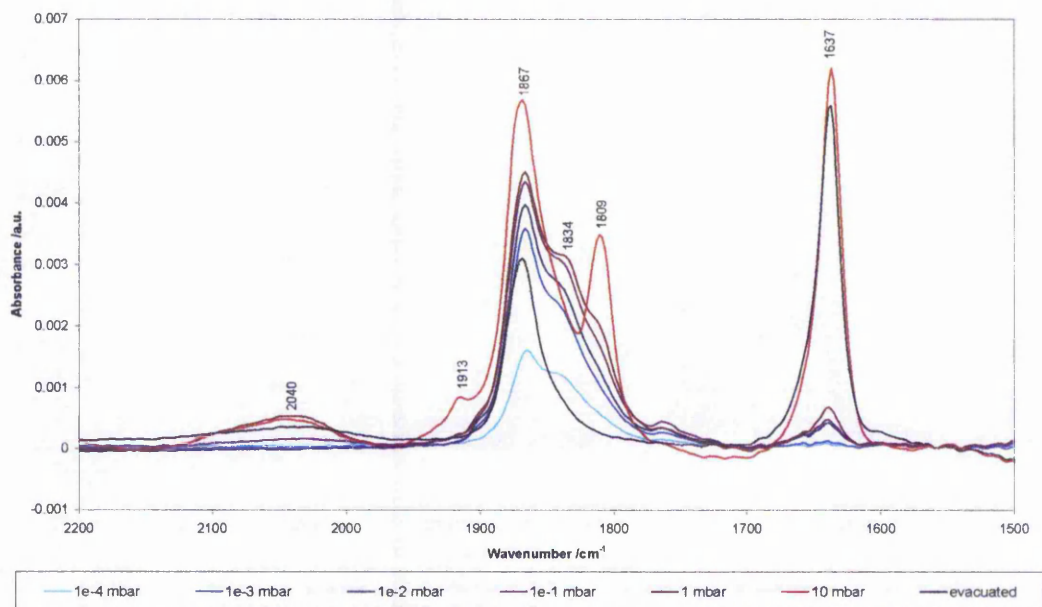
Figure VI-18: Delta FTIR spectra recorded for the adsorption of NO onto Fe-MFI SYN24 at various pressures.

The variation in intensity of the bands, together with their assignment discussed previously for Fe-ZSM-5s (see table VI-2), allowed the identification of nitrosyl vibrations observed here, despite their shift on the frequency scale.

The band at 1809 cm^{-1}, successively increasing then decreasing in intensity as the nitric oxide partial pressure increased was attributed to mononitrosyl species adsorbed onto isolated iron atoms in the zeolite framework, similarly to the 1845 cm^{-1} band observed in Fe-ZSM-5. This was accompanied by the appearance of two additional bands at high pressure, centred at 1913 and 1760 cm^{-1}, which were assigned to the symmetric and anti-symmetric vibrations of dinitrosyl species formed by the

adsorption of a second NO molecule onto the same isolated iron site. A good linear agreement between the decrease in intensity of the 1809 cm^{-1} band and the increase of both dinitrosyl bands confirmed this assignment. Moreover a good linear relationship was observed between the intensity of the two dinitrosyl bands (fig. VI-20). The ratio between these two bands allowed the calculation of an angle of 120 degrees between the two adsorbed nitrosyl species, consistently with expectations for a deformed octahedral geometry of iron.
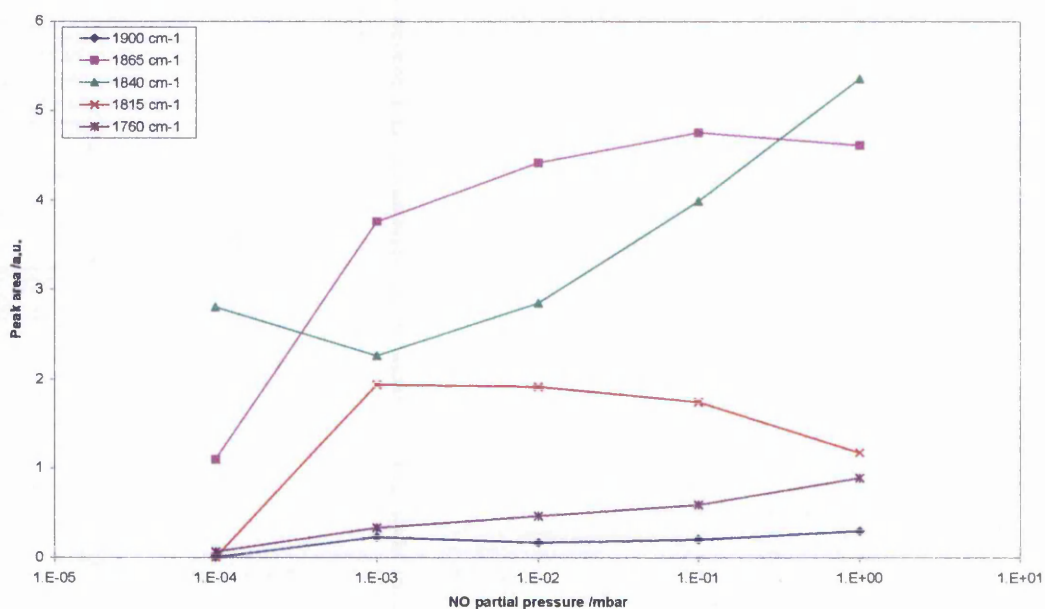
Figure VI-19: Area of the peaks fitted for the adsorption of NO onto Fe-MFI SYN24 as a function of NO partial pressure.

The band at 1840 cm^{-1} was attributed to nitrosyl species adsorbed onto iron clusters of hematite like structure. Such clusters were suspected to be present in the zeolite following TPR studies (see chapter IV, pp. 96). The shape of this adsorption isotherm is similar to the one observed in Fe-ZSM-5, i.e. significant amounts adsorb only at higher NO partial pressure, and are readily desorbed upon evacuation of the system (figs. VI-13 and VI-19).
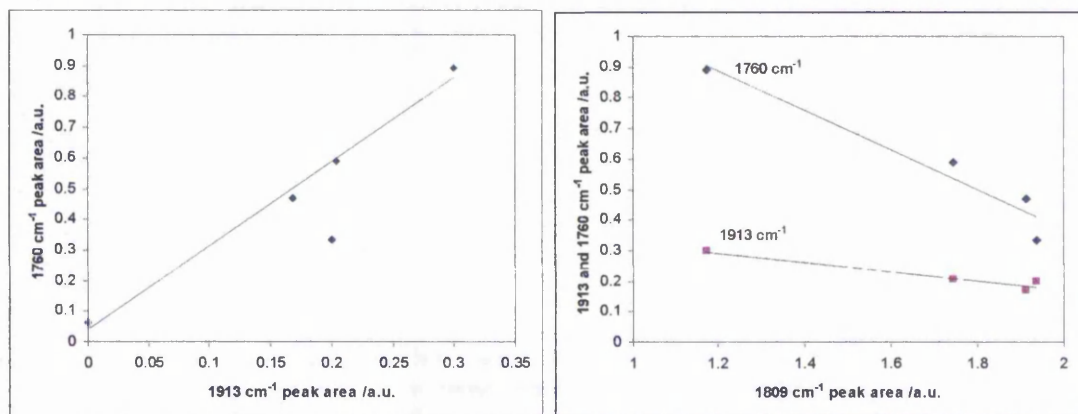
Figure VI-20: Correlation between bands assigned to mono- and dinitrosyl species adsorbed onto isolated iron sites in Fe-MFI SYN24. (left) 1760 cm^{-1} vs. 1913 cm^{-1}; (right) 1760 cm^{-1} and 1913 cm^{-1} vs. 1809 cm^{-1}.

Finally the band found at 1865 cm^{-1} was attributed to mononitrosyl species adsorbed onto small iron clusters, possibly of the same structure as the Fe$_4$O$_4$ nanoclusters reported in Fe-ZSM-5s. Evidence of such clusters in aluminium free MFI zeolites has not been reported in the literature, however it is believed that iron oligomers are stabilised by a structural feature of the MFI framework. It is therefore possible that such clusters occur in aluminium free MFIs. It is also possible that this band corresponds to NO adsorbed onto iron dimers at the same type as reported by Panov *et.al.*, often referred to as *alpha* sites [2, 4, 5].

The latter sites, oligomers or dimers, are the most abundant in the prepared Fe-MFI, and only a minor amount of isolated sites seem present, assuming similar extinction coefficients for NO adsorbed on different iron structures. This is in agreement with data reported in the literature [26]. Some clustering of iron occurred in Fe-MFI SYN24, as observed by means of NO adsorption and TPR (see chapter IV, pp. 96). The prepared Fe-MFIs with higher Fe/Si ratio are expected to have a similar iron structure distribution, as their reduction patterns were similar.

The assignment of nitrosyl vibration bands is summarised in the following table, together with a comparison of the corresponding vibrations observed in Fe-ZSM-5s.

Table VI-3: Assignment of nitrosyl bands observed in the delta FTIR spectra of NO adsorbed onto Fe-MFI SYN24 and comparison to their vibration frequency in Fe-ZSM-5s.

Frequency / cm^{-1}	Assignment	Corresponding frequency in Fe-ZSM-5 EX / cm^{-1}
2040	Cat-NO$^+$	2133
1913	Fe(NO)$_2$	1920
1867	Fe$_4$O$_4$(NO)	1892
1834	(FeO)$_x$(NO)	1865
1809	Fe(NO)	1845
1760	Fe(NO)$_2$	1815

Following the adsorption of nitric oxide onto MFI type materials it is important to notice their relative activity towards the oxidation of the probe gas to nitrogen dioxide NO$_2$. It is thought that NO reacts with some active framework oxygen species, which could relate to the active species in the oxidation of hydrocarbons. The formulation of an exact mechanism of oxidation of NO is beyond the scope of this thesis. It will however be considered that the sites responsible for this oxidation could be identical to the ones responsible for hydrocarbon oxidation.

Of all materials studied here the aluminium free Fe-MFI showed the most interesting behaviour, with a single adsorbed NO$_2$ vibration peak (fig. VI-21). This peak was also more intense than the ones found in most Fe-ZSM-5s, which could indicate that the species responsible for oxidation is predominant in Fe-MFI. The alpha sites reported by Panov *et.al.* [5] could be considered as good candidates for the role of active site. However, the evacuated delta spectrum of Fe-ZSM-5 (hem) reveals a very intense

adsorbed NO_2 band, which would indicate a possible role of hematite clusters in oxidation activity.
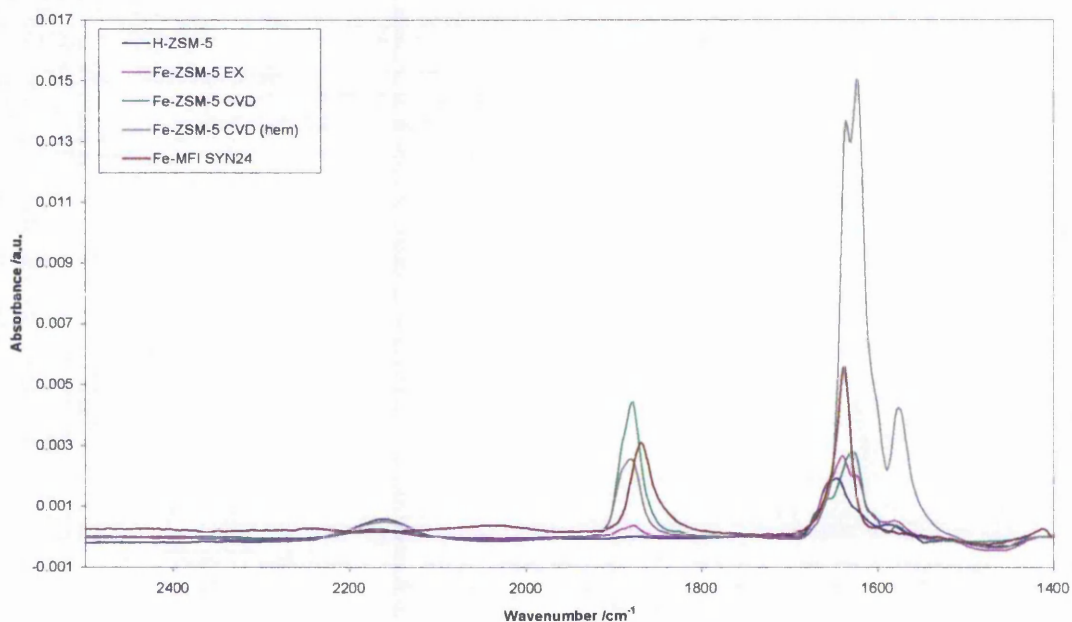
Figure VI-21: FTIR delta spectra recorded for the adsorption of NO onto selected MFI type zeolites after exposure to 10 mbar of probe gas and evacuation to base pressure for 10 minutes.

This brief discussion of the oxidative activity of the materials is only preliminary and, will be considered in the following chapter. An in-depth consideration of structure / activity relationships in the prepared materials will be discussed in the context of their testing for the oxidation of ethane.

VI-4 Summary

A study of the nature of iron species in the prepared materials has been performed, using the adsorption of nitric oxide with *in-situ* FTIR detection. As suggested by previous literature reports, the vibration of M-NO complexes varies with the local environment of the metal, by population or de-population of bonding and anti-bonding molecular orbitals of the complex formed. Some degree of disagreement was

found in reports, concerning the assignment of vibration bands to NO adsorbed onto specific iron structures. Based upon these reports, previously formulated hypotheses, and the knowledge acquired from this series of experiments a revised assignment of bands was formulated, which is outlined in tables throughout this chapter. The main changes concerned a more defined assignment of NO adsorbed onto hematite-like clusters in the zeolite, and the assignment of the 1880 cm^{-1} vibration band to a weakly adsorbed NO multilayer at cationic sites. All the prepared materials could unfortunately not be studied by adsorption of NO to date, however a good insight of the structure of iron was obtained for most. Unsupported iron phosphates showed different behaviours towards NO, depending on their preparation method. The concentration of adsorbing sites was very low, but of apparent regular structure, as indicated by a single recorded vibration band. Iron was found in MCM-41 as mainly isolated species, with a little fraction of dimers, accordingly to existing literature. Some NO was adsorbed onto Al-MCM-41, indicating the presence of aluminium as octahedral species, which showed some oxidative activity. The Fe-Al-MCM-41 prepared contained a mixture of both sites found in Fe-MCM-41 and Al-MCM-41, together with isolated iron ions at ion-exchange positions. Materials of MFI structure showed a more complex distribution of species. Respectively isolated, oligomers and hematite-like clusters were found in different ratios, depending on the preparation method used. It appears that chemical vapour deposition favours the formation of isolated species, where aqueous ion exchange favours the formation of iron oligomers. The aluminium free Fe-MFI seemed to contain mostly iron oligomers or dimers, identified as *alpha* sites, together with some larger hematite-like clusters. A fraction of isolated iron sites were found in all the prepared materials. The oxidative activity of the materials towards the NO to NO_2 reaction seemed favoured by the presence of

larger hematite-like clusters in the zeolites, which could be of interest when the partial

oxidation of ethane is considered in the next chapter.

VI-5 References

1.   Zhu, Q., et al., *Effect of high-temperature treatment on Fe/ZSM-5 prepared by chemical vapor deposition of FeCl3II. Nitrous oxide decomposition, selective oxidation of benzene to phenol, and selective reduction of nitric oxide by isobutane.* Journal of Catalysis, 2004. **221**(2): p. 575-583.

2.   Perez-Ramirez, J., M.S. Kumar, and A. Bruckner, *Reduction of N_2O with CO over FeMFI zeolites: influence of the preparation method on the iron species and catalytic behavior.* Journal of Catalysis, 2004. **223**(1): p. 13-27.

3.   Perez-Ramirez, J., *Active iron sites associated with the reaction mechanism of N2O conversions over steam-activated FeMFI zeolites.* Journal of Catalysis, 2004. **227**(2): p. 512-522.

4.   Starokon, E.V., et al., *Mechanisms of iron activation on Fe-containing zeolites and the charge of alpha-oxygen.* Topics in Catalysis, 2003. **23**(1-4): p. 137-143.

5.   Dubkov, K.A., et al., *Evolution of iron states and formation of alpha-sites upon activation of FeZSM-5 zeolites.* Journal of Catalysis, 2002. **207**(2): p. 341-352.

6.   El-Malki, E.M., R.A. van Santen, and W.M.H. Sachtler, *Active sites in Fe/MFI catalysts for NOx reduction and oscillating N_2O decomposition.* Journal of Catalysis, 2000. **196**(2): p. 212-223.

7.   Bordiga, S., et al., *Structure and reactivity of framework and extraframework iron in Fe-silicalite as investigated by spectroscopic and physicochemical methods.* Journal of Catalysis, 1996. **158**(2): p. 486-501.

8.   Jermyn, J.W., et al., *Iron-nitrosyl complexes formed in zeolites.* Journal of Physical Chemistry, 1973. **77**(25): p. 2964-9.

9.   Banwell, C.N. and E.M.C.N.B.a.E.M.M. McCash, *Fundamentals of molecular spectroscopy.* 4th ed. 1994, London: McGraw-Hill. xii,308p.

10.   Bochmann, M., *Organometallics 2: Complexes with Transition Metal-Carbon Pi-bonds.* 1994. 96 pp.

11.   Nakamoto, K., *Infrared and Raman Spectra of Inorganic and Coordination Compounds.* 4th ed. 1986: Wiley-Interscience.

12.   Mul, G., et al., *NO adsorption on ex-framework Fe,X MFI catalysts: novel IR bands and evaluation of assignments.* Catalysis Letters, 2002. **80**(3-4): p. 129-138.

13.   Hadjiivanov, K., et al., *FT-IR study of NO+O-2 co-adsorption on H-ZSM-5: re-assignment of the 2133 cm(-1) band to NO+ species.* Catalysis Letters, 1998. **52**(1-2): p. 103-108.

14.   Segawa, K., et al., *Infrared and Mossbauer Spectroscopic Studies of the Interaction of Nitric-Oxide with Fe-Y Zeolite.* Journal of Catalysis, 1982. **76**(1): p. 112-132.

15.   Lobree, L.J., et al., *Investigations of the State of Fe in H-ZSM-5.* Journal of Catalysis, 1999. **186**(2): p. 242-253.

16. Lezcano, M., V.I. Kovalchuk, and J.L. d'Itri, *FTIR study of the interaction of nitric oxide with Fe-ZSM-5(1).* Kinetics and Catalysis, 2001. **42**(1): p. 104-111.

17. Spoto, G., et al., *FTIR and UV-Vis characterization of Fe-silicalite.* Journal of Molecular Catalysis a-Chemical, 2000. **158**(1): p. 107-114.

18. Joyner, R. and M. Stockenhuber, *Preparation, Characterization, and Performance of Fe-ZSM-5 Catalysts.* Journal of Physical Chemistry B, 1999. **103**(29): p. 5963-5976.

19. Glazneva, G.V., et al., *IR spectra of nitric oxide and nitric oxide + carbon monoxide mixtures adsorbed on iron(III) oxide.* Reaction Kinetics and Catalysis Letters, 1978. **9**(2): p. 131-6.

20. Grubert, G., et al., *The room temperature, stoichiometric conversion of N2O to adsorbed NO by Fe-MCM-41 and Fe-ZSM-5.* Journal of Catalysis, 2000. **196**(1): p. 126-133.

21. Sanchez, M., et al., *Model size effects on calculated electronic and bonding properties of adsorption sites in zeolites.* Ciencia (Maracaibo, Venezuela), 2005. **13**(1): p. 94-102.

22. Woerz, A.S., et al., *Cluster Size-Dependent Mechanisms of the CO + NO Reaction on Small Pdn (n < 30) Clusters on Oxide Surfaces.* Journal of the American Chemical Society, 2003. **125**(26): p. 7964-7970.

23. Cotton, F.A. and G. Wilkinson, *Advanced Inorganic Chemistry.* 5th ed. ed. 1988: John Wiley & Sons.

24. Berlier, G., et al., *Evolution of Extraframework Iron Species in Fe Silicalite.* Journal of Catalysis, 2002. **208**(1): p. 64-82.

25. Raptis, R.G., I.P. Georgakaki, and D.C.R. Hockless, *A FeIII/oxo cubane contained in an octanuclear complex of T symmetry that is stable over five oxidation states.* Angewandte Chemie, International Edition, 1999. **38**(11): p. 1632-1634.

26. Handreck, G.P. and T.D. Smith, *A physicochemical study of iron(III)-containing MFI zeolitic materials: the iron(III) isomorph of zeolite ZSM-5.* Journal of the Chemical Society, Faraday Transactions 1: Physical Chemistry in Condensed Phases, 1989. **85**(10): p. 3195-214.

Chapter VII: <u>Oxidation studies</u>

VII-1   Introduction

The final step of the characterisation of the materials prepared in this study was their testing for the partial oxidation of ethane. This was performed in a microreactor equipped with on line gas chromatographic detection. Firstly materials previously reported to show some catalytic activity towards the partial oxidation of ethane were tested and the reproducibility of the methods are discussed here. The development of the catalytic system involved the search for more active or more selective catalysts, which involved the supporting of the iron phosphate, the proposed active site, onto ZSM-5 and MCM-41 supports. The results of this study, together with a comparison with iron-only containing ZSM-5 and MCM-41 are also discussed.

Following this development step more structural and mechanistic concerns are discussed, such as the effect of acidity, the structure of iron and activation conditions on the activity of catalysts. Some conclusions as to the identity of the active site for the partial oxidation of ethane to ethanol are proposed, which relate to the discussions presented earlier in this thesis and current state of knowledge. It is not attempted to formulate elaborate mechanisms which could be taking place in the reaction, but different possibilities are discussed and evaluated, by comparison of the catalytic behaviour of different materials characterised during this project.

VII-2 Background and Method

VII-2.1 Gas Chromatography

Gas chromatography consists in the separation of chemical species in the gas phase through interactions with a stationary phase. This is where its main constraint relies, as analytes have to be stable enough to be vaporised in an injector without decomposition [1]. It is otherwise a very precise and quantitative method of analysis. A schematic of a typical gas chromatograph setup is presented in figure VII-1.
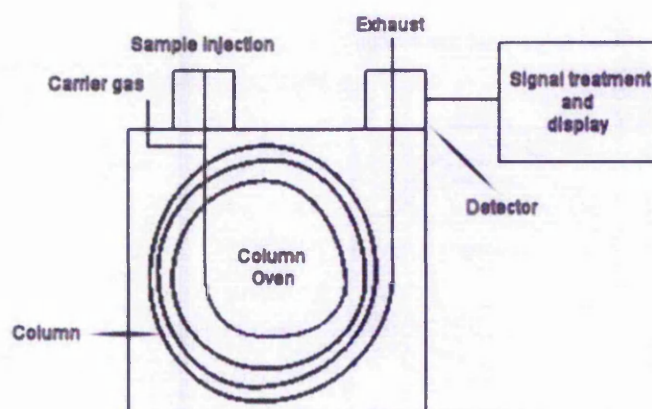
Figure VII-1: Schematic diagram of a general gas chromatographer setup

The sample to be analysed is vaporised in the injector, the volume injected being measured precisely in the sample loop. Analytes are then carried along the stationary phase in an inert carrier gas, being retained and therefore separated through polar or size (sieving) interactions. At the outlet of the column individual components can be detected using various types of detectors, where electrical output signals are transferred to a computer and plotted against time for analysis [2].

Apart from the properties of the stationary phase, the two main factors influencing separation are the carrier gas flow rate and column temperature. Variation of one or

both these parameters alters retention times and peak shapes by affecting the partition coefficient (equation VII-1) and the dispersion of analytes on the column. This latter effect is described in the Van Deemter equation (equation VII-2) [3].

Equation VII-1: Partition coefficient equation

$$Partition\ coefficient\ K = \frac{\lfloor Analytes\ in\ the\ mobile\ phase \rfloor}{\lfloor Analytes\ in\ the\ stationary\ phase \rfloor}$$

Equation VII-2: Van Deemter equation

$$H = H_p + H_d + H_m$$

$$H = 2\lambda d_p + 2\frac{\gamma D_m}{v} + \frac{\omega d_p^2}{D_m}v$$

The distribution constant is given for a particular compound, at a set temperature with a certain mobile and stationary phase. It is expressed as a function of a constant k, dependant on temperature, and phase ratio β, depending on the column's properties.

The three components of the Van Deemter equation represent the possible diffusion modes occurring in the mobile phase and responsible for broadening of chromatographic peaks. Eddy diffusion, molecular diffusion and mass transfer are respectively due to heterogeneity of column packings, dispersion of analyte molecules in the mobile phase, and the lack of adsorption equilibrium between the mobile and stationary phase [4].

Figure VII-2 illustrates how the three terms of the van Deemter equation vary as a function of the average linear velocity of the carrier gas. From this it arises that the gas flow rate has to be optimised to minimise peak broadening.
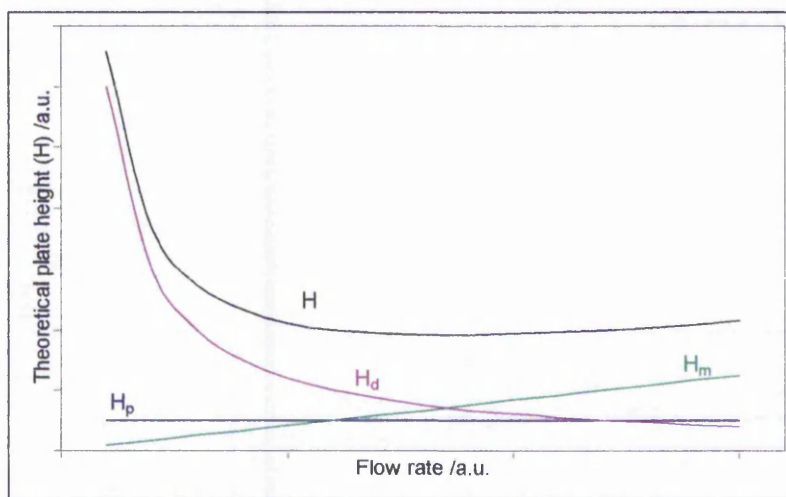
Figure VII-2: Plot of the three components of the Van Deemter equation versus carrier gas linear velocity

Even though being most important, carrier gas flow rate and column temperature are not the only factors affecting the quality of chromatographic data. The volume injected, type of injector, and detection parameters also have some weight in the balance. The volume injected should be large enough to allow detection of trace analytes, yet small enough to avoid "dragging" of peaks, again due to diffusion and saturation of adsorption sites [5].

The type of injector is mostly dependent on the type of column used. In the case of packed columns it is common to use direct vaporisation injection, where the sample is vaporised in a glass insert, in carrier flow, directly linked to the column. When capillary columns are used even tiny amounts of sample can saturate the column, and so called split/splitless injectors are used. The sample is vaporised within a glass insert connected with the column, as for packed columns, but these injectors offer the possibility to split the carrier gas flow. Most of the sample is carried directly to a vent, and the smallest part enters the column [6].
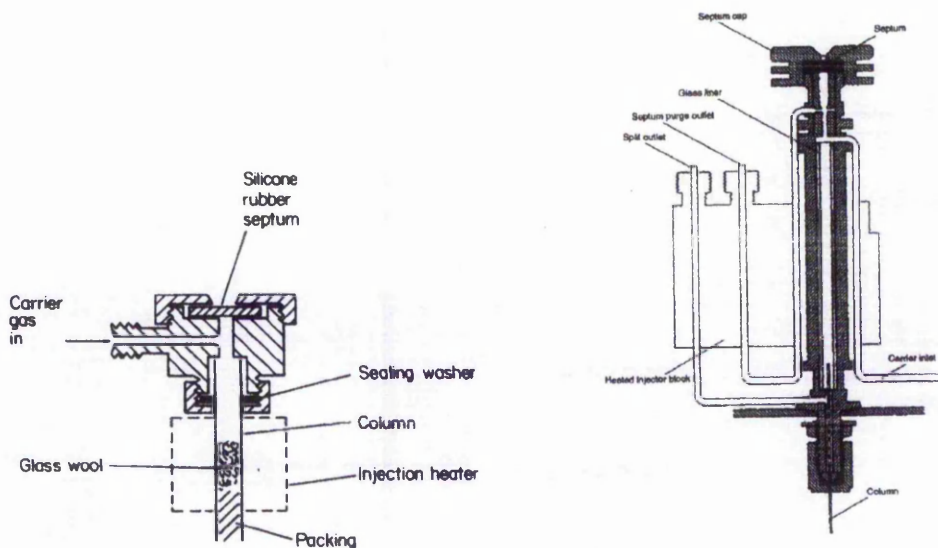
Figure VII-3: Schematic diagram of the direct injection and split/splitless injector used in gas chromatography [4]

Various detector types can be used in gas chromatography. These include thermal conductivity (TCD), flame ionisation (FID), electron capture (ECD), flame photometric (FPD), photo-ionisation (PID), mass spectrometry (GC-MS). The choice of detector is mostly dictated by the nature of the substrates analysed, as most detector types respond to certain compounds selectively or specifically. A TCD is an example of "universal" detector, and FID is selective to most organic compounds [7]. These two types of detectors were used during this project and only their principles will be discussed here.

Thermal conductivity detection relies, as suggested by its name, on the variation of thermal conductivity between mixtures of components. The sample gas is flown over a filament enclosed in a brass heat sink. As the thermal conductivity of the gas mixture changes, the rate of heat loss of the filament changes. The temperature difference of the filament is used to create an electric potential, through imbalance with a parallel reference cell connected to the opposite arms of a Wheatstone bridge (fig. VII-4).
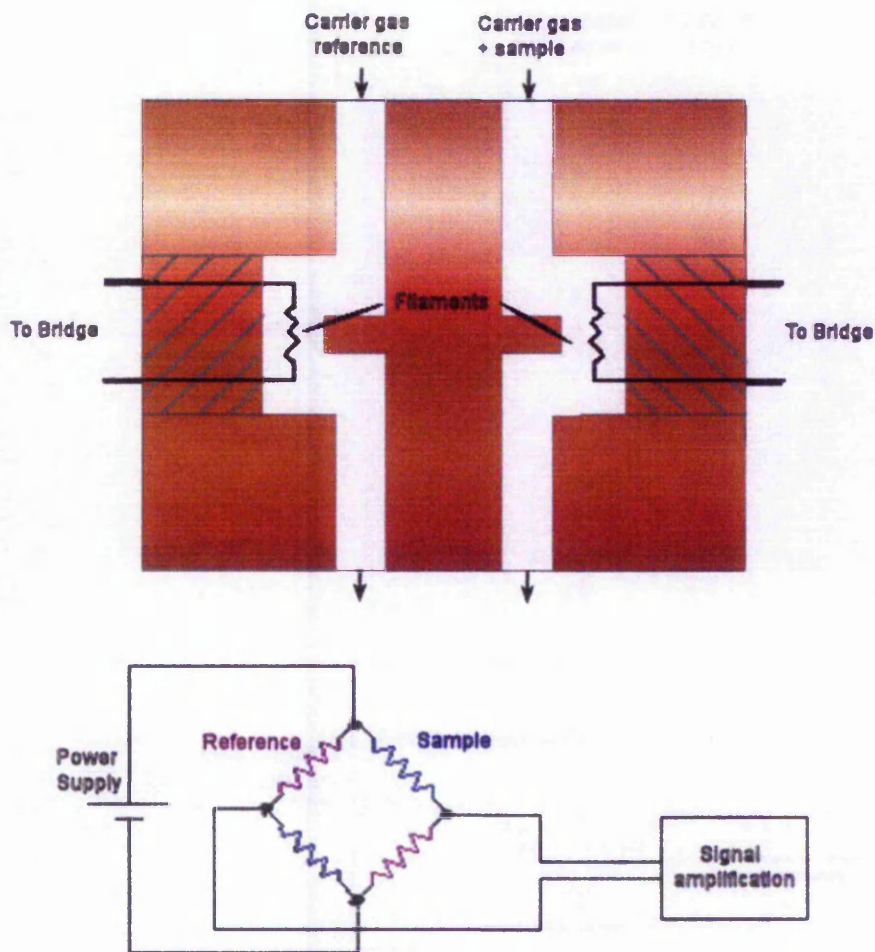
Figure VII-4: Schematic diagram of (top) a thermal conductivity detector cell and (bottom) a Wheatstone bridge

Flame ionisation detectors are used for the quantification of oxidisable hydrocarbons.

Free ions and electrons are formed during the burning of these hydrocarbons in a hydrogen and air flame, which are collected using an electrostatic field, to be converted to a current. The response of the detector is dependent on the number of carbon atoms ionised, making it more sensitive to higher hydrocarbons. Their main disadvantage is their lack of sensitivity towards partially oxidised analytes such as carbonyl- or multi-hydroxyl- substituted hydrocarbons. This is however counter-

balanced by their low detection limit, around 5 ng ml^{-1}. A possible FID design is presented in figure VII-5.
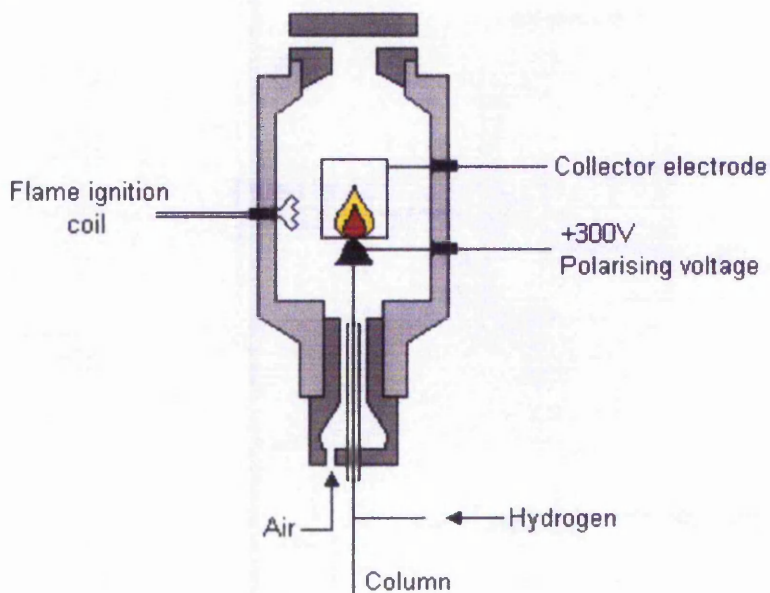
Figure VII-5: Schematic diagram of a flame ionisation detector

VII-2.2 Catalysis – Partial oxidation of ethane

Catalytic testing of the prepared materials was performed in a purpose-built reactor, with online gas chromatographic analysis (fig. VII-6).
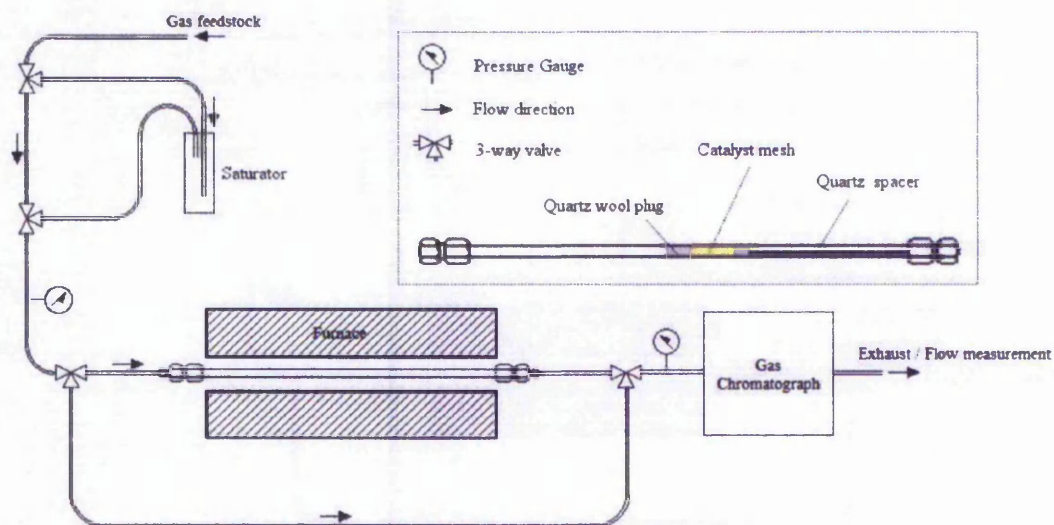
Figure VII-6: Schematic of the reactor used for catalytic testing.

The sample was pressed into a wafer under 2 tons cm^{-2} pressure, and ground to pellets which were then sieved, to keep the fraction of size $250 - 425$ µm. Typically 100 mg of these pellets were introduced into a ¼ in. O.D. quartz tube and kept in place using quartz wool plugs. A quartz rod in the tube, on the outlet side, aided quick removal of the products from the heated zone of the reactor. A thermocouple was taped on the outside of the glass tube, its tip as close as possible to the reactor bed, for more accurate temperature measurement. The tube was then introduced into a tubular furnace and fixed into position using poly(tetrafluoroethylene) (PTFE) and stainless steel compression fittings.

Gas flows were set using mass flow controllers, and measured at the system's exhaust using a bubble meter. A stainless steel saturator could be placed in-flow, when reagents liquid at room temperature were to be used. The reactor/furnace could be bypassed for calibration purposes.

The reacted mixture was analysed using an online Varian 3400 gas chromatograph equipped with a Porapak® QX column and flame ionisation detector (FID), for hydrocarbon analysis, and a CTR I double-packed column (fig. VII-7) connected to a thermal conductivity detector (TCD) for permanent gases analysis.
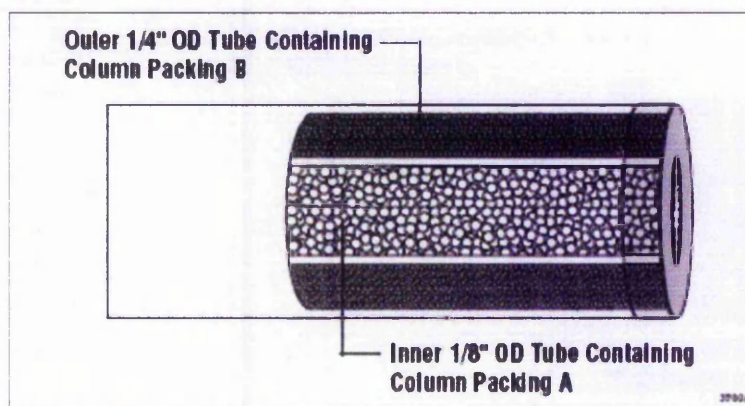
Figure VII-7: CTR I packed column, used for permanent gases separation [8]

The behaviour in the gas chromatograph of individual reagents and a range of expected products was calibrated, using helium as carrier gas.

As the feedstock used for this study consisted in a mixture of flammable and oxidising materials at high temperature, it was essential to consider the risk of explosion during the reactions. As for all explosive materials, a deflagration risk exists only when the oxidising and reducing agents are present in certain concentrations. Upper and lower concentration limits are known for explosive materials, usually defined as their concentration in air. These limits are less known when the oxidising agent is other than oxygen, however the defined limits can be taken as a guideline. These limits are termed L.E.L and U.E.L., respectively standing for lower and upper explosive limit. The explosive materials used in this study were ethane and hydrogen, and their explosive limits are summarised in the following table [9]:

Table VII-1: Lower and Upper Explosive Limits for ethane and hydrogen in air

Material	L.E.L. $/\%_{vol}$	U.E.L. $/\%_{vol}$
Ethane	2.9	13
Hydrogen	4	74.2

In all reactor studies performed the concentrations of gases were carefully chosen to avoid falling within these limits. Possible ways to avoid this include working at concentrations below L.E.L. or above H.E.L., or reducing the concentration of the oxidiser. Specific feedstock mixtures used are presented in following sections (see pp. 178 and 182).

VII-3   Results and discussion

VII-3.1 Study of iron phosphate and related materials

VII-3.1.1   Unsupported iron phosphates

Activity studies started with attempts to reproduce some work published by Wang and Otsuka [10, 11]. They reported the possibility of partially oxidising methane and ethane over iron phosphate catalysts, using either oxygen or nitrous oxide as oxidising agent. Their account cited ethanol and acetaldehyde as products of reaction, together with ethene and carbon dioxide. The selectivity to the different products depended on the oxidising system used.

Our first attempt to reproduce this work consisted in co-feeding ethane and oxygen, diluted with helium, with a feed volumetric composition of 2% ethane, 2% O_2 and 96 % He at a gas hourly space velocity (GHSV) of 25,000 h^{-1}. 100 mg of $FePO_4$ were pelletted to a 250-425 mm mesh and pre-oxidised in 15% O_2 diluted with helium at 773 K for 1 h. A 5 K min^{-1} heating gradient was used when ramping up the temperature. There was no detectable conversion of ethane or oxygen using this reaction mixture in the range from room temperature to 923 K.

A further attempt to reproduce this work was made by adding hydrogen to the reacting feed. This was reported to increase the conversion of ethane and also the selectivities to partial oxygenates [12]. It was decided to admit reacting gases in concentrations above their higher explosive limit (HEL), in an attempt to favour the detection of minor reaction products. The same co-precipitated $FePO_4$ was used, and prepared in the same conditions as before. The reacting feed composition in this case was 50% H_2, 8% O_2, 30% ethane in helium. Yet again no conversion of ethane to

oxygenates was observed at temperatures ranging from 293 to 823 K. Ethene was obtained as the main reaction product, detected from temperatures as low as 673 K and its yield increasing with temperature, with a maximum of 0.3% at 773 K (fig. VII-8).
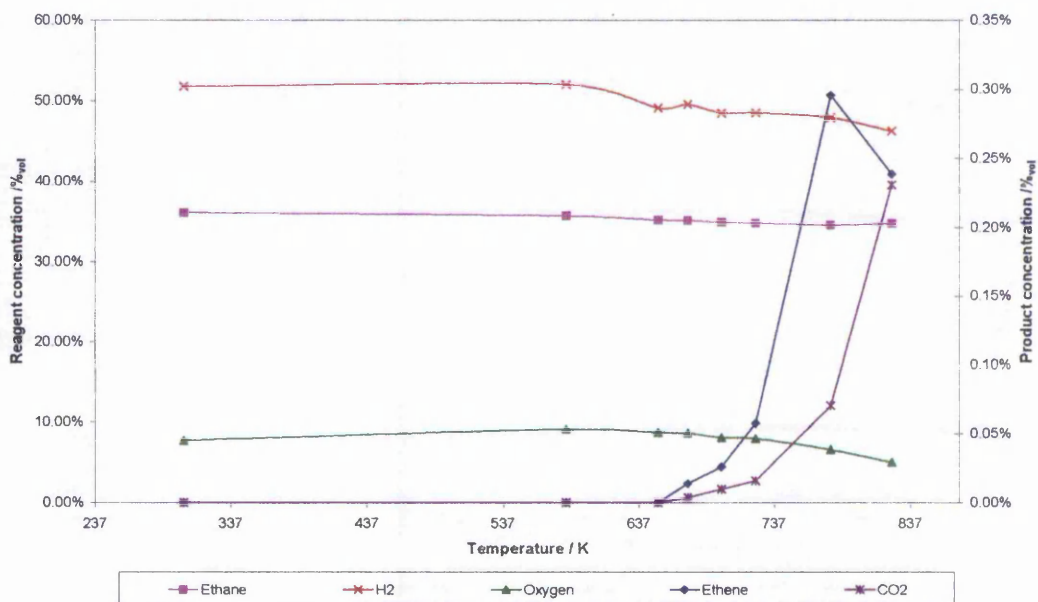
Figure VII-8: Reagent and product concentration measured at the reactor's outlet versus reaction temperature for the conversion of ethane with oxygen, with hydrogen co-fed over FePO₄.

It is believed that ethene was formed following an oxidative dehydrogenation catalytic pathway at lower temperatures, which was then competing with the gas phase homogeneous dehydrogenation of ethane above 723 – 748 K [13]. The addition of hydrogen to the reacting feed seemed efficient in limiting the amount of total oxidation product carbon dioxide, produced in a maximum yield of 0.23 % at 823 K.

These results do not agree with those reported by Wang and Otsuka [11], which was assumed to be due to different physical properties of our catalyst. Indeed, little detail about the preparation and structure of their catalyst was provided, however in another study McCormick reported activity of a quartz-like iron phosphate in the partial oxidation of methane [14].

Our attempts to produce an iron phosphate material with quartz-like crystal structure were unsuccessful, as outlined in chapter IV (see pp. 82), however one material was found to have some degree of crystallinity at high temperature, and some possible oxidative activity, namely $FePO_4$ pH6. This material was tested in our microreactor, using the same pre-treatment and reaction conditions as stated for a reaction feed containing hydrogen (see pp. 183). The results were similar in every point.

When nitrous oxide was used as oxidising agent with the latter catalyst, however, the conversion of ethane was significantly increased. A reacting feedstock of 20% ethane, 20% N_2O diluted with helium to reach a GHSV of 20,000 h^{-1} was flowed over 100 mg of pelleted $FePO_4$, pH6 at increasing temperature. The same activation conditions as used before in this study were used. The temperature was ramped up using a 5 K min^{-1} gradient and the system was left to equilibrate for typically 15 minutes prior to injection. Ethane conversion found a maximum of 27% at 773 K (fig. VII-9).
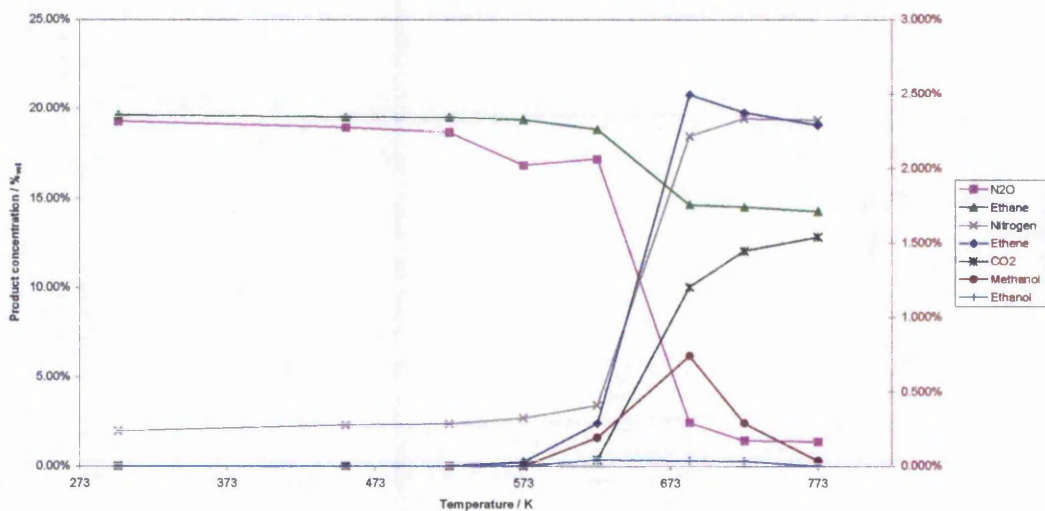

Figure VII-9: Reagent and product concentration measured at the reactor's outlet versus reaction temperature for the conversion of ethane with nitrous oxide over $FePO_4$, pH6.

The products detected were mainly ethene, carbon dioxide and nitrogen, but some selectivity to oxygenates was observed at temperatures in the range 573 – 823 K. The detected oxygenates were identified as methanol and ethanol.

The highest selectivity to ethanol was observed at 623 K, reaching 8% selectivity with 4% conversion of ethane. The conversions and selectivities here were in better agreement with the data reported [10], however we observed a higher amount of total oxidation products. Methanol was detected as a reaction product with 34% selectivity at 623 K. The selectivity to ethene was constant above 623 K at around 50%.

The initial part of this study confirmed that nitrous oxide would be a milder and more successful partial oxidant than oxygen. When the latter was used, even with hydrogen co-fed, only oxidative dehydrogenation and total oxidation was achieved, in yields much lower than reported in the literature [11, 12]. Despite this the oxygen-hydrogen system was studied further with the supported iron phosphates. The feasibility of performing the reaction with reasonable selectivity was confirmed when nitrous oxide was used as oxidiser, however the presence of methanol as a product was surprising. It is assumed here that ethane adsorbed on some iron site could undergo cleavage of the C-C bond, following a mechanism similar to the one suggested by Kulikova *et.al.* (equation VII-3) [15].

Equation VII-3: C-C bond cleavage mechanism proposed by Kulikova *et.al.* [15]

$$L_nMO \xrightarrow{\text{CH}_3\text{R}} L_nMO \cdots \overset{\overset{\displaystyle H \quad R}{\diagdown \diagup}}{\underset{\underset{\displaystyle H \quad H}{\diagup \diagdown}}{C}} \longrightarrow L_nM-OMe \ + \ R\cdot$$
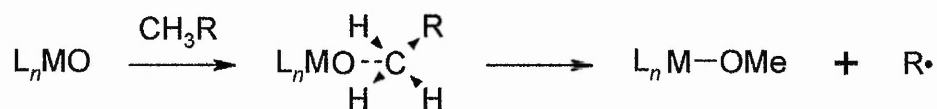
Two methyl groups are produced from ethane, one adsorbed onto oxygen neighbouring the metal could readily react further to form methanol. The other methyl group produced was suggested by the authors to be a radical, however the product

distribution in our case doesn't support this hypothesis. It is suggested here that the cleaved methyl group can readily react with framework oxygen or the surrounding nitrous oxide gas, to form an oxygenate which would follow the normal possible sequence of reactions leading to total oxidation products.

VII-3.1.2   Supported iron phosphates

The conversions observed when unsupported iron phosphates were tested for the partial oxidation of ethane were low. It was thought that this lack of activity could be overcome by increasing the amount of active sites in the catalyst. An easy way to increase this number is to increase the exposed surface area of the material. This can be done in two ways, the first of which is creating a porous structure in the material, e.g. by developing a templated synthetic route. Such a strategy was attempted, however it was unsuccessful and is not reported in this thesis. The second strategy consisted in supporting the active phase onto a material with a defined porous structure. Ideally the support should have a well-defined structure and be inert to the studied reaction. The two supports used were the silicates of MFI and MCM-41 structure. The synthesis and characterisation of the prepared supported iron phosphates were discussed alongside other materials in chapters II to VI.

The catalysts discussed in this section were tested using the following conditions. A mixture of 30% ethane, 50% H_2, 8% O_2, diluted in helium was flown over a fixed bed of 100 mg of pelleted catalyst with a GHSV of 25,000 h^{-1}. The reactions were carried out in a temperature-programmed way, with one sample taken at room temperature, then between 573 and 823 K typically. These conditions were chosen accordingly to the results obtained with unsupported iron phosphates as catalysts, showing that the co-feed of hydrogen in the reaction feedstock effectively diminished the amount of

total oxidation products and favoured the formation of partially oxidised hydrocarbons (see section VII-3.1.1). Oxygen was used as the main oxidising agent, despite the more encouraging results observed with nitrous oxide, due to its position as ideal oxidising agent, cheap, readily available and safe to use. The catalysts were pre-treated in a 60 mL min^{-1} flow of 15 % oxygen in helium at 773 K for 60 minutes. The heating gradient used for activation and heating phases during the reaction was 5 K min^{-1}, except for the more stable Fe-ZSM-5, where 10 K min^{-1} was used.

Fe-ZSM-5 and Fe-MCM-41 were tested and are discussed in this section as comparison and reference to the relevant supported $FePO_4$. A blank reaction was run, where only quartz wool was present in the reactor, to confirm that ethane was not converted in a homogeneous process over the tested temperature range. The results of the reactions are summarised in table VII-2.

Table VII-2: Conversion of ethane and selectivity to oxidation products at selected temperatures for the catalytic testing of iron phosphate related materials with a $O_2:H_2$ feedstock.

Material	Conversion / %	Selectivity / %				Temperature / K
		Ethene	CO$_2$	Ethanol	Methanol	
n/a	0	0	0	0	0	293-773
FePO$_4$	3.0	80	20	0	0	773
Fe-ZSM-5	1.5	99	0	0	0	723
FePO$_4$-ZSM-5	0.5	100	0	0	0	723
Fe-MCM-41	1.1	100	0	0	0	723
FePO$_4$-MCM-41	0.7	100	0	0	0	723
PO$_4$-Fe-MCM-41	1	100	0	0	0	698

The temperature points presented here were chosen on the basis of the highest selectivity to partial oxidation products over the tested temperature range. It has first

to be noticed that partially oxygenated hydrocarbons were not observed over the whole temperature range when oxygen was used as oxidising agent. This correlates with the results obtained for our unsupported iron phosphates. It is thought that the "harder" oxidising character of oxygen [16] is responsible for this lack of selectivity to partial oxygenates. As the hydroxylation product of the reaction is more prone to be oxidised than ethane, it is likely that a cascade reaction with surrounding oxygen leads to the production of total oxidation products from the activated ethane molecules. Nevertheless the conversion of ethane and selectivity to ethene, the oxidative dehydrogenation product were increased in some cases, and the optimal reaction temperature lowered in most. When $FePO_4$-ZSM-5 was tested the conversion of ethane was significantly reduced, found at 1.4 % at 773 K (fig. VII-10).
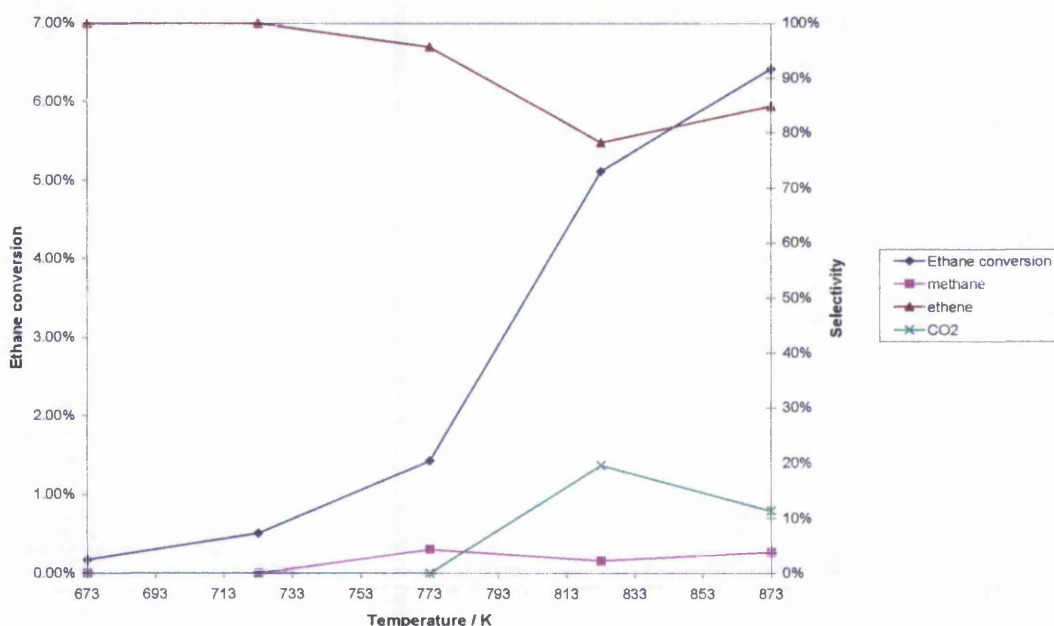
Figure VII-10: Ethane conversion and selectivity to products for the partial oxidation of ethane with O_2:H_2 over $FePO_4$-ZSM-5

The selectivity to ethene however was increased at this temperature, calculated to be approximately 95 %, and only methane found as a by-product. At 723 K only ethene

was observed as a product, combined with a minimised conversion of ethane however.

It is debatable whether these changes in oxidative activity between $FePO_4$ and $FePO_4$-ZSM-5 are due to a better dispersion of the active sites. Indeed an increase in the conversion rate is expected from an increased active surface area, which was not observed. Instead the conversion of ethane and product distribution was very similar to the one found when Fe-ZSM-5 EX was used as catalyst using the same conditions (fig. VII-11). Moreover, Fe-ZSM-5 EX was found to have a better conversion rate with better selectivity to ethene at a lower temperature, ca. 723 K.
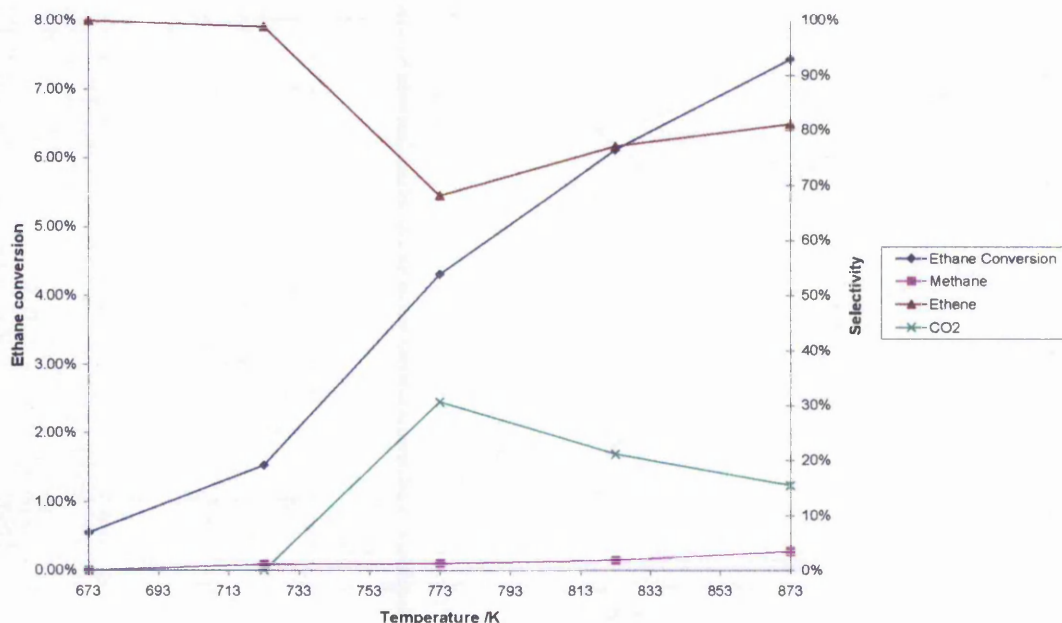
Figure VII-11: Ethane conversion and selectivity to products for the partial oxidation of ethane with O_2:H_2 over Fe-ZSM-5 EX.

It is therefore assumed that the activity found in $FePO_4$-ZSM-5 could originate from a fraction of iron present at ion exchange sites in the zeolite, rather than from a deposited iron phosphate phase. Proof of such an iron phase could not be confirmed in this study, however some hint suggesting the presence of two species with distinct reductive behaviour was presented earlier in chapter IV: Reducibility of the transition

metal. An intense reduction centred around 873 K was attributed to a supported iron phosphate phase, but the presence of a shoulder at around 723 K could relate to the species active in the oxidation of ethane with MFI supported catalysts (see pp. 84). The reduction of iron in Fe-ZSM-5 EX occurred at 673 K, a temperature below which the conversion of ethane was not achieved.

Moreover if the conversion of ethane is normalised to the amount of iron present in the material, as thought to be the active species, it is found that $FePO_4$-ZSM-5 and Fe-ZSM-5 are by far more active than our unsupported $FePO_4$ (fig. VII-12).
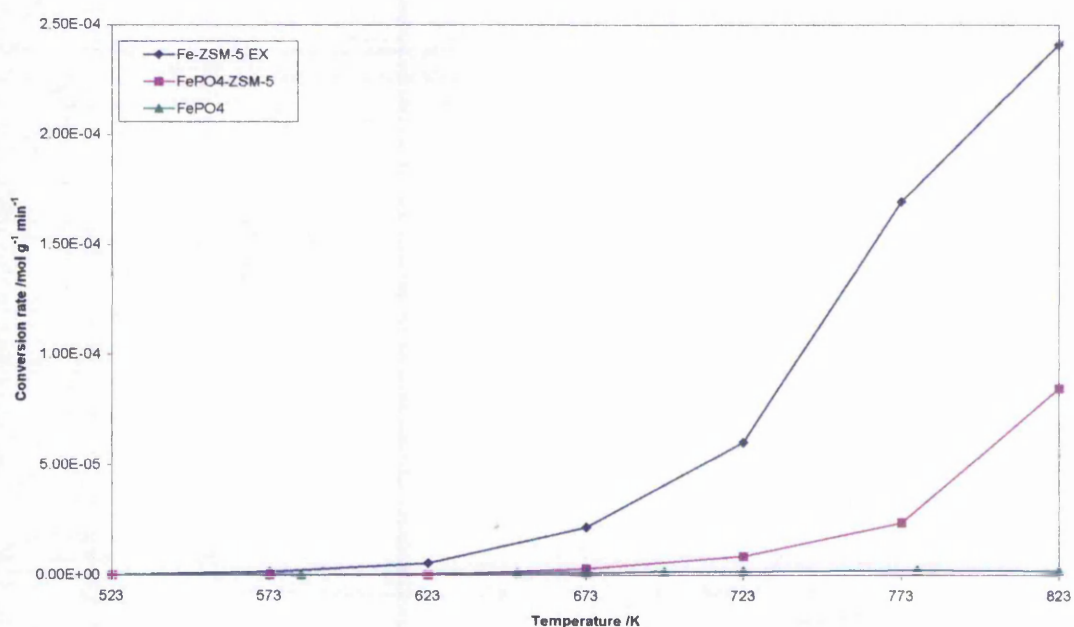
Figure VII-12: Plot of ethane conversion rates normalised to the reactor's iron content as a function of temperature for $FePO_4$, $FePO_4$-ZSM-5 and Fe-ZSM-5 EX.

It is possible that the increase in ethane conversion rate relates to a higher $FePO_4$ surface area due to its dispersion in the zeolite's pores, or that some iron species of the same structure as in Fe-ZSM-5 EX are present in $FePO_4$-ZSM-5. Both the one-pot synthetic method used for impregnation (see chapter II, pp. 42), providing little

control over the species formed, and the similar product distribution in reactions over Fe-ZSM-5 EX and $FePO_4$-ZSM-5 favour the latter hypothesis.

The results observed when MCM-41 was used as a support for $FePO_4$, however, favour the former hypothesis. The presence of phosphorus in addition to iron on the silicate's surface considerably increases the selectivity to ethene, effectively reducing the amount of total oxidation above 700 K (fig. VII-13).
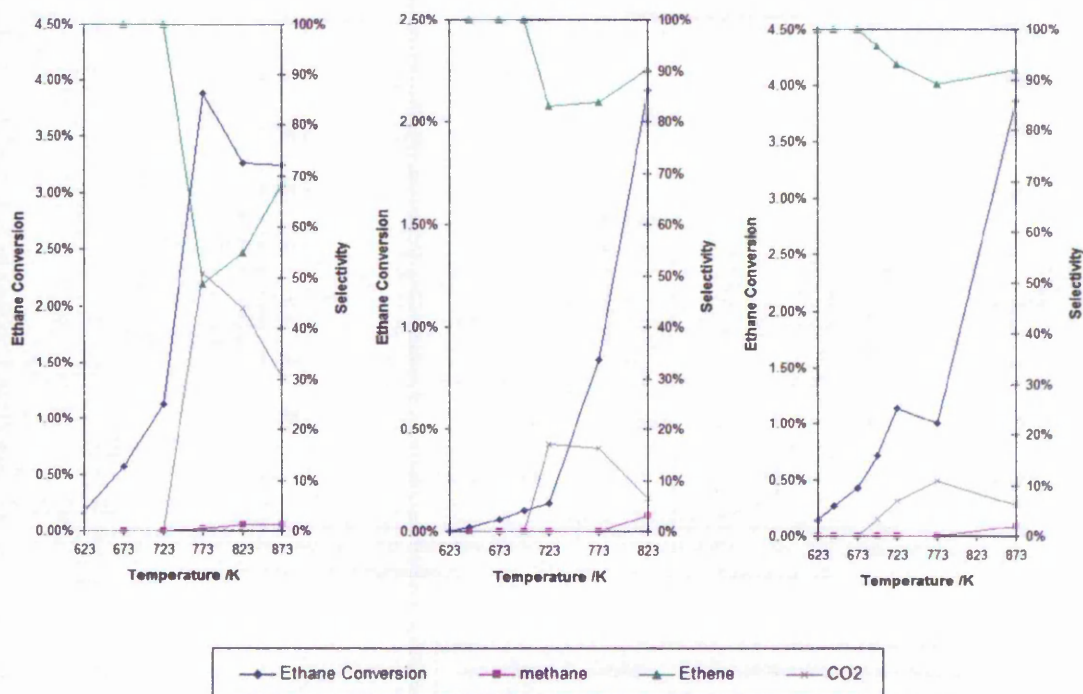
Figure VII-13: Plot of ethane conversion and selectivity to products versus temperature for (left) Fe-MCM-41, (centre) PO_4-Fe-MCM-41, (right) $FePO_4$-MCM-41

The conversion of ethane, similarly to $FePO_4$-ZSM-5, was reduced in both phosphorus-containing MCM-41s, compared to materials containing iron only. A plot of the conversion rate of ethane normalised to the amount of iron present in the reactor as a function of temperature reveals that Fe-MCM-41 may contain more active centres than PO_4-Fe-MCM-41 and $FePO_4$-MCM-41 (fig. VII-14). These data therefore cannot completely rule out the hypothesis that some isolated iron species in the framework are responsible for the material's activity.
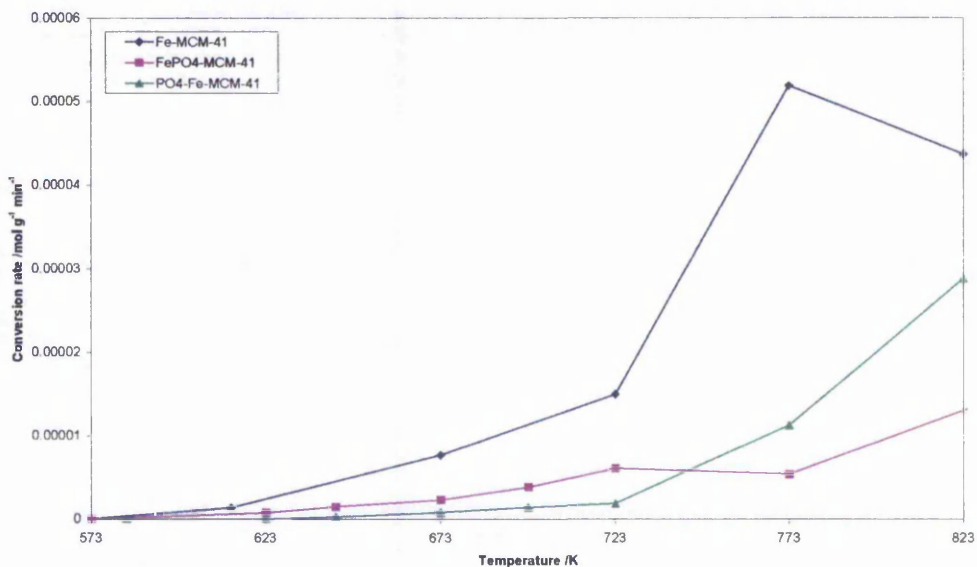
Figure VII-14: Comparison of the conversion rate of ethane observed during the catalytic testing of MCM-41 based materials with a $O_2:H_2$ feedstock as a function of reaction temperature.

It is possible, however unlikely, that the concentration of active sites alone affects the selectivity to products. In order to verify such a theory a plot of the conversion of ethane versus the amount of reducible sites in the material was drawn. Indeed, it was brought forward by different authors that the partial oxidation of hydrocarbons over iron and iron phosphate catalysts involved a redox mechanism for the formation of active oxygen species [12, 17]. According to these reported mechanisms the activity of the materials should therefore not only depend on the amount of reducible species in the material, but also on the temperature at which the metal is reduced. Table VII-3 presents temperature points at which a good agreement between the ethane conversion and amount of reducible sites was found. It can be noticed that the chosen temperature point for each material is in relation with the ease of reducibility of iron.

Table VII-3: Comparison of selected temperature points and conversions the reducibility of the metal centres as determined by TPR.

Material	Selected temperature point /K	Ethane conversion /%	Hydrogen uptake from TPR /mol g^{-1}	Iron reduction temperature from TPR /K
Fe-MCM-41	613	0.10	1.00×10^{-4}	622
PO$_4$-Fe-MCM-41	673	0.06	6.22×10^{-5}	753
FePO$_4$-MCM-41	723	1.13	8.98×10^{-4}	874

As the main reduction feature in the TPR study of iron phosphate materials was attributed to the reduction of iron in the vicinity of phosphorus (see chapter IV, pp. 82), it is possible that an iron phosphate phase is responsible for the reaction with enhanced selectivity to partially oxidised products.

It cannot be concluded here that iron phosphate only is responsible for the enhanced selectivity to partial oxidation products as differences in the acidic character of the materials have also been observed previously. In the case of supported iron phosphate good relationships between the number of acid sites and acid strength could not be devised, and this contribution will also be discussed further on in this chapter (see section VII-3.4, pp 205).

As summary of this study of the partial oxidation of ethane with a O$_2$:H$_2$ oxidising system over iron phosphate and related materials the higher selectivity to ethene, partial oxidation product, over CO$_2$ in phosphorus-containing materials is proven. The reason for such behaviour however could not be attributed to phosphorus itself at this point of the discussion, as the acidic and redox properties of all tested materials vary considerably. In phosphorus-free materials, i.e. Fe-ZSM-5 and Fe-MCM-41, different behaviours were also observed, which may indicate a strong contribution of the acidity to the oxidative activity of the catalysts. However significant structural

differences between both supports and the iron ions on their surfaces are known, and their contribution to the reaction will be discussed too. Using the stated reaction conditions, however, the prime product sought in this study, ethanol, was not obtained, instead oxidative dehydrogenation was prevalent.

The potency of iron phosphate for the production of ethanol was evident when nitrous oxide was used as oxidiser. Better conversions were not observed when supported iron phosphate catalysts were tested in an oxygen-hydrogen atmosphere. Therefore some of our materials were tested using the former more selective oxidising agent.

The reaction conditions were again the same as stated before, for the testing of unsupported iron phosphate with N_2O as oxidising agent. A feedstock of 20% ethane and 20% nitrous oxide, diluted with helium, was flowed over 100 mg of pelleted catalyst at a GHSV of 20,000 h^{-1}. The reaction was studied in a temperature-programmed manner, taking samples at selected temperatures after leaving the system to equilibrate for typically 15 minutes. A heating gradient of 5 K min^{-1} was used, and the samples were pre-activated in a 60 mL min^{-1} flow of 15% oxygen in helium at 773 K for one hour.

When unsupported iron phosphate was tested using these conditions a conversion of ethane of 4% was observed at highest selectivity to partial oxidation products. Then ethene was still the predominant product, with 50% selectivity, but a significant fraction of ethanol and methanol was detected, with respectively 8% and 34% selectivity. The latter together with Fe-ZSM-5 EX and Fe-MCM-41 were once again used as reference for the discussion of results. The conversion of ethane and selectivity to products observed is summarised in table VII-4, the temperature point presented being the one when highest selectivity to ethanol, or by default partial oxidation products, was recorded.

Table VII-4: Ethane conversion and selectivity to oxidation products for the catalytic testing of reference materials with nitrous oxide, at the temperature of highest selectivity to partial oxidation products.

Material	Conversion / %	Selectivity / %				Temperature / K
		Ethene	CO_2	Ethanol	Methanol	
$FePO_4$	4	50	8	8	34	623
Fe-ZSM-5	8	64	29	0	5	623
Fe-MCM-41	0.5	100	0	0	0	623

The first and notable fact observed is the relatively low temperature at which highest selectivity to partial oxidation products was reached, 623 K, compared to 723 to 773 K when the oxygen-hydrogen mixture was used (see table VII-2, pp. 184). Other differences were the increase in conversion for Fe-ZSM-5 EX, at the price of a lower selectivity to ethene, however methanol was identified as a reaction product, with 5% selectivity. The selectivity was not affected for Fe-MCM-41 when the oxidising agent was changed, but the conversion of ethane considerably reduced, calculated to be at around 0.5%. The reactor's outlet composition as a function of temperature is plotted in figure VII-15.

It is thought, as before, that methane and methanol are products of the cracking of ethane at active oxygen sites. The selectivity to methanol finds a maximum at around 623 K when Fe-ZSM-5 EX was used as catalyst. Above this temperature methane seems to be favoured over the oxygenate. With both Fe-MCM-41 and Fe-ZSM-5 EX as catalyst the amount of total oxidation product CO_2 considerably increases above 623 K. It therefore seems that this temperature is optimal for both materials for partial oxidation purposes.
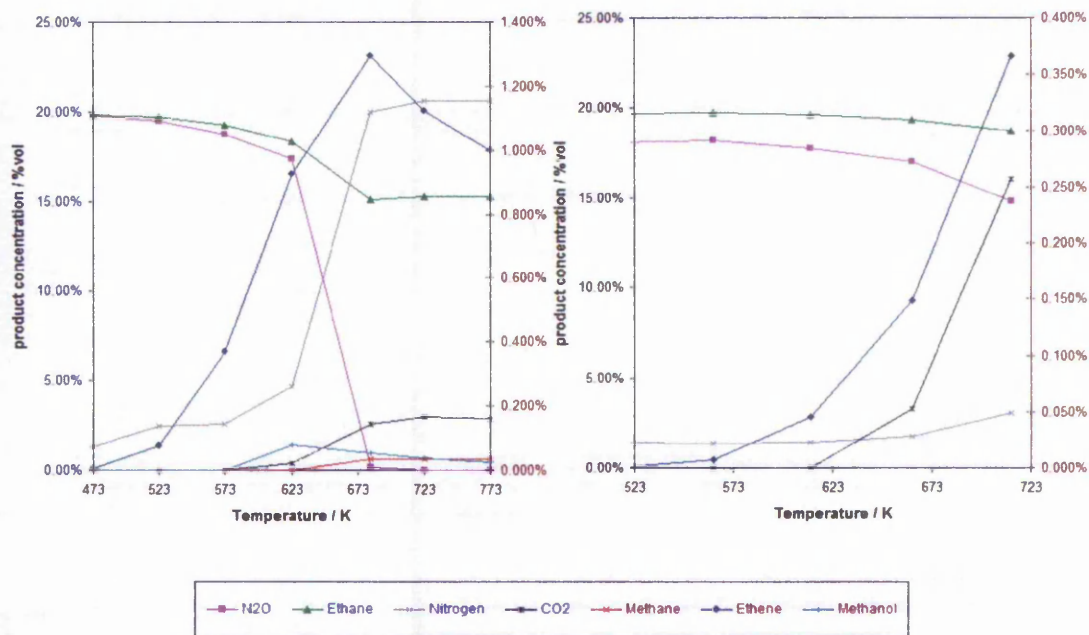
Figure VII-15: Product distribution for the partial oxidation of ethane over (left) Fe-ZSM-5 EX and (right) Fe-MCM-41, using N_2O as oxidising agent.

As the nature of the active sites for partial oxidation of hydrocarbons is considered in this thesis, the comparison of product distributions obtained with both Fe-MCM-41 and Fe-ZSM-5 EX indicates a low probability of isolated iron sites being responsible for the production of oxygenated hydrocarbons. Indeed two major differences exist between both supports, the presence of iron as mostly isolated sites in Fe-MCM-41, compared to a more heterogeneous distribution of iron cluster sizes in Fe-ZSM-5s, and the strong acidic character of ZSM-5, MCM-41 being virtually non-acidic (see chapters V and VI). The presence of ethene in the product mixture analysed after reaction over Fe-MCM-41 could originate from a low turnover oxidative dehydrogenation reaction over the catalyst, however the observed yield is 5 to 10 fold lower than with Fe-ZSM-5 EX. These isolated iron species could therefore have some activity to the activation of hydrocarbons, however limited. It is thought, as well, that the acidic character of ZSM-5 may favour the production of oxygenates, by providing an obvious source of protons, or hydroxyl groups, which could react with an activated

hydrocarbon chain. Due to the low conversion rates observed in MCM-41 based materials and the dubious structure of phosphorus-containing Fe-MCM-41s it was decided to not test for their activity in the partial oxidation of ethane with N_2O.

When $FePO_4$-ZSM-5 was tested for the partial oxidation of ethane with nitrous oxide a negative effect of the support on the ideal reaction temperature was observed, i.e. the temperature at which the highest conversion with highest selectivity to partial oxidation products was increased by ca. 100 K. The conversion of ethane, however, increased 4-fold compared to our unsupported iron phosphate, reaching 16% at 623 K. The results of this reaction are presented in figure VII-16 in the form of the product distribution plotted as a function of the reaction temperature. This plot reveals that a maximum in yield of partial oxidation products was not observed when using $FePO_4$-ZSM-5 as catalyst. Instead an increase in the yield of partial oxidation products was observed with increasing temperature.
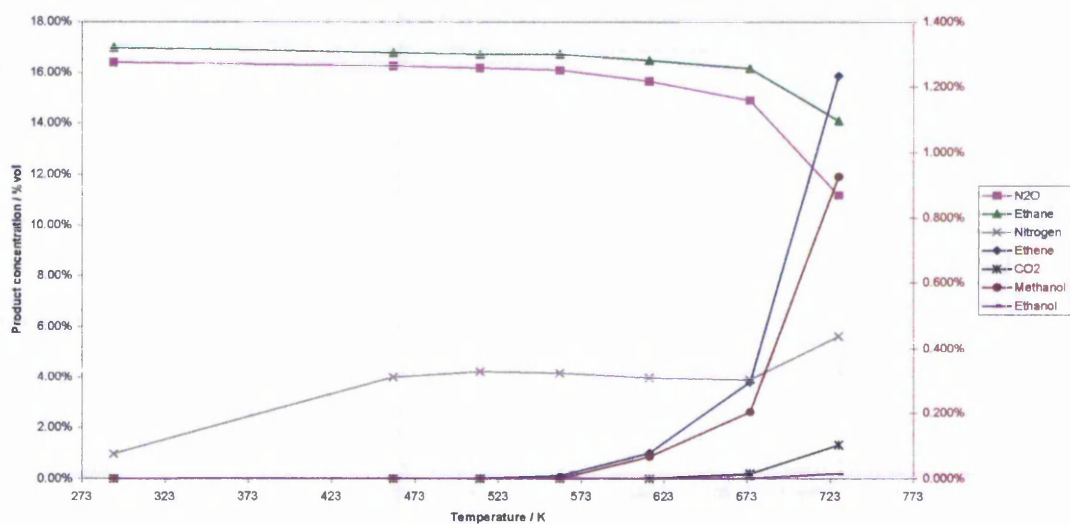
Figure VII-16: Plot of the product distribution recorded at the reactor's outlet for the catalytic testing of $FePO_4$-ZSM-5 with nitrous oxide as a function of reaction temperature.

At 623 K methane and propene were also detected, in respectively 0.12 and 0.07 %$_{vol}$ concentration, however not shown on the previous plot for clarity. The presence of

these two products could confirm the radical mechanism proposed by Kulikova *et.al.* for C-C bond cleavage at active oxygen sites [15]. This results in an overall loss of selectivity to the desired product as phenomena similar to cracking and reforming occur as competing reactions.

Following the recording of these data it was decided to end our study of iron phosphate based materials despite their consequently increased activity when ethane conversion was considered. The selectivity to oxygenates observed was not sufficient to hope for a good industrial catalyst on this basis, and the temperature of reaction needed to obtain any selectivity to ethanol too high to avoid the competing C-C cleavage. Moreover iron phosphate based catalysts seem to favour the production of methanol rather than ethanol. It is proposed here that methanol is obtained following the homolytic cleavage of ethane's C-C bond at an active oxygen site, followed by the protonation of this oxygen to obtain the hydroxyl group. The involvement of framework oxygen in the reaction is therefore proposed, similarly to hypotheses formulated in the direct hydroxylation of benzene, with regeneration of the active site by the surrounding oxidising agent [17-19]. The study of the mechanisms of activation and hydroxylation of hydrocarbons being beyond the scope of this thesis a schematic of the imagined catalytic cycle is not presented here, but proposed only as explanation of the results observed. Further studies of the reaction using for example isotopically substituted materials may be needed for the confirmation of our hypothesis.

Nevertheless it was decided to follow other routes in an attempt to produce ethanol from ethane in significant yield. From this preliminary study it was concluded that nitrous oxide offered better selectivity to oxygenates than oxygen, and higher conversions of ethane were observed at lower temperatures. The use of lower reaction

temperatures is essential especially when using a ZSM-5 support, considering its potency as cracking/reforming catalyst. The possibility of using oxygen as oxidising agent was investigated further, where it was attempted to promote the activation of oxygen with gold. More details on the choice of gold and effects hoped for are explained elsewhere (see chapter I, pp. 32).

It was observed that isolated iron sites are probably not the active sites for the activation of ethane, however this cannot be confirmed without a further study of the influence of the structure of iron on the reaction. This was achieved by reaction-testing the different materials discussed previously in this thesis and is presented later in this chapter (see section VII-3.5). Also the involvement of acid sites on the support was necessary in order to explain the different catalytic behaviour of Fe-ZSM-5 and Fe-MCM-41.

The material presenting the best properties for our further studies proved to be Fe-ZSM-5. A reasonable conversion rate of ethane was recorded at a temperature sufficiently low to avoid extensive cracking. Its selectivity to partial oxidation products was somewhat lower than $FePO_4$ or Fe-MCM-41, however high enough to make it a potentially good catalyst for this application. It ease of preparation with good reproducibility is a further advantage. The possibility to slightly vary the position and clustering of iron on the support's surface, the possibility to easily alter its acidity makes it designated for the relevant subsequent studies.

VII-3.2 In-situ activation of oxygen: gold-containing materials

Due to the high selectivity to ethene observed in the preliminary study discussed above, a strategy was imagined for the promotion of a hydroxylation or hydration reaction to occur in the reacting system. This strategy consisted in doping

Fe-ZSM-5 EX with a small amount of gold, which has been found over the past years to activate oxygen and hydrogen, as outlined earlier in this thesis (see chapter I, pp. 32) [20]. The quenching of the total oxidation process using hydrogen as additive to the reaction was successful, however the partial oxidation of ethane with oxygen invariably produced the more favoured oxidative dehydrogenation product ethene. It was thought that by producing a source of hydroxyl groups or radicals *in-situ* could increase the selectivity to the hydroxylation product ethanol. It was reported previously that hydrogen peroxide could be produced using noble metal catalysts [21, 22]. Also a few authors reported the possibility of producing alcohols or epoxides from alkanes using H_2O_2 [23-25]. In theory hydrogen peroxide may be formed at gold sites, and decomposed at iron sites, where the alkane is activated. Both reactions occurring in a close environment could favour the production of ethanol from ethane.

The gold-doped Fe-ZSM-5 EX was prepared using an ion exchange method, in order to increase the chances to obtain a good dispersion of the noble metal onto the catalyst's surface. An impregnation method was also developed, in order to ensure the presence of gold in the material, should the ion exchange be unsuccessful. The methods used are described in chapter II of this thesis. The materials were then tested for the oxidation of ethane under the conditions stated where a $O_2:H_2$ gas mixture was used (see pp. 183). The presence of gold in the catalysts tested being hoped to alter the reaction pathway, it was necessary to run the testing in a temperature-programmed manner.

The conversion of ethane was only slightly affected at low temperatures by the presence of gold in the catalysts (fig. VII-17).
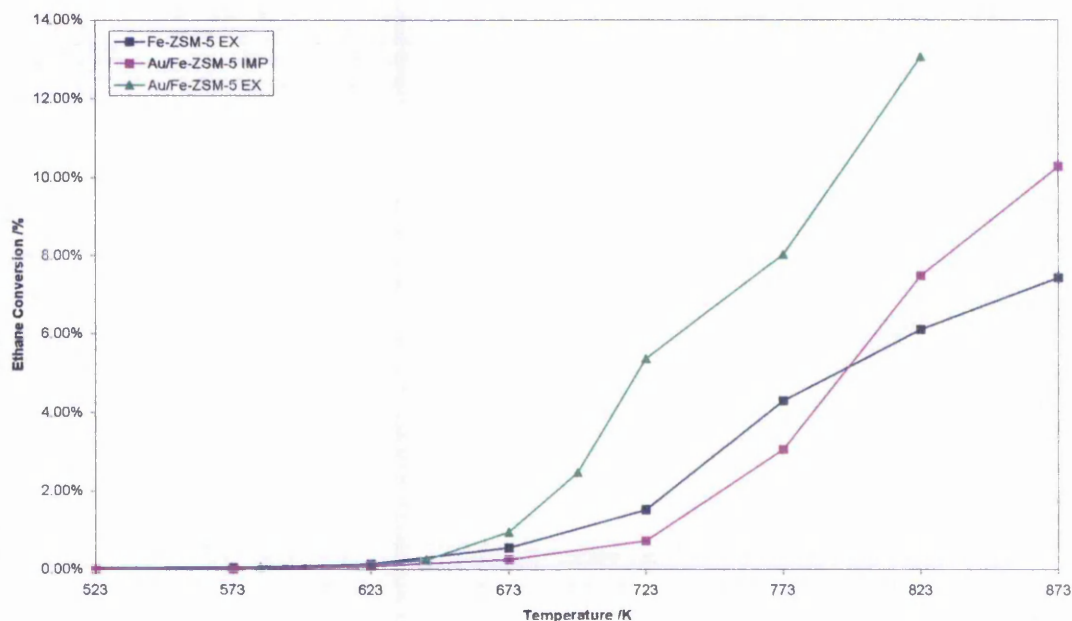
Figure VII-17: Comparison of the recorded conversion of ethane over gold-containing Fe-ZSM-5s with a $O_2:H_2$ feedstock as a function of reaction temperature.

Above 673 K however, this conversion was increased two to two and a half fold in the case of Au/Fe-ZSM-5 EX. This was not observed when Au/Fe-ZSM-5 IMP was tested, which is possibly due to the aggregation state of gold in the material. Indeed in our previous studies of Fe-ZSM-5s it was concluded that their post-exchange with gold did not affect the structure of iron on the zeolite's surface or their acidity to a great extent (see chapters V and VI). The reducibility of iron in these materials was mostly affected by the presence of gold, and more differences were observed between the reduction pattern of Au/Fe-ZSM-5 EX than Au/Fe-ZSM-5 IMP with reference to Fe-ZSM-5 EX (see chapter IV). The same order of difference was observed in the conversion of ethane. Direct relationships between the reducibility of iron and the conversion of ethane in this case could not be drawn due to the complexity of the reduction patterns recorded earlier. It was suggested recently, in the study of the epoxidation of hydrocarbons over gold catalysts, that microcrystalline gold particles

provided excellent conversion rates through the activation of oxygen molecules [24]. It is therefore assumed here that a better dispersion of gold in Au/Fe-ZSM-5 EX could explain the origin of the observed enhanced ethane conversion. Unfortunately the presence of gold had only little effect on product distribution and selectivity.

As presented on figure VII-18 the main products of reaction were still ethene, CO and CO_2, the two latter considered as total oxidation products here. As for the conversion of ethane, the product distribution recorded in the testing of Fe-ZSM-5 EX and Au/Fe-ZSM-5 IMP were mostly similar.

When Au/Fe-ZSM-5 EX was used as catalyst for the reaction, a lower selectivity to ethene was observed, counter-balanced however by a higher selectivity to total oxidation products. Nevertheless trace amounts of methanol and ethanol were detected above ca. 700 K, which were not present with the two other catalysts (fig. VII-19).
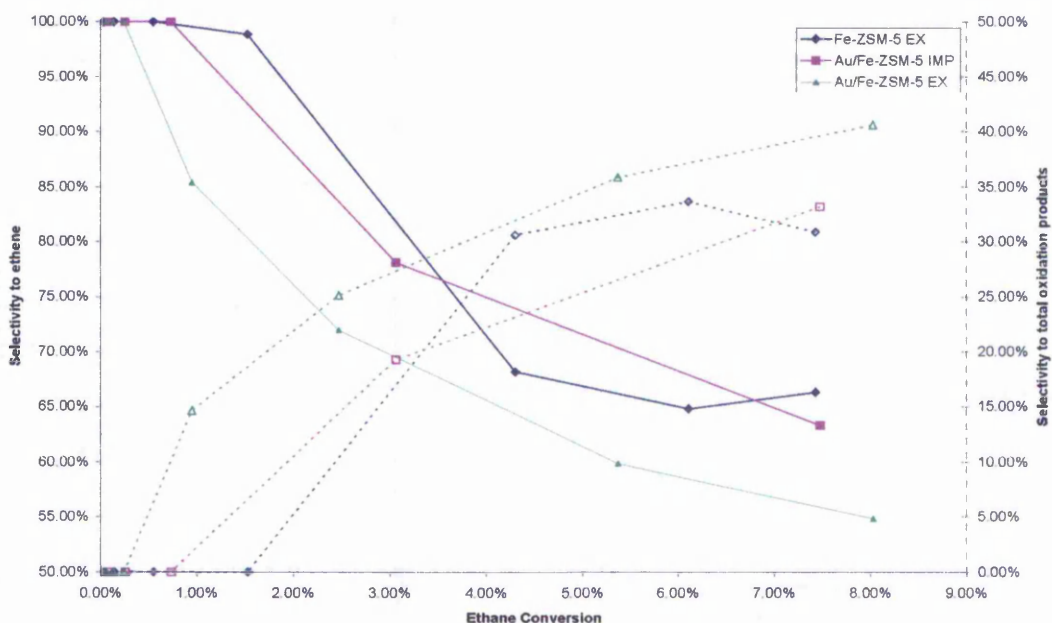
Figure VII-18: Selectivity to (plain lines) ethene and (dotted lines) total oxidation products for the catalytic testing of gold-containing Fe-ZSM-5s using a $O_2:H_2$ feedstock, as a function of the conversion of ethane.
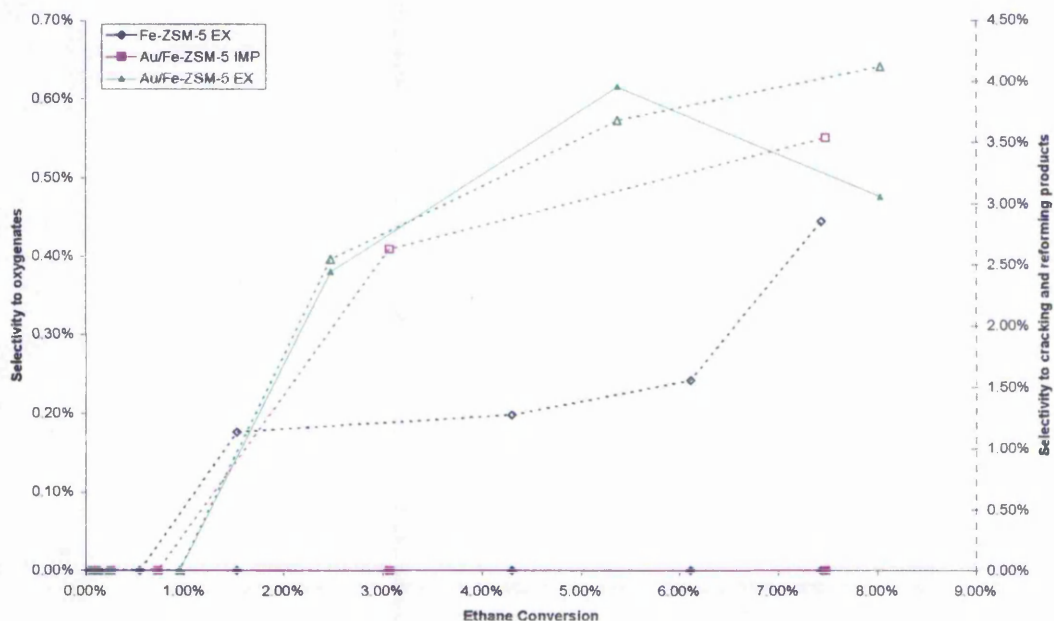
Figure VII-19: Selectivity to (plain lines) oxygenates and (dotted lines) C-C cleavage products for the catalytic testing of gold-containing Fe-ZSM-5s using a O_2:H_2 feedstock, as a function of the conversion of ethane.

The products resulting from ethane's C-C bond cleavage were also favoured in the reactions involving the gold-containing Fe-ZSM-5s. Methane and propene were detected with a maximum selectivity of 3.5 to 4% together. This increase can be directly related to the increase in production of methyl radicals during the reaction. Figure VII-20 illustrates the evolution of the selectivity to the different products detected in the reaction over Au/Fe-ZSM-5 EX as a function of temperature. It can be noticed that at lower temperatures, between ca. 650 and 700 K, the selectivity to ethene decreases in favour of carbon dioxide, methane and ethanol. Above 700 K the selectivity to ethene decreases further, but carbon monoxide is favoured over carbon dioxide, methanol and propene are detected, and the selectivity to ethanol decreases. This could be explained by a reaction pathway involving the activation of ethane in a first place, to produce ethanol or ethene in competition. Ethanol, due to its low thermal stability and being more reactive that ethane, may react further to be decomposed to methane and carbon dioxide.
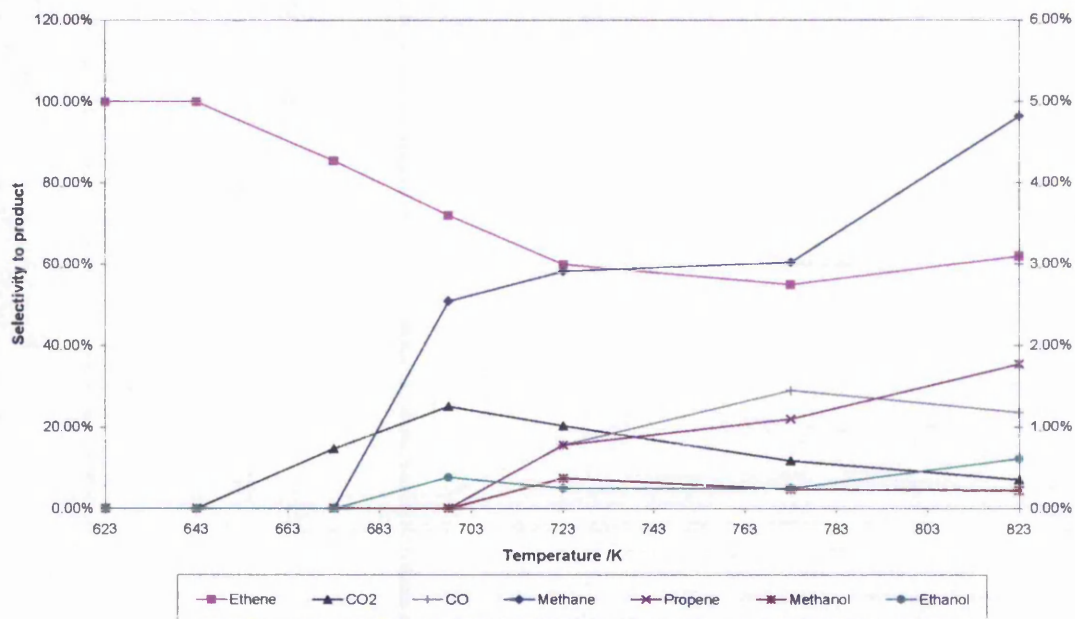
Figure VII-20: Plot of the product distribution recorded at the reactor's outlet for the catalytic testing of Au/Fe-ZSM-5 EX with a O_2:H_2 feedstock as a function of the temperature of reaction.

At higher temperature carbon monoxide is thermodynamically favoured over carbon dioxide, explaining the change in selectivity observed. The methane produced could be activated in turn to undergo hydroxylation, in a similar manner as ethane. It is believed that these sequences of reactions follow a radical mechanism, as suggested by the low selectivity of the reaction and supported by the mechanism proposed by Kulikova [15] for the cleavage of C-C bonds. At high temperatures a high concentration of methyl radicals would therefore be found near active sites as product of the decomposition of ethane and/or activation of methane. As a result of their collision with the surrounding ethane or ethene longer chain hydrocarbon are produced.

It is possible that hydrogen peroxide or hydroxyl radicals are involved in the first step of the reaction, produced from the activation of hydrogen and oxygen as discussed previously. Their reaction with ethane or ethene has ethanol as product. An evidence

of the production of such radicals would be the presence of water in the reaction products mixture. A significant amount of water should be produced from the reaction of hydroxyl radicals with the hydrogen in excess in the feed. Unfortunately it was not possible to detect water in our chromatographic system. An interesting relation could be derived, however, from the conversion rates of hydrogen and oxygen (fig. VII-21). The ratio between oxygen and hydrogen conversion rates in the case of both Au/Fe-ZSM-5 EX and IMP was calculated to be 0.55 on average. This is within experimental error of the 0.5 ratio expected for the stoichiometric reaction between O_2 and H_2, to produce water. As the conversion of oxygen at 700 K was ca. 50% the presence of water is highly probable and hydroxyl radicals most likely.
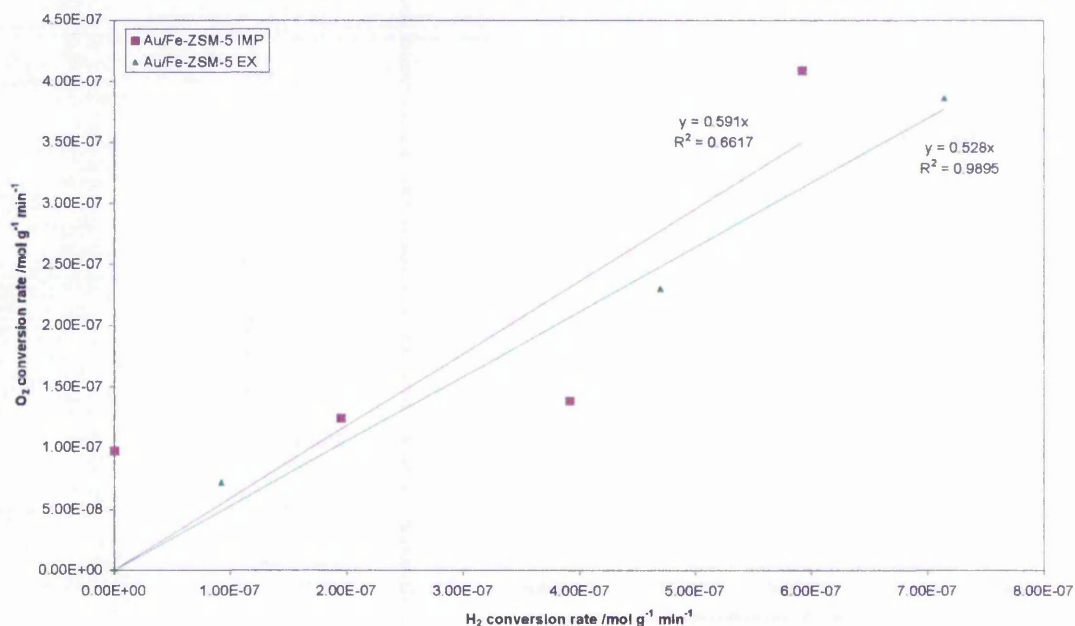
Figure VII-21: Oxygen conversion rate as a function of hydrogen conversion rate measured in the catalytic testing of gold-containing Fe-ZSM-5s with a O_2:H_2 feedstock.

Although yielding interesting results, the doping of Fe-ZSM-5 EX with gold did not favour the conversion of ethane to ethanol greatly. The selectivity of the reaction was

nearing zero, the main products remaining ethene and carbon dioxide. It seems that a fine distribution of gold particles may favour the activation of oxygen and/or hydrogen and/or ethane. The effect of gold doping on the selectivity to ethene was minimal, and it was decided that a further understanding of the mechanism producing the latter would offer better chances to design a successful catalyst. The gold-containing Fe-ZSM-5s were therefore not studied further.

VII-3.3 The effect of the support: ZSM-5 versus MCM-41

The differences in catalytic behaviour between iron supported on ZSM-5 and MCM-41 have been presented and briefly discussed in our preliminary study, however they are gathered here and analysed as an introduction to the following subchapters.

Fe-ZSM-5 EX and Fe-MCM-41 have been tested as standards in our preliminary study, using either oxygen or nitrous oxide as oxidising agent. The feedstock gas mixtures used are summarised in table VII-5, the makeup gas used was helium. The respective mixtures were flowed over 100 mg of catalyst pelleted to a 250-425 mm mesh, with a total flow adjusted to reach a GHSV of 20,000 to 25,000 h^{-1}.

Table VII-5: Feedstock composition used when oxygen or nitrous oxide were used as oxidising agents in the catalytic testing of our materials.

Oxidising agent used	Feedstock composition /%$_{vol}$		
	Oxidising agent	Ethane	Hydrogen
Oxygen	8	30	50
Nitrous oxide	20	20	0

The results of the catalytic testing are presented in figures VII-22 and VII-23 as plots of the conversion of ethane and selectivities to products as a function of the temperature of reaction.

The main outcome of this study was the absence of oxygenates in most cases. Only when N_2O was used as oxidising agent over Fe-ZSM-5 EX was methanol detected in the products mixture. The favoured reaction product, in all cases, was ethene, assumed to be formed via an oxidative dehydrogenation mechanism at lower temperature, and homogeneous gas phase dehydrogenation at higher temperature, possibly above 823 K, which was suggested as the selectivity to ethene drops with increasing temperature, up to 773-823 K, to increase again thereafter.
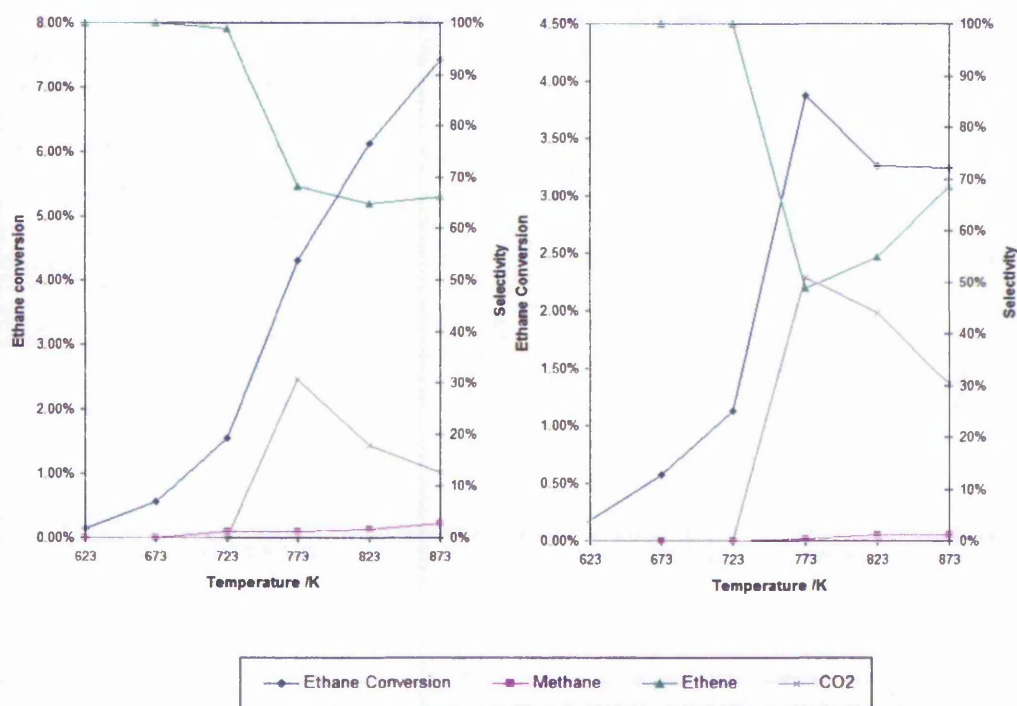
Figure VII-22: Plot of the conversion of ethane and selectivity to products as a function of the temperature of reaction for (left) Fe-ZSM-5 EX and (right) Fe-MCM-41 when oxygen was used as oxidising agent
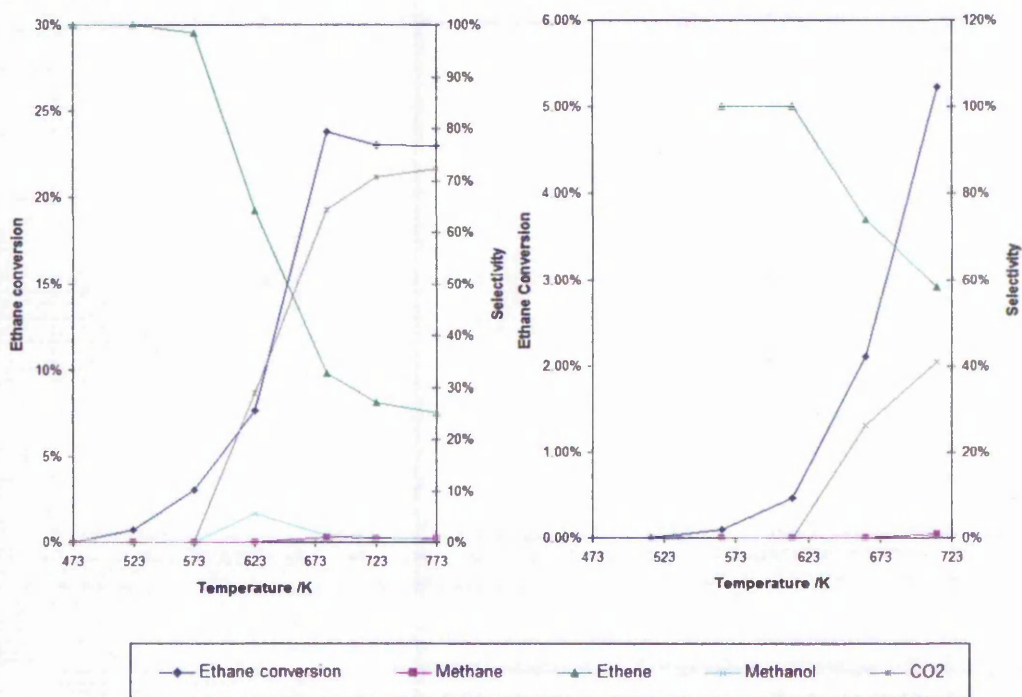
Figure VII-23: : Plot of the conversion of ethane and selectivity to products as a function of the temperature of reaction for (left) Fe-ZSM-5 EX and (right) Fe-MCM-41 when nitrous oxide was used as oxidising agent

Methane was detected as a minor reaction product in all cases, revealing a certain potency of our iron based materials for the cleavage of ethane's C-C bond. It was decided that this bond cleavage may follow a radical mechanism as propene was detected amongst the reaction products [15]. The selectivity to the latter being negligible it was not included on the previous plots.

Fe-ZSM-5 EX offered better conversion rates than Fe-MCM-41, with a 2:1 ratio when oxygen was the oxidising agent and 5:1 when nitrous oxide was used, reaching near 25% conversion of ethane at 473 K. This increase in activity suffered a decrease in selectivity to ethene, however methanol was detected in this system only, with 5% selectivity at 623 K and 8% ethane conversion. Methanol is supposed to originate

from the partial oxidation of methane, or methyl radicals, produced during ethane's C-C bond cleavage.

The lower activity of Fe-MCM-41 could not be attributed to the concentration of iron in the silicate, as the latter has a slightly higher iron concentration than its ZSM-5 pair. Instead, the differences in iron aggregation state in- and acidic character of the materials are considered as the main factors influencing the reaction. Indeed, Fe-MCM-41 is non-acidic and contains mostly iron as isolated ions, when Fe-ZSM-5 EX has a strong Brønsted acidic character and iron present as isolated ions, dimers or oligomers, and larger clusters (see chapters V and VI). These peculiarities are studied in the following two subchapters. Nitrous oxide was chosen as oxidising agent due to the higher conversion rates recorded.

VII-3.4 The presence of aluminium and effect of acid strength

As the direct comparison of Fe-ZSM-5 EX and Fe-MCM-41 suggests a possible role of acid sites in their catalytic activity, the supports possess other major structural differences preventing their direct comparison. Therefore a silicalite, an aluminium-free ZSM-5 of MFI structure, was synthesised (Fe-MFI SYN24) for comparison with Fe-ZSM-5 EX. Similarly an aluminium –containing Fe-MCM-41 was prepared (Fe-Al-MCM-41). The preparation methods used and characterisation of these materials is presented in chapter II.

It is noteworthy to remind the reader the acidic character of these materials here, for the scope of this section. Their number of acid sites, their strength – represented by the temperature of desorption of ammonia in TPD experiments – and type, *i.e.* Brønsted or Lewis, are summarised in table VII-6 (ref. chapter V).

The catalysts will be compared in pairs, successively Fe-ZSM-5 EX and Fe-MFI SYN24, followed by Fe-MCM-41 and Fe-Al-MCM-41. The catalysts were tested for the partial oxidation reaction using N_2O as oxidising agent with a GHSV of 20,000 h^{-1} and feedstock composition presented in table VII-5.

Table VII-6: Summary of the concentration, strength and type of acid sites found in iron and aluminium-containing MFI and MCM-41 materials.

Material	Number of acid sites /mol g^{-1}	NH_3 desorption temperature /K	Type of acid sites present
Fe-ZSM-5 EX	1.22 x 10^{-4}	618	Mostly Brønsted
Fe-MFI SYN24	4.48 x 10^{-4}	524	Mostly Lewis
Fe-MCM-41	5.11 x 10^{-5}	586	Lewis only
Fe-Al-MCM-41	1.18 x 10^{-4}	519	Mixed

VII-3.4.1   ZSM-5 versus silicalite

The results of the catalytic testing of Fe-ZSM-5 EX and Fe-MFI SYN24 are presented in figure VII-24, as a plot of the conversion of ethane and selectivity to products as a function of the reaction temperature. When iron silicalite was used as a catalyst the conversion of ethane was high, reaching ca. 34 % at 573 K. A decrease in conversion rate was observed as the temperature was increased to 673 K. At higher temperatures the conversion of ethane increased again, reaching above 50% at 773 K. This strongly suggests the presence of two different thermally activated mechanisms of reaction. One, less thermally favoured, causes the burning of the hydrocarbon, as a 70% selectivity to carbon dioxide was recorded at 773 K. The other mechanism seemed to favour ethane dehydrogenation and C-C bond cleavage, with production of ethene, methane and methanol in the case of Fe-ZSM-5 EX. In the case of Fe-MFI SYN24,

however, a more important thermal gap between both reactions was recorded, and at

lower temperatures C-C bond cleavage was not as extensive.
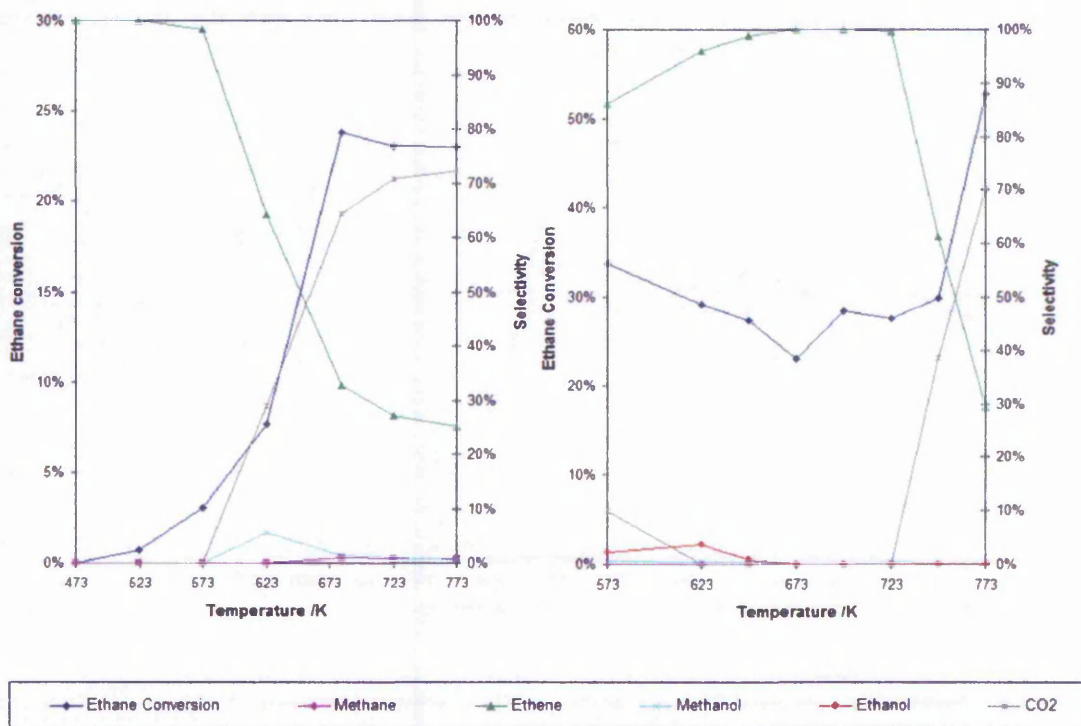
Figure VII-24: Conversion of ethane and selectivity to products as a function of reaction temperature for the catalytic testing of (left) Fe-ZSM-5 EX and (right) Fe-MFI SYN24 with nitrous oxide.

Some total oxidation was detected at 573 K, however this disappeared at 623 K,

where ethanol was detected in reasonable amounts. A selectivity to ethanol of ca. 4%

was calculated at 29% ethane conversion, with negligible selectivity to methane and

methanol. A first hypothesis can be devised from these data, attributing a role to

aluminium centres or strong Brønsted acid sites in the C-C bond cleavage and/or total

oxidation of ethane. The involvement of iron centres in these reactions is not excluded

yet, as it has been shown that both materials do not possess the same distribution of

iron species in their framework, after FTIR in-situ NO adsorption studies. Species

responsible for the partial oxidation of hydrocarbons seem to be present in both

materials, and it is suggested that the mechanism of C-C bond cleavage is favoured

over oxygenation on the surface of Fe-ZSM-5 EX, whereas the latter would be favoured on the more weakly acidic surface of Fe-MFI.

In order to account for the contribution of iron centres in the discussed processes, our parent H-ZSM-5 was tested for the catalytic application under the same conditions. Iron is present in the zeolite only as trace amount, as confirmed by nitric oxide absorption experiments, mostly as isolated sites at ion exchange positions or small (nano) clusters (see chapter VI, pp. 165). The results of this catalytic testing (fig. VII-25) reveal a significantly lower conversion of ethane than the ion exchanged Fe-ZSM-5, confirming the involvement of iron centres in the activation of the hydrocarbon.
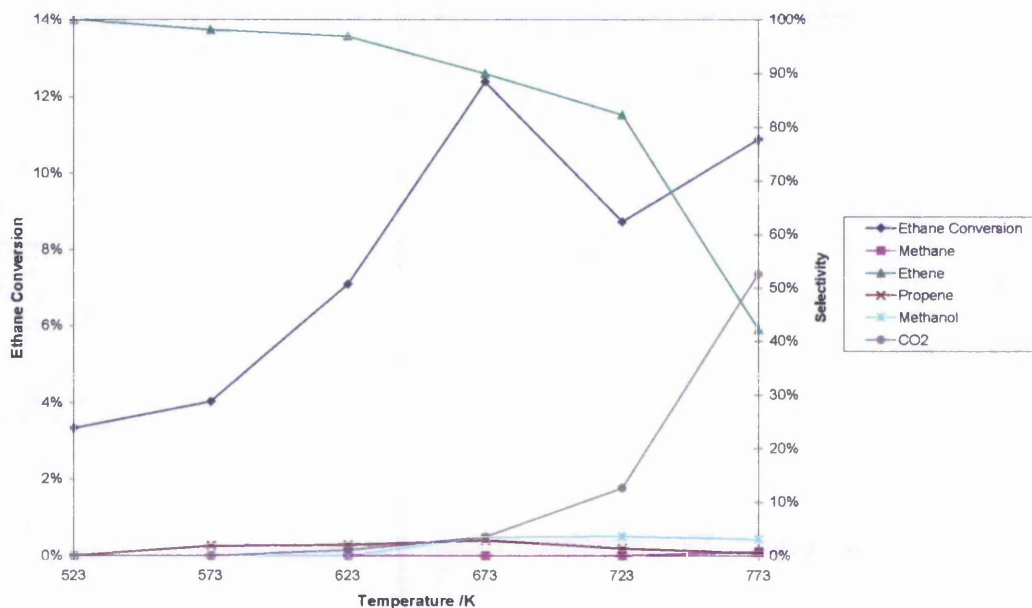
Figure VII-25: Conversion of ethane and selectivity to products as a function of reaction temperature for the catalytic testing of H-ZSM-5 with nitrous oxide.

Only minute changes in the selectivity to the detected products were noticed. The similar trends in ethene and carbon dioxide selectivities indicate that the latter is most likely the product of further oxidation of the former, at the same active site, and selectivity to one or the other is thermally driven. The selectivity to methanol was

similar as for Fe-ZSM-5 EX, and the only noticeable change in product distribution was an increase in the selectivity to propene.

The involvement of Brønsted acid sites in the cleavage of C-C bonds or production of oxygenates could not be confirmed from these data. It appears however that the conversions recorded are mostly driven by iron centres.

VII-3.4.2   Aluminium-containing MCM-41

Due to the complex structure of Fe-ZSM-5 catalysts it was necessary to obtain more data highlighting the difference in catalytic behaviour between silicates and aluminosilicates. This was achieved by introducing aluminium in MCM-41, which successfully increased the material's acidity (see chapter V, pp. 117). It was determined that the iron subsequently exchanged into Al-MCM-41 found position as isolated sites at either ion-exchange sites or was integrated in the silica framework, in similar positions to Fe-MCM-41 (see chapter VI, pp. 148). This more straight forward distribution of iron species may help the study of the influence of aluminium and/or acidity on the studied catalytic conversion.

As an optimal reaction temperature of 623 to 673 K was observed in all cases reported up to here, and due to the low conversions recorded with MCM-41 based materials, it was decided to test both Fe-MCM-41 and Fe-Al-MCM-41 isothermally. An isothermal reaction could result in higher conversion rates at the start of the reaction by avoiding an eventual deactivation of the active sites, e.g. by coking, during the lower temperature measurements and ramp up. This could, at low conversions, cause the quick decrease of low yield products below detection limits. This method was validated by comparing the results of the isothermal reaction of Fe-MCM-41 to the temperature-programmed one. After activation using standard conditions, the reactor

was left to cool down to reaction temperature, purged with helium, and addition of N_2O and ethane to the feedstock marked the start of the reaction. A good agreement between conversions and selectivities was found at 673 K, and is summarised in table VII-7. It was decided to run the isothermal reactions at 673 K, where ethane conversion was recorded at ca. 2% previously, compared to 0.5% at 623 K.

Table VII-7: Summary of the conversion of ethane and selectivity to products for the catalytic testing of Fe-MCM-41 and Fe-Al-MCM-41 at 673 K.

			Fe-MCM-41		Fe-Al-MCM-41
			Programmed	Isothermal	Isothermal
Ethane conversion /%			2.11	1.87	4.99
Selectivity /%		Ethene	74	74	58
		CO_2	26	26	35
		Methanol	0	0	5
		Methane	0	0	1
		Propene	0	0	1

The results of the testing of Fe-Al-MCM-41 are also presented in the previous table. All measurements presented here were taken at t = 10 to 15 minutes after the start of the reaction.

The conversion of ethane was hardly affected between the temperature-programmed and isothermal reactions, with respectively 2.11 and 1.87% recorded conversions, the difference falling within experimental error. This justifies a minimal amount of deactivation of the catalyst at the selected temperature. The selectivity to products was not affected by the change in reaction conditions.

When aluminium was present on the surface of Fe-MCM-41, the conversion of ethane was increased 2.5 fold, calculated to be 5% at t = 10 min at 673 K. More importantly

the product distribution changed significantly compared to the Al-free material. The amount of total oxidation was increased, with 35% selectivity to CO_2, and some C-C bond cleavage and oxygenation products were detected in small amounts. The differences between Fe-MCM-41 and Fe-Al-MCM-41 being the presence of Brønsted acid sites and iron at ion-exchange positions in the latter, it is believed that either of these factors are responsible for ethane's C-C bond cleavage and partial oxidation activity.

VII-3.4.3   Summary

Ethane conversion was observed in all cases and therefore it is believed, despite a good linear relationship observed between ethane conversion and the number of acid sites present in the catalyst (fig. VII-26), that the activation of ethane occurs at iron sites and involves a redox mechanism, accordingly to existing literature [26, 27]. The linear relationship observed is assumed to be an artefact originating from the Lewis acidic character of the metal centres. An increase in the concentration of iron in the catalyst is accompanied by an increase in its acidity and, independently, ethane conversion.
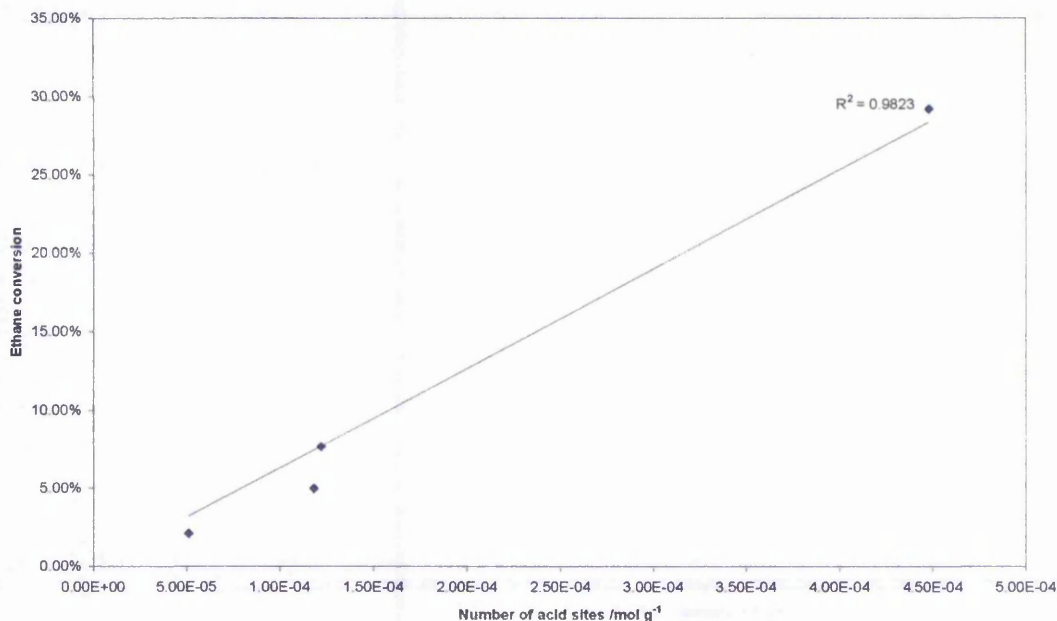
Figure VII-26: Plot of the recorded conversion of ethane at 673 K as a function of the number of acid sites in the catalysts tested, for their catalytic testing with nitrous oxide.

The types of acid sites in the studied catalysts varied greatly, and it may not be assumed that either Brønsted and Lewis acids activate the hydrocarbon in the same manner. Brønsted acid sites however may act as source of protons for the production of hydroxylated hydrocarbons, and also promote the cleavage of ethane's C-C bond. Whether C-C cleavage occurs before or after the partial oxidation of ethane cannot be discussed here. The presented plot of the selectivity to different products as a function of the number of acid sites in the material doesn't reveal any direct relationships (fig. VII-27).

The quantitative speciation of Lewis and Brønsted acid sites could not be achieved using the characterisation techniques available, however it appears that only materials containing Brønsted acid sites showed partial oxidation and cleavage activity. In Fe-MFI SYN24, containing less Brønsted acid sites of weaker strength, fewer cleavage products were noted. The amount of total oxidation was also reduced with

the latter catalyst, however it is not believed that this is related to the acidity of the

material as Fe-MCM-41, essentially non-acidic, showed some selectivity to CO_2.
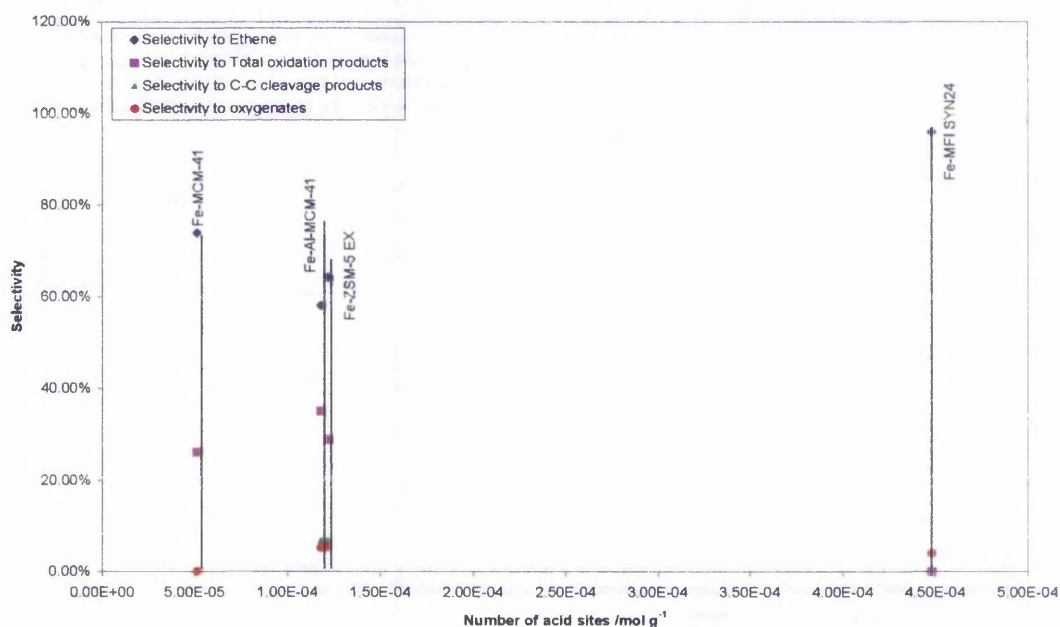
Figure VII-27: Plot of the selectivity to products as a function of the number of acid sites in the catalysts tested, for their catalytic testing with nitrous oxide.

VII-3.5 The effect of the structure of iron species

The effect of the structure, or aggregation state, of iron supported on zeotypes over

the catalytic activity of the materials was studied. The most extensive variation in iron

aggregation state distribution was observed between Fe-ZSM-5 EX and Fe-MCM-41,

however, as discussed previously the difference in acidic character of these materials

prevented a decisive analysis of the data (see section VII-3.4). It was shown,

following studies of the adsorption of NO with in-situ infrared detection, that Fe-

ZSM-5s prepared by different methods had different distribution of iron species in

their framework (see chapter VI, pp. 170). The materials did not contain exclusively

one or the other types of iron structures, but it was possible to preferentially form

them. When iron was exchanged in H-ZSM-5 in aqueous solution from an iron nitrate

salt, it was determined that the oligomers reported by Stockenhuber and Joyner [28] were formed in higher concentration than when other methods were used. The chemical vapour deposition of iron onto ZSM-5, from an iron chloride, was reported to preferentially form metal dimers at ion-exchange positions [29]. In our study of the adsorption of NO it was not possible to identify a M-NO band corresponding to such dimers in ZSM-5s. It was however determined that Fe-ZSM-5 CVD contained mostly isolated iron ions at ion-exchange positions. When the material was calcined in air rather than pure oxygen, following the vapour deposition, it was found that iron ions migrated on the zeolite's surface to form mainly hematite-like clusters, as observed in Fe-ZSM-5 CVD (hem). Iron silicalites of MFI structure were reported to contain iron as isolated sites and dimers [30]. Our study suggested the presence of iron dimers and hematite-like clusters. The former was assumed to be favoured to the latter, however a lack of further evidence prevented us from confirming this distribution. The possibility of a confusion between iron dimers and oligomers could not be confirmed, and even thought it is assumed in this study that both exist, they shall be taken as similar entities if their catalytic behaviour cannot be differentiated.

These four materials, Fe-ZSM-5 EX, Fe-ZSM-5 CVD, Fe-ZSM-5 CVD (hem) and Fe-MFI SYN24 contain all of the reported and possible aggregation states of iron in their framework, in different relative amounts, allowing us to study their effect on the partial oxidation reaction. They are used here as pillars for the discussion of their activity, data recorded from the catalysis using MCM-41 based materials used to support our investigations, in some cases.

The conversion rate of ethane and selectivity to different products recorded for the reaction of ethane with nitrous oxide over these catalysts are summarised in table VII-8. The data presented were recorded after 60 minutes of reaction at 673 K, and GHSV

of 20,000 h^{-1}. Nitrous oxide was used as an oxidising agent due to the higher conversions observed (see sections VII-3.1-3).

Table VII-8: Summary of the conversion of ethane and selectivity to products recorded after 60 minutes of the catalytic testing of various materials of MFI structure with nitrous oxide at 673 K.

Material	Ethane conversion /%	Selectivity /%			
		Ethene	CO_2	Oxygenates	Cleavage (- MeOH)
Fe-ZSM-5 EX	42	28	27	43	39 (1.13)
Fe-ZSM-5 CVD	25	33	54	11	12 (2.23)
Fe-ZSM-5 CVD (hem)	27	30	61	7	9 (2.11)
Fe-MFI SYN24	29	96	0	4	0

The material which showed the highest conversion of ethane when the reaction was run isothermally was Fe-ZSM-5 EX. This accounts for a considerable deactivation of the catalyst, reflected by the conversion recorded in our thermally programmed reaction, where 24% ethane conversion was recorded at 673 K. The most likely cause of deactivation was rapid coking of the active sites. This is confirmed as the catalyst was quickly deactivated under isothermal conditions, with the ethane conversion halved over 3 to 4 hours of reaction. Here the selectivity to ethene was considerably decreased, in favour of oxygenates, mainly methanol. A selectivity of approximately 5% to ethanol was recorded after 1 hour of reaction at 673 K, quickly dropping to zero. A high selectivity to C-C cleaved products was observed, however the main part of which was methanol, with only minor amounts of methane and propene produced.

In other cases the conversion of ethane was lower, found between 25 and 29%, despite the higher iron concentration in these materials. This clearly indicates the peculiar character of Fe-ZSM-5 EX for the activation of the hydrocarbon. Both

materials prepared by CVD showed similar product distributions, with a high selectivity to CO_2, 57% on average, most of the remaining selectivity going towards ethene. Some selectivity to oxygenates was still recorded, 11 and 7% for respectively Fe-ZSM-5 CVD and Fe-ZSM-5 CVD (hem). Only 1% selectivity to ethanol was recorded in the first case however, and nil when the latter was used as a catalyst in the stated conditions. Small amounts of the C-C cleavage products methane and propene were detected, with altogether ca. 2% selectivity. A somewhat lesser activity towards the hydroxylation of methyl radicals by these materials was deduced from this increased selectivity. The mechanism assumed here, involving the production of methyl radicals at active sites, is discussed elsewhere (see section VII-3.1.1, pp. 182).

Finally the product showing the highest selectivity to partial oxidation products was Fe-MFI SYN 24, where no total oxidation or cleavage of ethane was recorded. The data presented for this catalyst was recorded at 623 K, as only ethene was detected as product of reaction at 673 K. An attempt to correlate this difference in optimal reaction temperature to the ease of reducibility of iron – as the mechanism of activation of the hydrocarbon was proposed to involve oxidoreduction of the metal [17, 31] – was unsuccessful. It is therefore proposed that the activity of these materials towards the partial oxidation of light hydrocarbons is related to the aggregation state of iron, with possible contribution of Brønsted acid sites, as discussed earlier in this report (see section VII-3.4, pp. 210). The stronger character of the Brønsted acid sites in aluminium-containing MFI may explain its higher potency to produce hydroxylated products, compared to Fe-MFI SYN24. The aggregation state of iron is proposed to affect the activation of the hydrocarbon, as discussed in the following paragraphs.

VII-3.5.1   Isolated sites

A fraction of isolated iron species at ion-exchange sites was present in all the Fe-ZSM-5 catalysts prepared. They were supposed to be favoured in Fe-ZSM-5 CVD, however their involvement in the activation of the hydrocarbon is not evident at first. The product distributions recorded when Fe-ZSM-5 EX and Fe-ZSM-5 CVD were used as catalysts were significantly different, however Fe-ZSM-5 CVD (hem) showed a similar behaviour as its pair prepared by CVD. Such similar behaviour could be explained by the migration of iron ions on the surface of Fe-ZSM-5 CVD during its activation to produce hematite-like clusters, at which the total oxidation of the hydrocarbon could occur. Fe-ZSM-5 CVD, however, was shown to have a lower iron concentration than Fe-ZSM-5 CVD (hem), and this hypothesis would be verified only if the latter showed a much higher CO_2 yield. It is therefore proposed that isolated iron sites may be responsible for this total oxidation. Indeed, Fe-ZSM-5 EX contained these sites to a lesser extent than our samples prepared by CVD, and they were not present in Fe-MFI SYN24.

VII-3.5.2   Dimers / oligomers

Iron dimers and Fe_4O_4 type oligomers are discussed together here, due to the debate concerning the existence of the latter. It was not possible, in this study, to produce a material which was thought to contain such nanoclusters exclusively.

It is believed that these iron pairs or nanoclusters are responsible for the gentle activation of ethane. They were found in all the catalysts studied here, including Fe-MFI SYN24. All these materials showed a significant selectivity to ethene, which is thought to be produced via an oxidative dehydrogenation mechanism [32]. This mechanism involves a monooxygenated ethane intermediate, from which ethanol can

be produced, or ethene by dehydration. The much higher conversion of ethane observed when Fe-ZSM-5 EX was used as a catalyst, together with its higher concentration in nanoclusters – determined by NO adsorption studies – supports our hypothesis. Small amounts of these clusters were also found in Fe-ZSM-5s prepared by CVD, explaining their selectivity to oxygenates. The cleavage of ethane's C-C bond is not believed to occur as part of this oxidative mechanism, as was proposed by Kulikova [15], but rather by a subsequent reaction of ethanol or ethene at strong Brønsted acid sites in the zeolite. Indeed, C-C bond cleavage was not observed when Fe-MFI SYN24 was used as a catalyst, even though both ethene and ethanol were produced. The latter catalyst possessed weaker Brønsted acidity than its aluminium-containing equivalent. It is therefore accepted that the activation of ethane occurs at nanoclustered iron sites, with the participation of neighbouring Brønsted acid sites causing the following cascade of reactions summarised in figure VII-28:
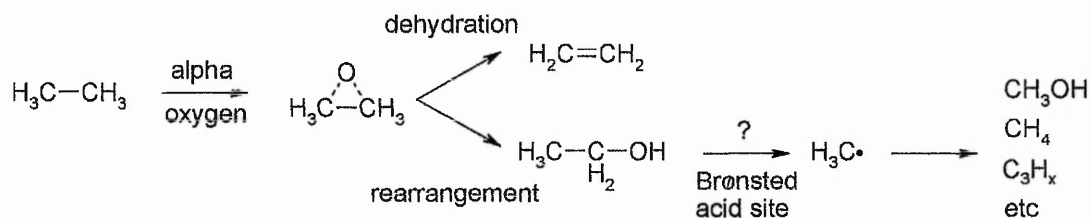
Figure VII-28: Possible cascade of reactions occurring during the conversion of ethane over the materials tested.

A definite mechanism of reaction could not be proposed however, due to the lack of knowledge on the structure and location of these sites. It is believed that the strength of the Brønsted acid sites in the zeolite is a major factor influencing product selectivity, where the presence of iron nanoclusters neighbouring aluminium centres promotes the activation of the hydrocarbon. This activation would occur in a way similar to the one reported for the direct hydroxylation of benzene to phenol, involving the formation of "alpha" oxygen species [17, 31].

VII-3.5.3   Clusters

The involvement of hematite-like clusters in the activation of ethane is proposed to be limited. All the Fe-ZSM-5 catalysts studied here were shown to contain such sites in various concentrations, and they were present as a majority in Fe-ZSM-5 CVD (hem). A direct consequence in this increase in the concentration of these clusters on the reaction products mixture was not observed. It is believed that these larger clusters do not take part in the studied oxidation of ethane.

VII-3.6 The effect of activation conditions and iron concentration

As a mechanism involving "alpha" oxygen species is believed to drive the partial oxidation reaction it was decided to study the effect of the activation of the catalyst on the yield of partial oxygenates. Indeed in studies of the direct hydroxylation of benzene to phenol it was reported that various pre-treatments of the catalysts could increase the concentration of "alpha" oxygen [31, 33]. For example the activation of samples in vacuum at high temperature or in the presence of water vapour was reported to increase the yields and selectivity to phenol in these studies. The steaming of the catalyst was reported to be more effective than vacuum treatment, however several attempts to perform this activation in our reactor resulted in severe disruptions of our analytical system, and it was decided to use a more easy to implement activation technique in order to confirm the thought involvement of alpha-oxygen species. The vacuum pre-treatment of samples was not possible in-situ in our system, and it was decided to perform a high-temperature activation of samples in an inert atmosphere, which would result in the same reductive effect on the metal centres.

For this study Fe-ZSM-5 EX and Fe-MFIs, respectively the most active and most selective catalysts tested so far, were subjected to an activation temperature of 1323 K for 1 hour under a 20 mL min^{-1} flow of helium. A 10 K min^{-1} heating gradient was used to prevent the uncontrolled collapse of their framework. After the activation time, the reactor was cooled down to reaction temperature, and the catalytic testing was performed using the normal ethane and nitrous oxide feedstock.

The catalytic testing of Fe-MFI SYN24 in the conditions stated above, when the reaction was carried out isothermally at 623 K, led to a low conversion of ethane (below 1%) with no selectivity to ethanol over 2 hours of reaction (fig. VII-29). As this considerable decrease in activity possibly originated from the destruction of active sites due to the collapse of the zeolite's framework, it was also possible that the temperature window in which the material was active was missed, as the high-temperature reductive treatment on the catalyst may have altered the structure of the active site. It was therefore decided to run the catalytic testing in a temperature-programmed way, ramping the temperature from 373 up to 623 K typically.
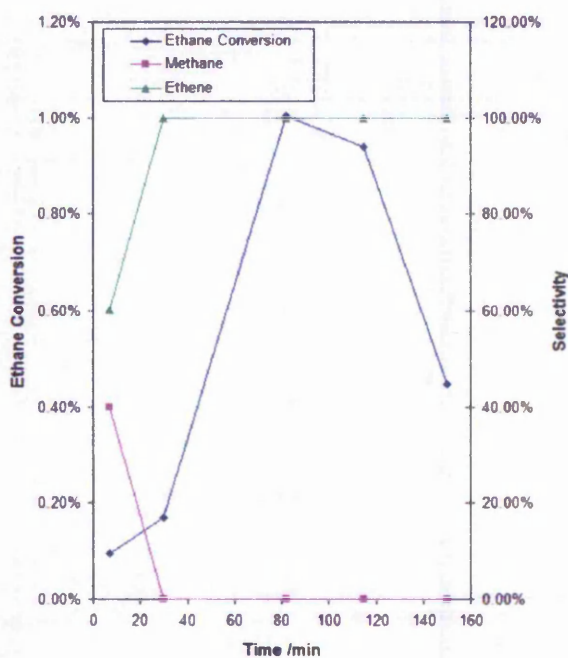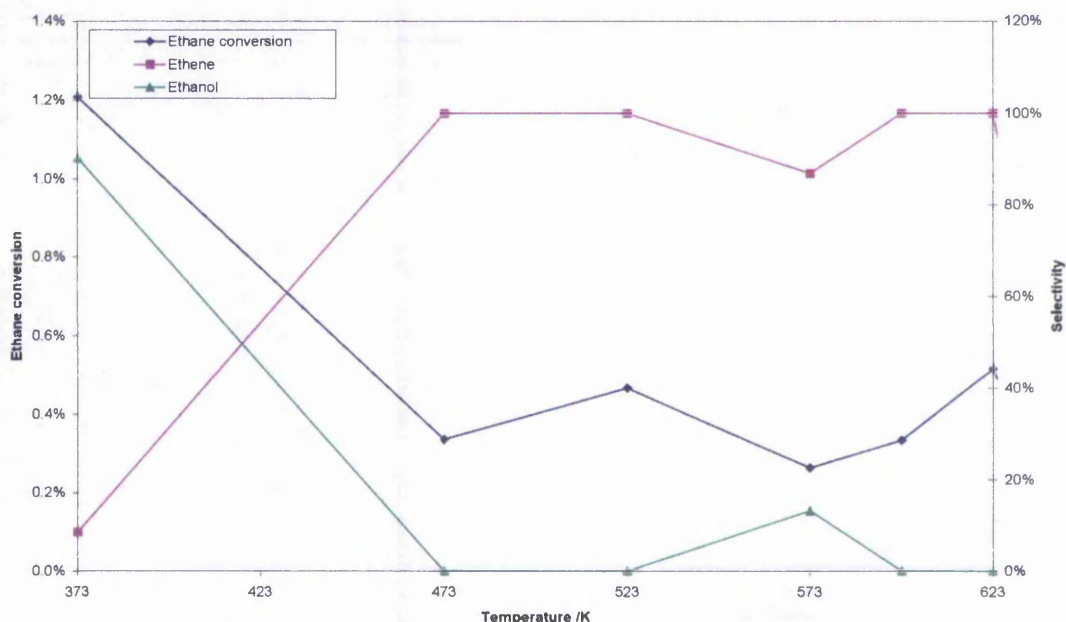

Figure VII-29: Plot of the conversion of ethane and selectivity to products versus time, recorded in the isothermal catalytic testing of reductively activated Fe-MFI SYN24 at 623 K with

The results of the testing of Fe-MFI SYN24 in these conditions is presented in figure VII-30. The conversion of ethane in this experiment was barely

increased, on average 1% over the tested temperature range.

Figure VII-30: Plot of the conversion of ethane and selectivity to products as a function of temperature, recorded for the testing of Fe-MFI SYN24 with nitrous oxide, following a reductive activation.

Two features of interest were recorded however, which were some selectivity to ethanol at 373 K and 573 K. This selectivity reached 90% at lower temperature, and nearly 15% thereafter. At intermediate temperatures only selectivity to ethene was recorded. Again the much lower conversion of ethane observed, compared to samples pre-treated in an oxidative environment, was attributed to a collapse of the MFI framework, possibly accompanied by the migration of iron species to form larger clusters. Unfortunately it was not possible to account for this fact experimentally due to limitations of the instruments available.

During this reaction of ethane with nitrous oxide over Fe-MFI SYN24 the selectivity to ethanol was very high at 373 K, however the conversion of ethane was low, resulting in a poor yield of ethanol overall. The successive injection of two samples at 373 K revealed the complete disappearance of ethanol from the products mixture in a

short time, and it was assumed that the amount of ethanol detected in the sample analysed was the average of the amount of ethanol produced in the reaction over the 30 minutes needed for the chromatographic run. A turnover number of 0.8 mol_{EtOH} mol_{Fe}^{-1} was calculated. Such a low turnover indicates that ethanol may be produced from the stoichiometric reaction of ethane with species formed during the activation of our material. The selectivity to ethanol observed at 573 K, however, may arise from the regeneration of active sites through the decomposition of nitrous oxide, which would be in agreement with the reported behaviour of alpha sites [17, 31].
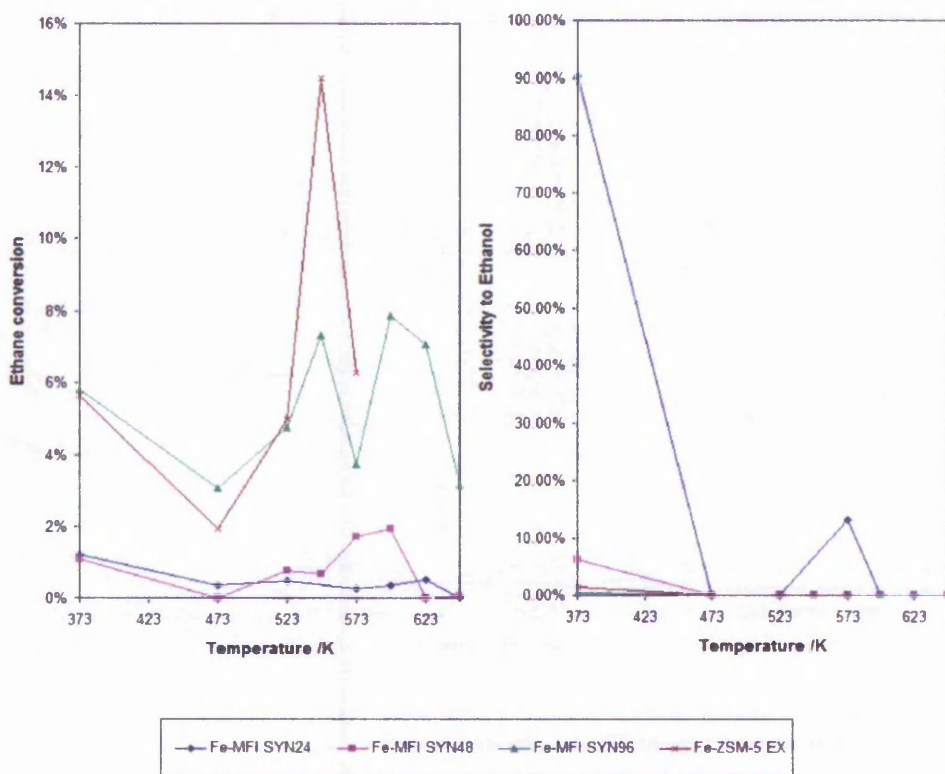
Figure VII-31: Plots of (left) the conversion of ethane and (right) the selectivity to ethanol as a function of reaction temperature, recorded during the catalytic testing of reductively activated materials of MFI structure with nitrous oxide.

In order to differentiate between the possible contributions of stoichiometric and catalytic mechanisms in the production of ethanol over MFI based catalysts with varying iron concentration were tested in the application. Fe-MFI SYN48, Fe-MFI SYN96, and Fe-ZSM-5 EX were therefore subjected to the described reductive pre-

treatment, followed by the temperature-programmed reaction of ethane with nitrous oxide. The results of this study are summarised in the following plots of the calculated conversion of ethane and selectivity to ethanol (fig. VII-31). It is to note that total oxidation products were not observed at any point during the reaction. Minor side products are thought to be present in the outlet mixture, such as methane and possibly acetic acid, however this was not obvious due to their presence in amounts close to detection limits.
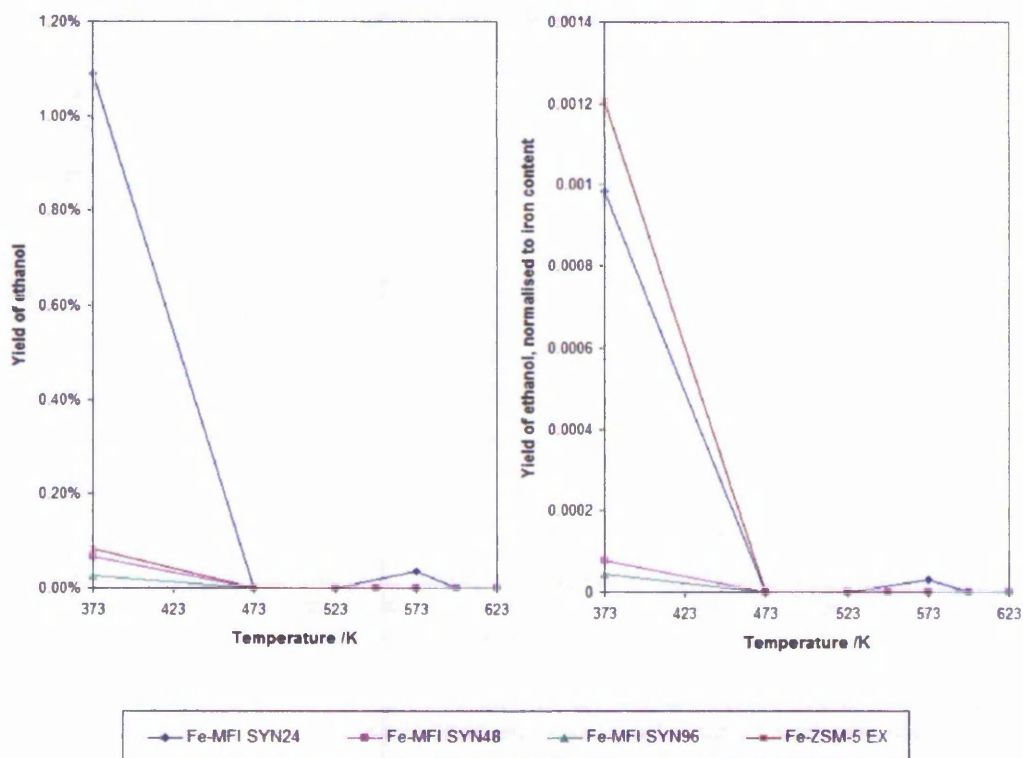
Figure VII-32: Plots of (left) the yield of ethanol and (right) the yield of ethanol normalised to iron concentration as a function of reaction temperature, recorded during the catalytic testing of reductively activated materials of MFI structure with nitrous oxide.

The variation of the concentration of iron in MFI structured materials had a surprising effect on the conversion of ethane. Indeed, figure VII-32 reveals a possible inverse relationship between the iron concentration in our materials and the conversion of ethane. This, again, can be related to the thermal degradation of the zeolites during

their reductive pre-treatment. It is known that both a low Si/Al ratio or a high concentration of protons favour the thermal collapse of the zeolitic framework [34, 35], due to the weakening of Al-O bonds by protons during thermal treatments. The effect of replacing aluminium in the framework with iron is assumed to be similar, as they are both trivalent and integrated in the silica framework in a similar manner, the concentration of protons in the zeolite should be proportional to the concentration of iron. Therefore the observed increase in the conversion of ethane as the iron content of the zeolite is decreased is likely to be related to a lesser extent of the thermal damages in the highest Si/Fe materials.

All the tested materials showed some conversion of ethane at 373 K, followed by a decrease to increase again and find a maximum in the range 523 to 598 K. As discussed the observed conversion was inversely related to the iron content of the material. The selectivity to ethanol, however was proportional to the amount of iron in the material. The high-temperature maximum in conversion observed with all catalysts was accompanied by some selectivity to ethanol only in the case of Fe-MFI SYN24. It is possible that, as the production of ethanol seems related to the concentration of iron in the material, its concentration in the products mixture fell below detection limits at higher temperature. However the increase in ethane conversion observed was only reflected by an increase in the yield of ethene. A sensible explanation for these cannot be developed given the level of structural knowledge of the catalysts.

When the amounts of ethanol detected from the reactions were expressed as yields, and yields normalised to the amount of iron present in the reactor (fig. VII-32), the lowest selectivity of Fe-ZSM-5 EX to ethanol was compensated by the highest activity of its iron centres.

Turnover numbers were calculated, based on the yield of ethanol at 373 K, assuming the latter by averaging the amount of ethanol produced over 30 minutes. The values found for Fe-MFI SYN48 and –SYN96 were 0.08 and 0.04 mol_{EtOH} mol_{Fe}^{-1} respectively, much lower than what was calculated for Fe-MFI SYN24, 0.80 mol_{EtOH} mol_{Fe}^{-1}. For Fe-ZSM-5 EX a turnover number of 1.18 mol_{EtOH} mol_{Fe}^{-1} was found. The production of ethanol from ethane over these materials at 373 K was therefore assumed to be stoichiometric, and it is proposed that Fe-MFI SYN24 is the best candidate for an eventual further study aiming at improving the catalytic system.

VII-4   Summary

The materials synthesised have been tested for the partial oxidation of ethane in a microreactor with online gas chromatographic analysis. Two oxidising agents have been used for this purpose, namely oxygen and nitrous oxide.

A preliminary study consisted in the catalytic testing of $FePO_4$ and supported $FePO_4$ materials, as it has been reported that they show a useful activity for the desired reaction [10, 11]. The results reported were reproduced with only limited agreement. The oxidation of ethane with oxygen only could not be detected on our system. When hydrogen was co-fed to the reaction, however, some activity to partial oxidation was observed. Nitrous oxide was found to be a much more active and selective oxidising agent for the purpose, it appeared however that methanol was a favoured product of reaction. It was assumed that a C-C cleavage mechanism occurred at active oxygen species, likely to involve the production of methyl radicals. It was not possible to enhance the quality of the iron phosphate catalyst by supporting it on either ZSM-5 or MCM-41, as a general loss of selectivity to the oxygenates was obtained with these catalysts. Instead ethene was recorded as major reaction product, originating from the

oxidative dehydrogenation of ethane at moderate temperature and its homogeneous dehydrogenation at higher temperature. During the catalytic testing of Fe-ZSM-5 and Fe-MCM-41,originally taken as comparison for the supported iron phosphates, it was found that they exhibited worthwhile activities for the activation of ethane, and some selectivity to oxygenates in the case of Fe-ZSM-5. In all cases the use of nitrous oxide as oxidising agent resulted in better conversions and selectivity to partial oxygenates. The attempt to favour the activation of dioxygen and dihydrogen to form hydrogen peroxide *in-situ*, by doping Fe-ZSM-5 with minute amounts of gold, showed some limited improvement in the selectivity of the catalysts to partial oxygenates.

The effect of the acidity and the structure of iron on the activity and selectivity of the catalysts was studied by comparing the results of the catalytic testing of various aluminium-free and aluminium-containing silicates of MFI and MCM-41 structure. As some structural information about these materials was obtained following adsorption studies, we were able to suggest that the species responsible for the activation of the alkane were iron dimers or oligomers of structure Fe_4O_4. It was also suggested that Brønsted acid sites in the material participate in the production of hydroxylated species by donating their proton to an oxygenated intermediate. It is thought that a fine tuning of the number and strength of these acidic protons is necessary to promote the formation of alcohols, as they are also believed to be responsible for the dehydration of the latter. The catalyst which yielded the best selectivity to partially oxidised products was Fe-MFI SYN24, and it is believed that the active species in this reaction are the so-called *alpha* oxygens, also responsible for the direct hydroxylation of benzene [17, 31, 36]. Other iron species present in the catalysts, i.e. isolated ions and hematite-like clusters, are thought to have only limited to no activity in the activation of ethane. The selectivity of reaction to ethanol could

be increased further by activating the catalysts in a reducing environment, rather that oxygen, however at the cost of activity, i.e. severely reduced ethane conversion rates. This is in agreement with the proposal that *alpha* oxygen species are the active species in this partial oxidation reaction.

VII-5   References

1.   Willard, H.H., *Instrumental methods of analysis*. 7th . ed. 1988, Belmont, CA: Wadsworth.
2.   McNair, H.M. and J.M. Miller, *Basic gas chromatography / Harold M. McNair, James M. Miller*. Techniques in analytical chemistry series. 1998: John Wiley.
3.   Rouessac, F. and A. Rouessac, *Chemical Analysis - Modern Instrumentation Methods and Techniques*. 5th ed, ed. J.W. Sons. 2000.
4.   Fowlis, I.A., *Gas chromatography*. 2nd . ed. analytical chemistry by open learning. 1995, Chichester: John Wiley & Sons, on behalf of ACOL.
5.   Jennings, W., *Analytical gas chromatography / [by] Walter Jennings*. 1987: Academic.
6.   Handley, A.J. and E.R. Adlard, *Gas chromatographic techniques and applications / e dited by Alan J. Handley, Edward R. Adlard*. Sheffield analytical chemistry. 2000: CRC Press.
7.   David, D.J., *Gas chromatographic detectors / D.J. David*. 1974: Wiley-Interscience.
8.   Alltech Associates, I., *CTR Columns Data Sheet 8700U*. 2002: Deerfield, IL.
9.   Gases, B.O.C. *BOC UK Safety Data Sheets*. 2002-2005 [cited; Available from: http://www1.boc.com/uk/sds/.
10. Wang, Y. and K. Otsuka, *Direct Conversion of Methane and Ethane to the Corresponding Alcohols Using Nitrous-Oxide over Iron Phosphate Catalysts*. Journal of the Chemical Society-Faraday Transactions, 1995. **91**(21): p. 3953-3961.
11. Wang, Y. and K. Otsuka, *Partial oxidation of ethane by reductively activated oxygen over iron phosphate catalyst*. Journal of Catalysis, 1997. **171**(1): p. 106-114.
12. Wang, Y. and K. Otsuka, *Catalytic-Oxidation of Methane to Methanol with H-2-O-2 Gas- Mixture at Atmospheric-Pressure*. Journal of Catalysis, 1995. **155**(2): p. 256-267.
13. Corneille, J.L. and R. Brais, *Thermal dehydrogenation of ethane*. Annales de l'ACFAS, 1951. **17**: p. 88-90.
14. McCormick, R.L., et al., *Methane partial oxidation by silica-supported iron phosphate catalysts. Influence of iron phosphate content on selectivity and catalyst structure*. Topics in Catalysis, 2000. **10**(1-2): p. 115-122.
15. Kulikova, V.S., A.F. Shestakov, and A.E. Shilov, *Possible mechanism of C-C bond cleavage in the oxidation of alkanes mediated by iron compounds*. Kinetics and Catalysis, 1999. **40**(2): p. 287-288.

16. Buijs, W., *Challenges in oxidation catalysis.* Topics in Catalysis, 2003. **24**(1-4): p. 73-78.

17. Starokon, E.V., et al., *Mechanisms of iron activation on Fe-containing zeolites and the charge of alpha-oxygen.* Topics in Catalysis, 2003. **23**(1-4): p. 137-143.

18. Jia, J.F., et al., *Identification of highly active iron sites in N₂O-activated Fe/MFI.* Catalysis Letters, 2002. **82**(1-2): p. 7-11.

19. Ivanov, A.A., et al., *Kinetics of benzene to phenol oxidation over Fe-ZSM-5 catalyst.* Applied Catalysis a-General, 2003. **249**(2): p. 327-343.

20. Bond, G.C. and D.T. Thompson, *Catalysis by gold.* Catalysis Reviews-Science and Engineering, 1999. **41**(3-4): p. 319-388.

21. Okumura, M., et al., *Direct production of hydrogen peroxide from H₂ and O₂ over highly dispersed Au catalysts.* Chemistry Letters, 2003. **32**(9): p. 822-823.

22. Landon, P., et al., *Direct synthesis of hydrogen peroxide from H₂ and O₂ using Pd and Au catalysts.* Physical Chemistry Chemical Physics, 2003. **5**(9): p. 1917-1923.

23. Wang, Y., et al., *Characterizations of iron-containing MCM-41 and its catalytic properties in epoxidation of styrene with hydrogen peroxide.* Journal of Catalysis, 2002. **209**(1): p. 186-196.

24. Hughes, M.D., et al., *Tunable gold catalysts for selective hydrocarbon oxidation under mild conditions.* Nature, 2005. **437**(7062): p. 1132-1135.

25. Frusteri, F., et al., *Partial Oxidation of Ethane by in-Situ Generated H₂O₂.* Catalysis Letters, 1994. **27**(3-4): p. 355-360.

26. Otsuka, K. and Y. Wang, *Direct conversion of methane into oxygenates.* Applied Catalysis a-General, 2001. **222**(1-2): p. 145-161.

27. Berlier, G., et al., *Evolution of Extraframework Iron Species in Fe Silicalite.* Journal of Catalysis, 2002. **208**(1): p. 64-82.

28. Joyner, R. and M. Stockenhuber, *Preparation, Characterization, and Performance of Fe-ZSM-5 Catalysts.* Journal of Physical Chemistry B, 1999. **103**(29): p. 5963-5976.

29. Marturano, P., et al., *The mechanism of formation of the Fe species in Fe/ZSM-5 prepared by CVD.* Physical Chemistry Chemical Physics, 2001. **3**(24): p. 5585-5595.

30. Capek, L., et al., *Analysis of Fe species in zeolites by UV-VIS-NIR, IR spectra and voltammetry. Effect of preparation, Fe loading and zeolite type.* Microporous and Mesoporous Materials, 2005. **80**(1-3): p. 279-289.

31. Dubkov, K.A., et al., *Evolution of iron states and formation of alpha-sites upon activation of FeZSM-5 zeolites.* Journal of Catalysis, 2002. **207**(2): p. 341-352.

32. Schuurman, Y., et al., *Low temperature oxidative dehydrogenation of ethane over catalysts based on group VIII metals.* Applied Catalysis, A: General, 1997. **163**(1-2): p. 227-235.

33. Zhu, Q., et al., *Effect of high-temperature treatment on Fe/ZSM-5 prepared by chemical vapor deposition of FeCl₃II. Nitrous oxide decomposition, selective oxidation of benzene to phenol, and selective reduction of nitric oxide by isobutane.* Journal of Catalysis, 2004. **221**(2): p. 575-583.

34. Li, C.Y. and L.V.C. Rees, *Ion-Exchange, Thermal-Stability and Water Desorption Studies of Faujasites with Different Si Al Ratios.* 1988. **7**(2-3): p. 89-99.

35.   Ambs, W.J. and W.H. Flank, *Calcined Faujasite Series - Reply.* 1970. **18**(2): p. 238-&.

36.   Pillai, K.S., J.F. Jia, and W.M.H. Sachtler, *Effect of steaming on one-step oxidation of benzene to phenol with nitrous oxide over Fe/MFI catalysts.* Applied Catalysis a-General, 2004. **264**(2): p. 133-139.

General Summary and Conclusions

During this study iron and iron phosphate based materials have been prepared, characterised, and tested for the partial oxidation of ethane to ethanol. The principal aims of the study were to develop, characterise and understand catalyst for the reaction stated above. Parameters thought to influence the reaction and studied here include the reducibility of the transition metal, its local structure in the catalysts, the acidity of the materials, and some reaction conditions such as the catalyst's activation conditions, temperature of reaction and oxidising agent used. The potential catalysts studied included bulk iron phosphates, as well as iron phosphates, iron and gold supported on zeotypes of MFI and MCM-41 structure. The preparation procedures used for the modification of silicate and aluminosilicate supports included aqueous ion-exchange, impregnation, chemical vapour deposition and bulk synthesis.

The crystalline or bulk structures of the materials prepared were characterised by powder x-ray diffraction Physical adsorption of nitrogen at 77 K was used for the study of their surface area and porosity, using the Brunauer, Emmet, and Teller model of adsorption. The concentration of iron in silica-supported materials was assessed by digestion of the samples and analysis of the resulting solutions by atomic absorption spectroscopy. It resulted from these studies that the bulk iron phosphate materials prepared had a low surface area but little crystalline character, in contrast with the quartz-like structure reported in similar studies. The parent MCM-41 silica prepared had a good long-range order, which was partially destroyed by their post-synthetic treatment with iron, aluminium, or phosphorus. This occurred by thinning of the walls separating the hexagonal array of pores characteristic of these materials. Silicates and aluminosilicates of MFI structure had a much higher stability to these various post-

synthetic treatments, with little to no alterations of their crystalline and porous structures observed.

As the hydrocarbon and oxidising agents studied here are believed to be catalytically activated through a redox reaction at an iron centre, the reducibility of the materials was studied by temperature programmed reduction experiments. The main outcome of this study was the lowering of the reduction temperature of iron by 50 to 100 K when iron phosphates were supported on the stated zeotypes. It is believed that this lower reduction temperature is due to the presence of smaller particles of $FePO_4$ on the surface of the support, more readily reduced than the bulk material. It was also recorded that the presence of phosphorus in the vicinity of iron had the effect of increasing the reduction temperature of iron by on average 200 K, compared to their iron-only containing pairs. The presence of aluminium in materials of MFI and MCM-41 structure lowered the temperature of reduction of iron by 200 K in the former, but increased it by 75 K in the latter. Following the catalytic testing of the iron phosphate based materials a relationship was observed between the ease of reducibility of iron and the temperature at which the highest selectivity to partially oxygenated products was recorded. Such a relationship was not observed with phosphate-free catalysts, however this was interpreted as to be due to the presence of more varied structures of iron species in their framework. Indeed, in TPR studies of materials of MFI structure various hydrogen uptake peaks were recorded, attributed to the reduction of iron species of different structures. Minor reduction features were recorded at temperatures as low as 473 K and may be related to the iron species responsible for the materials' catalytic activity. However, apart from the attribution of high temperature hydrogen uptake peaks to the reduction of iron in larger, hematite-like clusters, to its metallic state, the speciation of various iron species from TPR data

is speculative. It was nevertheless possible to give a more specific account of the iron species present on the zeotypes' surface using nitric oxide as a probe gas in adsorption studies with *in-situ* infrared detection. The population or de-population of bonding and anti-bonding molecular orbitals in different iron - nitric oxide complexes cause a variation of the frequency of the Fe-NO vibration band. A revised assignment of the iron – nitric oxide vibration bands observed in the studied zeotypes was formulated, as disagreement was found in previous reports. Infrared vibration bands were assigned for nitric oxide adsorbed on isolated iron sites, dimers, oligomers of Fe_4O_4 formula, and larger hematite-like clusters. From these assignments it was proposed that iron is present in siliceous MCM-41 nearly exclusively as isolated sites. When MCM-41 contained aluminium as well as iron, it was found that iron was not located preferentially at ion-exchange sites, instead isolated iron species were observed at both aluminium and non-aluminium sites. In materials of MFI structure, iron was present as a mixture of the four structures reported, in relative amounts depending on the preparation method used: the aqueous ion-exchange method favoured the formation of oligomers and iron dimers seemed to be formed preferentially in the bulk synthesis. The chemical vapour deposition method favoured the formation of isolated sites when the sample was calcined in pure oxygen, and larger clusters when calcined in air. A 10 cm^{-1} blue shift of the band corresponding to nitric oxide adsorbed on isolated iron ions at ion-exchange position, compared to isolated iron species in siliceous materials, indicates a more pronounced electron donation from the (FeAl) pair to its surroundings than iron only. Little nitric oxide was adsorbed on iron phosphate related materials. Following the catalytic testing of these materials, using nitrous oxide as the oxidising agent, it was proposed that the iron species active for the partial oxidation of ethane were dimers or oligomers, with little activity from

isolated iron sites and larger clusters being spectator species. Iron phosphate related materials were found inappropriate catalysts for the desired reaction, only low conversions were calculated at temperatures below 673 K (approximately 4%), and lacked selectivity to partial oxidation products, as some total oxidation occurred at these temperatures. It is believed that the reaction follows a pathway similar to the one reported in the direct hydroxylation of benzene over Fe-MFI catalysts, where nitrous oxide is dissociated at active iron sites, forming a reactive "alpha" oxygen species. Indeed, and similarly to the benzene to phenol conversion, the properties of the catalysts were enhanced when activated in a reducing environment, their selectivity to partial oxygenates increasing. It is proposed that the reaction of the hydrocarbon with "alpha" oxygen results in an oxygenated intermediate, which is easily cleaved to methyl and methoxy species. Indeed, with most materials that were catalytically active and selective to partial oxygenates a significant part of the products consisted in methanol and methane. In some cases higher chain hydrocarbons were also detected as products of the reaction, indicating than the methyl species formed from the cleavage of the oxygenated intermediate probably has a radical character. Some ethanol was detected in the pool of products, with a maximum yield of 1% over an iron silicalite catalyst, which could result from the protonation of a non cleaved oxygenated intermediate at a Brønsted acid site in the catalyst. The amount and strength of the acid sites present in the catalyst is thought to have an important effect on the product distribution of the reaction. The type and strength of acid sites in our materials was studied by adsorption and thermal desorption of ammonia, and revealed that only materials containing a mostly Brønsted acid character were able to catalyse the formation of alcohols from the alkane. The stronger sites however promoted the subsequent dehydration of the alcohol, as highlighted by the higher selectivity to

ethene observed with Fe-ZSM-5 materials, where Fe-MFI materials favoured oxygenates.

Dioxygen proved to be too strong an oxidising agent for the desired reaction. When the materials were tested for catalytic activity using the latter mostly carbon dioxide, the total oxidation product was obtained. The selectivity to partial oxygenates was found zero in all cases, and as the co-feed of hydrogen effectively quenched the total oxidation process, mostly the oxidative dehydrogenation product ethene was detected. Moreover the calculated conversions of ethane were systematically lower than the ones observed when nitrous oxide was used as the oxidising agent, which indicates that our materials have a lesser ability to produce active oxygen species, responsible for the activation of ethane, from dioxygen than nitrous oxide. The doping of the materials with small amounts of gold, to favour the *in situ* activation of dioxygen and hydrogen, showed only limited success. Oxygenates were detected only in the case of a catalyst where gold was introduced by aqueous ion exchange, rather than impregnation, with a maximum selectivity of only 0.6 %.

The materials which showed the most promising results for the desired application were Fe-ZSM-5 prepared by aqueous ion-exchange, and Fe-MFI, using nitrous oxide as oxidising agent. A yield of 18% oxygenates was obtained with the former catalyst when the reaction was carried out isothermally at 673 K, of which the yield of ethanol was only 1.5 % however. Its main disadvantage was its lack of selectivity to partial oxidation, as a selectivity of 27 % to carbon dioxide was calculated. The latter catalyst yielded 1 % ethanol at 673 K, however was selective to partial oxidation products as only ethene was detected as a secondary product. The position of these two materials as best catalysts tested during this project confirms the involvement and value of iron dimers and/or oligomers for partial oxidation purposes.

Future Work

A variety of strategies and catalysts have been imagined and tested for the partial oxidation of ethane to ethanol. The least successful of these was an attempt to favour the *in situ* production of hydrogen peroxide from dioxygen and hydrogen over gold containing materials. Even though the yield of ethanol obtained with these materials was minimal, an improvement in selectivity to the partial oxygenate was recorded, compared to their gold free equivalents. As it is generally believed that fine gold dispersions give better oxidation catalysts some further effort could be put in the synthesis of such materials, with higher gold loading than the ones presented in this work. Methods for the preparation of supported ultrafine gold particles have been reported and could be worthwhile investigating. It could be imagined that a support containing iron as mainly isolated cations may give best results, in the biomimetic approach to the P450 cytomchrome monooxygenase enzyme. The preparation of such iron-gold materials supported on zeolites may be challenging due to the little control over species formed on their surface, however an iron phosphate supported gold dispersion may be easier to prepare. Even though iron phosphate materials were reported to be unviable catalysts for the studied reaction, supporting an iron phosphate phase on a silica or aluminosilicate generally caused an increase in activity of the material, reflected by an increase in turnover. This was attributed to the increase of the number of active sites available for activation of the hydrocarbon, related to the surface area of the material. In some recent study porous iron phosphate materials have been produced, and their catalytic behaviour is believed to be worth investigating. Similarly aluminium phosphate (AlPO) based materials could raise interest for partial oxidation purposes. AlPO materials are crystalline microporous

materials which structure can be directed in the same way as zeolites. A number of different structures have been synthesised to date, including one MFI type framework (AlPO-5). Good results have already been achieved using these structures as catalysts for aromatic compounds partial oxidation [130].

The most promising materials in this study were Fe-ZSM-5 prepared by aqueous ion-exchange and Fe-MFI, an isomorphously substituted equivalent of ZSM-5. It was concluded that the active species in the former were iron oligomers of Fe_4O_4 formula, formed preferentially when the zeolite was modified in aqueous medium. The further development of the post-modification method used, to yield a material containing exclusively such oligomers, is believed feasible. The further characterisation of the material by a combination of nitric oxide adsorption and x-ray absorption spectroscopy would give valuable information about the structure of active sites, still subject to debate. The investigation of the electron-donating effect of the (FeAl) pair noticed upon adsorption of nitric oxide, by means of x-ray absorption spectroscopy, could yield interesting information potentially leading to a further understanding and development of good electron-transfer catalysts. Our Fe-MFI materials showed excellent selectivity to partial oxidation products, when activated under reducing conditions. It is believed however that the Si/Fe ratio of 24 in our most active catalyst is not optimal and the preparation and testing of more Fe-MFI catalysts with various iron concentrations should be attempted. Their mechanism of reaction is believed to be similar to the one proposed for the direct hydroxylation of benzene, in which the pre-treatment of the catalyst in steam was reported to yield best conversions. A comparison of the effect of a reductive or steaming pre-treatment on this type of catalyst towards the partial oxidation of ethane may be the most important next step of the study.

Some reaction conditions may also be varied, as only the optimal temperature range for the discussed conversion was studied here. For example only brief adjustments of the reagents contact time with the catalyst were made and, as the potential catalyst range has been effectively reduced, a finer adjustment of this parameter is believed worthwhile. Some other conditions that could be considered include the pressure of the reactor, in order to favour the thermodynamics of the reaction, and, as acid sites are believed to be part of the catalytic process as proton donors, their regeneration *in situ*, by co-feed of hydrogen to the nitrous oxide and ethane mixture for example, could be studied.

A good further understanding of factors affecting the activity of catalysts for the partial oxidation of ethane to ethanol was obtained during this study, however due to the difficulty to catalyse such reactions a number of parameters and materials are still left to investigate. Some ideas were given here, in the hope to inspire the reader.